FAILURE CHARACTERIZATION IN ROCK ENGINEERING USING A UNIFIED DFN-FDEM ANALYSIS APPROACH

by

Ladan Karimi Sharif

B.Eng., University of Tehran, 2011

M.A.Sc., Laurentian University, 2013

A THESIS SUBMITTED IN PARTIAL FULFILLMENT OF

THE REQUIREMENTS FOR THE DEGREE OF

DOCTOR OF PHILOSOPHY

in

THE FACULTY OF GRADUATE AND POSTDOCTORAL STUDIES

(Mining Engineering)

THE UNIVERSITY OF BRITISH COLUMBIA

(Vancouver)

August 2019

The following individuals certify that they have read, and recommend to the Faculty of Graduate and Postdoctoral Studies for acceptance, the dissertation entitled:

FAILURE CHARACTERIZATION IN ROCK ENGINEERING USING A UNIFIED DFN-FDEM ANALYSIS APPROACH

submitted by Ladan Karimi Sharif in partial fulfillment of the requirements for

the degree of Doctor of Philosophy

in Mining Engineering

Examining Committee:

Dr. Davide Elmo
Co-supervisor

Professor Doug Stead
Co-supervisor

Professor Erik Eberhardt
Supervisory Committee Member

Dr. Maria Holuszko
University Examiner

Professor Mahdi Taiebat
University Examiner

Professor Giovanni Barla
University Examiner

Additional Supervisory Committee Members:

Professor Scott Dunbar
Supervisory Committee Member

Abstract

This thesis presents a unified approach for better understanding the failure mechanisms associated with naturally fractured rock masses. With the advances in computing power, it is now possible to simulate rock engineering problems in a more realistic manner by including the effects of natural fracture networks. By integrating discrete fracture networks (DFN) with hybrid finite-discrete element models (FDEM), it is possible to fully account for block kinematics, fracturing processes and to capture anisotropic behaviour in an explicit manner. Key contributions include:

i) Developing techniques to provide geometrical and statistical analysis of discrete fracture networks prior to implementation in geomechanical software;

ii) Developing techniques that allow for direct integration of discrete fractures in FDEM models by solving key issues relating to generating good quality finite element meshes and minimizing the presence of distorted elements.

iii) Developing a series of techniques to improve on the analysis of FDEM outputs; the proposed methods are capable of calculating the length of induced fractures and tracking whether these fractures interact with existing fractures to form new blocks.

iv) Developing methods to capture block formation directly from simulation mesh data, skipping the simplification and inaccuracy of fracture lines, by utilizing graph data structures and graph theory.

v) Developing methods to analyze blocks spatially within each timestep, and more importantly, introducing techniques relating those blocks and their analysis temporally, across timesteps.

The entire set of newly developed techniques is applied to investigate the behaviour exhibited in simulated pillar models using existing empirical and numerical methods to make the problem more

tractable and allow calibration of the results. The innovative techniques developed in this thesis are generic and could be applied to a variety of rock engineering problems in which it is important to determine the relative role of brittle and structurally controlled failures, including block caving fragmentation, and slope and tunnel stability analysis.

The techniques developed in this thesis are defined as sets of rules to be followed in certain order and they provide the ground work needed to utilize machine leaning algorithms to investigate the relationship between initial DFN configuration and structural and brittle damage.

Lay Summary

This thesis explores the process and potential implications including mathematical representation of natural fracture systems, termed discrete fracture networks (DFN), with advanced computer models capable of simulating stress-induced fracturing arising from engineering activities (e.g., underground excavations). Current methods of analyzing stress-induced fracturing are presented, together with their limitations, to highlight the need for improved methods. These are developed to provide improved static fracture analyses. DFN and mesh cleaning algorithms are introduced to provide good quality finite element meshes that reduce associated errors in the simulation results. Rock mass failure mechanisms for rock engineering projects can be both structurally controlled and stress-induced brittle failures. This thesis demonstrates the effectiveness of new approaches to analyze rock mass failure and how it is possible to relate the observed mechanisms to the initial fracture configuration (spatially and temporally). Insights are provided into future integration of the proposed methodologies with machine learning.

Preface

The thesis is original and independent work by the author. The author was the lead author of four published conference papers and one journal paper and two submitted journal papers based on the work of this thesis. The co-authors of these papers are the thesis supervisors.

The paper *"Simulation of rock bridge failure at the laboratory scale using a combined FDEM modeling and discrete crack network approach using Irazu and Elfen FDEM"* published in the Proceeding of 2016 50th U.S. the American Rock Mechanics Association in Texas, Houston is based on chapter 3 of this thesis.

The paper *"DFNAnalyzer: A web-Based application for Discrete Fracture Network Analysis"* published in the Proceedings of 2018 2nd International Discrete Fracture Network Engineering the Seattle, Washington is based on chapter 4 of this thesis.

The paper *"DFNCleaner: A novel automated approach to improve DFN integration for geomechanical analysis"* published in the Proceeding of 2018 2nd International Discrete Fracture Network Engineering the Seattle, Washington is based on chapter 4 of this thesis.

The paper *"Investigating the factors controlling intact rock damage mechanisms in jointed pillars" published in the* in the Proceeding of 2019 53th U.S. the American Rock Mechanics Association in New York City is based on chapter 6 of this thesis.

The paper *"Improving DFN-geomechanical model integration using a novel automated approach"* is published in the Computer and Geotechnics Journal is based on chapter 4 of this thesis.

The paper *"New methods to quantify damage and rock mass blockiness formation"* is to be submitted to journal based on chapter 5 of this thesis.

The paper *"Investigating the factors controlling intact rock damage mechanisms for naturally fractured pillars"* is submitted to journal based on chapter 6 of this thesis.

Table of Contents

List of Tables

List of Figures

Glossary

DFN	Discrete Fracture Network
KDE	Kernel Density Function
FDEM	Finite-Discrete Element Model
DEMFA	Discrete Element Method Fracture Analysis
$\boldsymbol{D_{20}}$	Total number of fractures divided by area
$\boldsymbol{D_{21}}$	Total length of fractures divided by area
DEMBA	Discrete Element Method Block Analysis
BSD	Block Size Distribution
$\boldsymbol{B_{10}}$	Specific block size in which 10% of total blocks are smaller than that size
$\boldsymbol{B_{25}}$	Specific block size in which 25% of total blocks are smaller than that size
$\boldsymbol{B_{50}}$	Specific block size in which 50% of total blocks are smaller than that size

Acknowledgements

I would like to thank Dr. Davide Elmo and Professor Doug Stead for their continuous supervision and support during my studies. I would like to thank the members of the Supervisory Committee, Professor Erik Eberhardt, Professor Scott Dunbar, and Mr. Charles Hunt for their valuable contribution and feedback through our meetings. I would like to thank my examiners, Professor Mahdi Taiebat, Dr. Maria Holuszko and Professor Giovanni Barla for their comments and suggestions.

I acknowledge the financial support through the Natural Sciences and Engineering Research Council of Canada (NSERC) grants held by Dr. Davide Elmo.

Thank you to my family and friends for their unconditional support.

Dedication

To my parents:

Alemeh and Habib

Chapter 1: Introduction

1.1 Problem Statement

The mechanical behaviour of fractured rock masses depends on three fundamental parameters: i) geological structures, including the intensity, orientation and size of natural fractures; ii) stress, including the relationship between in-situ and induced stresses, which may result in new cracks to be created and existing fractures to be extended; and iii) strength, including that of the intact rock material in between fractures and the shear strength of the fractures. The use of an integrated discrete fracture network (DFN) and finite-discrete element method (FDEM) numerical analysis allows to fully capture the interdependence of those parameters. However, a comprehensive characterization of failure mechanisms at various scales using dedicated DFN-FDEM techniques requires the development of a "*unified approach"* to ensure that model generation becomes a more objective process, and more importantly allows to quantify modelling outputs, including pre- and post- fracture properties, indicators of fracture network characterization and block fragmentation.

This thesis introduces new techniques for DFN analysis and integration with FDEM software; furthermore, new post-processing capabilities have been added with the ability to correlate fracture traces in the pre-existing DFN model, to newly generated fractures and the resulting fully formed blocks (parent-to-child genealogical tree approach). The latter has far reaching implications as it lays the foundations for machine learning applications for categorizing a variety of rock failure mechanisms.

1.2 Research Objectives

The primary objectives of this research are:

1. To develop improved means to fully analyze discrete fracture network models to eliminate the need for manual editing and maximize mesh quality when importing them into numerical simulation software;
2. To eliminate or significantly complement the use of image analysis or qualitative visualization of "screen-capture (snapshots)" in understanding the generation of newly-created fractures and/or newly-created blocks;
3. To establish the relationship between pre-existing fractures, stress-induced fractures and newly-generated blocks; and
4. To quantitatively categorize rock mass to various failure modes including brittle failure, structurally-controlled failure, and combinations of the two. Also, a quantitative approach has been adopted for failure characterization.

By accomplishing these research objectives, the following important contributions are expected:

1. The development of advanced geometrical and optimization methodologies to improve on key problems that to date have limited the use of DFN models in advanced geomechanical modelling, including use with FEM, DEM and FDEM modelling approaches. The newly developed techniques will offer a robust and fast solution to the problem of considering multiple generations of the same DFN model to account for the variability that is inherent in stochastic models such as DFNs;
2. The development of new techniques that enable spatial and temporal analysis of FDEM simulation output;

3. The development of methodologies that allow the reconstruction of newly-generated fractures within the finite element mesh, thus calculating induced fractures intensity indications (e.g., D_{21}, total length of induced fractures per area; I_{20}, total number of fractures intersection per area) and relating these to the initial fracture network;
4. The development of new techniques that capture the block formation and analyze their properties. Furthermore, new techniques will be introduced to relate these blocks temporally, in a parent-to-child genealogical tree approach, in addition to relating them to the blocks in the initial fracture network; and
5. The development of new techniques (maps and indices) and methodologies to establish the relationship between DFN configurations and the resulting rock failure mechanisms. These new techniques will include brittle-block tracking tree and brittle fracture maps.

1.3 Thesis Structure

This thesis consists of seven chapters and two appendices. The present chapter serves as an introduction to the entire dissertation, while chapter 7 provides a discussion and recommendations for future research. One peer-reviewed journal paper was submitted and published during the time required to complete the dissertation, in addition to four conference papers that underwent minor peer-reviewing and two papers that are to be submitted to international peer-refereed journals. The thesis structure is presented graphically in Figure 1, and is detailed as follows:

- Chapter 2 reviews some of the fundamental aspects of Discrete Fracture Network (DFN) and characterization in which various DFN properties are described and a chronological review of block calculation and analysis is also presented. A review of optimization techniques, block

characterization and numerical modelling in rock mechanics, with specific attention to numerical modelling of fractured rock masses is also completed. State of the art numerical methods for rock mechanics problems are introduced, with a discussion on the difference between continuum and discontinuum methods and on the use of numerical methods to investigate brittle failure of rock.

- Chapter 3 reviews the computational characteristics of the hybrid software Elfen and Irazu and shows their application in modelling a simple laboratory sample with two pre-existing fractures. This chapter highlights the use of the FDEM method to capture the various stages involved in brittle fracturing of a laboratory rock sample from crack initiation to crack coalescence, propagation and failure. Also, this chapter describes preliminary work by the author exploring problematic areas in the use of the DFN-FDEM numerical modelling approach. The results of this chapter prompt new questions that are subsequently addressed in chapters 4, 5 and 6 of this thesis.
- Chapter 4 presents innovative new algorithms for analyzing and cleaning complex discrete fracture networks using geometrical and Monte Carlo simulation methods. These analytical algorithms provide quantitative metrics for measuring various geometrical DFN properties. The DFN cleaning algorithms provide a suitable DFN which can be implemented within a variety of numerical modelling software, while minimizing the changes to the initial DFN.

- Chapter 5 presents new innovative computational and graph analysis algorithms to compute fracture lines and blocks in geomechanical modelling software, in addition to analyzing them.

- Chapter 6 demonstrates the applicability of the developed methods described in the first four chapters to the simulation of sixteen pillar models with four of these models being chosen for further detailed analysis and failure mechanism investigations.

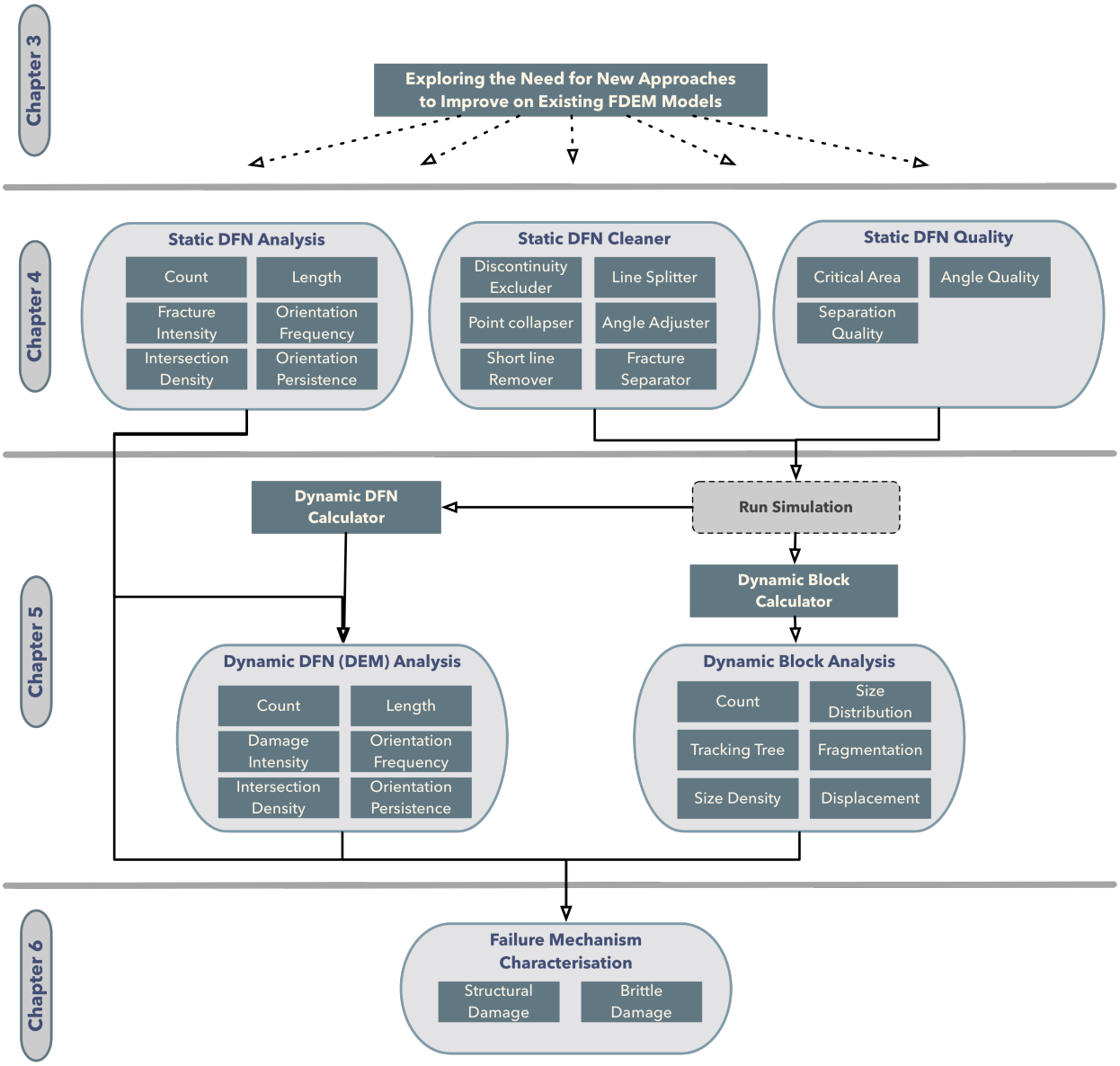

Figure 1.1 Research and thesis structure.

Chapter 2: A Review of Numerical Analysis Techniques

This chapter provides a review of numerical approaches for rock engineering problems, with emphasis on the use of discrete fracture network (DFN) models when integrated with geomechanical models. A large number of numerical models have been developed in the past 20-30 years; this chapter does not aim to describe those numerical models and their mathematical formulations in detail, rather the objective is to provide the required framework to understand the driving ideas that form the foundation of the current research project.

2.1 Discrete Fracture Network (DFN) Models

DFN modelling is the process of simulating realistic fracture networks based on statistical distributions obtained from field surveys of key properties such as fracture orientation, fracture length and fracture intensity. DFN models could be generated using either a fully stochastic approach, or using a hybrid stochastic-deterministic approach, whereby faults and bedding planes may be modelled deterministically, while smaller-scale features (e.g. joints) would be simulated using field based statistical distributions (e.g. Schlotfeldt et al., 2018; Miyoshi et al., 2018, Zuo et al., 2019).

As discussed in Elmo et al. (2015), it is important to consider the limitations that are inherently introduced in the analysis by the sampling methods used to derive the key statistical information for DFN analysis. The stochastic nature of DFN models is such that there are an infinite number of equiprobable fractures simulations that could be generated based on the mapped data. This is a key aspect of the integration of DFN models in geomechanical models and the focus of Chapter 4,

which presents an example of the importance of better characterizing the inherent variability associated with the stochastic analysis of fracture networks and the associated implications for stability analyses. DFN models are at the core of the current research, therefore it is important to review fundamental principles of DFN modelling. These are briefly described in the following sections.

2.1.1 Fracture Orientation

Fracture orientation is usually measured as the dip angle (measured from the horizontal) and the azimuth (dip direction) of the line that represents the steepest inclination across the fracture plane. Note that in this thesis the terms "discontinuity" and "fracture" and "joint" are used as synonyms to define structural features other than bedding planes and faults, independently of their genesis.

Fractures may be grouped into sets based on their relative orientation, and well accepted hemispherical distributions such as Fisher, Bingham, bivariate Fisher or bivariate Bingham could be used to represent a symmetrical distribution of the fracture orientations around a given mean (Priest, 1993). The degree of clustering is determined using the dispersion coefficient (K), whereby a larger K value indicates a well-defined cluster, Figure 2.1. The Fisher probability density function is given in Equation 1 (Priest, 1993), where θ denotes the angular deviation from discontinuity orientation value (Dip).

$$\boldsymbol{f(\theta) = \frac{K \sin\theta e^{K\cos\theta}}{e^{K} - e^{-K}}} \qquad \textbf{[Eq. 1]}$$

So-called "bootstrapping" techniques could be used to describe orientation data that does not conform to any specific statistical method (Elmo et al., 2015; Schlotfeldt et al., 2018). The

"bootstrapping" technique is described in (Elmo et al., 2015) as a method whereby multiple random sampling is used to create a pseudo-replicate sample of fracture orientations.

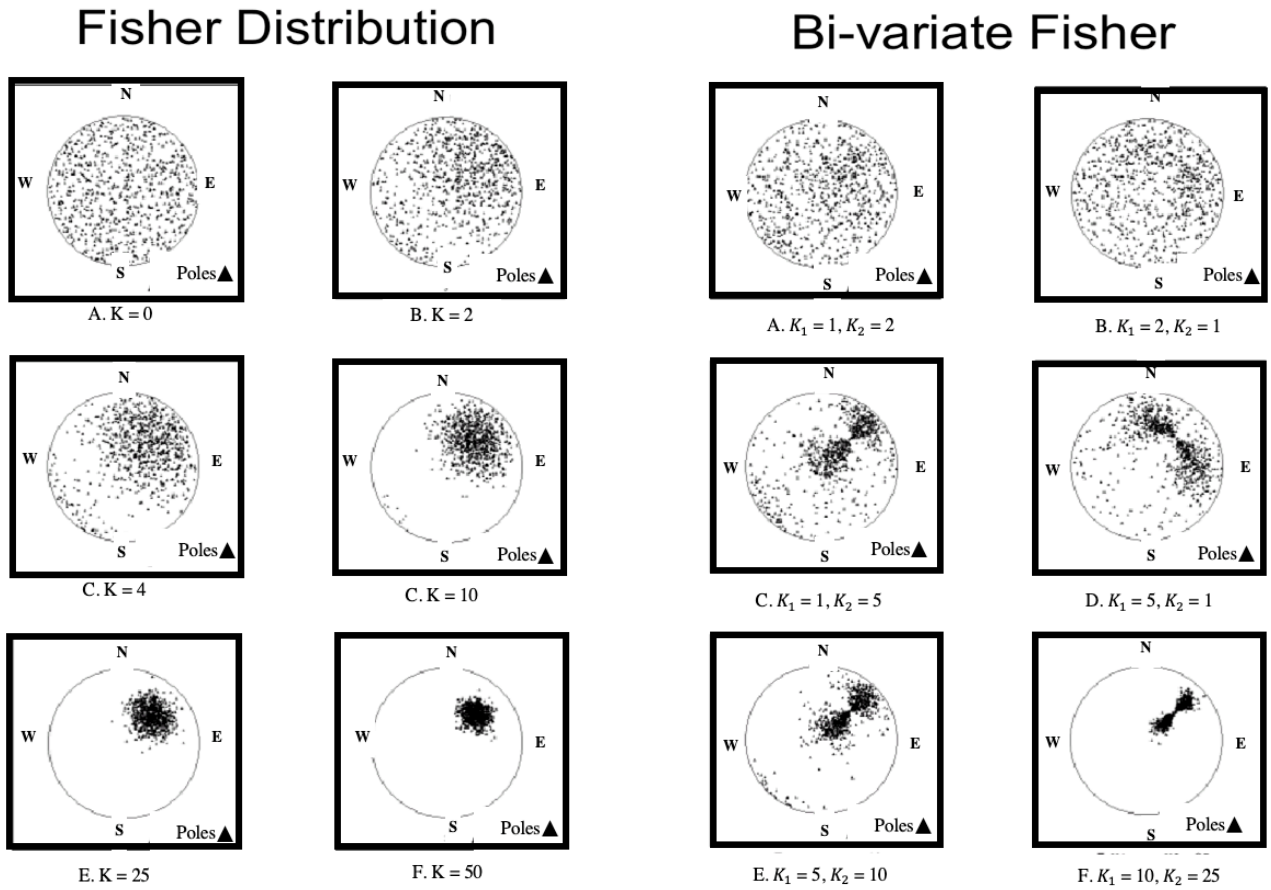

Figure 2.1. Example of orientation distributions (reproduced from the FracMan manual, Golder, 2018).

2.1.2 Fracture Size

The size of a fracture can be described by either its length or its equivalent radius, Figure 2.2. The two definitions are not equivalent, and care should be taken not to confuse the two definitions when generating a DFN model (Elmo et al., 2015). Measurements of fracture length can be obtained by mapping 2D rock exposures, using conventional (scanline or window mapping) or remote sensing mapping techniques, in which case the fracture size is often measured as the radius

of a disc inscribing the mapped feature (e.g. Vivas et al., 2013; Tannant, 2015). Despite its geometrical definition (radius), fracture size measured using remote sensing techniques does not coincide with the actual equivalent radius of the fracture whose trace length is being measured. Theoretical models exist that define the diameter of an idealized fracture with elliptical shape (e.g. Mauldon, 1998; Zhang and Einstein, 1998), or the edge length of a conceptual square fracture (Jennings, 1970). However, in practical applications, persistence is the length of the joint which intersects the scanline or mapping window (e.g. Zhang and Einstein, 1998).

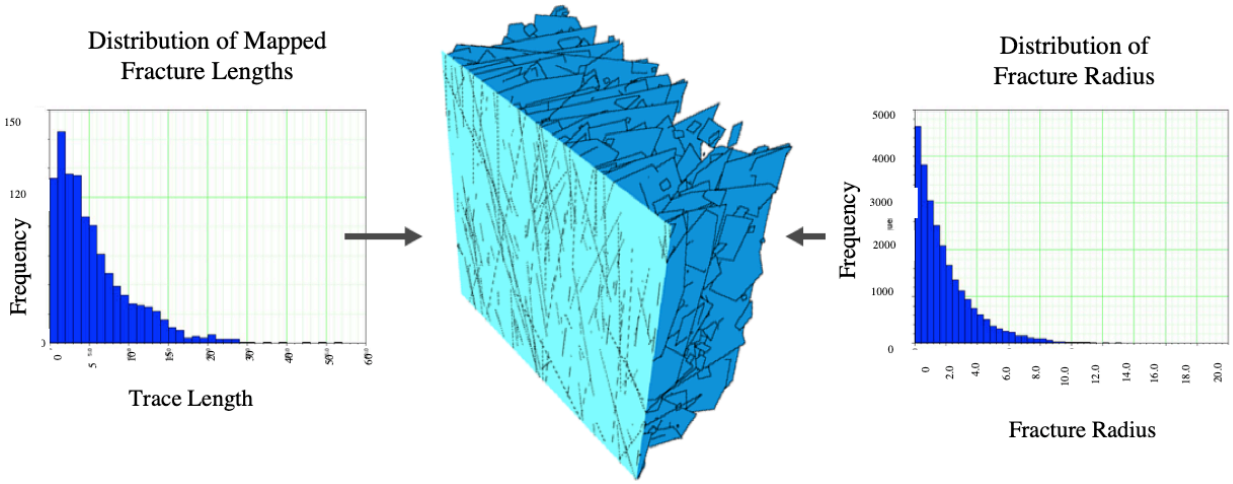

Figure 2.2. Difference between mapped fracture length (data source) and fracture radius (required DFN input) (Elmo et al., 2015).

2.1.3 Fracture Intensity

There are different ways to define fracture intensity. In this thesis, we adopt the method developed by Dershowitz and Herda, (1992), also known as the P_{ij} intensity system (Figure 2.3), in which the subscript i indicates the dimensions of sample, and subscript j indicates the dimensions of measurement. Using this system, the volumetric fracture intensity (P_{32}) is defined as the ratio of total fracture area to unit volume. P_{32} is a true intrinsic rock mass property; however, due to the

impossibility of measuring fracture area directly in the field, it can only be measured based on correlations with 1D data (P_{10}, linear fracture intensity) or 2D data (P_{21}, areal fracture intensity) using a simulated sampling methodology (Dershowitz and Herda, 1992). Examples are given in Elmo, 2006 and Elmo et al., 2015).

		Dimension of feature				
		0	**1**	**2**	**3**	
Dimension of sampling region	**0**	**P00** Length^0 Number of fractures				Point Measure
	1	**P10** Length^{-1} Number of fractures per unit length of scanline (Frequency or linear intensity)	**P11** Length^0 Length of fractures intersects per unit length of scanline			Linear Measure
	2	**P20** Length^{-2} Number of traces per unit area of sampling plane (Areal density)	**P21** Length^{-1} Length of fracture traces per unit area of sampling plane (Areal intensity)	**P22** Length^0 Area of fractures per unit area of sampling plane		Areal Measure
	3	**P30** Length^{-3} Number of fracture per unit volume of rock mass (Volumetric density)		**P32** Length^{-1} Area of fractures per unit volume of rock mass (Volumetric intensity)	**P33** Length^{-2} Volume of fractures per unit volume of rock mass	Volumetric Measure

Figure 2.3. P_{ij} intensity system used in DFN generation (in Elmo, 2006; originally modified after Dershowitz and Herda, 1992).

2.1.4 Fractures Intersections

The concept of fractures intersections is of a great importance as it governs the interaction between fractures and the mechanical behaviour of a rock mass. Various attempts have been made in the literature to ensure an effective quantification of fracture intersection. In this thesis, we adopt the definition given as part of the proprietary DFN code FracMan (Golder, 2018), which was used as part of this research to synthetize DFN models and obtain 2D fractures traces.

Intersections can be differentiated based on whether a fracture terminates against another fracture (T type) or fully intersect each other (X type), Figure 2.4. Fractures intersections (X and T types) will be used in chapter 4 as an indicator of fracture connectivity.

Figure 2.4. Definition of T and X types of intersections (reproduced from the FracMan manual, Golder Associates, 2018).

As shown in Figure 2.5 below, collecting fracture intersections data may be rendered challenging by field conditions, since it would depend on the ability to clearly identify and measure all fracture traces within a specific window. This would also impact the use of fracture intersections as an indicator to validate a DFN model; indeed, validation of a DFN model is generally based on some type of areal or linear intensity (see also Section 2.1.3), in which case it is assumed the number of fracture intersections in the validated DFN model would approximate the one of the fracture network in the field.

As mentioned earlier, fracture network connectivity plays a major role in determining the failure mechanisms a rock mass may undergo when subjected to a set of external forces. Early attempts to measure network connectivity with respect to the permeability of a discrete fracture network can be traced back to Robinson (1984), who used percolation theory. Berkowitz (1995) also used percolation theory to calculate the probability of fracture connectivity using power-law relationships between numbers of individual fractures.

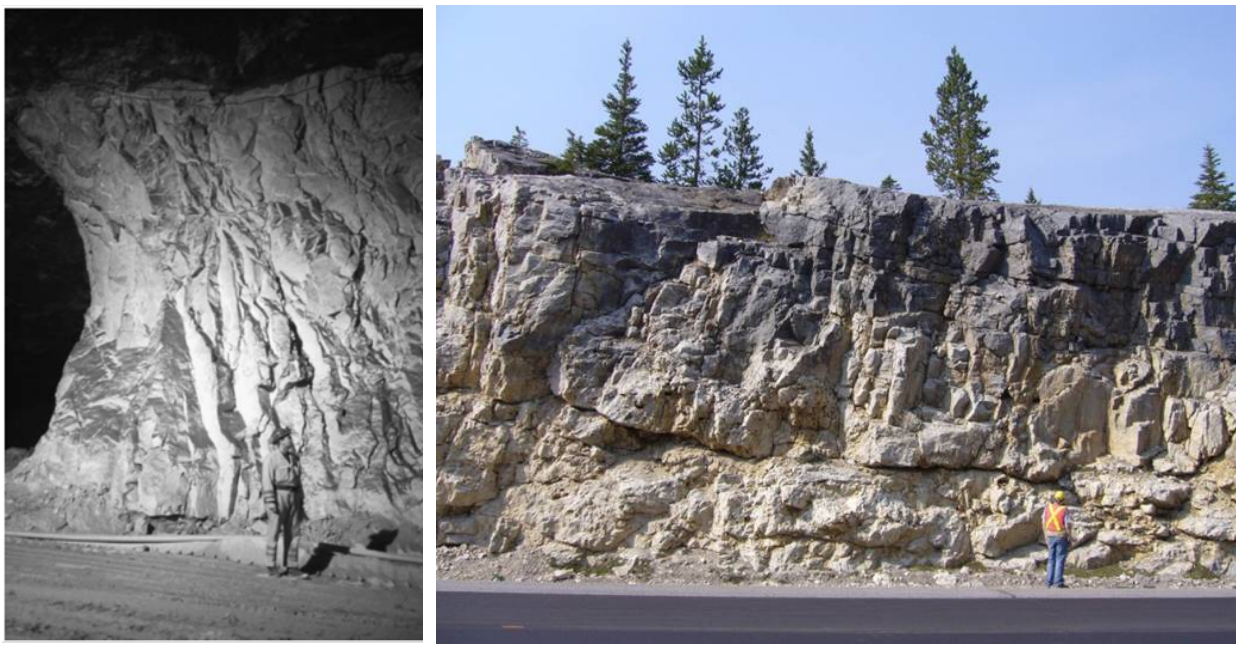

Figure 2.5. Example of rock exposures, which show the difficulty to obtain precise measurements of fracture intersections (figure on the left reproduced from Pine and Harrison, 2003; figure on the right, Elmo, personal communication, 2019).

Zhang et al. (1992) developed a connectivity index using several fracture parameters; an example is given in Figure 2.6. (a). The idea behind the approach used by Zhang et al. (1992) has been adapted in chapter 4, together with the definition of *X*- and *T*-type of intersection shown in Figure 2.4, to define the connectivity of a DFN network generated using the DFN code FracMan. Other authors that have studied network connectivity include Meyer and Einstein (2002), Manzocchi (2002), and Darcel et al. (2003). Xu et al. (2006) introduced a connectivity index integrated with the concept of connectivity maps (Figure 2.6. b).

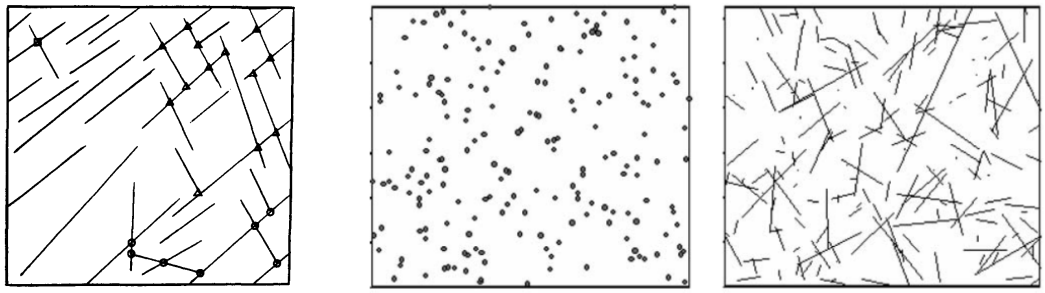

(a) (b)

Figure 2.6. Examples of the approaches used by a) Zhang et al. (2002); and b) and Xu et al. (2006) to develop a connectivity index for DFN models.

Heatmaps are visualization techniques frequently used to show events occurrence or density; various smoothing algorithms exist that could be used to create a heatmap. In this thesis the Kernel Density Estimation (KDE) is used to create intersection density maps. Early work on KDE algorithms can be traced back to Wand and Jones (1995); the technique has evolved to become one of the most widely used non-parametric data smoothing technique (Duong, 2007). In the literature, applications of KDE to study the intersection density of DFN models are given, among others, by Xu et al. (2006) and Fadakar-A. (2014), Figure 2.7. KDE are used in this thesis (chapter 4) to study the distribution of fracture intersections across for 2D sections derived from 3D DFN model generated to study the behaviour of engineered structures (e.g. mine pillars). Such heatmaps will be herein referred to as Intersection Density Maps.

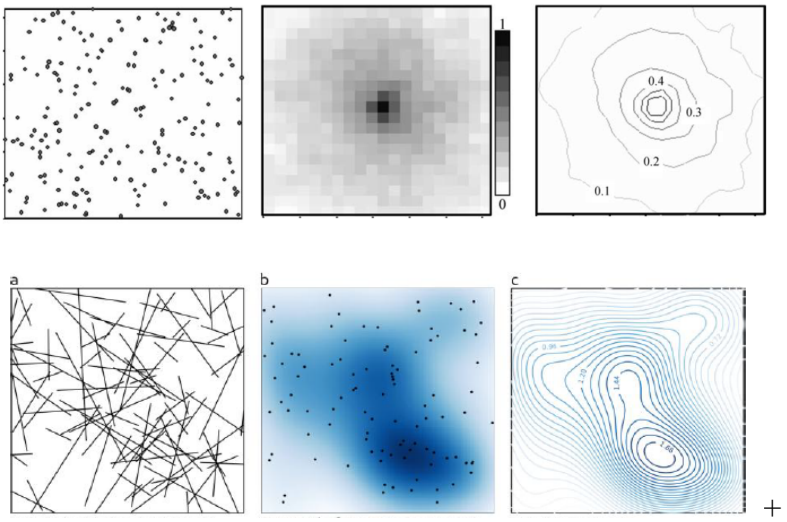

Figure 2.7. Examples of heatmaps for fracture intersections. a) Xu et al. (2006); b) Fadakar-A (2014).

2.2 DFN Models and Rock Mass Blockiness

The degree of blockiness of a rock mass is one of the most important factors controlling rock mass behaviour (ISRM, 1978; Hoek et al., 1995). Methods to estimate the degree of blockiness of a rock mass, and the associated in-situ block size distribution (IBSD) include estimating parameters such as volumetric joint count (J_v) (Palmstrom, 1974) and block size index (I_b) (ISRM, 1978). These methods are based on the knowledge of the average fracture spacing for a series of fracture sets and therefore can only provide an estimate of the average dimension of a typical rock block. Cai et al. (2004), Kim et al. (2006), and Kim et al. (2015) used a similar approach to calculate the volume of a block based on the knowledge of fracture spacing, fracture orientation and fracture persistence for a rock mass with three fracture sets, Figure 2.8.

As discussed in Elmo et al. (2008), the volume, shape, and removability of rock blocks formed as a result of an excavation would be a function of the characteristics of the natural fracture network. Methods for calculating blocks geometry (e.g. size and shape) using DFN models have been

proposed, among others, by Glynn and Einstein (1979), Goodman and Shi, (1985), Warburton, (1987), and Dershowitz and Carvalho (1996). Using the DFN code FracMan, Elmo et al. (2008) and Elmo et al. (2014) studied the continuity of rock blocks and associated rock bridges as a function of fracture size. Additionally, DFN models have been used for kinematic analysis (wedge analysis) and rock mass characterization by Rogers et al. (2007), Elmouttie and Poropat (2012), Kim et al. (2015), Miyoshi et al. (2018) and McQueen et al. (2019). Examples are provided in Figure 2.9.

Generally, a DFN based block analysis would represent a static condition, i.e. fully formed blocks would only depend on the geometrical characteristics of the fracture network and the excavation, but it would not include any consideration of the stresses induced by the opening of the excavations. When considering the relationship between rock mass blockiness and rock mass strength, it is important to consider the temporal aspect. For instance, Kemeny (2003) has proposed an approach to characterize time dependent damage and study its influence on rock mass strength. The aspect has been further explored in chapter 5 of this thesis with respect to in-situ (natural) fragmentation and the fragmentation processes a rock mass may undergo when subjected to loading.

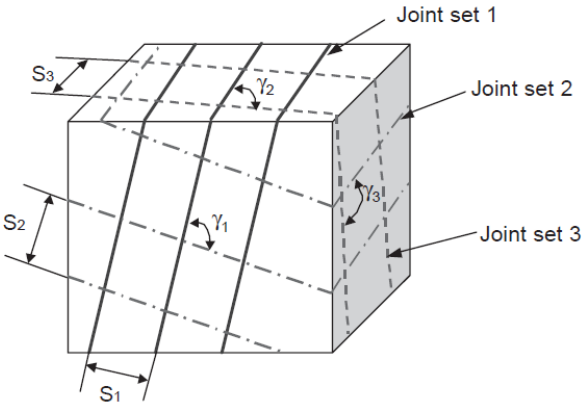

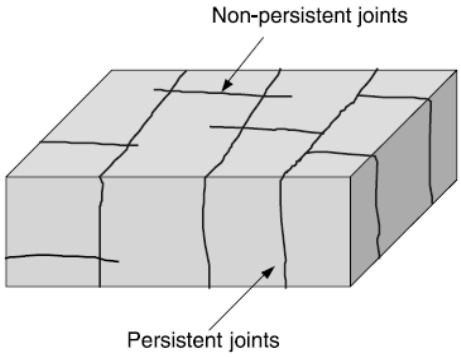

$$V_b = \frac{s_1 s_2 s_3}{\sin\gamma_1 \sin\gamma_2 \sin\gamma_3}$$

(a)

$$V_b = \frac{s_1 s_2 s_3}{\sqrt[3]{p_1 p_2 p_3}\sin\gamma_1 \sin\gamma_2 \sin\gamma_3}$$

(b)

Figure 2.8. a) Blocks formed by the intersection of three joint sets (after Kim et al. 2015); and b) illustration of blocks formed by non-persistent joints and equations used to define the average block volume, in which p_i represents the persistence factor (after Kim et al., 2006).

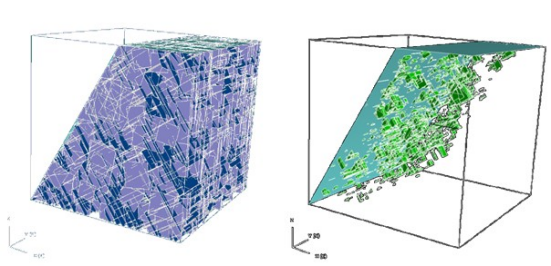

(a)

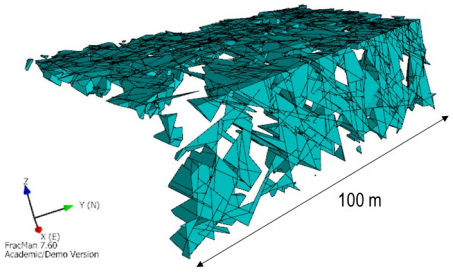

(b)

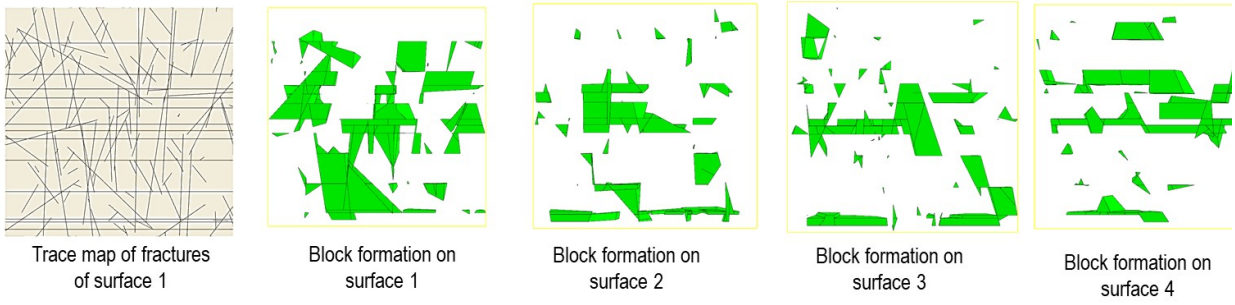

(c)

Figure 2.9. Example of block search and analysis using DFN models. a) after Elmo et al. (2008); b) and c) after Miyoshi et al. (2018).

It is important to recognize that the blockiness observed on 2D rock exposures does not necessarily correspond to the true 3D blockiness of the rock mass (Min and Thoraval, 2012). Therefore, the analysis of failure mechanisms in 2D would have to recognize the limitation imposed by the variability in block forming potential as a function of the location of the sampling plane. In principle, 3D geomechanical codes that allow the integration of DFN models and a full consideration of fracturing processes in 3D would obviate this issue. However, as discussed in Section 2.4, simulating failure mechanisms in 3D is still a challenging proposition that requires an adequate trade-off between computational times and model resolution, the latter unequivocally affecting the size distribution of the natural blocks that could be realistically simulated in a model. For these reasons, the numerical analysis in this thesis adopts a 2D approach for the characterization of rock mass blockiness. The author believes that the limitation discussed by Miyoshi et al. (2018) could be reduced by considering multiple realizations of the same DFN model, as the modelled failure mechanisms would provide a range of possible outcomes, thus capturing the inherent variability of the rock mass fracture network.

2.3 Numerical Simulation Methods for the Simulation of Brittle Failure

Consideration of damage mechanisms and brittle failure for both rock and geotechnical engineering problems has increased significantly since the early 2000s (Stead and Elmo, 2015). However, modelling brittle failure processes requires the correct treatment of the intrinsic rock material properties in addition to the model being able to capture non-linear load-displacement responses under different loading conditions (Lisjak and Grasselli, 2014). The presence of fractures can further increase the complexity of the problem being modelled, resulting in the

displacement of large individual blocks and the potential for opening/closing and sliding along fracture surfaces (Elmo and Stead, 2015).

The progressive and cumulative damage that rock material undergoes during the deformation process, together with the presence of natural fractures, requires the different numerical modelling techniques to strike a balance with respect to whether failure processes are represented explicitly or implicitly. A comprehensive review of numerical modelling techniques for rock mechanics and rock engineering, including a detailed literature source, is provided by Jing (2003). More recently, Lisjak and Grasselli (2014b) have compiled a detailed review of discrete modelling techniques for fracturing processes in jointed rock masses.

With reference to Figure 2.10, a rock mass could be treated as either a continuous or discontinuous media. A continuum approach would reflect mainly the deformation of the system, whilst a discontinuum approach would better capture kinematics controls (Elmo, 2006). Whereas continuum mechanics calculations for stress are based on plasticity theory, changes at the micro-structure level are based on fracture mechanics (Lisjak and Grasselli, 2014b). The literature sources reviewed in the following sections specifically refer to numerical analysis of brittle failure, as this is the key feature of the models later presented in chapters 3, 4 and 5.

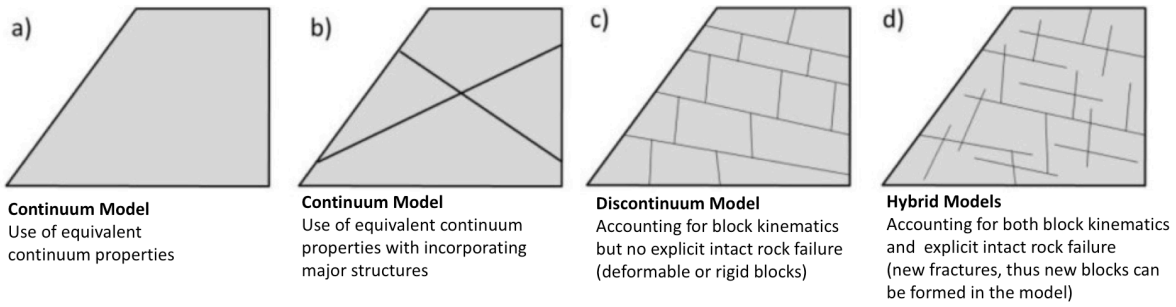

Figure 2.10. Examples of numerical approaches available to model a rock engineering problem in relation to the natural fracture network (from Elmo and Stead, 2015).

2.3.1 Continuum Models

Despite their definition, continuum models are indeed capable of simulating brittle fracture using fracture mechanics principles. Examples of recent finite element models (FEM) for simulating fracturing processes include FRAN2D (Wawryznek and Ingraffea, 1989), DIANA and NUMA (Alehossein and Hood, 1996), RFPA (Tang et al., 2001, 2004), and R-T2D (Liu, 2003). Conventional FEM models are also capable to capture the elasto-plastic yielding associated with brittle failure by using dedicated constitutive criteria (e.g. cohesion weakening and frictional hardening, Hajiabdolmajid, 2002). However, continuum models cannot truly capture the interaction between brittle failure and kinematics processes.

2.3.2 Discontinuum Models

Discontinuum models include conventional discrete element method (DEM) and particle-based models. Theoretically, DFN models also belong to the category of discontinuum models. In conventional DEMs, the rock mass is represented as an assemblage of discrete blocks separated by fractures, which numerically are considered equivalent to a boundary condition (Elmo, 2006).

Deformation and failure along fractures is governed by specific constitutive criteria. Recent examples of DEM simulations of brittle failure processes include Christianson et al. (2006), Alzo'ubi (2009), Gao (2013), Havaej et al. (2015), Gao and Stead, (2014), and Ghazvinian et al. (2014). Those authors used the discontinuum codes (UDEC and 3DEC; Itasca, 2018) in which brittle failure is modelled indirectly (i.e. without consideration of the principles of fracture mechanics) using a Voronoi tessellation approach, Figure 2.11. As explained in Elmo and Stead (2015), the Voronoi tessellation divides the rock mass into polygonal blocks, and failure (fracturing) occurs when the contact between adjacent Voronoi blocks is lost. The strength of the Voronoi contact is defined according to a standard Mohr-Coulomb shear failure criterion, with tensile cut-off; new fractures can therefore be generated either in tension or shear, Figure 2.12. A new Trigon tessellation was introduced by Gao (2013) to overcome some of the limitations of the conventional Voronoi approach. The parameters governing the behaviour of Voronoi elements must be calibrated and verified against reliable laboratory experiments. Uniaxial compression tests (UCS) and indirect tensile strength tests are usually simulated to obtain the calibrated Voronoi or Trigon properties. For large scale models, care must be taken to account for the size dependency of the Voronoi/Trigon properties (Insana et al., 2016, Mayer and Stead, 2017).

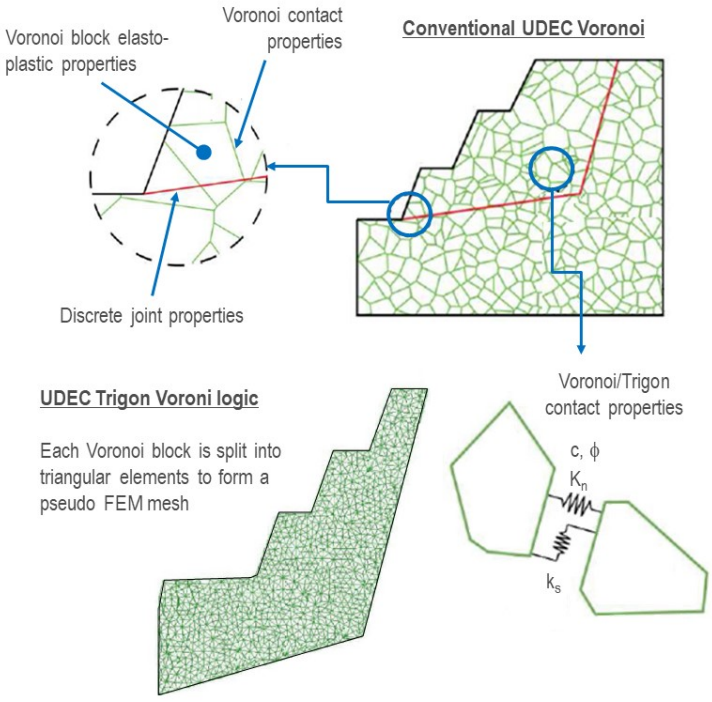

Figure 2.11. UDEC Voronoi and Trigon 2D approach to simulate brittle failure (modified by Elmo, 2018, personal communication, and based on figures included in Gao, 2013).

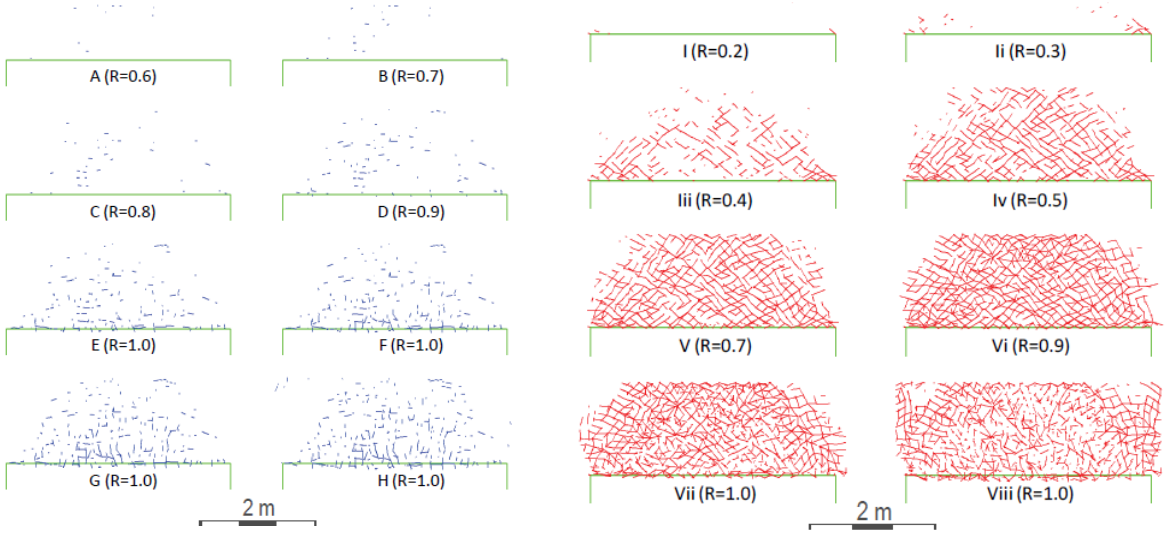

(a) (b)

Figure 2.12. Development of a) tension cracks and b) shear cracks in the roadway roof during the shear failure process (after Gao, 2013).

Particle-based models have proven effective in simulating the granular micro-structure of the material by creating an ensemble of rigid circular particles of varying diameters (Cundall and Strack, 1979). In Particle flow analysis, the rock mass is represented as a dense packing of non-uniform-sized circular (2D) or spherical (3D) particles that are bonded together at their contact points. Examples of particle flow codes include PFC (Potyondy and Cundall, 2004; Itasca, 2018) and Yade (Kozicki and Donze, 2008).

Compared to conventional DEM, PFC type codes do not require either a mesh or complex constitutive models to represent a material (i.e. the rock mass properties are not specified directly) (Mehranpour and Kulatilake, 2017), instead a particle contact logic is used, Figure 2.13, based on a series of springs with constant normal and shear stiffness, k_n and k_s.

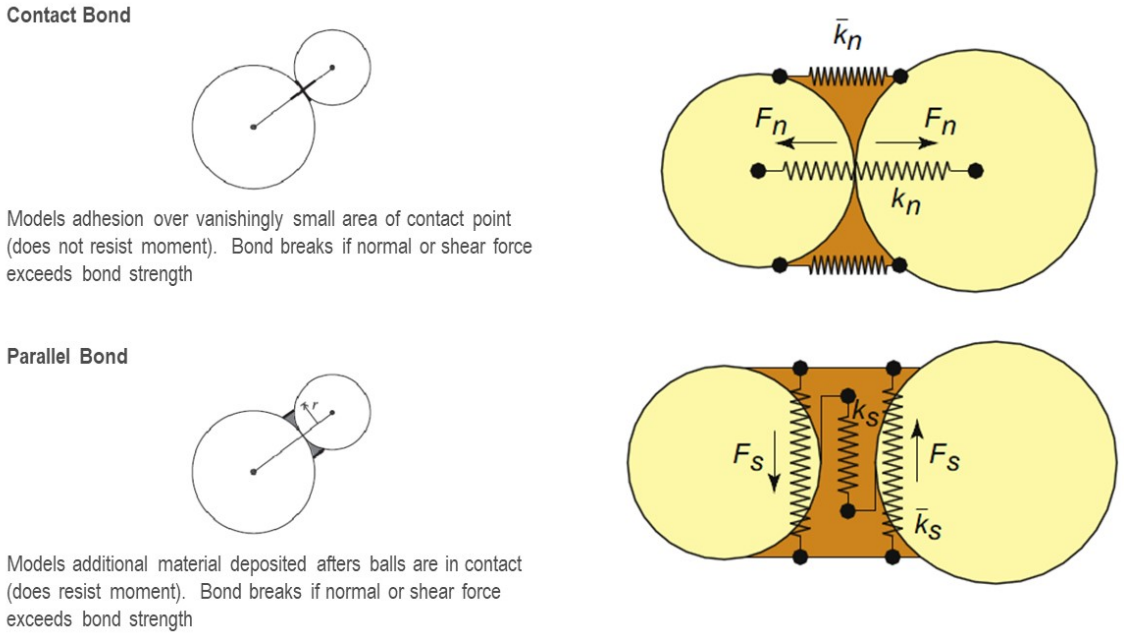

Figure 2.13. Definition of bond contact logic in PFC (modified from Potyondy and Cundall (2004)).

Several examples exist in the literature of the application of PFC codes to simulate brittle failure, including Pierce et al. (2007), Wang et al. (2003), Zhang et al. (2015) and Yang et al. (2016). In particular, Yang et al. (2016) used PFC to investigate the influence of joint persistency, k, on the mechanical behaviour of rock blocks having non-persistent open joints (Figure 2.14), while Zhang et al. (2015) used PFC to model the strength of jointed rock pillars, Figure 2.15.

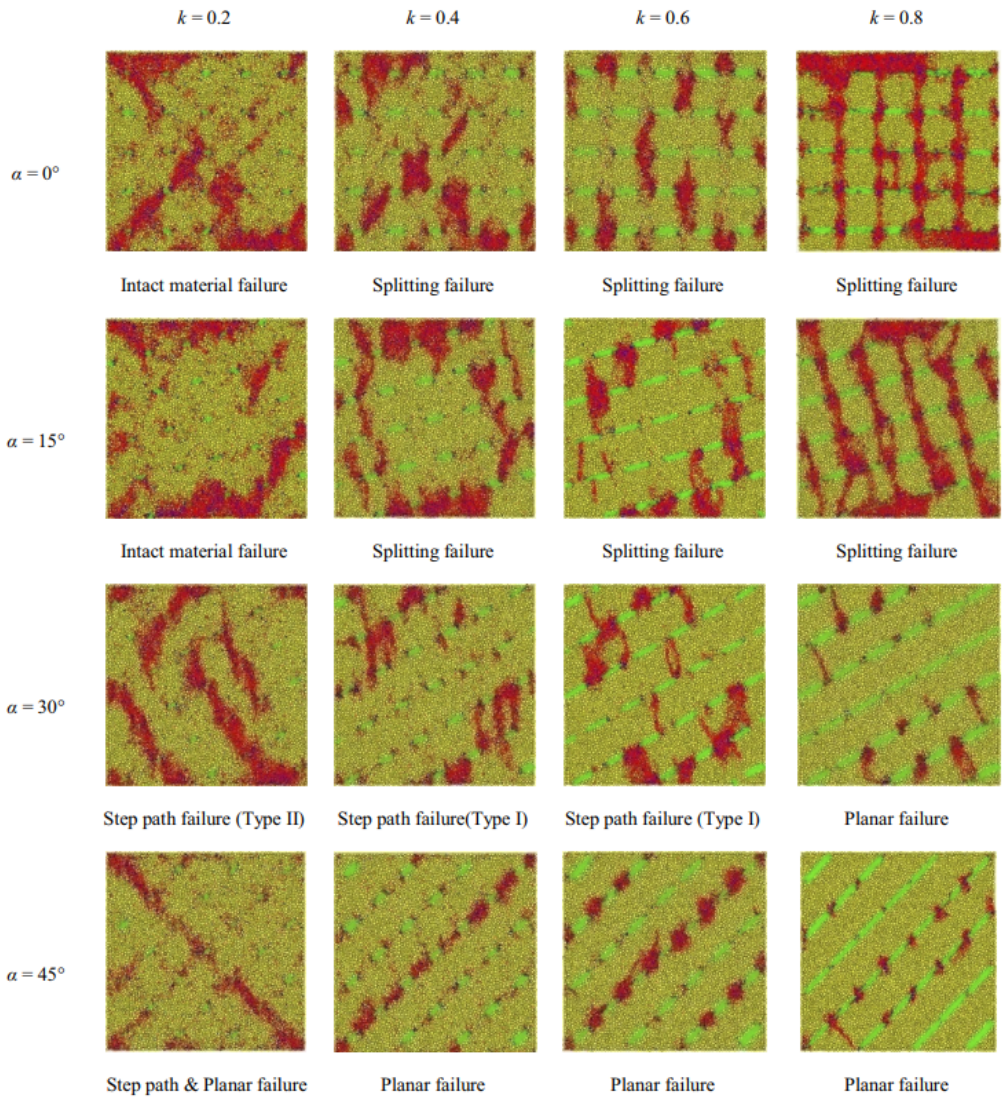

Figure 2.14. Failure modes of jointed rock blocks for different joint persistence and dip angle (after Yang et al., 2016).

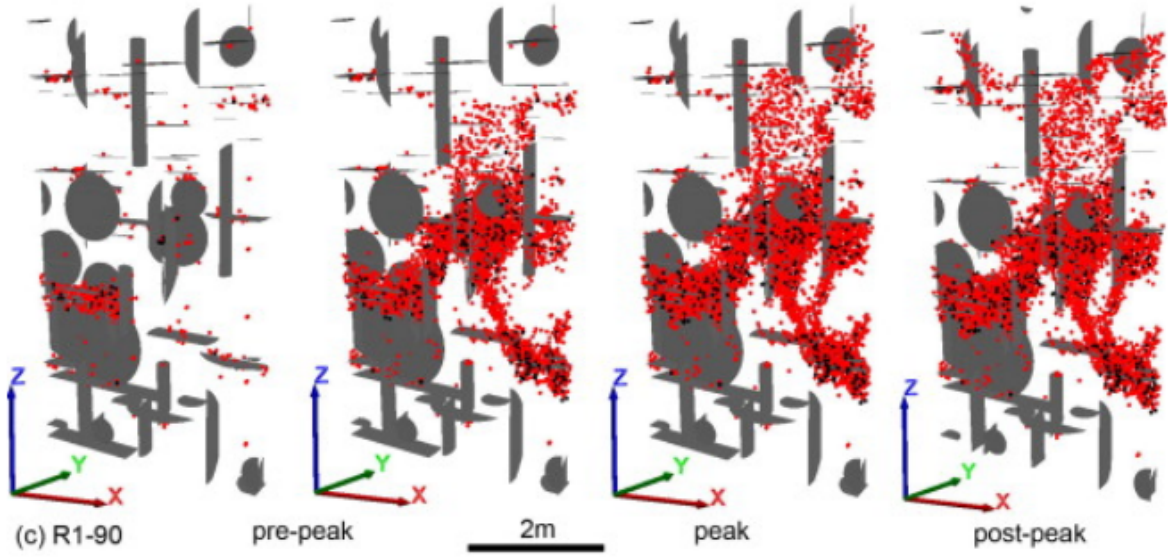

Figure 2.15. Progressive crack propagation in selected models during the loading process. Tensile and shear cracks are shown in red and black, respectively (after Zhang et al., 2015).

2.4 Finite-Discrete Element Methods (FDEM)

The existence of defects in rocks together with stress-induced crack and fragmentation processes often limit the applicability of continuum-based methods in rock engineering. Recent developments in numerical modelling using discontinuum-based methods have provided a more realistic approach. A FDEM approach combines aspects of both finite elements and discrete elements and can incorporate fracture mechanics principles.

As part of this study, numerical simulations were carried out using two FDEM programs, Irazu 2D (Geomechanica Inc., 2015) and ELFEN 2D (Rockfield, 2014). Irazu 2D (Geomechanica Inc., 2015) represents an enhanced and computationally improved version of two previously open-source FDEM codes, namely Y-2D and Y-Geo. The Irazu code is able to simulate crack initiation, propagation and coalescence as the rock is strained. The elastic deformation of the solid rock is modeled according to the continuum theory of linear elasticity using constant-strain triangular

elements. Under the assumption of isotropic behaviour, the elastic response is characterized by the Young's modulus E, and Poisson's ratio υ, if the failure criterion with the intact rock is fulfilled, then a crack is initiated (Munjiza and Andrews, 2000).

Since no adaptive re-meshing is performed as the simulation progresses, potential crack trajectories are restricted to the existing mesh topology and do not cut across the existing mesh elements (Irazu; Geomehanica, 2016). The insertion of discrete cracks within the Irazu models can be inter-element fracturing. Therefore, to minimize the bias induced on the model response, sufficiently refined unstructured meshes should be used.

Rock discontinuities (i.e. either pre-existing or newly created cracks) are treated by a rock joint model, computing the contact forces between all pairs of triangular elements that overlap in space. Two types of forces are applied to the elements of each contacting pair: 1) repulsive forces; and 2) frictional forces. The repulsive forces are calculated using a penalty function based on the Young's modulus of the material.

The overlapping area between two bodies is evaluated by the associated shape and size and the value of stiffness. The frictional forces between contacting couples are also calculated in the tangential direction using Coulomb's law of friction. Upon exceeding the peak strength of the material (in tension, shear, or a mixed-mode), the strains are assumed to localize within a zone, called the Fracture Process Zone (FPZ). The mechanical response of the FPZ is shown by a non-linear linkage between stress and crack displacements at the crack element level.

The hybrid FDEM code ELFEN (Rockfield, 2014) has increasingly been used as a numerical tool to simulate the fracture process for laboratory tests. The fracture initiation, propagation and coalescence of the strained rock can be simulated using ELFEN. Using ELFEN 2D, the fracture propagation is not limited to the boundary of elements and can cut cross the elements and create a new element. However, this option is seldom used (e.g. Hamdi, 2015) and the issue of mesh dependency is still present. The detailed description of this issue is addressed in chapter 4.

Figure 2.16 and Figure 2.17 show the yield surface and softening curve for rotating crack and Rankine models, and Mohr-Coulomb yield criterion implemented in the code Elfen (Rockfield, 2014).

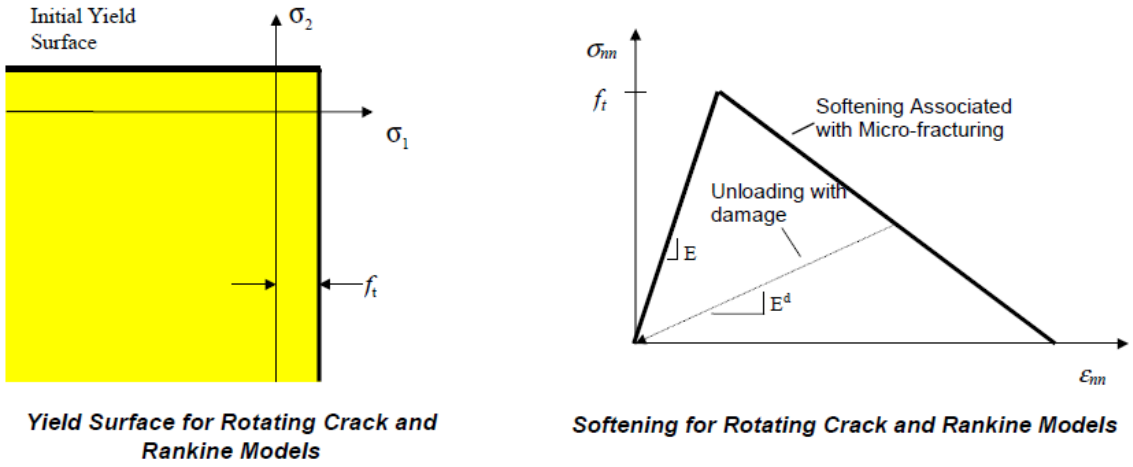

Figure 2.16. Yield surface and softening curve for rotating crack and Rankine models (after Elfen user's manual, Rockfield, 2014).

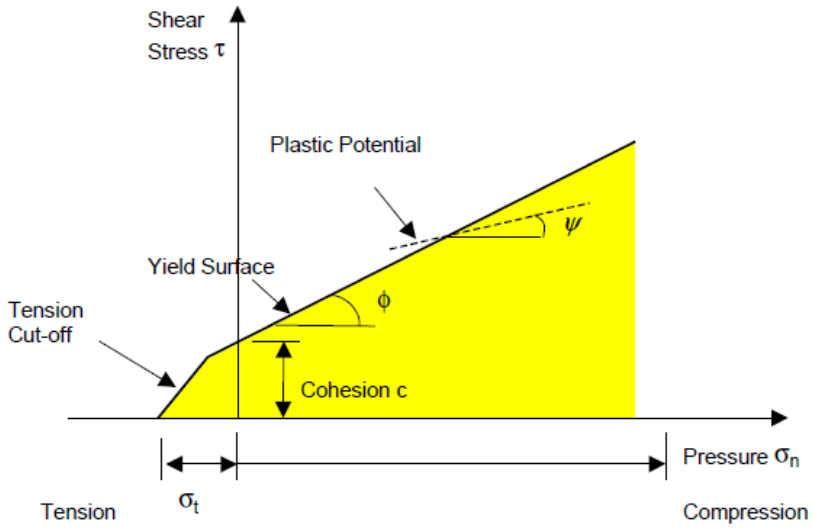

Figure 2.17. Mohr-Coulomb material model for compression states (after Elfen user's manual, Rockfield, 2014).

The advancement of the numerical and mathematical approaches along with the emergence of powerful computers have enabled many engineering fields including rock mechanics and rock engineering to develop tools that facilitate the study of fracturing and block formation in brittle rocks. The FDEM proposed by Munjiza et al. (1995a), for instance, has provided a basis to model the transition from continuum to discrete form as well as the post-failure interactions typical of brittle rock materials (Owen et al. 2004).

2.4.1 Contact Detection and Interaction in FDEM

FDEM simulations can involve a large number of interacting discrete elements. To correctly capture this behaviour, contacting couples (i.e., pair of contacting discrete elements) is detected in the initial stage. Detection is accomplished using No Binary Search (NBS) method (Munjiza and Andrews, 2000). According to this method, it is assumed that pairs of contacting couples

interpenetrate into each other and create contact forces that are determined by the size and shape of the resulting overlapping area, Figure 2.18.

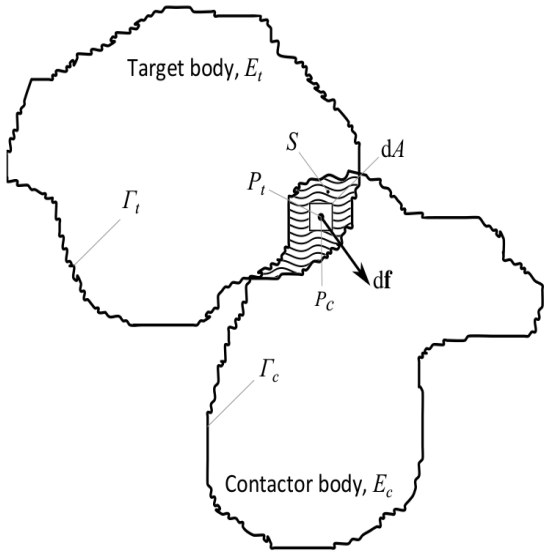

Figure 2.18. Illustration of infinitesimal repulsive force generated due to infinitesimal penetration of two discrete bodies (after Munjiza and Andrews, 2000a).

In ELFEN (Rockfield, 2014), the simulation starts with a continuous representation of the solid domain of interest. In general, the approach combines FEM techniques with DEM concepts. The DEM algorithms include techniques for detecting new contacts and dealing with the interaction between discrete bodies, while the former techniques are used for the computation of internal forces and for the evaluation of the failure criterion and the creation of new cracks (Owen and Feng, 2001).

Unlike most numerical codes, where fractures can only propagate around the boundary of the meshed elements, the ELFEN code allows new fractures to cut across the existing meshed elements. As shown in Figure 2.19, the insertion of a new crack can be achieved using two different

algorithms (Klerck et al., 2004). The intra-element insertion (Figure 2.19a) results in a new fracture in the crack propagation direction by directly splitting the finite elements. In this case, care should be taken that the resulting element topology does not decrease the minimum integration time step. The Elfen approach presents the mesh topology that is based on a nodal fracture scheme with all new fractures developing in tension (i.e. Mode I) in the direction orthogonal to the principal stress direction where the tensile strength becomes zero.

Conversely, with the inter-element insertion (Figure 2.19b), the cracking will continue in the direction most favorably oriented relative to the failure plane. Following the crack insertion, the damage variables in the adjacent finite elements are set to zero and the contact along the two newly-created surfaces is treated using a contact interaction algorithm (e.g. penalty or Lagrangian multiplier method) (Munjiza and Andrews, 2000).

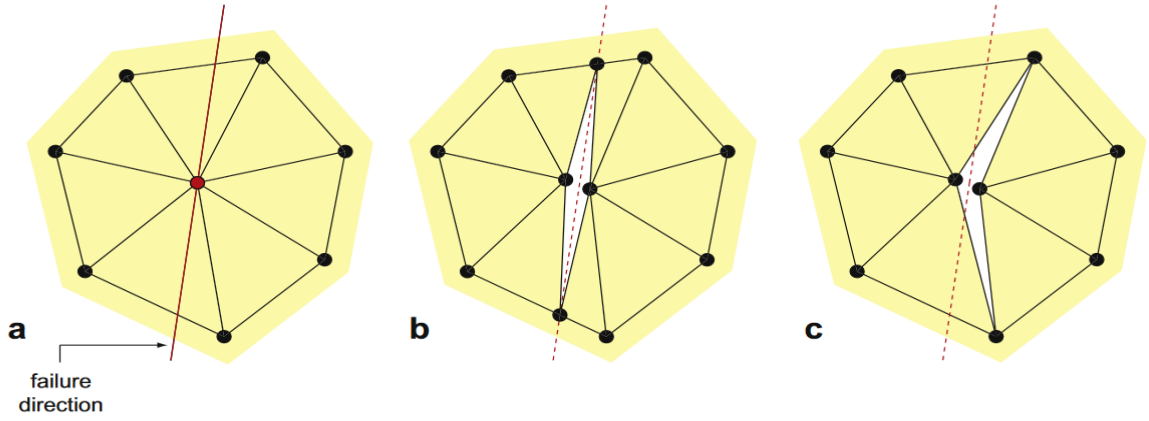

Figure 2.19. Approach used for discrete crack insertion and topological updating in ELFEN as explained in Owen et al. (2004). a) the actual failure direction defined by weighted-average configuration. b) intra-element fracturing, c) inter-element fracturing. (after Klerck et al., 2003).

Hybrid finite-discrete element modelling has been used successfully in various geotechnical fields including blasting (Munjiza. et al., 1995b), underground rock engineering (Klerck, 2000) and rock

slope instability (Stead et al., 2006) simulated triaxial, plane strain and strip punch tests in addition to the borehole breakout problem. Simulation results, constrained by experimental observations, have shown that the hybrid finite/discrete element ELFEN code can effectively reproduce rock failure by discrete fracturing under compressive stress fields.

The ELFEN code has the capability to show the internal damage and strength degradation under varied stresses. The Mohr-Coulomb with rotating crack constitutive model (Rockfield Software Ltd. 2014) can be adopted to simulate the fracturing process at various scales. The cohesion (c), friction angle (ϕ), dilation (ψ), tensile strength (σ_t) and fracture energy (G_f)should be specified for the material. Due to the inherent extensional fracturing process in ELFEN, the fracture energy is specified according to Mode I type of failure. The coupling of Mohr-Coulomb with a rotating crack constitutive criterion in ELFEN provides a realistic representation of both shear and tensile fracturing. The examples of ELFEN models are given in chapters 4, 5 and 6 of this thesis.

A new, commercially-available finite-discrete element modelling tool, Irazu was developed by Geomechanica (2015) to overcome the computational limitations of rock mechanic simulations by incorporating parallel processing power using General Purpose Graphics Processing Units (GPGPUs) (Mahabadi et al., 2016). According to Mahabadi et al. (2016), the parallel processing power of GPGPUs has been developed to gain upgrade performance compared to a regular non-parallel code running on the CPU (i.e., Y-Geo).

The Irazu code represents an extension of the original Y2D code of (Munjiza, 2004) and continues to undergo development for geomechanical applications. The fundamental principles of FDEM implemented in Irazu, include contact detection and interaction, and damage and fracture

modelling; the governing parameters which are later determined accordingly to the calibration procedure developed by Tatone and Grasselli (2015a) are introduced and defined through a trial and error procedure.

In Irazu, each intact body is discretized with a mesh comprising 3-noded triangular elements Figure 2.20. The elastic deformation of the discrete bodies is governed by the continuum theory of linear elasticity using constant-strain triangular elements (Munjiza, 2004). The elastic deformation of intact material is modelled according to the element deformation (strain) at each time step and is described by the differences between its initial configuration (i.e. unreformed) and current configuration (i.e. deformed). From the strain tensor, the element stress tensor is calculated using isotropic linear elasticity based on plane stress or plane strain assumptions and transversely isotropic linear elasticity (Mahabadi et al., 2016). An explicit second-order forward finite-difference integration scheme is employed to solve the equations of motion for the discretized system and update the nodal coordinates at each simulation time step.

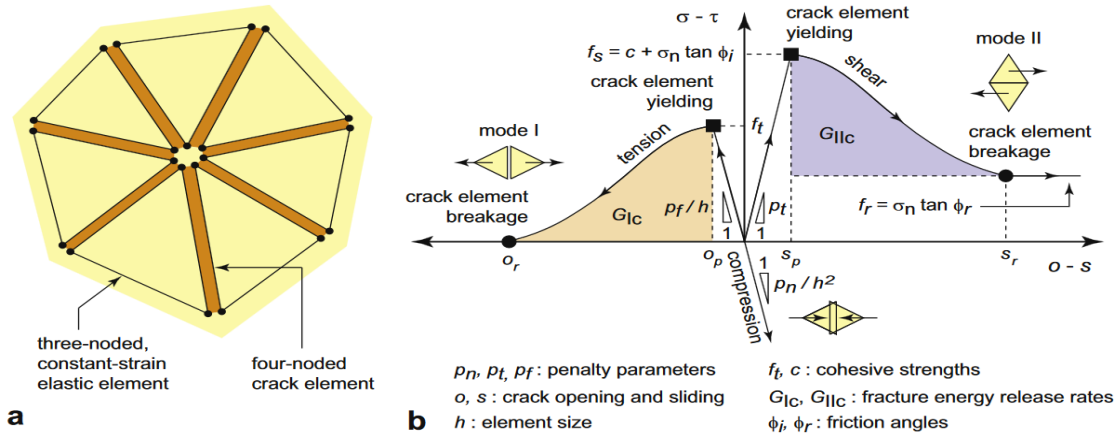

Figure 2.20. Simulation of fracture propagation with Y-Geo. (a) Representation of a continuum using cohesive elements dispersed across a mesh of triangular elements. (b) Constitutive behaviour of crack elements defined in terms of bonding stress (tensile, σ, and shear, τ) vs. relative displacement (opening, o and sliding, s) between the edges of adjacent triangular elements (after Geomechanica, 2015).

The introduction of numerical viscous damping is required to account for energy dissipation due to non-linear material behaviour and model quasi-static phenomenon by dynamic relaxation (Munjiza, 2004).

In Irazu, the fracture trajectories are explicitly simulated using the approach of non-linear fracture mechanics in which as the tensile strength of the material is exceeded, the fracture process zone is developed in Mode I (tensile). Mode I fracture initiates when the opening of a crack element reaches a critical value that corresponds to the inherent tensile strength of the element. As a crack element is opened, the stress is reduced to the residual opening value at which a traction-free surface is shown. Mode II fracture initiates when the tangential displacement of a crack element surpasses the displacement associated with the intrinsic shear strength of the element. As the crack

element undergoes further tangential slip, the tangential stress is progressively reduced until it reaches the residual slip.

Instead of Pure Mode I and Pure Mode II displacements, crack elements often experience a combination of two (mixed Mode I and II displacement). In Irazu FDEM, a mixed-mode I-II crack initiation and propagation is employed. The mesh topology can be modified such that it combines a random triangulation for the intra-layer material (i.e., matrix) with crack elements aligned along preferentially oriented planes of weakness. In this method, the crack is allowed to propagate through the element boundary. In this procedure, no new element is created and the updating procedure is simplified. This procedure requires a relatively finely discretized mesh around the potential fracture area. Within the current algorithm, a minimum element size should be used to ensure that excessively small elements are not created.

Material softening and hardening can be modelled using a non-associative Mohr-Coulomb elasto-plastic model with shear strength parameters, including cohesion, friction angle and dilation, defined as the function of effective plastic strain. A variety of constitutive models for material failure have been developed within softening plasticity and damage theory. The optimum propagation paths maintain an orientation normal to the maximum extensile strains. The localization of micro-cracking into effective crack bands results in softening normal to the crack directions. Fracture is considered in the form of a rate dependent rotating smeared- crack model using the tensile strain-softening to indicate the material degradation. For a more comprehensive review of the principles and mathematical formulations used in Irazu, the reader is referred to Irazu

theory manual (Geomechanica, 2015). The examples of Irazu models are given in chapter 3 of this thesis.

2.5 Concluding Remarks

This chapter began by reviewing the main concepts in discrete fracture network (DFN) models for simulating the natural discontinuity systems with a description of both deterministic and stochastic approaches used in solving DFNs.

The concept of rock mass blockiness is described with examples of how researchers attempt to calculate the block area and volume. The Discrete Fracture Network parameters considered in the calculation of blockiness are discussed.

Various numerical modelling techniques (e.g. continuum and discontinuum) are described and examples are given for the various techniques. The reader can get a sense of how each numerical code works. Particular attention has been given to explain Finite-Discrete Element codes. The material properties, mesh elements and calculation procedure are discussed for the two FDEM software (e.g. Elfen and Irazu) used in this thesis.

Chapter 3: The Need for New Approaches to Improve on Existing FDEM Models

3.1 Introduction

The main objective of this chapter is to identify the types of output processing required to improve on existing Finite-Discrete Element Methods (FDEM). Emphasis is given to the development of numerical algorithms that could help engineers and practitioners to better define and quantify, in the context of a FDEM model, fracturing processes (e.g. initiation, coalescence and propagation of existing fractures) and blocks formation. The models presented in this chapter are by intention relatively simple (laboratory scale samples with two pre-existing cracks); simple models are better suited to prototype the framework and structure of the algorithms and, if necessary, isolate specific functions that may need changes. These simple models are also easy to mesh, which avoids issues related to the integration of discrete fracture network (DFN) models and FDEM; this topic will be discussed in detail in chapter 4.

3.2 Research Framework

Simulating the failure of a model with two pre-existing fractures under uniaxial loading conditions allows understanding of the role of rock bridge failure in the context of FDEM analysis. Whereas rock bridge analysis is not the main focus of this dissertation, various approaches are herein introduced that can help in the processing and monitoring of fracture nucleation and development; these are of fundamental importance in the analysis of rock bridge failure. It is well accepted that stability analysis for high natural or engineering rock slopes should account for brittle failure due to high stress concentrations that may exist leading to the development of stress-induced rock cracks (Hajiabdolmajid et al., 2002). Note that in this thesis the terms “cracks”, “traces”, and

"fractures" are used as synonyms, with no distinction in terms of the scale of the feature. These stress-induced cracks may provide kinematic freedom for a previously stable block and result in underground structure failure (e.g. pillar). The stochastic character of geometric parameters, persistence and water pressure all need to be considered in various rock bridge configurations as well as computation of an overall probability of pillar failure. A partially structurally-controlled failure occurs through a combination of different mechanisms such as tensile cracking and sliding on pre-existing structures in the rock mass. In these cases, development of the stress-induced cracks is required for failure as the rock mass is not kinematically free to move out of the pillar. This type of failure often occurs at larger scales where high stress levels may cause the development of secondary, stress-induced damage zones. Due to the importance of rock bridge formation in geotechnical engineering studies (Elmo et al., 2018), the cracking stages and the rock bridge response should be investigated at the laboratory-scale.

Strain measurement or acoustic emission monitoring (AE) during laboratory uniaxial compression indicates several stages of crack development including, crack closure, crack initiation, crack damage and peak strength. An example of a numerical tool that allows for such a continuum-discontinuum transformation is the finite-discrete element method, FDEM. The suitability of the hybrid finite-discrete element method (FDEM) for simulating brittle failure has been described by numerous researchers (Mahabadi et al., 2010; Munjiza and Andrews, 2000; Cai and Kaiser, 2004), as the method is able to clearly describe the transition from an intact continuum to a discontinuum cracked state. To date, a large number of 2D-FDEM numerical simulations have been undertaken to simulate the mechanical response of rock samples subjected to varying loading conditions.

The mechanical behaviour of anisotropic rocks in the laboratory has been studied with the combined FDEM method by Cai and Kaiser (2004) using ELFEN 2D (Rockfield Software Ltd. 2002) and by Mahabadi et al. (2012) using Y-Geo. Klerck (2000) carried out numerical simulations on unconfined compressive strength, UCS, and biaxial tests and showed the suitability of this method for simulating both load-displacement response and the observed evolution of discrete fracturing. Numerically simulated acoustic emission activity of brittle rock was monitored during uniaxial compression testing with a pre-existing crack using the Y-Geo FDEM code (Lisjak et al., 2013).

There remains however a real need to further characterize brittle rock failure by quantifying the newly generated cracks and the type of failure. The presence of pre-existing damage and the formation of new micro-cracks during laboratory testing requires the analysis of the properties of the newly-generated cracks. The objective of this chapter is to introduce new methods to detect cracking levels in rock subject to stress, especially micro-cracking and macro-cracking.

Newly generated cracks can be quantified using properties such as the number of newly generated cracks, the length of the newly generated cracks, the angle of the newly generated crack with respect to the applied load, the locations at which the numerical cohesive crack elements intersect and the failure mode responsible for the initiation and propagation of the cracks. These properties can then be used for interpreting various stages of the cracking process. Understanding the crack stress levels such as crack initiation, crack propagation and crack coalescence in rock allows a better understanding of rock behaviour. The crack stress levels are determined based on the different failure modes (tensile/shear), the crack counts and number of crack intersection counts.

3.3 Model Setup

The experimental data used in this study is based on the laboratory experiments conducted by Moradian et al. (2015), who presented uniaxial compression testing on a prismatic Barre Granite specimen (dimensions of 152 mm × 76 mm) as shown in Figure 3.1. The crack patterns obtained from a high-speed camera and the stress-strain curves by Moradian et al. (2015) are used in the current analysis for both a qualitative and quantitative comparison with the FDEM results (Figure 3.3 and Figure 3.4).

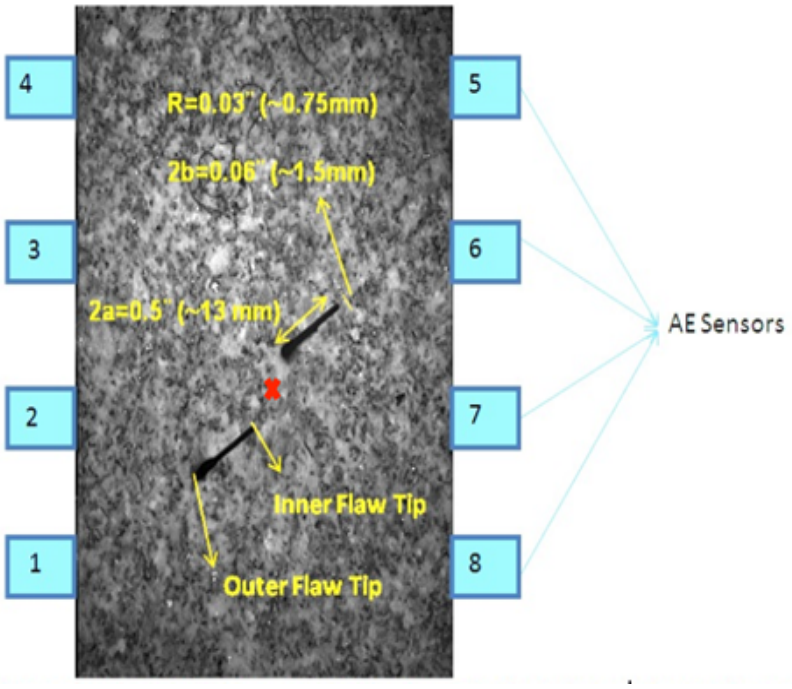

Figure 3.1. Prismatic granite specimen tested under uniaxial compression loading configuration. The dimensions of the specimen are 152 mm × 76 mm × 25 mm. The flaws have a length of 13 mm. Acoustic emission sensors were attached to sides of the specimen (after Moradian et al., 2015).

The model consists of a homogeneous sample containing two pre-existing flaws of 13 mm in length, inclined at 30 ° to the horizontal and located at the centre of the model (Figure 3.2). The

sample was discretized using a Delaunay triangulation with an average edge size of h = 1 mm which resembles the average grain size of Barre Granite of approximately 0.9 mm (Nasseri et al., 2006); this resulted in a total of 36756 triangular elements in the FEM mesh.

A constant strain rate was imposed to the model by means of two rigid platens moving in opposite directions at a constant velocity of 0.05 mm/s. A sensitivity analysis of the loading rate indicated constant values of strengths with a change of loading rate less than approximately 0.05 mm/s. A constant integration time step of 5×10^{-6} s was used to solve the governing equations for the FDEM system.

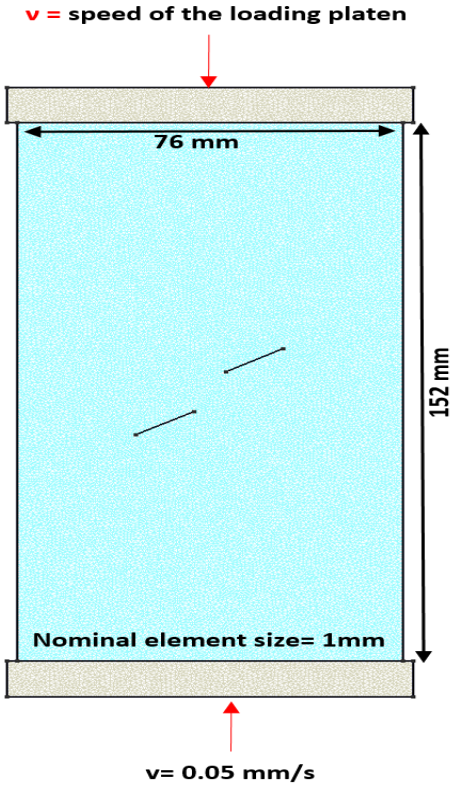

Figure 3.2. Schematic of the simulated rock sample meshed with 31720 triangular elements; v is the rate of displacement of the load platens.

Material properties using Elfen and Irazu are listed in Table 3.1. The results were obtained after calibrating the numerical model against laboratory testing results conducted by Moradian et al. (2015).

Table 3.1. Material properties used in Elfen and Irazu.

Properties of the Intact Rock	**Value**	Software
Bulk density, ρ (kg m^{-3})	2500	Elfen and Irazu
Young's modulus, *E (GPa)*	60	Elfen and Irazu
Poisson's ratio, ν (-)	0.25	Elfen and Irazu
Damping coefficient, μ (kg m s^{-1})	7.41	Elfen
Tensile strength, σ_t (MPa)	8	Elfen and Irazu
Cohesion, c (MPa)	40	Elfen and Irazu
Mode I crack energy, G_{Ic} (J m^{-2})	40	Elfen and Irazu
Mode II crack energy, G_{IIc} (J m^{-2})	20	Irazu
Friction angle, $\emptyset_i$ (°)	38	Elfen and Irazu
Normal contact penalty, Pn (GPa/m)	19.2	Elfen and Irazu
Tangential contact penalty, Pt (GPa/m)	19.2	Elfen and Irazu
Fracture penalty, Pf (GPa)	19.2	Irazu
Discrete Fracture Network Properties	**Value**	
Normal contact penalty, Pn (GPa m)	17	Elfen and Irazu
Tangential contact penalty, Pt (GPa m^{-1})	17	Elfen and Irazu
Friction angle, $\emptyset_i$ (°)	45	Elfen and Irazu

Initially, the uniaxial compression test was simulated to obtain the uniaxial compressive strength of 151 MPa Barre Granite (Miller, 2008), and then the same properties were used for simulating the uniaxial compression test of the Barre Granite with two pre-existing cracks. A sensitivity analysis was undertaken for the properties of the model with pre-existing cracks to obtain a stress-strain curve equivalent to that presented by Moradian et al. (2015). The code RocData (RocScience Inc, 2002) was used to obtain Mohr-Coulomb parameters for the model without pre-existing cracks. Using a Young's modulus of 60 GPa and a tensile strength of 12 MPa, the fracture energy

was calculated to be 50 Jm^{-2}. In plane strain conditions, fracture energy, and Mode I fracture toughness is related through Young's modulus by (Irwin, 1957):

$$G_{IC} = {K_{IC}^2}/{E} \qquad \textbf{[Eq. 2]}$$

A friction coefficient of 0.1 (equivalent to approximately 6°) was assumed for the interface between the rock sample and the loading platens to minimize end-effects.

3.4 Modelling Results

The simulated failure process in uniaxial compression can be explained using the critical stress levels and cracking stages typical of brittle rocks described by Brace (1964) and Bieniawski, (1967a). They identified five stages based on the stress-strain behaviour of rocks: (1) closure of micro-cracks and crushing of asperities; (2) linear elastic behaviour (3) onset of dilation and stable crack propagation; (4) unstable crack growth; and (5) brittle post-peak. In this section, different plots, e.g. stress vs. strain, failure mode vs. strain, and failure mode vs. damage, are used to characterize four stages of brittle failure from linear elastic behaviour to brittle post-peak. The closure of micro-cracks is not tracked in the presented models. Note that options of simulating micro-cracks as voids in the model instead of meshed fracture lines may allow to better capture the initial non-linearity due to micro-cracks closure. However, this approach is not adopted in the current models.

3.4.1 Simulation Results using FDEM-Irazu

The triangular elements in the Irazu model can fail in shear, tension or both; accordingly, the contours of principal stress (Figure 3.3) show newly-generated cracks in green and red for tensile and shear failure, respectively. The broken joints are coloured differently based on the failure: Mode I, Mode II and Mixed-Mode (Geomechanica, 2015). The tensile cracks (Mode I) initiate at the tips of the pre-existing cracks and propagate when the tensile stress exceeds the tensile strength of the intact rock. Mode II cracks propagate when the shear stress exceeds the shear strength of the material.

The results of the fracturing process are presented for four different axial strain levels corresponding to the points A to D in Figure 3.3. Figure 3.4 shows stages A to D with respect to the stress-strain curve. Single, isolated tensile cracks are generated (Stage A) in pre-peak at 0.3% strain; these are aligned with the direction of the major principal stress (σ_1). Cracks propagation and nucleation continues in Stage B as the axial strain increases to 0.4%. By Stage C, 0.5% strain, cracks coalesce to form a large crack in the top right corner of the model. As the strain reaches 0.6%, cracks grow in an uncontrollable manner to form relatively large damage zones (Stage D). In Figure 3.3, the results are compared with the high-speed photographic images published by Moradian et al. (2015). Note that the strain level noted in the published images is not the same as the modelled strain, and therefore comparison is made only on a qualitative basis.

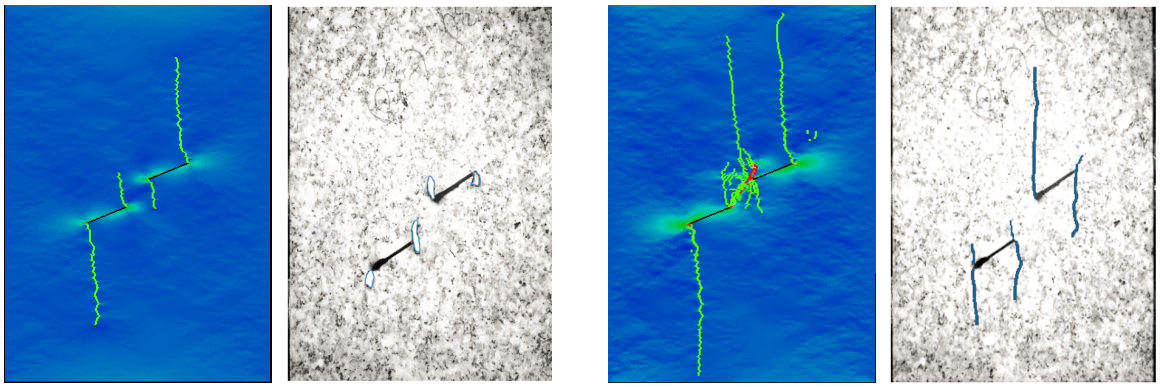

(a) 0.3% Strain (b) 0.4% Strain

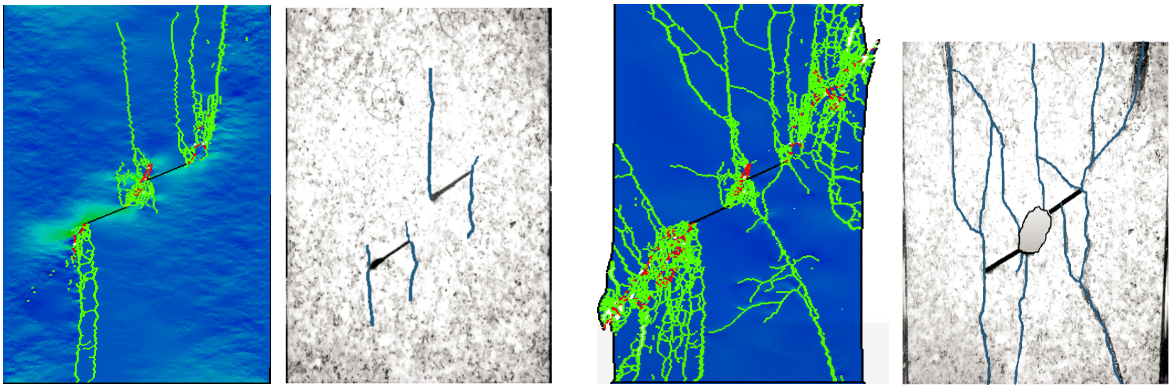

(c) 0.5% Strain (d) 0.6% Strain

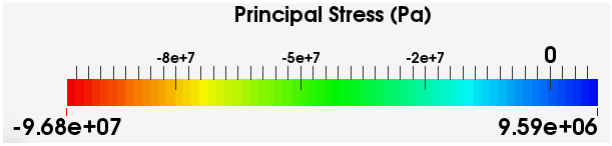

Figure 3.3. Simulated uniaxial compression in Irazu showing contours of major principal stress with the newly-generated cracks in green (tensile) and red (shear). The figures show cracking for strain levels of 0.3, 0.4, 0.5 and 0.6% (a-d). Photographic evidence of the tested Barre Granite specimen is shown for comparison (after, Moradian et.al., 2015).

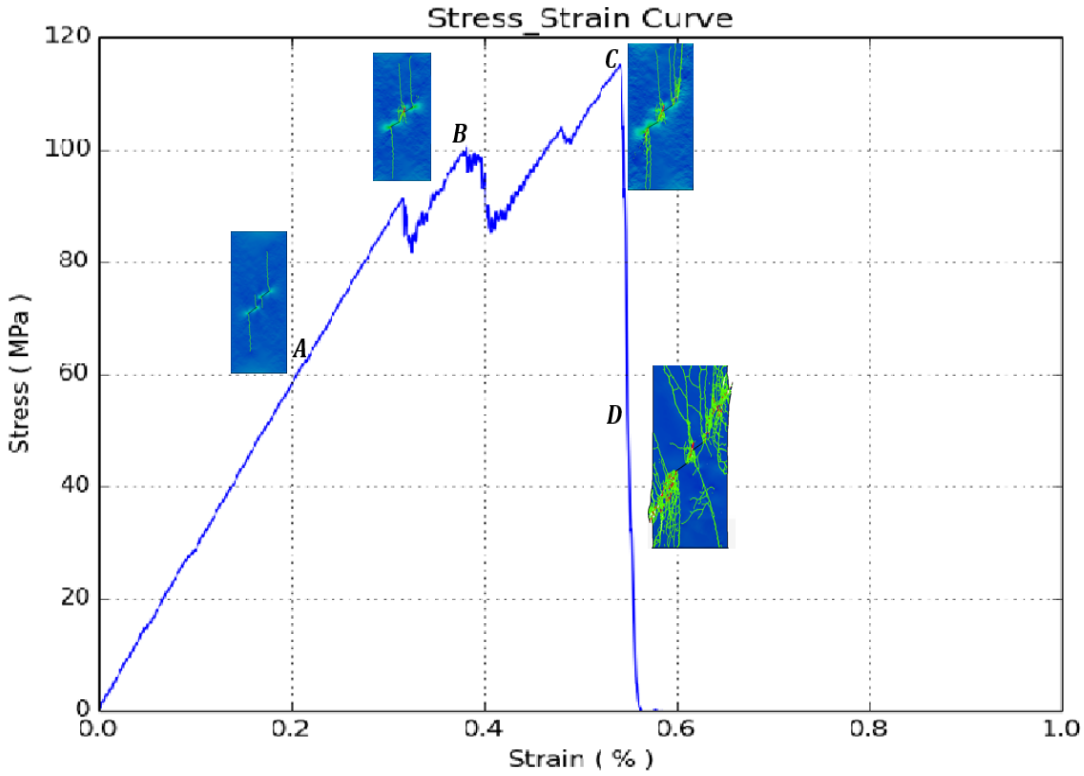

Figure 3.4. Axial stress versus axial strain for the UCS test simulation with two cracks. Letters A to D refer to the stages shown in Figure 3.3.

Indeed, although the model simulated the same peak strength as the tested rock specimen (approximately 110 MPa), the strain level in the model was only half that measured in the laboratory. It is argued that numerical models cannot truly capture the non-linear behaviour observed at the beginning of laboratory scale uniaxial testing since the models assume a perfect sample, whereas laboratory specimens would have micro-cracks and defects randomly distributed in the matrix. As the specimen is loaded under laboratory conditions, these micro-cracks tend to close, giving rise to a non-linear behaviour. A quantitative comparison of the laboratory testing and the Irazu simulation is possible by comparing the stress-strain curves from the test. The maximum uniaxial compressive strength of the laboratory uniaxial compressive strength with two pre-existing cracks had a value of 110 MPa at 1.1 % strain (Figure 3.5).

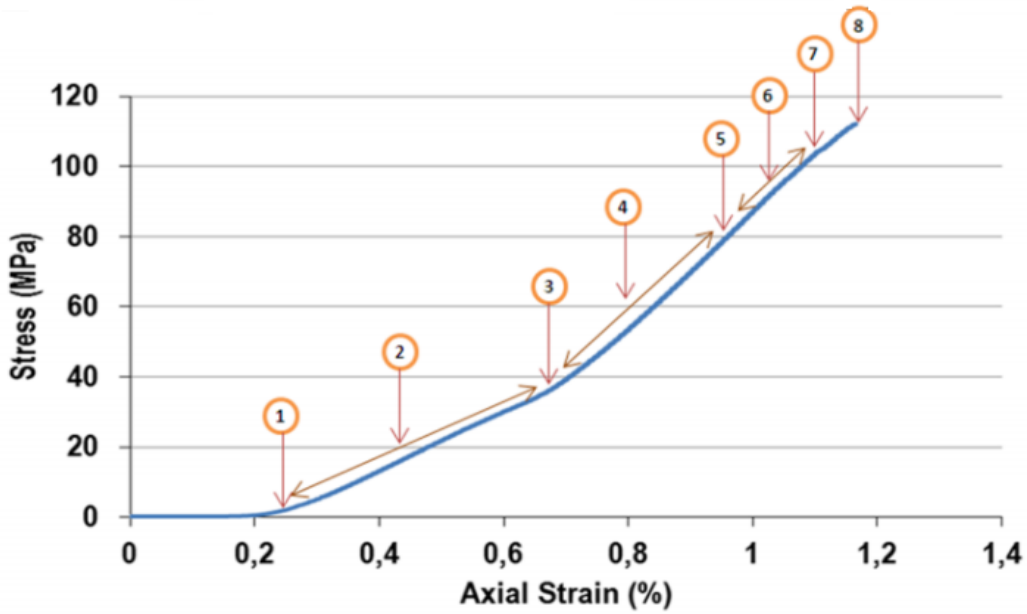

Figure 3.5. Axial stress (MPa) vs. axial strain (%) and cracking levels for the granite specimen with two pre-existing cracks. 1) crack closure, 2) linear elastic deformation, 3) micro-crack initiation, 4) micro-crack growth, 5) micro-crack coalescence, 6) macro-crack growth, 7) macro-crack coalescence and 8) failure (after, Moradian et al., 2015).

3.4.2 Simulation Results using FDEM-Elfen

The main difference between the models simulated in ELFEN and Irazu is the absence of direct Mode II fracture mechanisms in the former. Mode II in ELFEN models is indirectly simulated as the result of growth and coalescence of Mode I cracks. A Mohr-Coulomb with rotating crack constitutive model (Klerck, 2000) is used to simulate fracturing under both shear and tensile conditions. Figure 3.6 shows the different stages (A to D) of the failure process in the ELFEN model.

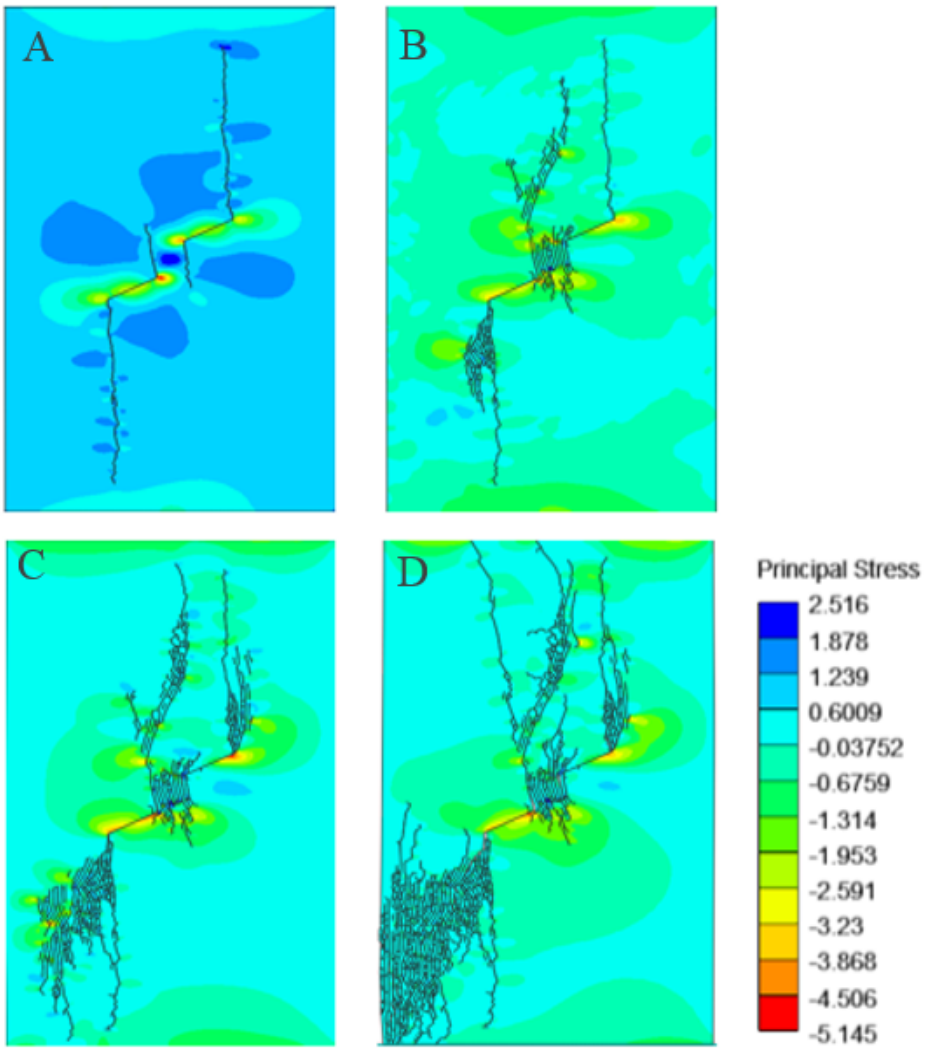

Figure 3.6. Simulated uniaxial compression in ELFEN showing the contours of the direct stress ZZ stress with the newly-generated cracks shown in black. Various stages of cracking are shown in A-D.

3.5 FDEM Fracture Analysis

The newly-generated fractures were exported from Irazu-FDEM software and various approaches to analyze are suggested and applied to the newly-generated fractures. Although, the developed methods are applied on Irazu models, the methodologies are also applicable to the ELFEN simulation models. Comprehensive methodologies for the application of these methods to any DEM and FDEM simulation outputs are presented in chapter 5.

3.5.1 Orientation Analysis and Number of Fractures in Irazu-FDEM

The orientation of newly-generated cracks can be shown using rosette plots, thus allowing to quantitatively analyze the increase in the number of cracks being generated in relation to their orientation at different strain levels (Figure 3.7). The same approach was used by Hamdi (2015) to better quantify the orientation of the newly-generated cracks in various confining pressures.

In this section, the crack intensity (percentage) is calculated as a percentage of the maximum number of cracks for a specific sector using eighteen different bins to represent angles of between 0 and 180 degrees with respect to the vertical axis of the sample. The fractures are shown as the percentage of the fractures being generated normalized with respect to the orientation with the maximum number of fractures. This means that 100% denotes the maximum number of fractures in a specific orientation. While any other bin shows the percentage of fractures with respect to the defined maximum number of fractures.

As the strain levels increases from 0.35 to 0.6%, the crack percentage distribution varies from semi-vertical (10-20 and 170-160 degrees; see Figure 3.7a and Figure 3.7b) to scattered (40-120 degrees, see Figure 3.7.c and d). Note that the fractures are measured with respect to the vertical axis of the sample. The percentage of cracks in each bin varies depending on the associated strain level. In the early stages of the simulation (pre-peak) with 0.35% strain, the highest percentage of fractures are vertical; this agrees well with the angle at which the tensile cracks are initiated from pre-existing cracks (parallel to major principal stress). As the simulation progresses, cracks are still predominantly aligned vertically. Once the sample fails, cracks are generated at a much shallower angle, which is attributed to the generation of shear fractures in the later stages of the simulation.

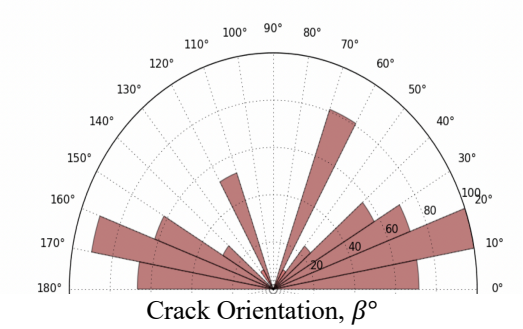

(a) 0.3% Strain

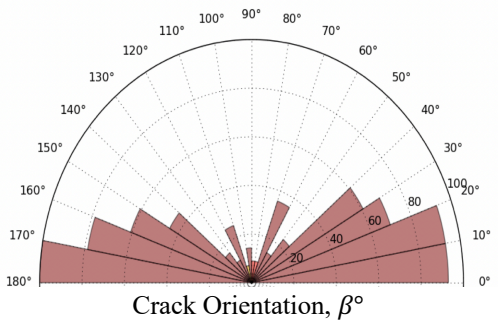

(b) 0.4% Strain

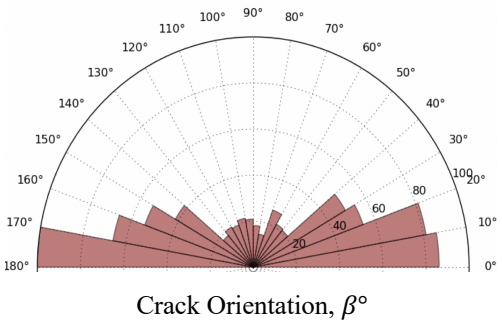

(c) 0.5% Strain

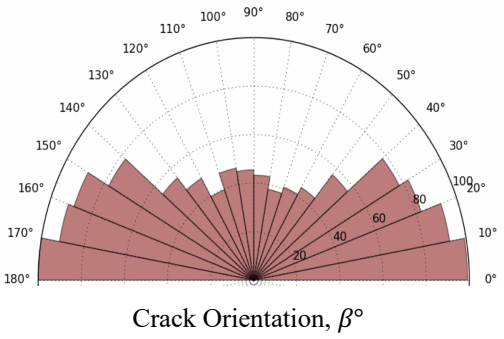

(d) 0.6% Strain

Figure 3.7. Rosette plots for the Irazu uniaxial compression test simulation showing the orientation of the newly-generated cracks with respect to the vertical. The percentage of the failed cracks is shown at four different strain levels, A. 0.35, B. 0. 4, C. 0.54 and D. 0.6 %.

3.5.2 Failure Mode Analysis and Damage Quantification in Irazu-FDEM

Newly-generated cracks are generated due to the relative displacement of the triangular meshed elements with respect to each other. Depending on the relative displacement (opening, sliding or both), various failure modes are associated with the crack generation process.

The lines of the newly-generated cracks in the FDEM Irazu models are identified by the edges of the triangular elements (Figure 3.8). Each edge of the triangular element has two points and the average coordinate of each point is calculated using the nodal coordinates for the elements. The coordinates of the newly-generated crack lines are used in the proposed simulation for calculating

the number of cracks at each numerical time step (crack counts) and the location of the cohesive crack element intersections.

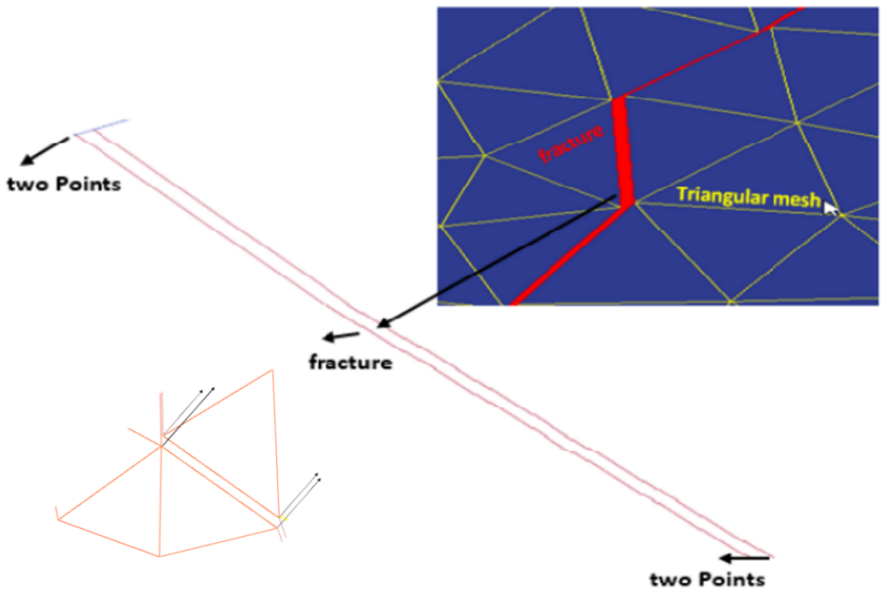

Figure 3.8. Crack generation in the Irazu-FDEM simulation, each triangle element has three nodes and each crack element has four nodes.

Figure 3.9 shows the percentage of the crack events due to Mode I fracture, which is 90% greater than the counts of Mode II events. These observations correspond well with the generally accepted damage process in brittle rocks, whereby damage initiates and accumulates originally due to tensile failure, while shear failure can only occur after the specimen has been sufficiently damaged by tensile failure mechanisms. As the loading continues, tensile stresses are generated in compression because of the pre-existing flaws. For this simulation, the sample remains undamaged for the first 13% of the total simulation time. Damage then increases with an increase in loading and remains constant over the last 40% of the simulation time.

The initiation of tensile fractures at the 0.05 % strain level can be associated with the linear elastic behaviour part of the stress-strain curve (Figure 3.3.A and Figure 3.4.A). The model correlates with Stage 2 shown by Moradian et al. (2015) (Figure 3.5, Stage 2). It also correlates with the initiation of tensile fractures at the 0.05% as shown in Figure 3.9. The propagation of tensile fractures between strain levels 0.05 – 0.35 % (Figure 3.3.B and Figure 3.4.B) is associated with onset of dilation and stable crack propagation as shown in (Figure 3.5, Stage 3-7). This is also shown in Figure 3.9 at 0.3% strain when tensile damage cracks coalesce and shear fracturing initiates.

The initiation of shear and mixed mode cracks at a strain level of 0.4 % (Figure 3.3.C and Figure 3.4.C) can be associated with unstable crack growth (Figure 3.5, Stage 8) and is evident the blue (tensile) and green (shear) curves presented in Figure 3.9 (0.4-0.55% strain level). The brittle post-peak stage is apparent in (Figure 3.3.D and Figure 3.4.D). The post-peak stage is simulated as a mixture of various failure modes in Figure 3.9 (0.55-0.7% strain). In the Irazu simulation, few mixed mode failures were observed when the joint opening and sliding reached the critical value simultaneously. In our model simulations, only approximately 1% of mixed-mode cracks were observed as this condition is only rarely satisfied.

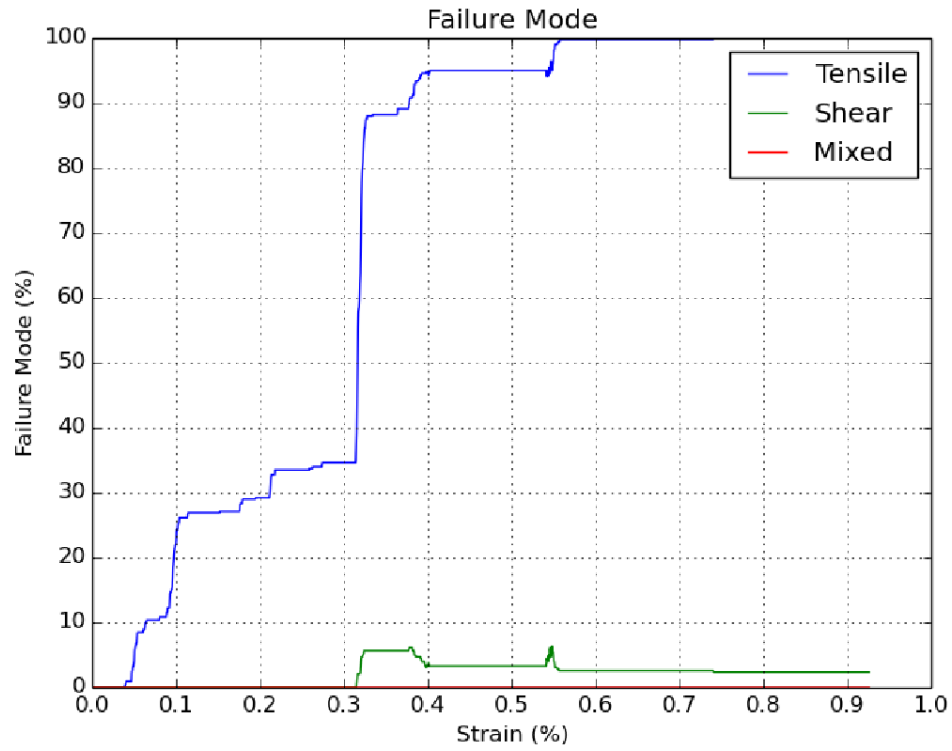

Figure 3.9. Frequency percentage with respect to strain for the Irazu uniaxial compression test simulation with two pre-existing cracks.

Many researchers have attempted to quantify rock damage by introducing different parameters. For example, Diederichs et al. (2004) introduced crack density to quantify damage in the PFC (Itasca, 1995) laboratory testing models. In the current analysis, Damage Intensity D_{21} is described as the ratio of the sum length of total damage to the sampling area:

$$\boldsymbol{D_{21} = \frac{\text{Sum length of damage}}{\text{Sampling area}}} \qquad \textbf{[Eq. 3]}$$

Gao (2013) employed the D_{21} concept to characterize brittle fracture above coal mine roadways. The concept of damage intensity was also used by Tuckey (2012) to characterize discontinuity persistence and intact rock bridges. In this study, the damage intensity (D_{21}) is calculated with respect to the failure mode percentage at different strain levels. Figure 3.10 presents the relationship between the failure mode percentage and the cumulative damage intensity values for

various modes of failure. Most of the damage is due to mode I fracturing, and the total tensile damage is approximately 14 times higher than the damage caused by shear mode. Tensile fractures are responsible for the damage intensity up to 45 mm/mm^2, while only 6% of the total shear fractures are responsible for 0.01 mm/mm^2 damage intensity.

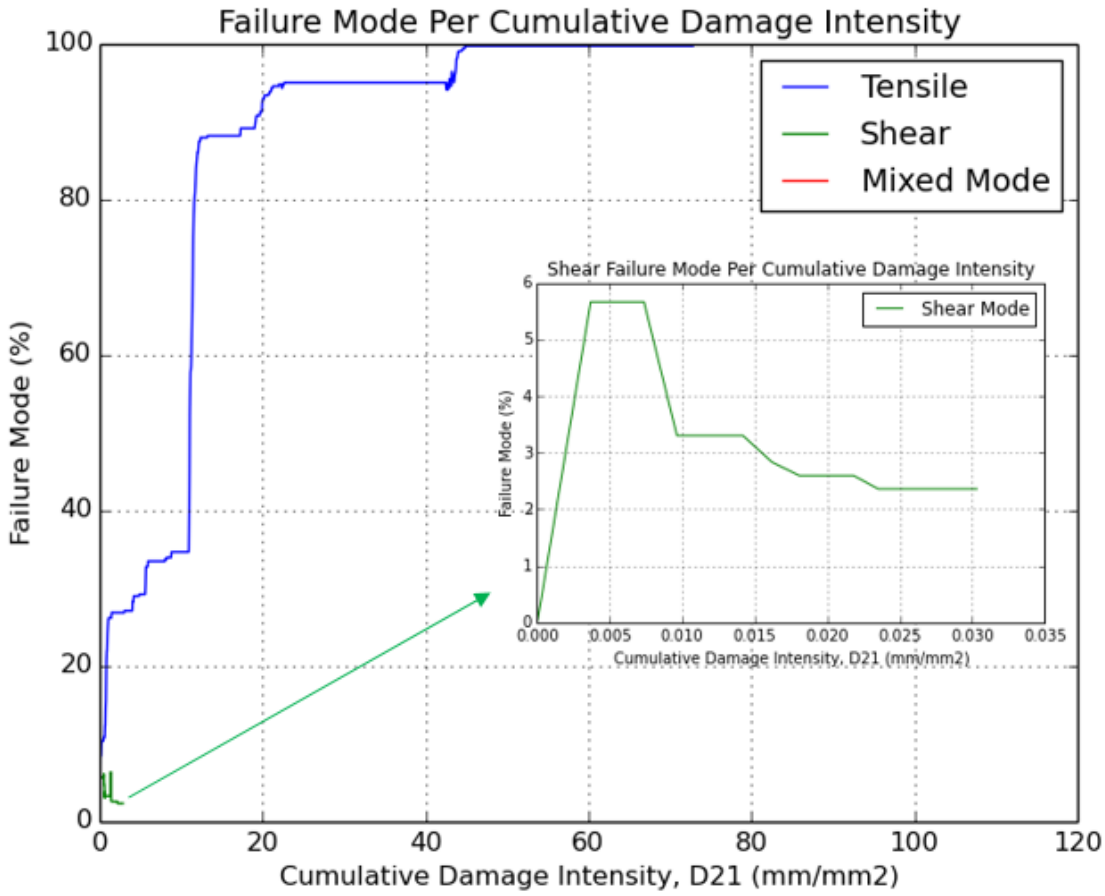

Figure 3.10. Variation of the frequency (percentage with respect to the maximum count of each failure mode) against the cumulative damage intensity for the Irazu simulated uniaxial compression test.

The main limitation of the damage intensity concept is its inability to differentiate between a system of connected and disconnected lines. Therefore, there is the need to use crack intersections as a better method to characterize damage. Simulated crack counts and crack intersection counts are plotted against progressive strain rates in Figure 3.11 and Figure 3.12, respectively. The

observed changes in the slope of the curve shown in Figure 3.11 are attributed to the various stages of fracture initiation and coalescence (A and B in Figure 3.11), propagation (C in Figure 3.11) and final failure (D in Figure 3.11).

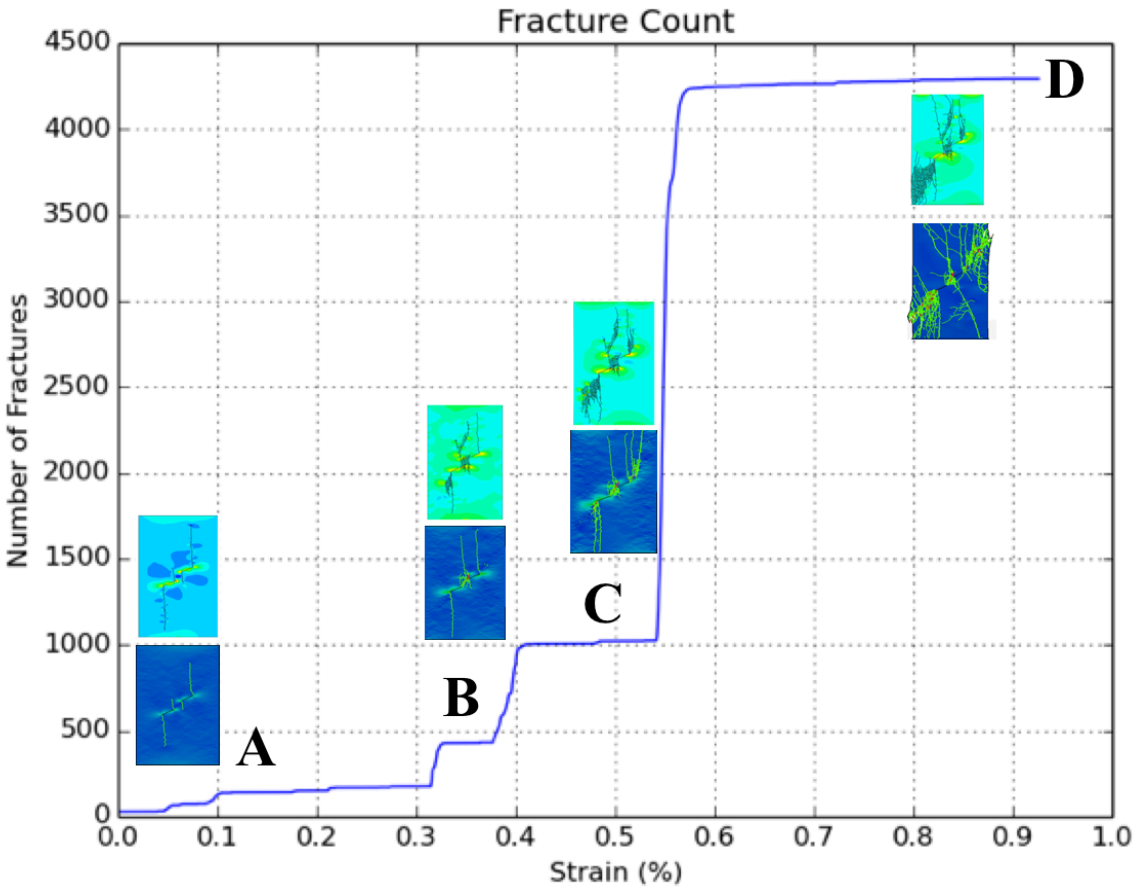

Figure 3.11. Number of cracks simulated at different strain levels during 2D uniaxial compression simulation. A. micro-crack initiation, B. micro-crack coalescence, C. macro-crack growth, D. macro-crack coalescence and failure.

The number of crack intersections is also plotted against strain (Figure 3.12). The number of intersections increases with strain almost exponentially, to reflect processes of cracks coalescence during the simulation. The slope change (Figure 3.12, Point B) at a strain of 0.35-0.5 % can be

attributed to the onset of dilation and stable crack propagation. The second and steeper slope change (Figure 3.12, Point C) occurs at a strain level of 0.5-0.6 % and correlates with the generation of a shear failure surface due to macro-crack initiation and unstable crack growth. The number of crack intersections remains constant in the post-peak.

Although, the number of crack intersections plot provides information on the various stages of crack evolution, it does not include spatial information about the locations where fractures intersections occur. The concept of crack intersections has been used by several researchers and explained in detail in chapter 2. Two cracks can be directly connected to each other (intersect) or can be indirectly connected through a pathway via other connected cracks within a crack network. This chapter focuses on analysing the dynamic behaviour of the simulated crack intersection density of the newly-generated fractures throughout the full Irazu FDEM simulations. This approach has the potential to accommodate a variable degree of complexity, e.g., complex intersections in a crack network including varying crack intensity, varying crack geometry and variations in numbers of cracks of different scale.

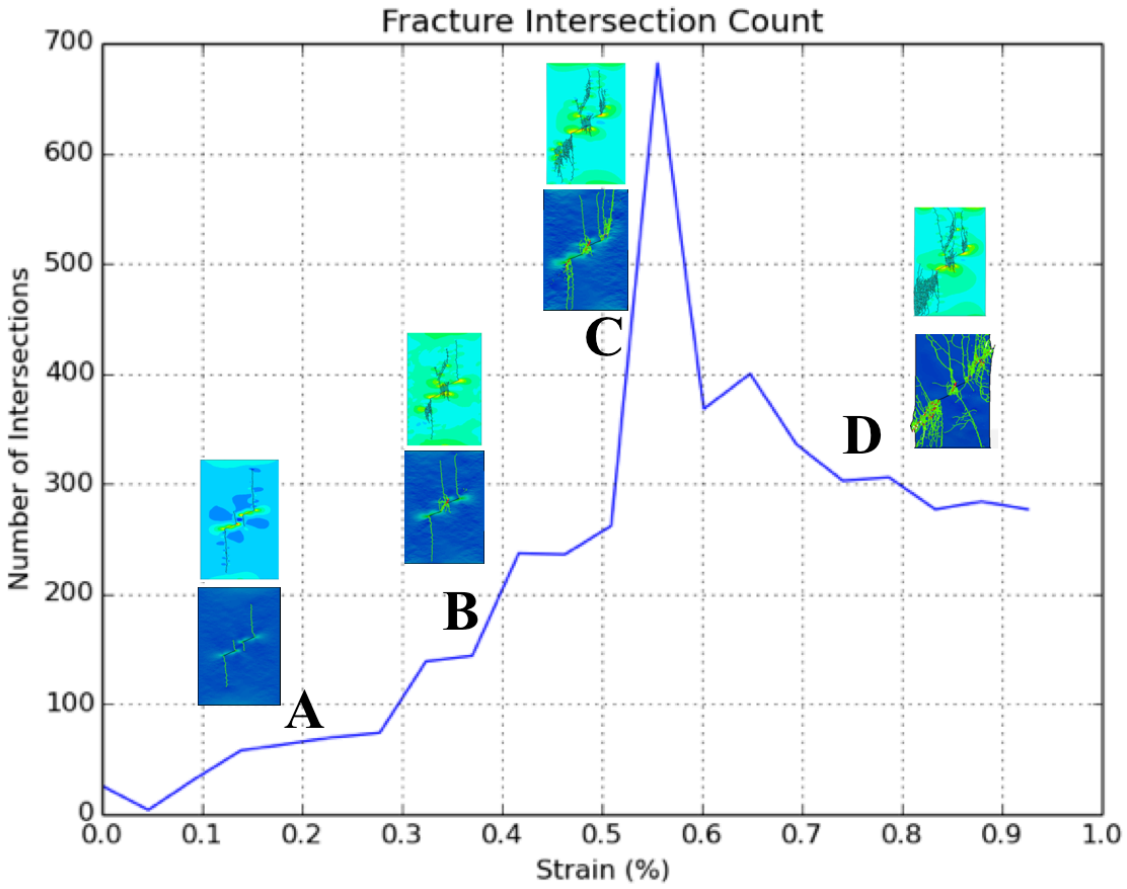

Figure 3.12. Number of crack intersections with respect to axial strain for a simulated uniaxial compression test with two 13 mm pre-existing cracks. A. micro-crack initiation. B. coalescence and growth. C. macro-crack coalescence and D. final failure.

A simple crack network can contain hundreds of cracks of different sizes and orientations. The geometrical intersections are critical control points for evaluating the behaviour of the system. The synthesized crack network that results from FDEM simulations depict significant features which could be the subject of comparison between different models.

The newly-generated crack segments and the crack intersection points are shown in Figure 3.13. It can be seen that the resulting intersection points follow the crack segments at 0.6% strain (It is possible to trace segments by simply joining up the intersections). The intersection of two cracks

at any time is a point and the connected cracks within different stages eventually form a continuous crack. The geometry of a continuous crack can be constructed by connecting several cohesive crack elements that belong to the crack. The coordinates of the crack intersections are calculated using an algorithm which loops through all the possibilities of how one crack can intersect another existing crack.

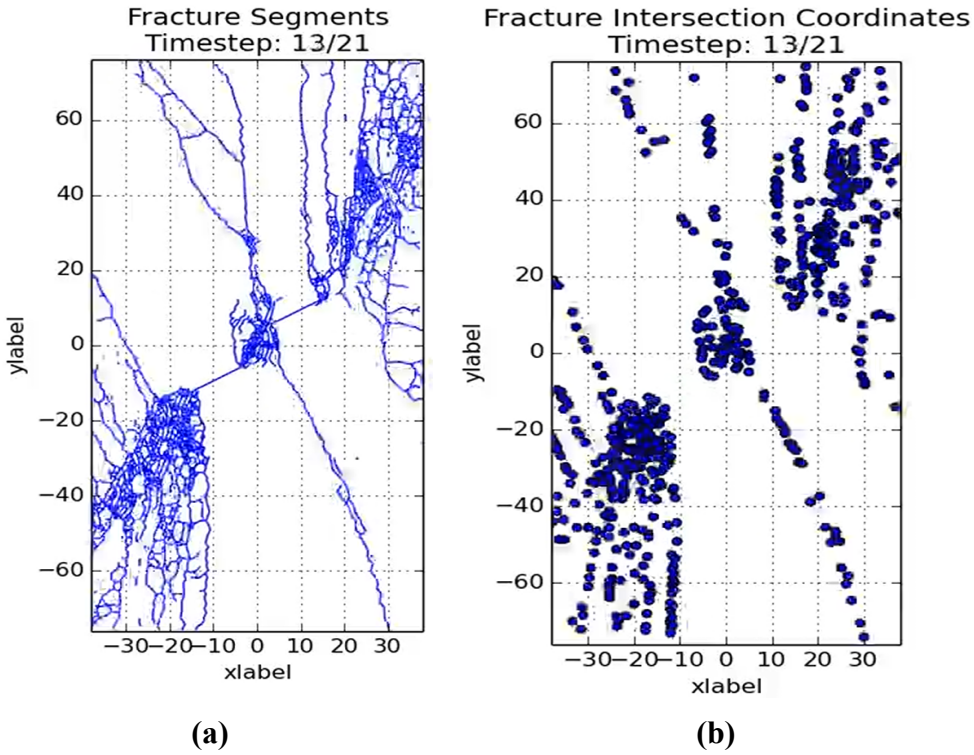

Figure 3.13: a) The crack segments and b) crack intersection points throughout the sample at a strain level of 0.6 %.

The coordinate points in Figure 3.13 do not explicitly indicate the type of interactions between cracks, such as intersections, terminations of one crack against another or extension. Therefore, colour code maps were generated based on the density of the crack intersection points throughout the sample. The weight of these intersection points is determined based on the number of points located in each cell. Using the density plot with hexagonal tiling and a grid size of 20 (the number

of hexagons in x-direction), the spatial and temporal density of the intersection points are calculated and shown in Figure 3.14. The number of intersection points is generally denser in the centre and at the beginning of the simulation. As the simulation progresses, the intersection density is more concentrated further away from the pre-existing cracks and closer to the platens. The regions shown in yellow and red colours have a higher crack intersection density which agrees with the areas in which shear crack development occurs.

This study will be expanded on in subsequent chapters to include various combinations of pre-existing cracks and using a Discrete Fracture Network models (DFN) approach for the detailed investigation of newly-generated cracks. This approach may allow the influence of rock bridges on the instability of geotechnical structures to be examined in a more robust manner. Rock bridge content is often considered a major factor in the magnitude of the hazards posed by brittle fracture in geotechnical and mining projects and hence further research using the proposed crack intersection and density approaches may have considerable potential.

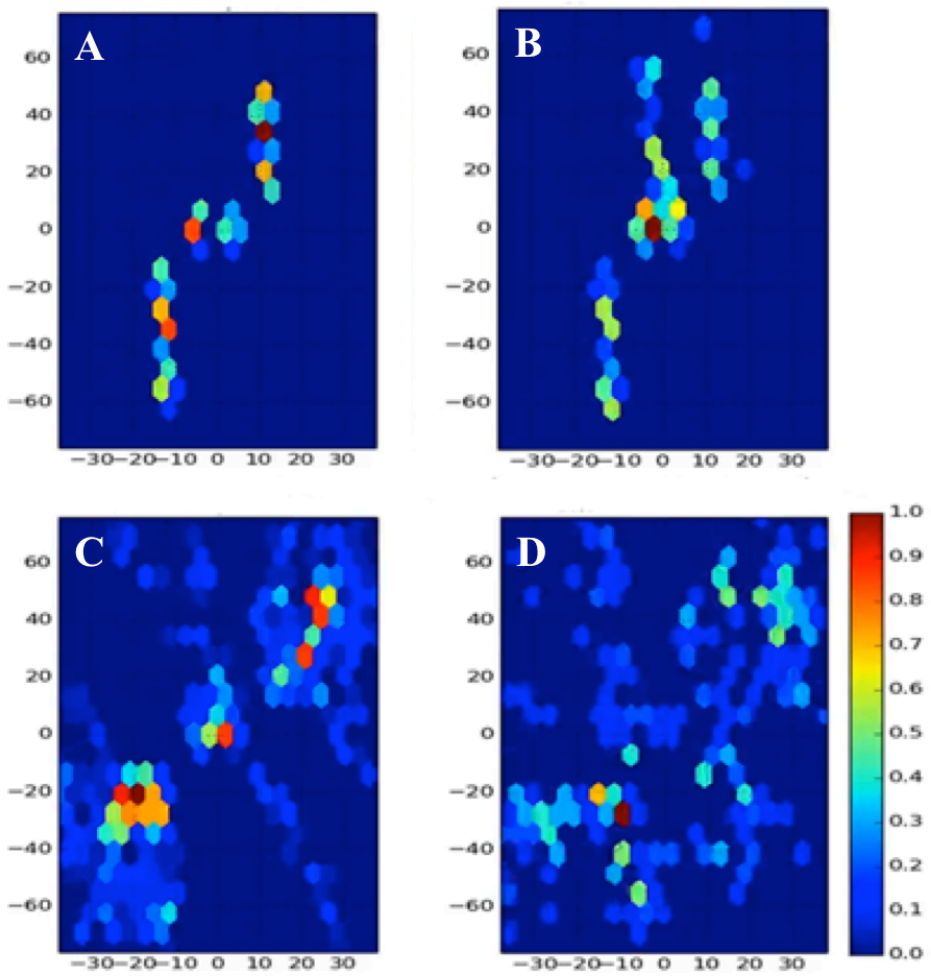

Figure 3.14. Crack intersection density map for uniaxial compression Irazu simulation at four different strain levels of 0.35%, 0.4%, 0.54 and 0.6%. The colour bar indicates the weight of the number of crack intersections in each cell.

3.6 Conclusions

The preliminary results presented in this chapter clearly show that the results of FDEM simulations cannot always provide the answers to problems such as failure of intact rock bridges and step-path mechanisms. The concept of damage, orientation and crack intersection density maps introduced in this chapter offers a promising method with which to obtain important geomechanical insights

into rock cracking and damage processes. This method allows the characterization of damage and crack intersections in a numerical simulation in a quantitative manner. Subsequent chapters will refine the concept of fracture analysis to account for aperture and sliding and allow improved damage and block analysis.

Chapter 4: Improving DFN-Geomechanical Model Integration Using Novel Algorithms

4.1 Introduction

The challenges in acquiring appropriate input parameters for numerical modelling increase with the complexity of the numerical method being adopted (Stead and Eberhardt, 2013). This becomes even more important for models in which discrete fracture network (DFN) models are integrated within a geomechanical analysis to characterisze the mechanical behaviour of fractured rock masses. The synthesis of a DFN model requires information on fracture intensity, fracture orientation, fracture length and fracture terminations. When generated, a DFN model can include thousands of fractures, which often lead to very complex geometric configurations. Lorig et al. (2015) describe how the local joint configurations and the large number of fractures required to realistically model the natural rock mass complexity represent a major limiting factor in the integration of DFNs within numerical models. As noted in Mayer, (2015), while algorithms used for DFN generation have greatly improved over recent years, they often do not consider the subsequent mesh generation routines that are required for geomechanical simulation. The reliability of any integrated DFN-geomechanical approach is therefore a function of the care given to the way in which the structural data are embedded in the geomechanical model at the required engineering scale.

Typically, once a DFN model is generated, 2D or 3D fracture networks can be embedded within the solid rock mass in a finite element geomechanical model by inserting fractures with both sides of the fracture represented as free surfaces. This solid model is then discretized using triangular (2D) and tetrahedral (3D) elements. Note that the specific case of particle flow codes

is not considered in this chapter. During the meshing procedure, dedicated algorithms should be employed to ensure a reasonable mesh quality is achieved, while at the same time preserving the original DFN fracture resolution. The process is herein referred to as *DFN Analysis and Cleaning*. The DFN resolution is directly linked to mesh size: while using a relatively small mesh size would help maintaining the original DFN resolution, this could result in exceedingly long computational times. Conversely, increasing the mesh size without changing the DFN resolution would potentially be the source of numerical instabilities due to the resulting very thin or low-angle intersections that could potentially distort the mesh elements. For example, Pine et al. (2006) suggest that excessively small or ‘‘sliver’’ elements may result from either very closely spaced fractures or from the termination of fractures in close proximity to each other. In the former case, the two fractures may be merged; in the latter case, the nodes defining the near fracture intersection may be snapped together. An example is shown in
Figure 4.1 for a synthetic rock mass. In other cases, fractures may be in too close proximity and would need to be moved relative to each other; this is particularly relevant if the DFN model is generated using a spatial definition of fracture positions based on a random Poisson process such as the widely employed Enhanced Baecher model (Elmo et al. 2014a). For such fracture adjustments to be truly effective, there is a need to preserve the overall fracture intensity and to maintain the orientation and connectivity of the original fracture network. The objective should be to minimize the impact that required adjustments have on the overall behaviour of the resulting simulated rock mass.

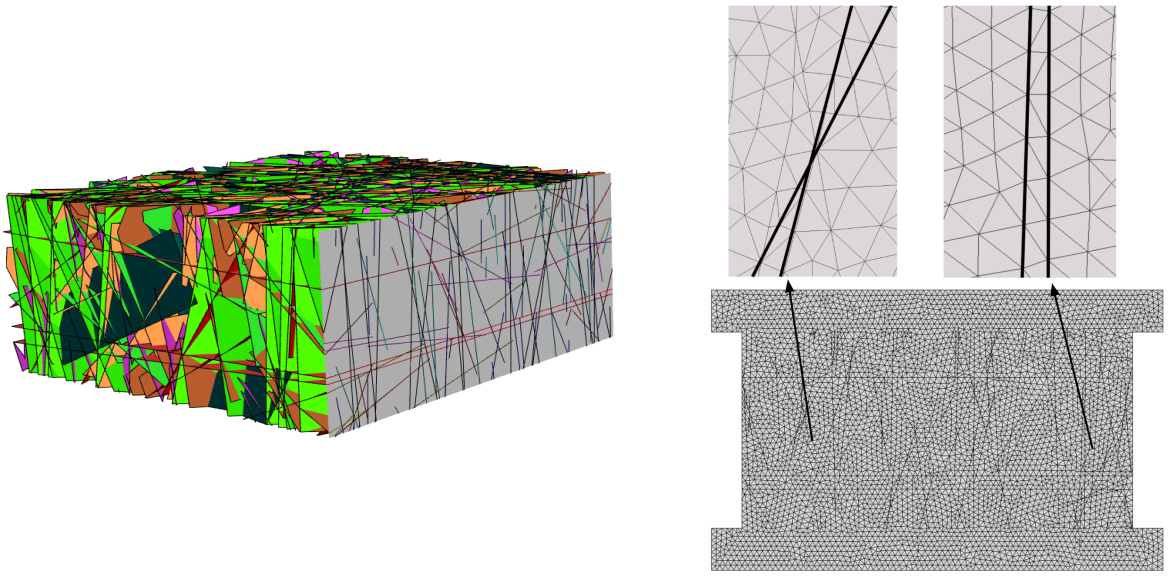

(a) (b)

Figure 4.1. (a) 2D plane corresponding to one of the outer faces of a 3D DFN model of a synthetic rock mass, and (b) resulting meshed fracture traces within a FEM-DEM geomechanical software clearly showing some of the meshing issues discussed in the text (e.g. the left black arrow denotes fractures which make acute angles to each other and the right black arrow denotes two close fractures).

Similarly, the stochastic nature of the DFN process is such that there are an infinite number of possible realizations of the fracture system based on the mapped data. This becomes a source of variability within geomechanical models (Olofsson and Fredriksson., 2005; Bagheri, 2009; Elmouttie and Poropat, 2011; Elmo et al., 2015). To characterize this variability multiple DFN realizations of the same statistical distributions need to be run; accordingly, the *DFN Analysis and Cleaning* procedure must be repeated several times. Depending on the complexity of the DFNs, the pre-processing and model set-up would therefore have a potentially high cost in terms of both computing and personnel time. It is obviously important to maintain the highest possible similarity of statistical properties of the "*cleaned*" DFN compared to the original DFN. Without the availability of an appropriate algorithm there is the risk of added human uncertainty, as the results

of manually cleaning the DFN model would depend on the experience of the user and how they interpret the need to correct/modify specific fracture intersections.

This chapter introduces new methods (DFN Analysis, DFN Cleaning, DFN Quality and Mesh Quality) that analyze the properties of an original fracture network, and then simplify it to ensure a reasonable mesh quality is achieved based on the calculated geometric characteristics. Mesh cleaning tools exist within specific numerical software (e.g. RS^{2D}; RocScience, 2017) that allow to fix a poor-quality mesh. Here, we introduce tunable methods that compute DFN traces that are easier to integrate within different geomechanical software, and assess and maintain the original DFN properties. The proposed approach is generic and could be used in conjunction with FEM based software (e.g., RS^{2D}; RocScience, 2017), distinct element codes (e.g., UDEC; Itasca, 2013) and hybrid FEM-DEM codes like Elfen2D (Rockfield, 2014) and Irazu2D (Geomechanica, 2017)).

To test the effectiveness of the proposed methods, the results of the automated DFN analysis/cleaning algorithm are compared against DFN models that are manually cleaned by two users with different working experience with DFN models (intermediate to senior level). The resulting DFNs are then embedded within a FDEM code to simulate the failure of synthetic 2D pillars and investigate the variation of the modelled pillar strength, pillar mechanical response and calculated factor of safety with respect to the adopted DFN cleaning methods.

4.2 Automated Methods to Characterize the DFN

The use of DFN modelling in geomechanics as a numerical technique that allows for a more detailed consideration of the structural character of the rock mass can be traced back to Fakhimi et al. (2002). Subsequently, DFN modelling gained further momentum with the work of several

researchers, including (Elmo, 2006; Pierce et al., 2007; Diego Mas Ivars et al., 2008). Although these authors mention the limitations of the process of integrating DFN fractures (3D) and traces (2D) within geomechanical software, no solution is offered to the problem of optimizing and simplifying fractures and/or traces of the initially generated DFN model to minimize meshing issues while preserving the appropriate DFN properties.

Typically, in the DFN community, fracture intensity/density parameters are expressed with reference to a unified system of fracture measures that incorporates reference to scales and dimensions (Elmo et al., 2014). The P_{ij} system, where the subscript i refers to the dimensions of sample, and subscript j refers to the dimensions of measurement was originally introduced by Dershowitz and Herda (1992). Accordingly, for 2D analysis it is possible to define P_{21} (m/m^2) as the total trace length of fractures per unit area (areal intensity), while P_{20} (m^{-2}) is the total number of fractures per unit area (areal density). These parameters are used in the current study, in addition to intersections and terminations, to provide engineers and geoscientists with a set of unique DFN properties for the characterization of an initial fracture network. The process employed herein uses the proposed algorithms termed DFN Analysis.

The DFN Analysis algorithms are independent from the software used to generate the DFN. It requires the coordinates of the fracture lines. Flow diagrams describing the steps in the analysis for a single DFN and multiple DFNs are shown in Figure 4.2 (a) and (b), respectively. The related algorithms are presented in Appendix II.

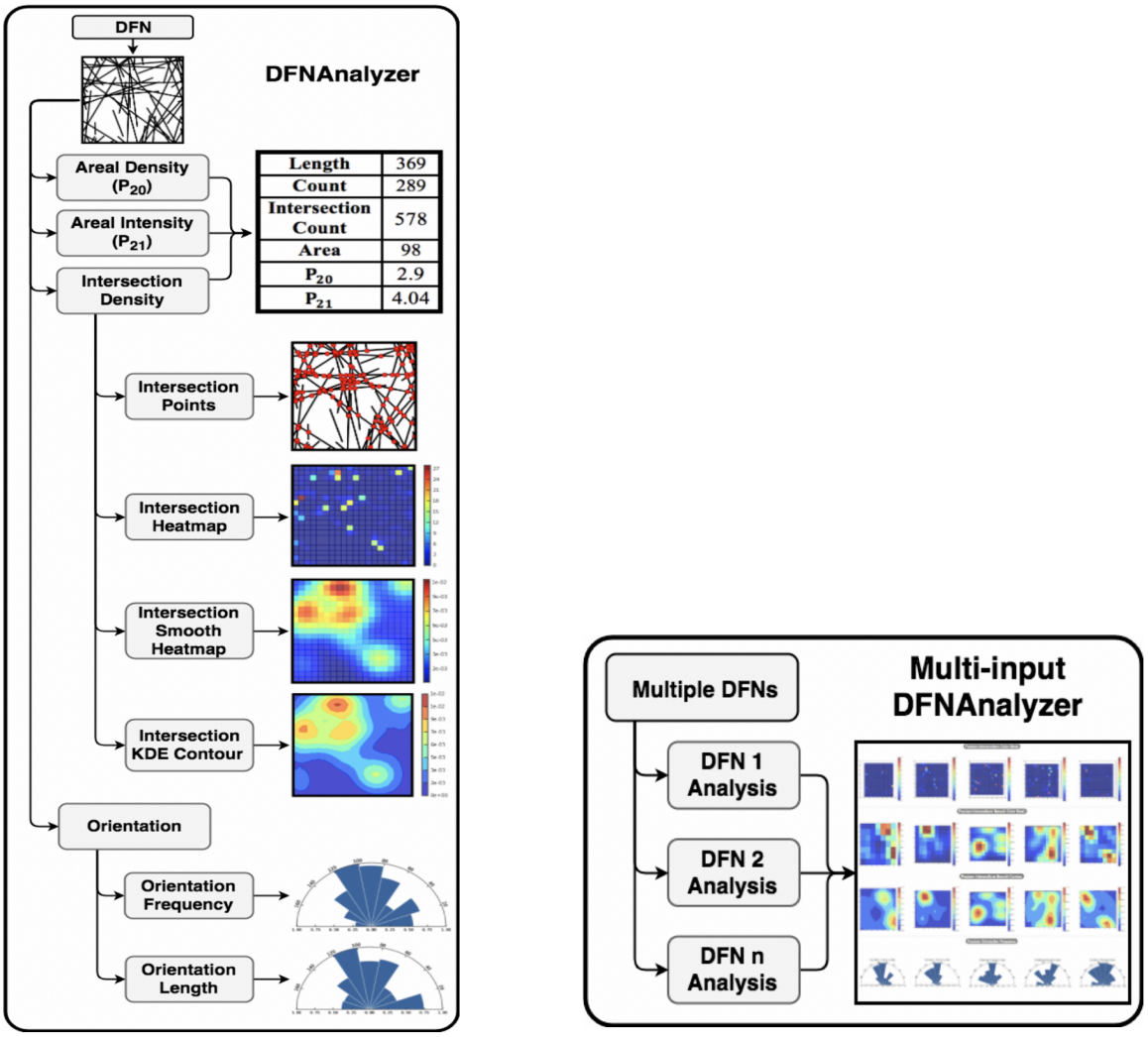

(a) (b)

Figure 4.2. (a) Flowchart illustrating the different steps in the analysis using a single DFN model. (b) multiple DFNs.

4.2.1 Analysis of Areal Fracture Density P_{20}

The number of fractures per unit area (P_{20}) can be easily calculated as the ratio of total count of fracture lines to the problem area. It is important to consider that when 2D sections are derived

from 3D DFN models that employ tessellated planar fractures (Figure 4.3), the calculated P_{20} refers to the number of segments rather than the actual number of fractures. From a meshing perspective, this would in effect lead to adjoining segments being defined by different nodes that overlap each other.

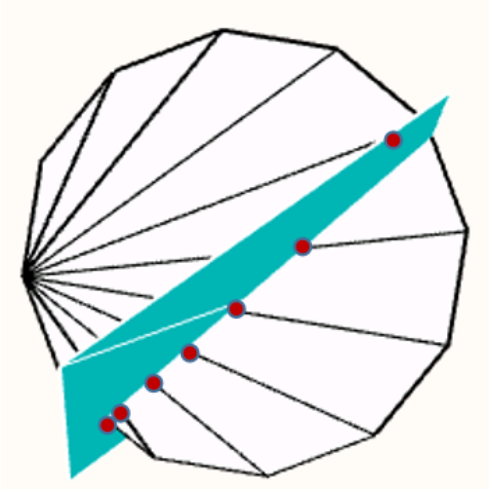

Figure 4.3. Circular fracture generated using the proprietary DFN code FracMan (Golder, 2018; Dershowitz et al., 1998), showing tessellation lines and how these would introduce adjoining segments when considering the intersection of the fracture with a plane.

The segmentation of an otherwise continuous trace impacts mesh quality, especially when some of the segments are critically small, with respect to the mesh element size. This is clearly shown in Figure 4.4, in which two fractures would be counted as eight separate fractures in the presence of tessellated lines. In the proposed approach, a procedure is implemented to remove any overlapping nodes if they are part of the same continuous fracture.

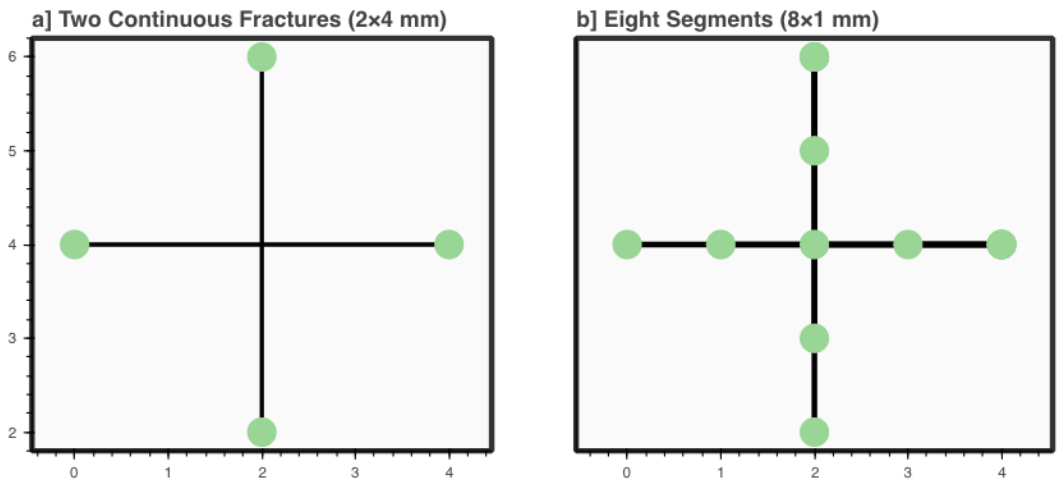

Figure 4.4. Demonstration of the limitations associated with fracture count measurement. (a) Two fractures in DFN, (b) eight fractures in DFN.

4.2.2 Fracture Length and Areal Fracture Intensity P_{21}

Areal fracture intensity is defined as the total fracture length divided by area. When considering P_{21} as an indicator for DFN analysis, there is the need to consider two important aspects:

i) P_{21} measurements are influenced by the relative orientation of the predominant fracture sets with respect to the orientation of the sampling plane; and

ii) A filtering approach is typically applied to the original 3D fracture network to make it amenable to 2D plane strain conditions and avoid consideration of artificial rock bridges. A detailed discussion on the 3D to 2D DFN filtering approach is given by Elmo et al. (2007).

Notwithstanding, P_{21} represents an important parameter that can be used to effectively characterize the variability of rock mass strength and the deformability of a fractured rock mass, as discussed in Elmo (2006) and Elmo and Stead, (2010). As shown in Figure 4.5, two different DFN models could be described using the same P_{21} intensity, when the number of fractures (P_{20}) and their individual lengths can be very different. In Elmo, (2006) and Elmo et al. (2016), the authors propose the ratio P_{21}: P_{20} as a more inclusive parameter for rock mass strength characterization.

However, the $P_{21}: P_{20}$ ratio alone cannot capture the underlying connectivity of the fracture network. This is particularly important when considering the influence of intact rock bridges on stability analysis. It is reasonable to assume that a higher degree of network connectivity would be reflected in a lower potential rock mass strength due to reduced rock bridge content. Note that the rock bridge strength itself does not change, however the rock mass strength decreases with decreasing rock bridge content. It is argued that connectivity would also be directionally dependent (with respect to the principal loading direction), and the proposed DFN Analysis algorithms can help decide whether a fracture network would be isotropically or anisotropically connected.

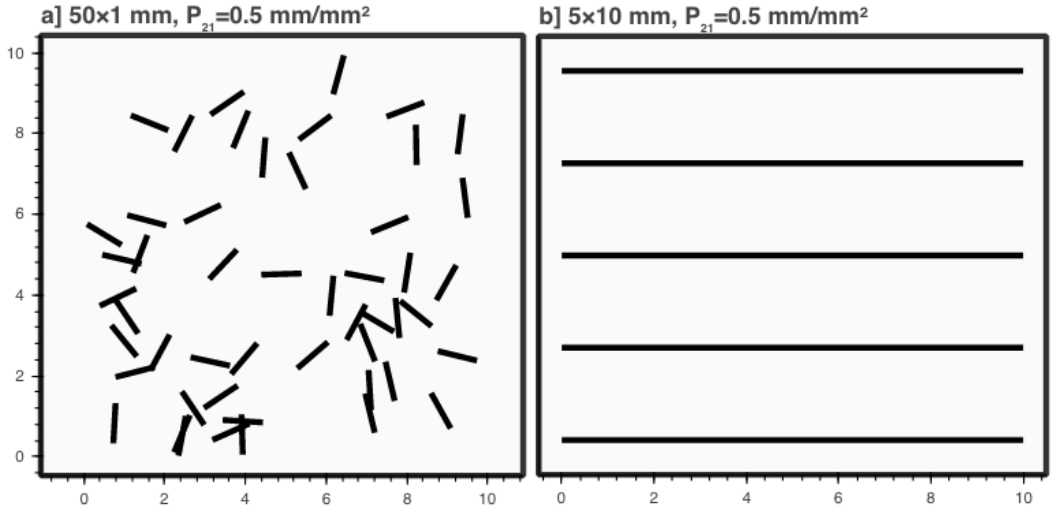

Figure 4.5. Demonstration of two different DFNs with the same P_{21} value of 0.5 (m/m2), but different fracture length.

4.2.3 Fracture Intersection Intensity and Density

The connectivity of a DFN model is clearly linked to the potential of a fracture to intersect or terminate against other fractures. This has clear implications for rock mass strength since fracture intersections determine the blockiness character of the rock mass and the rock bridge content. In

this context, fracture intersection density maps (e.g. Zhanga et al., 1992; Xu et al., 2006; Fadakar-A., 2014; Karimi et al., 2016, 2018), can be used as methods to relate the failure process observed in geomechanical models to parameters directly related to the characteristics of the initial fracture network.

Using the terminology adopted in the DFN software FracMan (Golder, 2018; Dershowitz et al., 1998), X-type and T-Type intersections can be defined and measured based on the type of termination style, as shown in Figure 4.6. The method proposed in this chapter currently considers only X-type intersections as these are the most commonly observed. The intersection density (number of intersections per sampling area) is then used as a measure of DFN connectivity.

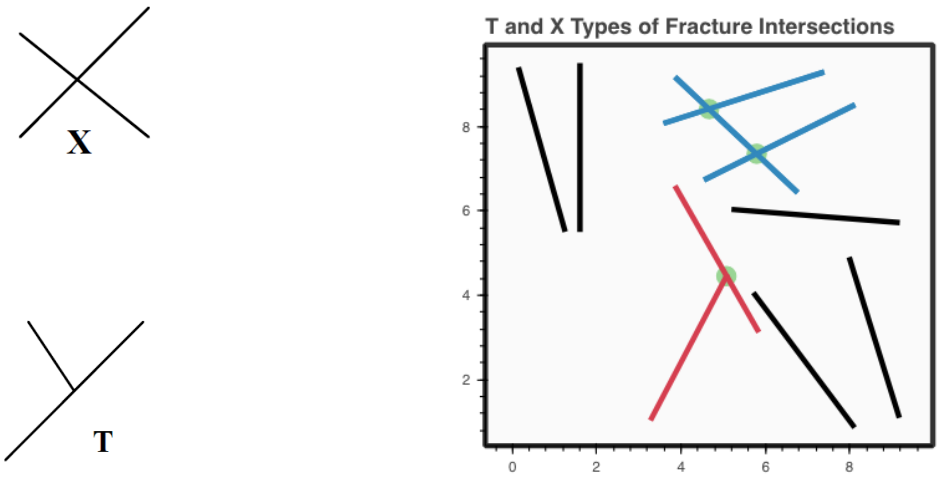

Figure 4.6. T and X types of fracture intersections and an example in which X-Type intersections are shown in blue and T-type terminations are shown in red.

Using the DFN Analysis algorithms, it is possible to calculate the location of fracture line intersections, as shown in Figure 4.7.a. The fracture lines are shown in blue, while intersection points are denoted in red colours. Heat-maps are also created to help visualize the location of areas with high fracture intersections counts (Figure 4.7.b) and high fracture intersection density (Figure

4.7.c), with warm colours denoting higher density of fracture intersections. The resolution of the heat-map is a function of the number of cells used to discretize the image. Because this may lead to an inaccurate visualization and interpretation of fracture intersection density, a smoothing algorithm (Kernel Density Estimation) is used to smooth the heat-map and the resulting image is shown in Figure 4.7.d. Kernel density estimation or KDE is a non-parametric method to estimate the probability density function of a random variable. Early work on KDE algorithms can be traced back to Wand and Jones (1995). According to Duong (2007), Kernel smoothing has become one of the most widely used non-parametric data smoothing techniques; The main difference between KDE and a normalized histogram is that it smooths the neighboring values of PDF (probability density function). The main rule for a PDF indicates that it must sum up to one. Consequently, the kernel which defines the PDF must also sum up to one (Silverman, 1986).

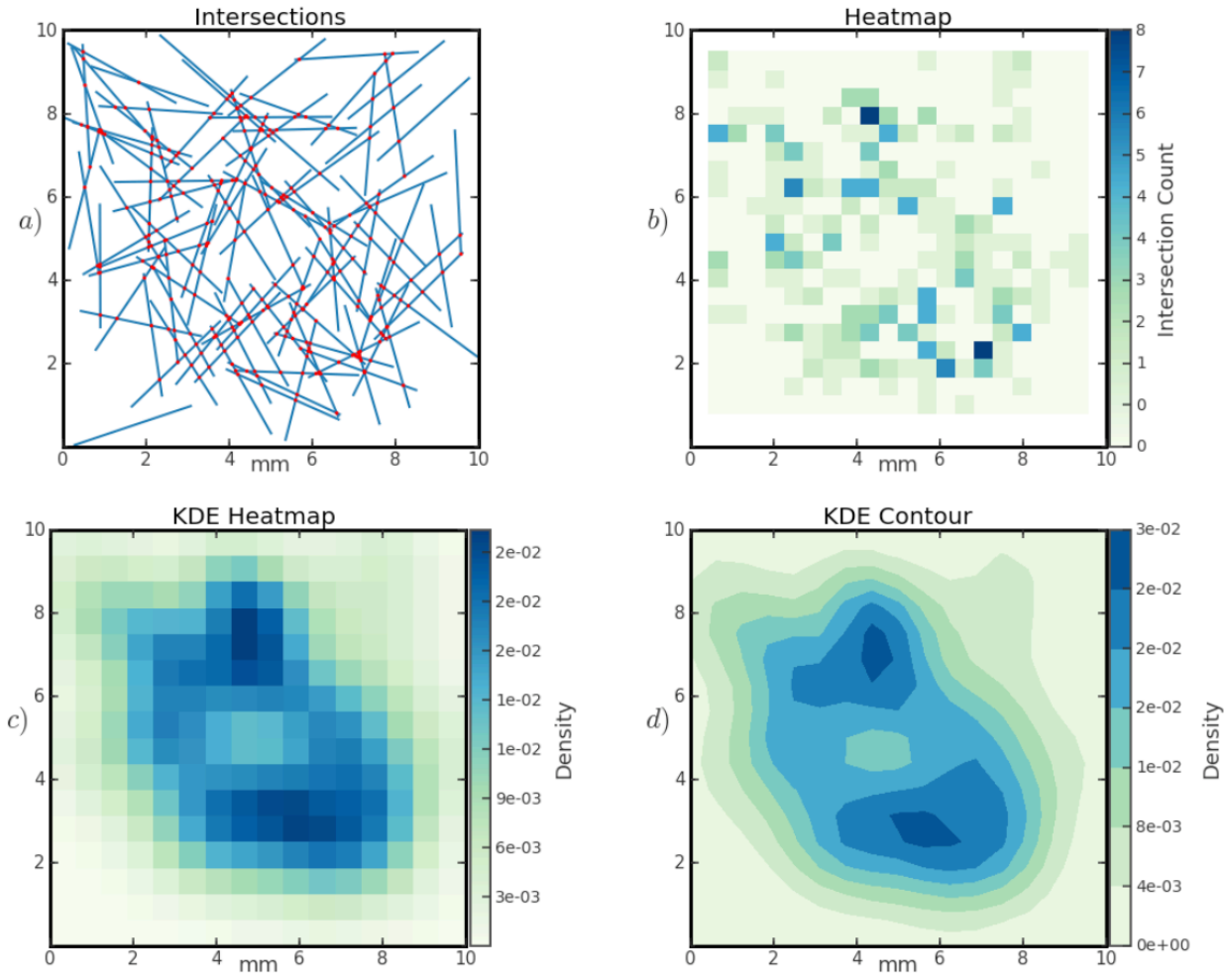

Figure 4.7. (a) Fracture lines shown in blue and fracture intersections as red points. (b) Heat-map visualization of the fracture intersection counts in which the colour bar denotes the number of fractures per cell (0.09 area) in the 100 square plane. (c) Normal smoothing applied to heat map and (d) Kernel density function applied to heat-map.

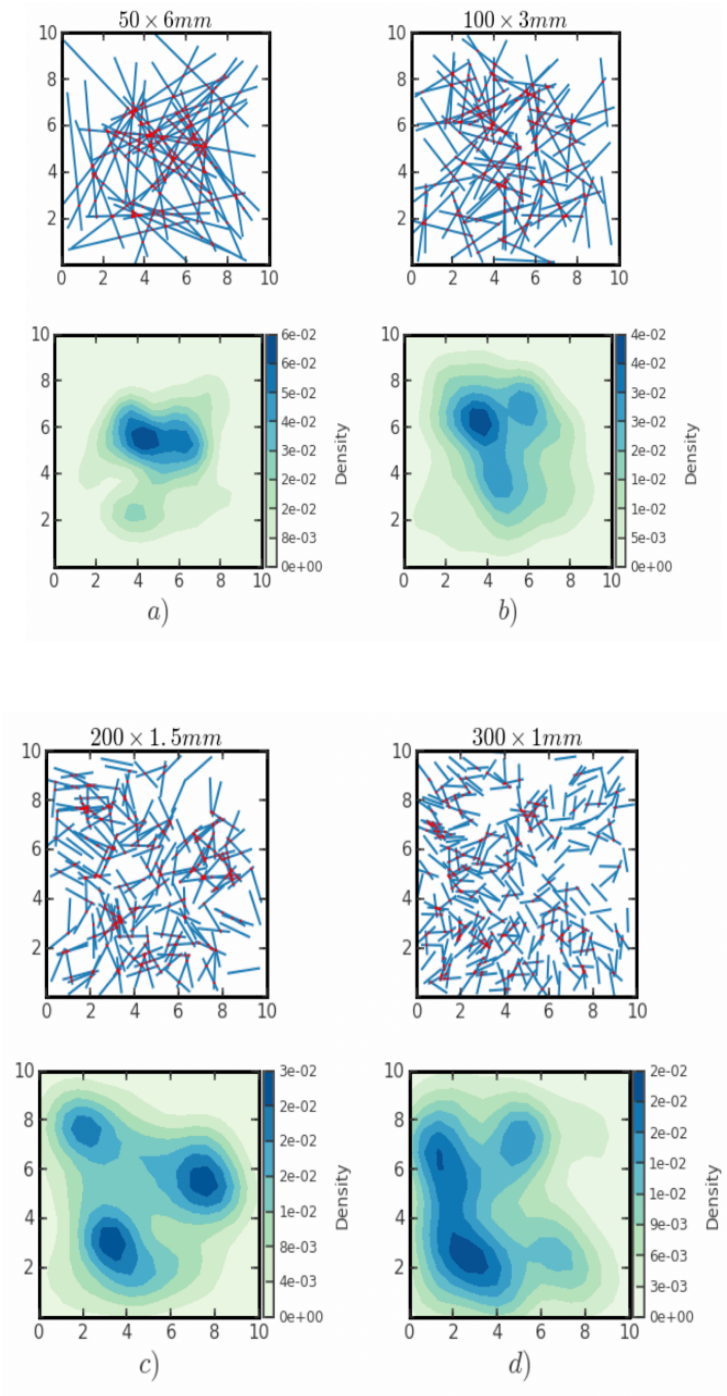

Figure 4.8. Examples of DFN's with the same P_{21}, but different fracture lengths resulting in different fracture intersection density maps with various density scales for each profile; (a) 50 fracture traces of 6 mm length; (b) 100 fracture traces of 3 mm length; (c) 200 fracture traces of 1.5 mm length; (d) 300 fracture traces of 1 mm length.

For better demonstrating the changes in fracture density values, the colour bar is kept the same for all profiles and the results shown in Figure 4.9. a-d. The colour intensity is clearly decreasing from $50 \times 6\ mm$ (Figure 4.9.a) to $300 \times 1\ mm$ (Figure 4.9.d). This implies a reduction in the fracture intersection density associated with an increase in the number of fracture lines and a decrease in the length of the fracture. Accordingly, P_{21} alone clearly cannot and should not be used as an indicator of rock mass quality.

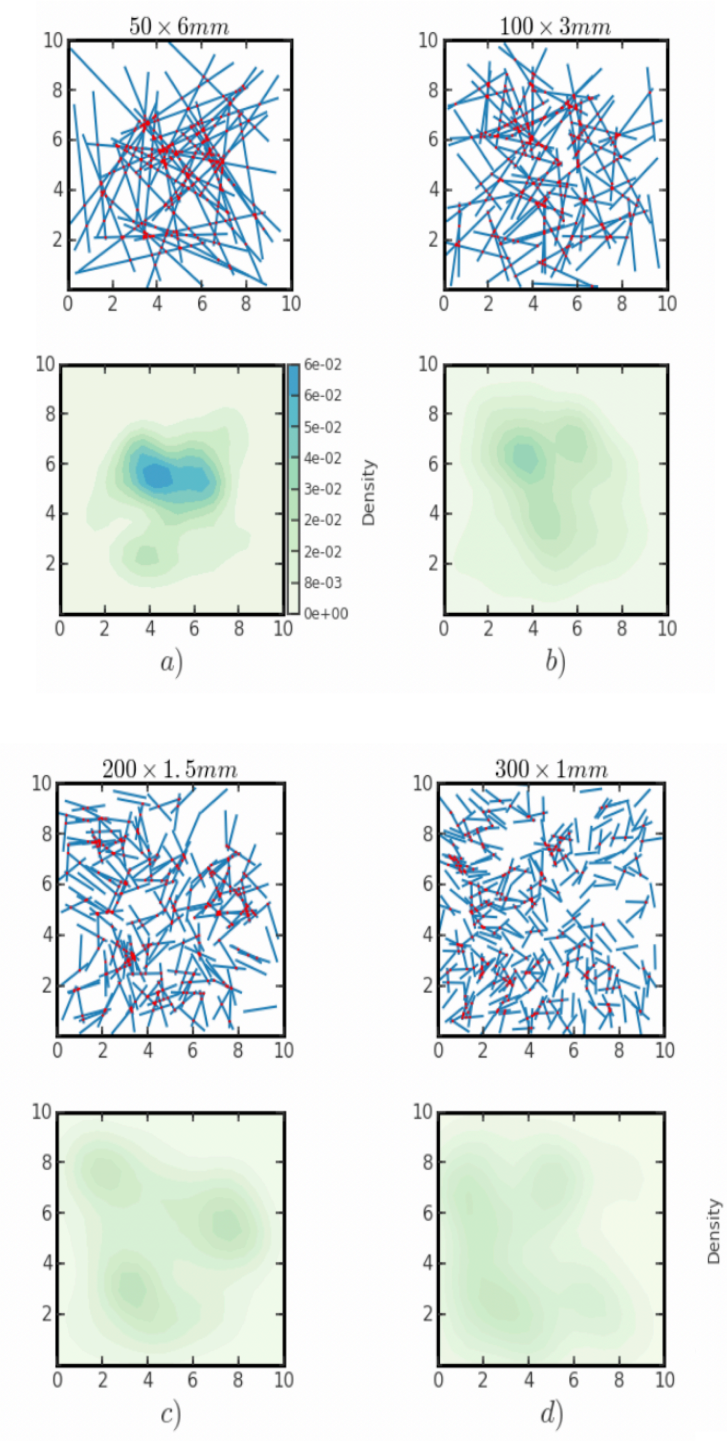

Figure 4.9. Examples of DFN's with the same P_{21}, but different fracture lengths resulting in different fracture intersection density maps shown with the same density colour bar for all profiles c; (a) 50 fracture traces of 6 mm length; (b) 100 fracture traces of 3 mm length; (c) 200 fracture traces of 1.5 mm length; (d) 300 fracture traces of 1 mm length.

4.2.4 Fracture Orientation Frequency and Length

Fracture orientation is an important parameter in DFN analysis and it is particularly important to identify acute angles of fracture intersections. In the current algorithm, fracture intersection angles are measured counter-clockwise from the horizontal (with a possible range of 0 to 180 degrees). Fractures are grouped into a number of defined bins and then normalized with respect to the maximum frequency, effectively measuring fracture frequency according to the orientation. A simple DFN section is shown in Figure 4.10.a with the associated fracture orientation frequency in Figure 4.10.b.

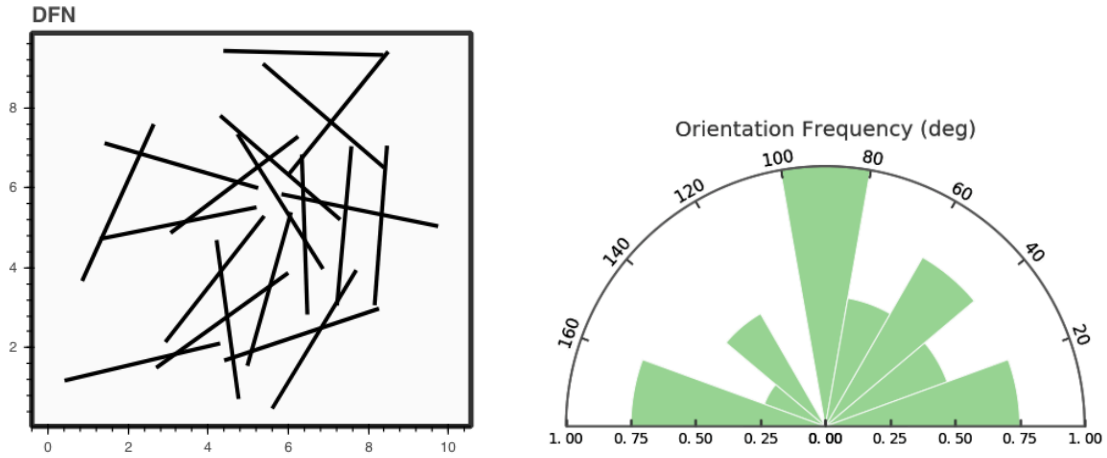

(a) (b)

Figure 4.10. (a) DFN and (b) associated fracture orientation plot with respect to the fracture count.

The analysis can also include fracture length in order to identify whether acute intersections are formed by random fractures, or whether they are formed by, for example, shorter fractures that could be removed from the DFN model without altering the overall rock mass response under loading. A simple DFN profile is shown in Figure 4.11.a with the associated orientation-fracture length (Figure 4.11.b) and orientation-frequency analysis (Figure 4.11.c). The orientation-fracture length analysis clearly shows that most fractures are in the bin (120°-140°), where the longest

fracture is dominant in the orientation map. However, the orientation frequency (Figure 4.11.c) shows that most of the fractures are in the bin (40°-60°) which is associated with the four short fractures in the sample DFN configuration. This is due to the single long fracture being oriented in the opposite direction to that of the majority of the shorter fractures.

Considering that the difference in fracture orientation map interpretation is related to both the number of fractures and the length of the fractures, the DFN Analysis included separate algorithms to show the various fracture orientation maps.

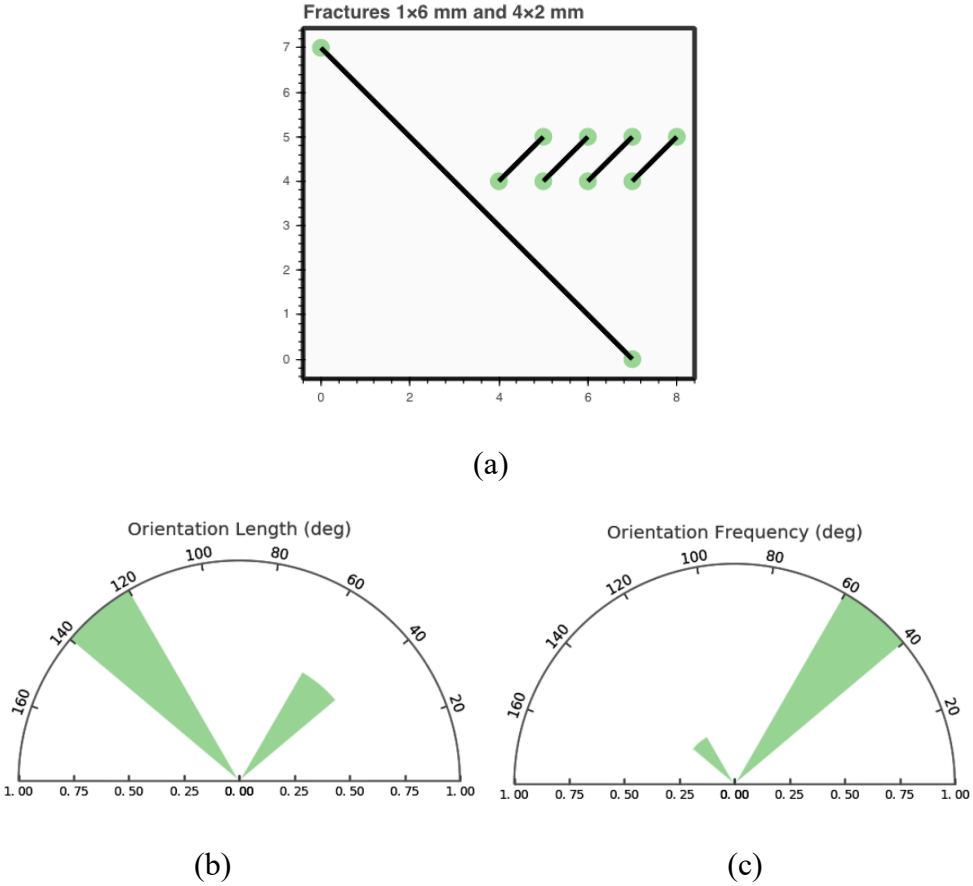

(a)

(b)

(c)

Figure 4.11. (a) DFN with long fracture trace (left side of the profile) and four short fracture traces (right side of the profile). (b) Fracture orientation with respect to the fracture length and (c) fracture orientation with respect to the number of fractures.

4.3 DFN Cleaning

In this section, we introduce DFN cleaning techniques, and collectively call them DFN Cleaning. The primary goal is to make the process of preparing 2D trace maps for geomechanical analysis more objective. The algorithms are intended for 2D applications, but the author believe it could also be expanded to 3D applications. The algorithms introduced as part of the DFN Cleaning can be applied separately or chained together in any order.

The algorithm uses the DFN Analysis to initially compute, for a given 2D DFN trace-map, the detailed DFN properties. Subsequently, several cleaning methods can be selected to make the 2D DFN trace-map ready for meshing and to guarantee a good quality mesh is achieved without altering the underlying properties of the simulated rock mass. At the end of each cleaning step the DFN Cleaning algorithm re-computes the DFN properties and calculates the DFN quality in each property compared to the original DFN trace-map. The various cleaning methods introduced as part of the DFN Cleaning are listed in Table 4.1 and shown in Appendix II.

Table 4.1. DFN Cleaning includes the following methods – the input is fracture traces – the output results are also fracture traces.

Method	Parameters
Critical Discontinuity Excluder	Angle and Length
Trace Length Remover	Not applicable
Line Splitter	Maximum length
Short Line Remover	Line Length
Point Collapse	Neighbour radius
Angle Adjuster	Angle increment and maximum rotation
Fracture Separator	Distance variation

The DFN Cleaning approach for adjusting the fracture angles and fracture separation utilizes Monte Carlo simulation. The DFN Quality method is used at the end of each Monte Carlo iteration, to compare results of cleaning. Monte Carlo simulations are ideal instruments for searching for an optimal fracture angle and separation distance, with tunable accuracy versus runtime. The proposed methods can have further implications in finding the best path for rock bridge connections.

4.3.1 Critical Discontinuity Excluder

A critical discontinuity can be defined as a plane along which a rock is easily separated or is naturally divided into layers parallel to a mineralogically defined structural weakness within the rock. The length of these layers can be quantified by observing the discontinuity trace lengths on the surface exposures (American Geological Institute, 1962) and defined herein as bedding length. Critical discontinuities may include highly persistent features such as bedding planes, faults, and shear surfaces.

A Critical Discontinuity Excluder algorithm is introduced to exclude critical discontinuities from the cleaning process. The algorithm considers each fracture trace and applies a specific method for sedimentary rocks or highly persistent structures. During the cleaning process, (e.g. line splitter, point remover, angle adjuster, and line separator methods) bedding features and other persistent discontinuities need not be artificially truncated; to facilitate this, a pre-cleaning step using the Critical Discontinuity Exclusion algorithm is added at the beginning of the cleaning process, with discontinuity length and orientation as input parameters. The algorithm considers all fractures in the DFN and then extracts the fractures with specified length and orientation, which are stored separately. The cleaning process can then begin without affecting the critical discontinuities. The

last step of the cleaning process is to add the critical discontinuities back to the cleaned DFN model.

4.3.2 Duplicate-Point Remover and Line Splitter

When exporting 2D fracture traces generated from a 3D DFN model, there may be cases in which duplicate points (with the same coordinates but different identification numbers) are shared among connecting segments. The occurrence of these duplicate points may cause errors in the mesh generators, or more simply hinder the visualization process as it is not possible to distinguish two identification numbers located on top of one another. The introduced algorithm searches for start and end points of all the traces and, if a given trace is a composed of multiple segments, the relevant segments are merged into a single trace (Table 4.2 and Figure 4.12). This cleaning step is important since DFN properties are measured taking into consideration fracture length, intersection and counting points that are shared between lines, therefore the existence of composite traces would artificially increase the intersection density.

Table 4.2. Example of a line comprising several adjacent segments.

Index	x1	y1	z1	x2	y2	z2	Segment ID	Trace ID
0	-4.09	-5	-3.5	-4.06	-5	-3.47	1	1
1	-4.06	-5	-3.47	-3.8	-5	-3.29	2	1
2	-6.22	-5	-3.5	-6.2	-5	-3.46	1	2
3	-6.21	-5	-3.46	-5.8	-5	-2.72	2	2
4	-5.82	-5	-2.73	-4.87	-5	-0.83	3	2

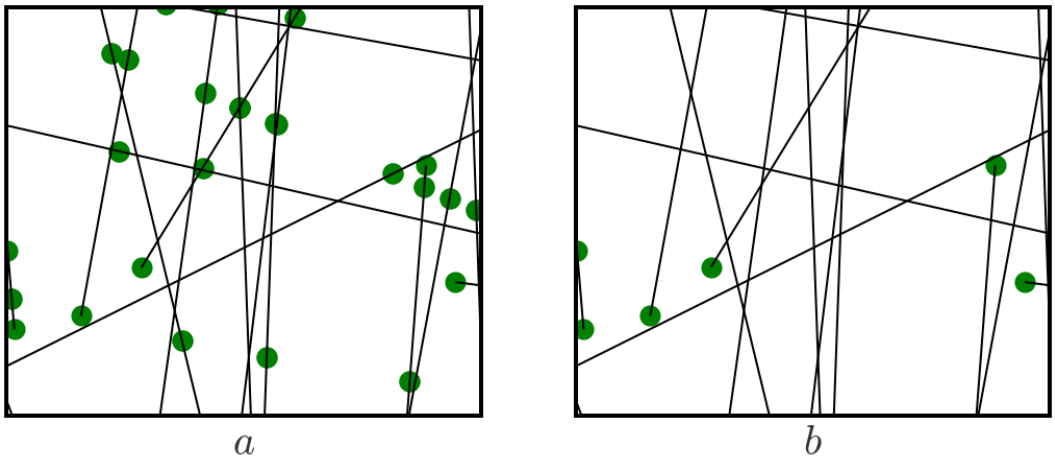

Figure 4.12. The application of the trace length algorithm (a) without use of the applied trace length algorithm (b) with use of applied trace length algorithm.

Conversely, there are cases in which it becomes necessary to create points to clearly define fracture intersections between lines, as shown in Figure 4.13, otherwise these intersections would not be counted in the fracture intersection density plots.

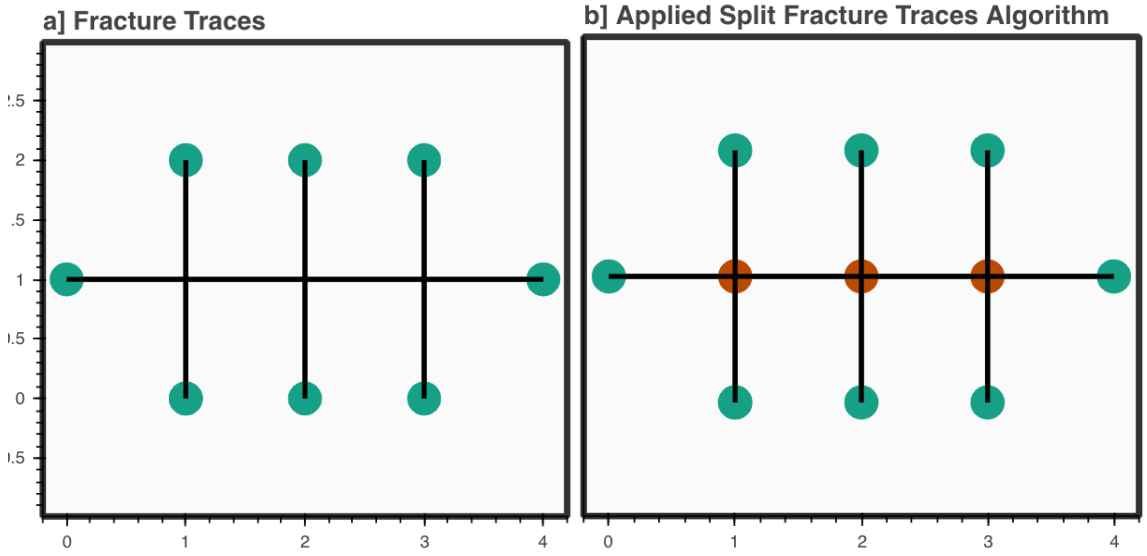

Figure 4.13. (a) Fracture traces and (b) Split fracture traces.

Distorted mesh elements may result when meshing fracture traces that are smaller than the assumed minimum mesh size. To avoid this problem, a simple algorithm has been developed to remove all traces that are below a certain defined length.

Figure 4.14.a shows the original DFN configuration comprising four distinct fractures which are compared against defined length. Red lines in Figure 4.14.b denote the selected traces smaller than a specified length that need to be removed. Figure 4.14.c shows the cleaned DFN after removing the selected lines.

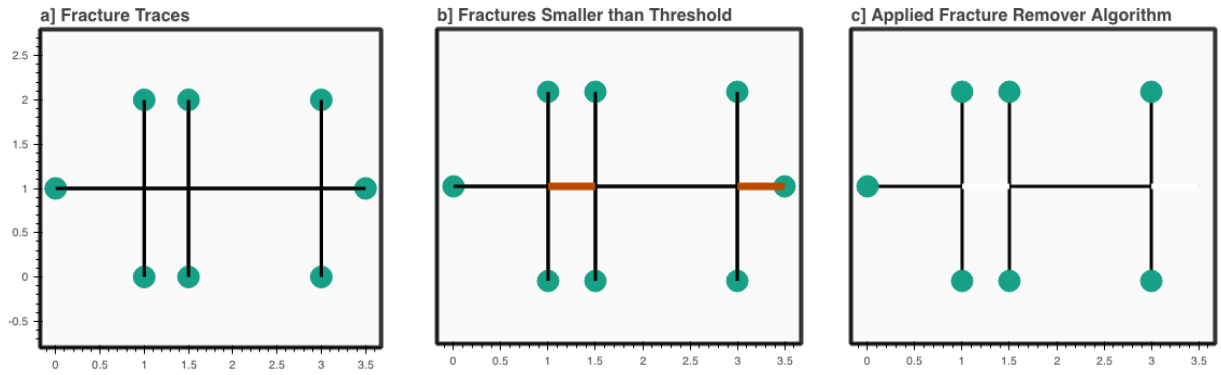

Figure 4.14. (a) Original DFN configuration comprising four distinct fractures. (b) Sub-division of fractures increases the number of points in all the trace intersections; red denotes the traces not meeting the specified criterion for minimum length and (c) Cleaned-DFN after removal of the short traces denoted in red.

There may be some cases in which relatively short traces are removed that belong to an otherwise long composite trace; clearly this would be incorrect when considering geological structures such as bedding planes or very persistent joints. Under these circumstances the traces that cross the more persistent features should be moved apart using the Critical Discontinuity/Bedding Excluder algorithm.

Very persistent discontinuities are initially excluded from the cleaning process to avoid them being split into shorter segments, which may subsequently be deleted by application of the short trace removal method. The traces should be excluded from the cleaning process, and then reinserted afterwards within the simplified network. If critical areas are still present, the cleaning procedure is to be repeated until satisfactory results are obtained in terms of final mesh quality.

4.3.3 Point Collapse Algorithm

This method is used to merge points belonging to different traces that are close to each other (Figure 4.15). Because of the very small distance between these points, it would not be possible to use them as the nodes of a closed meshed element. To solve this problem, each point is assigned a neighbour zone, defined as a circle with an assumed radius. As a guideline, the radius should be set as large as the minimum mesh size. The algorithm goes through each fracture and checks whether the termination of another fracture is close to one of its two ends. If yes, it collapses the fracture end to the neighboring one, effectively make them intersect at one point; otherwise it does not modify the current fracture. This process has runtime complexity of $O(n)$.

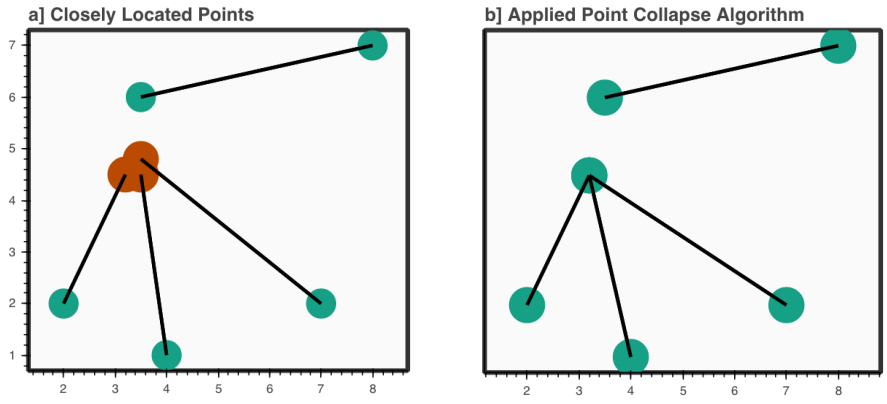

Figure 4.15. Example DFN configuration with three fracture traces and three distinct closely located points, shown in red (b) the same DFN with the applied point-collapse algorithm and circle radius set at 0.5 mm.

4.3.4 Fracture Trace Intersection Angle Adjuster

The ideal mesh element would be a triangle with equal angles, but there are cases in which traces intersect each other forming highly acute angles (e.g., Figure 4.16.a). To solve this problem, a method is introduced in DFN Cleaning that scans all traces and calculates all intersection angles. The algorithm's input is a minimum angle threshold and the algorithm rotates one of the traces until the intersection angle is larger than the assumed threshold (Figure 4.16.b).

Whereas locally increasing the angle between two fractures would result in a better mesh quality, globally, adjusting the angle between two fractures could result in an acute angle with a third fracture, resulting in a reduction in overall mesh quality. Therefore, the algorithm is designed to limit the rotation to a maximum angle to avoid the resulting global trace-map being significantly different to the original. To do so, the algorithm takes the number of Monte Carlo iterations as input, in which the algorithm attempts to increase the intersection angles, while at the same time measuring the global DFN quality. The more iterations specified, the cleaner the DFN results obtained, at the expense of increased processing time. In each iteration, the angles are adjusted locally, and the DFN quality then checked. The objective is to find the optimum balance between angle-increase and resulting DFN quality and return the cleanest DFN configuration it finds.

Note that a DFN quality measurement is introduced in this chapter as a method which considers the size of all intersection angles and the separation distance between all pairs of fractures. The sequence of steps required to solve Angle Adjuster is shown in Appendix II as Algorithm 9.

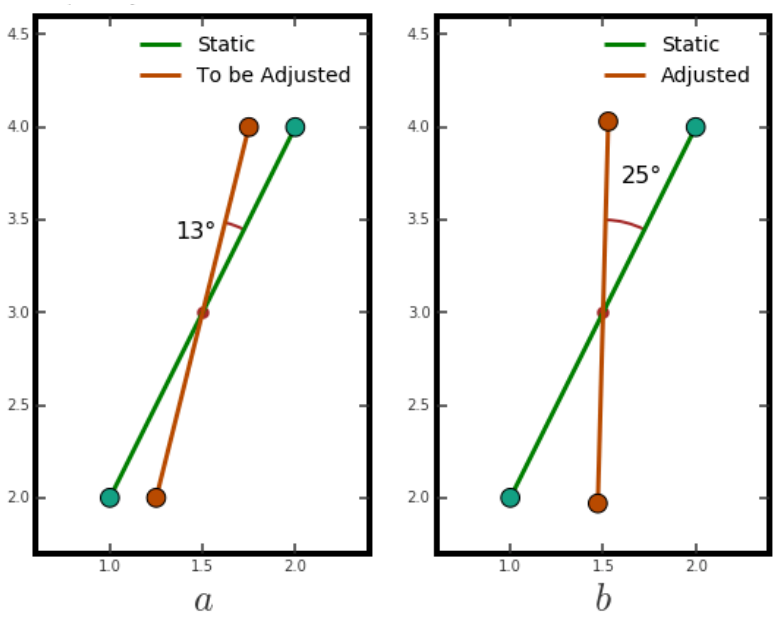

Figure 4.16. (a) Example of two fracture traces close to each other with an angle between them of 13° resulting in locally badly-shaped elements – Mesh created using unstructured-advancing front algorithm. (b) The Orientation Adjuster algorithm changes the angle to 25°.

4.3.5 Fracture Separator

There may be cases in which two traces are located very close to each other at a distance that is less than the assumed minimum mesh size, Figure 4.17. While it may be tempting to simply delete one of the traces, the deletion process would cause a reduction in the areal fracture intensity of the model and potentially change the overall characteristics of the trace map. Fracture separator is an algorithm that calculates the shortest distance between two traces; if the shortest distance is less than the minimum mesh size then the process of moving traces apart is initiated, Figure 4.18.

The shortest distance between the two traces can be computed by either measuring the shortest distance between the end points of each trace, or by computing the shortest distance between the end points of one trace and the other trace. Because the two traces would not necessarily have the

same horizontal or vertical coordinates, the second method is preferred. Once the distance is known, a trace would be moved, if necessary, to a target location such that the new distance is larger than the minimum mesh size.

Because trace maps can contain a large number of traces, it may be necessary to run multiple iterations of the process to guarantee that they all satisfy the minimum distance threshold. To avoid changing the overall DFN trace map by having traces being moved too far away from their initial location, a restriction is applied such that a trace can only be moved once. A Monte Carlo process is used such that the order in which the traces may be moved apart is randomized and the same trace is never used as the initial reference for calculating distances. The optimal Monte Carlo iteration is chosen based on the resulting mesh quality.

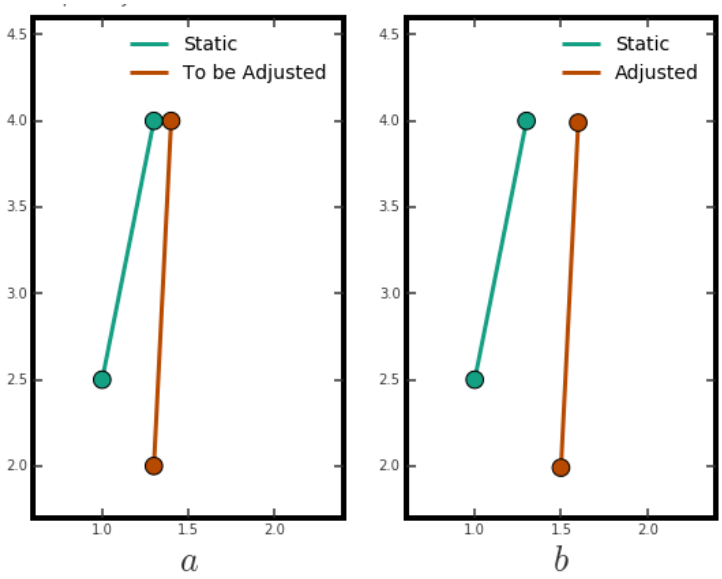

Figure 4.17. (a) Example of two fracture traces close to each other which results in locally badly-shaped elements, original distance between lines is 0.1 mm and (b) applying the separation algorithm, the distance is increased to 0.2 mm.

The algorithm begins by first measuring the shortest distance between two lines to determine whether any two lines need to be separated from each other - if they are below a specified threshold of closeness. The shortest distance between a line and a point is well understood mathematically and is illustrated in Figure 4.18.b. If the length of this line is less than the specified threshold, the lines are moved apart from each other. In this example, the lower line is moved away from the top line by first extending the dotted line to the threshold length, as shown in Figure 4.18.c. We then label two points: the anchor point, shown in yellow, and the target point, shown in green, as illustrated in Figure 4.18.d. We then translate the line, anchored in yellow, across the purple line, until it reaches the target green point. The resulting trace is shown in green in Figure 4.18.e. The result is that the two traces are exactly the specified threshold-distance apart from each other as shown in Figure 4.18.f.

Locally, the algorithm improves the mesh quality, because a moved trace is in a better position with respect to the trace it was moved away from. Globally, however, this trace might not meet the distance requirement with multiple other traces in the new DFN. Given that a trace can only be moved once, this is not a deterministic approach, since the order of the traces we select from the original DFN plays an important role in the new derived DFN. Therefore, in this section the use of Monte Carlo simulation is proposed as a DFN optimization technique. The Monte Carlo simulation is applied by first randomizing the order of the original traces, then applying the line separation method as described above. After moving all traces to the new DFN, we measure the global mesh quality and store separately the DFN with the best mesh quality derived at the current simulation step. The algorithm that outlines the DFN fracture separator process is shown in Appendix II as Algorithm 10.

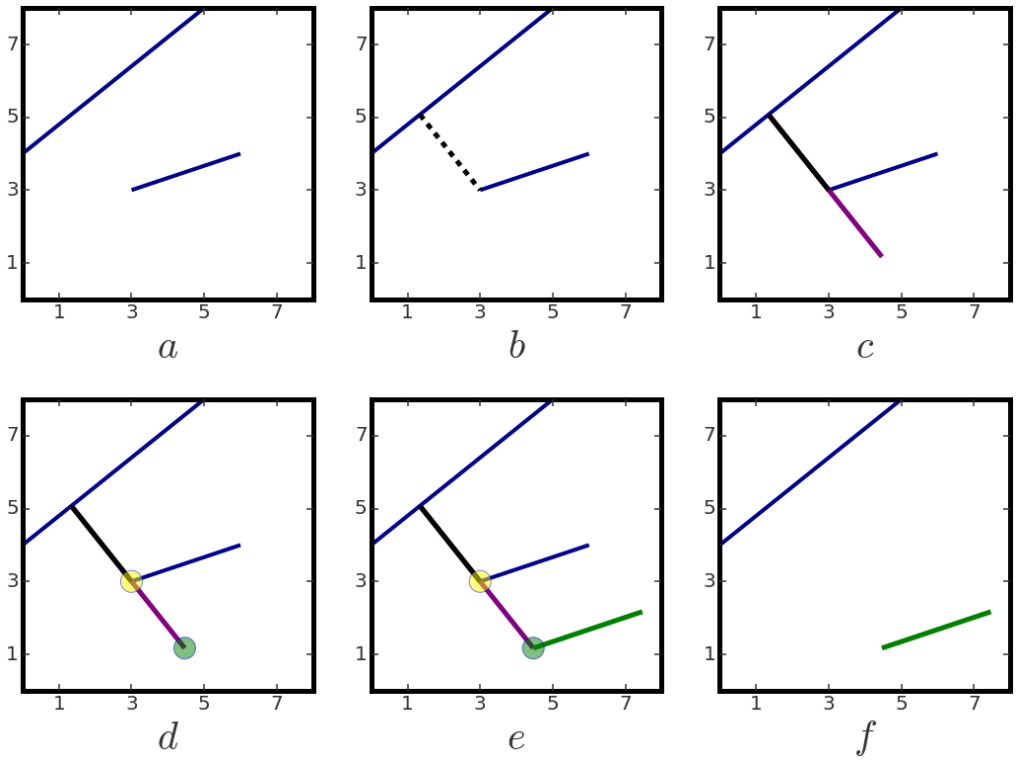

Figure 4.18. (a) Simple demonstration of two fractures within a specific separation distance, (b) Shortest distance between two fracture traces, (c) Extending the dotted line to the threshold length shown in purple, (d) Demonstration of anchor point, shown in yellow, and target point, shown in green. (e) Line translation to the new location across the purple line, (f) Two traces located at the threshold distance from each other.

It should be emphasized that cleaning DFN traces requires a trade-off between optimum mesh quality and the need to maintain original DFN characteristics (e.g. P_{10} and P_{21} and a degree of network intersection density) that closely match those of the original DFN trace map. The algorithm introduced in this section is tunable in terms of the aggressiveness of the DFN cleaning. It takes input values for both the minimum and maximum trace length (line removal and line splitter algorithms), neighbor radius (point collapse algorithm), angle increment and maximum rotation (angle adjuster algorithm) and distance variation (fracture separator algorithm).

Accordingly, these parameters control the cleaning procedure and the resulting fracture network characteristics.

4.4 DFN Quality Criteria for Meshing

4.4.1 Development of a Meshability Index for DFN Trace Maps

Mesh quality is a critical parameter that must be considered in a Finite Element (FE) analysis. Given the geometrical complexity of DFN configurations resulting from numerous fractures intersecting each other, a compromise must be established between mesh quality and the minimum element size. The smaller the element size, the easier it is to achieve a higher mesh quality but the larger the required computation model run time.

In the previous section, the DFN cleaning required an iterative process and a target to assess when a satisfactory result has been achieved. The target can be defined in terms of a specified mesh quality value. This section presents various mesh quality measurement methods that are independent of mesh generation software. A "meshability index" is introduced that contains three components: i) Critical Area Quality; ii) Separation Quality; and iii) Angle Quality. Each of these components is calculated independently, and their average defines the meshability index.

4.4.2 Critical Area

Fracture traces in a DFN trace map form enclosed regions of various shape and size. Depending on the mesh element size, the smaller regions might not be able to fit correctly shaped mesh elements that meet the minimum mesh element size requirements. From the perspective of the meshability index, these regions are uniquely defined herein as of "Critical Area".

Initially, a minimum area threshold value (Critical Area) that is related to the minimum mesh size is used as an input. The algorithm searches for enclosed regions that do not meet the Critical Area requirement, and furthermore scores each region (independently of area). If the area is larger than the defined Critical Area, the enclosed region would be given a 100% score. If it is less than the Critical Area, the score is then calculated as the ratio of the enclosed area to the Critical Area (%). The average score is then calculated for all enclosed regions; the lower the average score the larger the number of enclosed regions that potentially would be difficult to mesh. Figure 4.19 shows an example for a 2D pillar (14 m wide, 7 m high), with an assumed Critical Area of 0.1 m^2. By purposely assigning equal weight to each enclosed region, the scoring method provides a better indirect measurement of mesh quality. For instance, a scenario where several enclosed regions fall slightly below the threshold Critical Area would get a better Meshability Index, compared to a DFN with a few very small enclosed regions, as the latter would require an adjustment of the Critical Area target for the Meshability Index to increase.

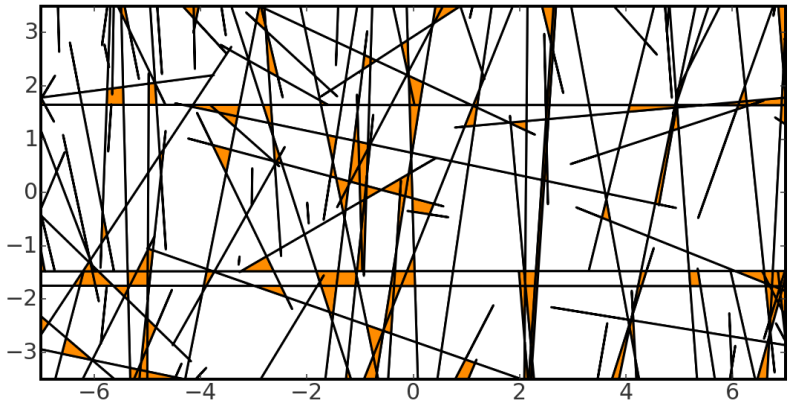

Figure 4.19. Critical areas are highlighted in orange for a critical area threshold of 0.1 m^2 and resulting mesh quality of 57%.

The critical area criterion is used as a quality indicator for the cleaning process. When visualized, it can also provide a visual guide to identify areas where further cleaning may be required.

4.4.2.1 Separation Quality

This method is used in conjunction with the fracture separator algorithm. The input is a minimum distance between fractures (related to minimum mesh size), and it has a scoring system similar to that described previously used to define the Meshability Index component. If the distance is larger than the minimum distance, it gets a full score; if it is less, then the score is calculated by dividing the calculated distance by the minimum distance. The scores of all distances are then averaged, resulting in a total score between 0% and 100%.

4.4.2.2 Angle Quality

Intersecting fracture traces that result in very small angles may produce a poor-quality mesh. During the cleaning process of the DFN traces, small angles can be corrected directly, but some traces may be moved to fulfil the Fracture Separator criterion, and in the process very small intersecting angles may be generated. Therefore, it is necessary to define a further constraint bounding the Fracture Separator criterion. In a similar fashion to the angle adjuster algorithm, all angles formed by intersecting traces are searched with respect to a threshold and are assigned a score. If the angle is larger than the target value, its score is 100%, otherwise its score is equivalent to the angle-to-target value ratio (%). The average of all the calculated scores provides the third component of the proposed meshability index.

4.5 Development of a Mesh Quality for DFN Trace Maps

As an alternative to the formulation of a meshability index, it is possible to define a mesh quality criterion, which for each element is measured as the ratio of the maximum edge length to the minimum edge length. The ideal value would be one where all edges are of the same size. As the ratio increases, the larger difference between the edge lengths would result in a lower mesh quality.

Figure 4.20 shows an example in which elements with the lower mesh quality are coloured using warmer (darker) colours.

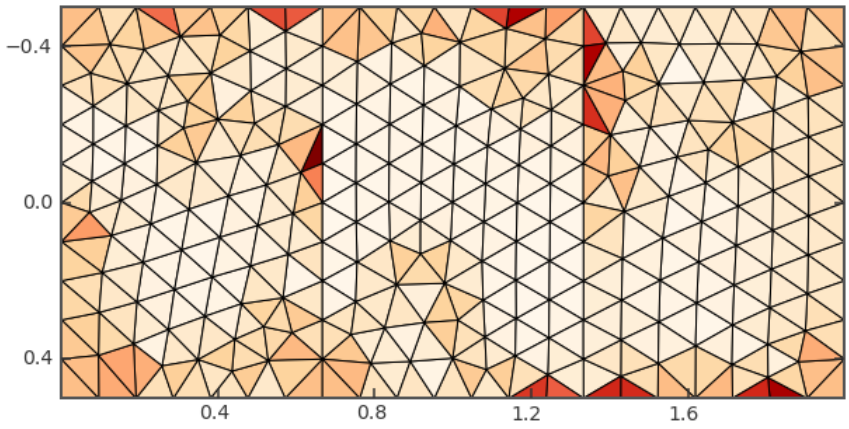

Figure 4.20. Example of mesh quality regions. The warmer (darker) colours indicate elements with a lower mesh quality; mm scale.

Visualizing the output of the mesh quality algorithm enables us to quickly see the location of potential problematic areas within a model mesh and is useful both during and after the cleaning of the DFN trace map to ensure a good mesh quality is achieved. A target ratio (average of the quality which is defined as the total cell qualities divided by the number of cells) can be set, (a value in the range of 0.1 to 1 is recommended based on the authors experience with preparing FE models with embedded DFN traces).

4.6 Application of New DFN Algorithms for the Characterization of Pillar Strength

Mine pillars provide an excellent example of the importance of accurately determining rock mass strength. To accurately simulate the mechanical behaviour of mine pillars by numerical modelling, it is necessary to incorporate a more realistic representation of the discrete fracture systems (Elmo and Stead, 2010). At the set-up stage the original DFN trace maps need to be prepared for the

geomechanical analysis to ensure that the process of incorporating the DFN traces within the geomechanical model does not influence the overall mechanical behaviour of the simulated pillars.

4.6.1 Model Set-up, DFN Analysis and Cleaning Process

Geological and geotechnical data from Pine et al., 2006, Elmo., 2006 and Elmo and Stead., 2010 were used to generate a DFN model for Middleton mine (Derbyshire, UK), which is a classic square room-and-pillar mining operation. The current study considers a 2D cross section of a 3D DFN model representing mapped jointed pillars at Middleton mine. The section is 14 m wide and 7 m high. The proprietary code FracMan (Golder, 2018, Dershowitz et al., 1998); is used in the current chapter for DFN synthesis. The properties (P_{20}, P_{21}, I_{21}) of the original 2D trace map are 2.95 $1/m^2$, 4.04 m/m^2 and 578 trace intersections, respectively. The original DFN trace map was processed using the DFN analysis and the cleaning algorithms introduced in the previous sections, to prepare for geomechanical analysis. Additionally, two individuals, with different modelling experience (intermediate and senior experienced level) prepared the same trace maps manually. The properties of the resulting DFN trace maps are presented in Table 4.3.

Table 4.3. DFN properties of the initial DFN, the new automated DFN and DFN's produced by both intermediate and senior experience level users.

Title	Fracture Length (m)	Fracture Count	Unique Intersections Count I_{21}	P_{20} $1/m$	P_{21} m/m^2
Initial	396.2	289	578	2.9	4.04
Automated	392.8	113	361	1.1	4.01
Intermediate	383.5	102	316	1.0	3.91
Senior	385.1	235	329	2.4	3.93

Connectivity maps and fracture intersection locations are presented in Figure 4.21 and Figure 4.22. The most similar connectivity distributions belong to the trace maps cleaned using the proposed algorithms which indicate properties similar to the original DFN. Conversely, the trace map processed by the intermediate experience level user shows an increase in intersection density for the lower part of the pillar, which does not match the initial DFN. The intermediate experience user cleaned most of the high density-high intersection areas by moving traces to locations with lower fracture density. Some of the more problematic traces were also deleted, which resulted in a processed P_{21} of 3.7 m^{-1} in comparison to the original P_{21} of 4.0 m^{-1}. The senior experience level user was able to maintain an overall agreement between the original and processed DFN network intersection density; however, the manual processing can take considerable time. Manual cleaning processes are therefore subject to large, user dependent, bias. The proposed algorithms, however, shows the closest similarity to the original DFN intersection density map.

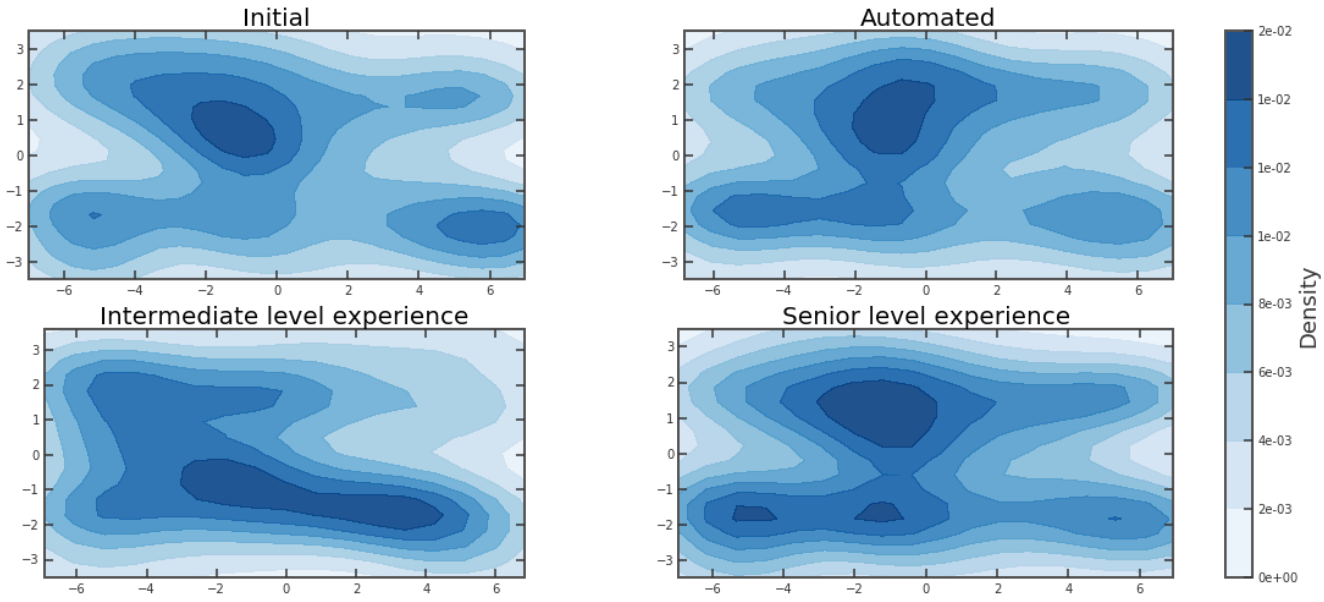

Figure 4.21. Intersection density plots of the initial DFN trace map compared to plots resulting from automated and manual cleaning procedures (intermediate and senior experienced level users). Unit of the colour bar is the kernel density estimation of the binned number of intersections in 2D.

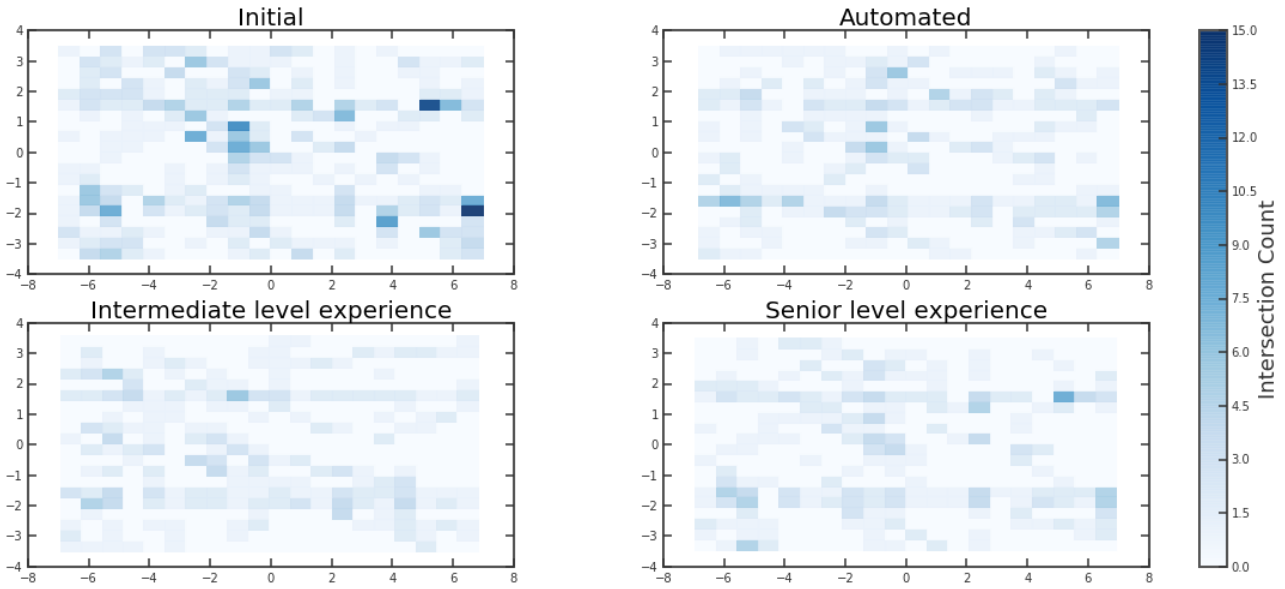

Figure 4.22. Number of fracture intersections of the initial DFN trace map compared to those resulting from automated and manual cleaning procedures (intermediate and senior experience level users). Unit of the colour bar is the number of intersections seen per cell.

To better compare the various cleaning methods, the density KDE histograms of all implemented methods are plotted with respect to the x-axis (Figure 4.23.a) and y-axis (Figure 4.23.b) of the pillar section, respectively. The left y-axis shows the KDE density, while the right y-axis shows the number of intersections in 15 bins.

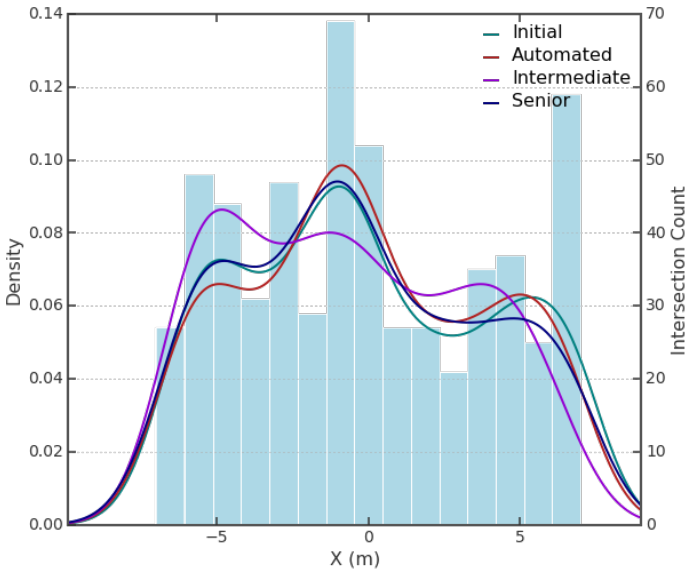

a

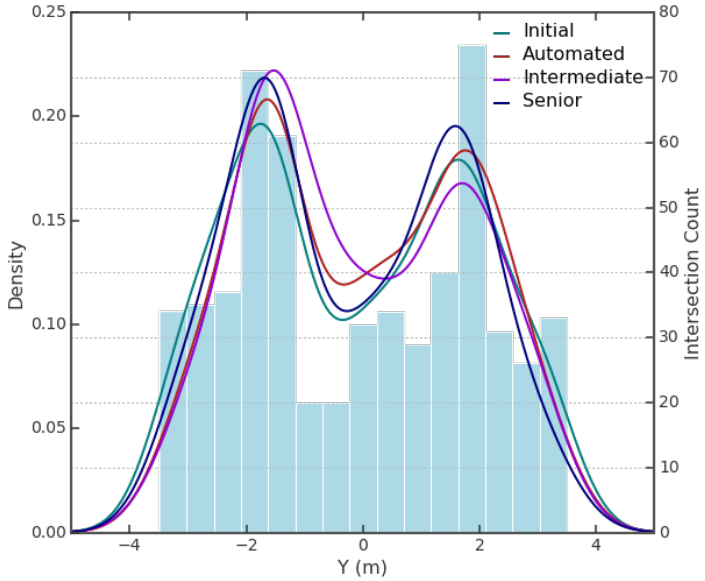

b

Figure 4.23. Intersection count histogram for initial DFN with KDE plots for initial, automated, intermediate and senior level users in (a) X axis and (b) Y axis.

The KDE curves for the automated, intermediate and senior experience level cleaning results are compared with respect to the initial KDE curve, by subtracting the density values in x and y

directions as explained in Appendix II using Algorithm 3. The values for the various cleaning methods are shown in Table 4.4 and show that the automated and senior experience level density values in the x axis have relatively low deviation from the initial KDE curve, compared to the intermediate level user results. The automated result has the least deviation from the initial state KDE in the y-axis.

Table 4.4. KDE comparison with respect to the initial KDE curve.

Title	X (m)	Y(m)
Automated	0.51	0.83
Intermediate	1.23	1.11
Senior	0.36	0.86

To further test for similarity between trace maps, the results of the Trace Orientation Frequency and Fracture Length analysis are shown in Figure 4.24 and Figure 4.25, respectively. In the original trace map the highest number of traces have an orientation of 80 to 100° with respect to the horizontal axis. All the processed trace maps show minor differences (e.g. some of the processed traces have an orientation between 100° to 120° with few in the range of 160° to 180°). In the processed trace maps some of the traces with orientation between 60° to 80° and 100° to 120° were moved from their original location (slightly left or right). Overall, the automated cleaning method yields the closest orientation similarity to the original DFN.

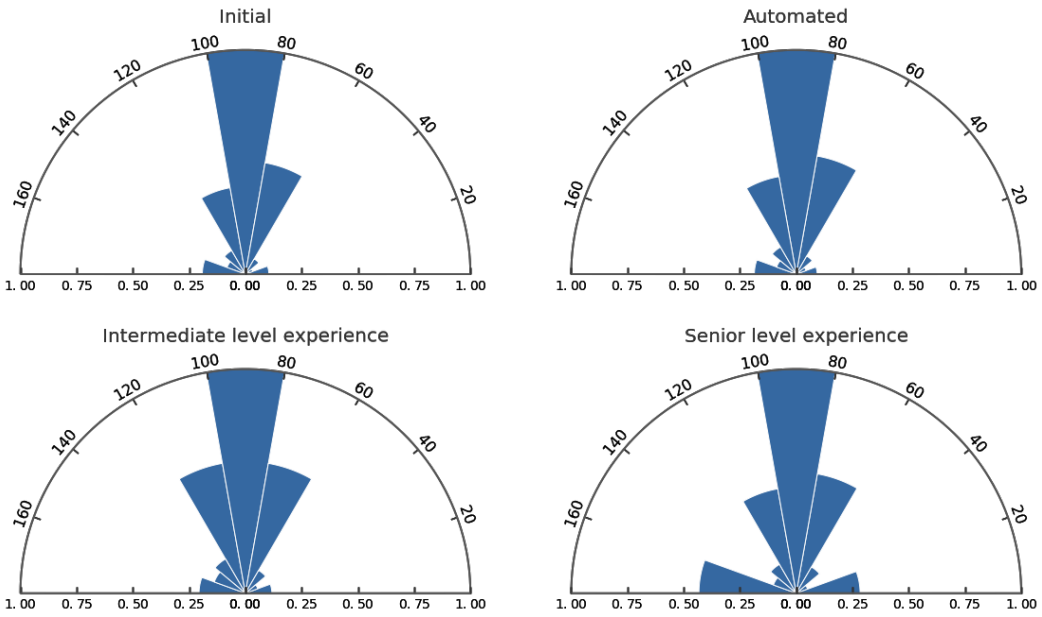

Figure 4.24. Trace orientation frequency plot of the initial trace map compared to those resulting from automated and manual cleaning (intermediate and senior experience level users). The x-axis is the normalized number of fractures.

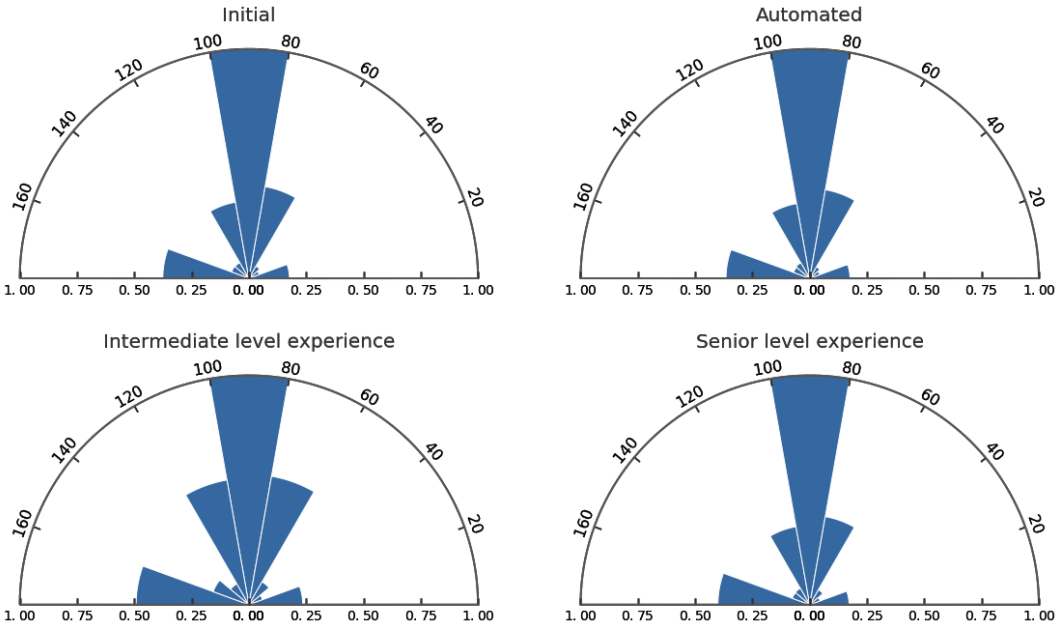

Figure 4.25. Trace orientation length plot of the initial trace map compared to those resulting from automated and manual cleaning (intermediate and senior experienced level users). The x-axis unit is the normalized length of fractures.

4.6.2 Comparison between Meshability Index and Mesh Quality

Using the Meshability Index and Mesh Quality methods, a comparison is made between various sections. The presence and location of smaller closed polygonal regions (Figure 4.26, orange colour) is also used to define similarity between the original trace map and those trace maps processed for geomechanical analysis.

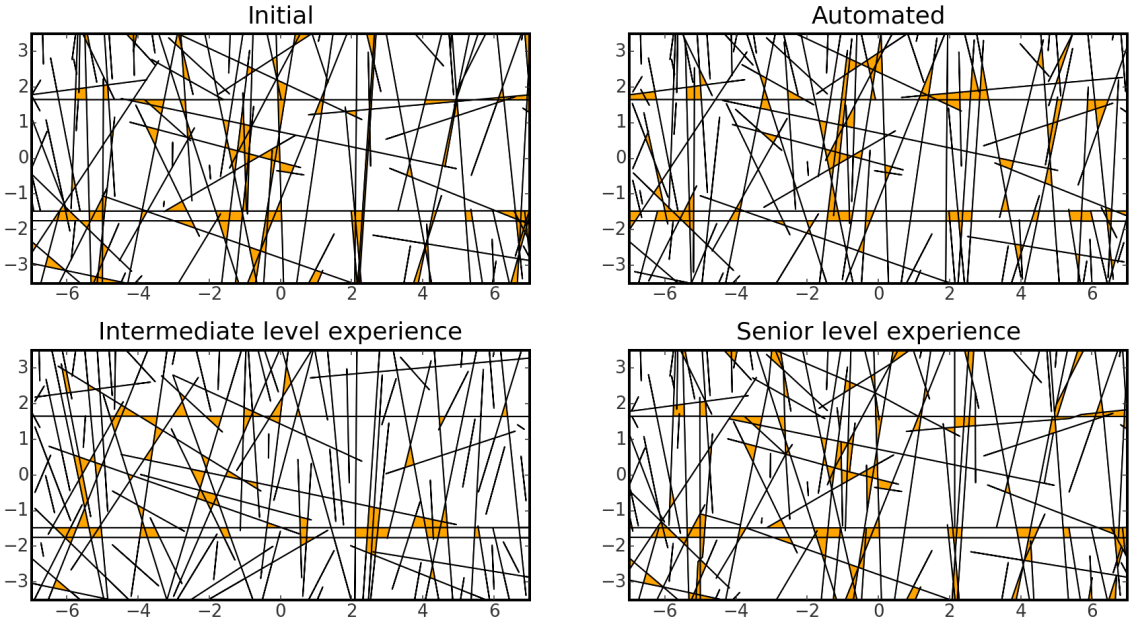

Figure 4.26. DFN Quality of the initial, automated, intermediate and senior experience level users. Dimension is meters.

The results of the Mesh Quality analysis are shown in Table 4.5 and Figure 4.27. The initial DFN trace map has the lowest Meshability Index, and the trace map could not be meshed using unstructured advancing front and Delaunay algorithms. Hence, no Mesh quality value is available. The values of meshability index and mesh quality are plotted with respect to various DFNs and shown in Figure 4.27. There is an overall increase in the Meshability index from initial DFN (0.57)

to automated, intermediate and senior experience level user DFNs with the corresponding values of 0.84, 0.87 and 0.75, respectively. There is a good agreement overall between the Meshability Index and the Mesh Quality, in which the increase in Meshability Index is proportional to an increase in Mesh Quality. This indicates that both methods can be used to constrain the cleaning of DFN traces.

Table 4.5. Meshability Index parameters and Mesh Quality are shown for the trace maps for the new, automated DFN and DFN's produced by both intermediate and senior experience level users.

Title	Critical Area Quality	Line Separation Quality	Orientation Quality	Meshability Index	Mesh Quality
Initial	0.58	0.73	0.40	0.57	Not Applicable
Automated	0.71	0.82	0.98	0.84	0.86
Intermediate	0.79	0.90	0.99	0.89	0.86
Senior	0.73	0.89	0.62	0.75	0.85

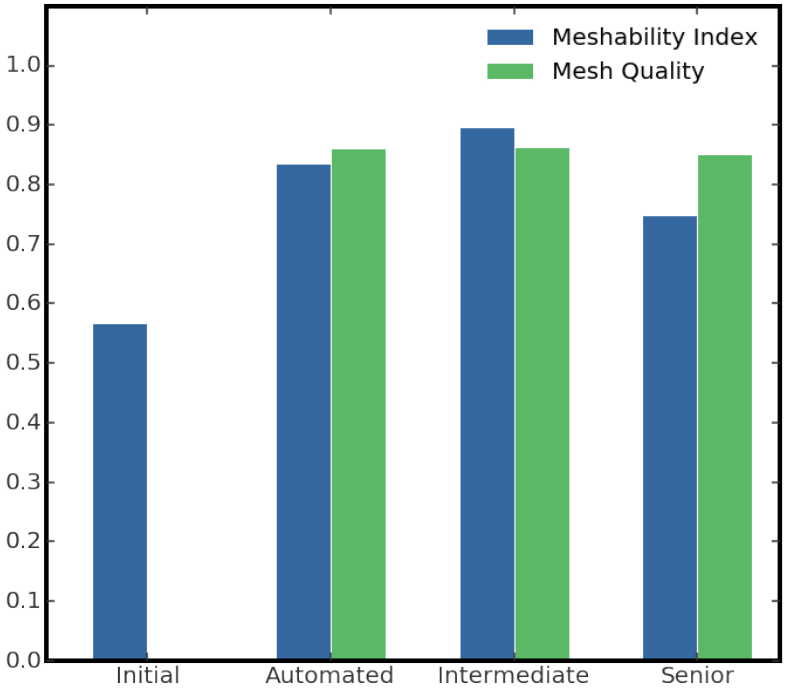

Figure 4.27. Meshability Index and Mesh Quality assessment for initial, automated, intermediate and senior experience level, respectively.

4.7 Geomechanical Simulation of Pillar Strength and Mechanical Behaviours

A hybrid FEM/DEM numerical approach that combines aspects of both finite elements and discrete elements with fracture mechanics principles was used for the geomechanical analysis using ELFEN (Rock field, 2017). The same material properties (intact rock and joints) and loading stages used in Elmo and Stead. (2010) are applied to the current FEM/DEM models; these parameter values were derived from a combination of laboratory measurements on the Middleton limestone and values for similar limestones in the literature.

In the design of room-and-pillar mines, the loading capacity of a pillar, i.e. its strength, is equally as important as the stability of the roof and walls (Nordlund and Radberg, 1995). As discussed by Elmo and Stead, (2010), the most generally accepted techniques for estimating pillar strength is

the use of empirical formulae based on survey data from actual mining conditions. However, empirical methods do not consider specific failure mechanisms. For a numerical analysis of pillar strength to be considered representative, it must be based on an objective modelling process, thus reducing the human uncertainty associated to level of experience of the user. Because a pillar would be considered to have failed when the average pillar stress is greater than the estimated pillar strength, any increased uncertainty in the estimated value of pillar strength would result in an increase in the risk associated with the design process.

4.7.1 Material Properties and Boundary Conditions

The material properties and boundary conditions are adopted from work by Elmo, 2006. The platens are placed on the top and bottom part of the pillar. They models are constrained in x-directions as shown in Figure 4.28. The pillar models in this chapter consist of a pre-fractured rock pillar, which was loaded as if it were subjected to uniaxial laboratory loading conditions. An initial state of stress was initiated with gravity loading and a displacement of 0.07 m (i.e. 2% of pillar height) was applied on top and bottom platens in the second stage.

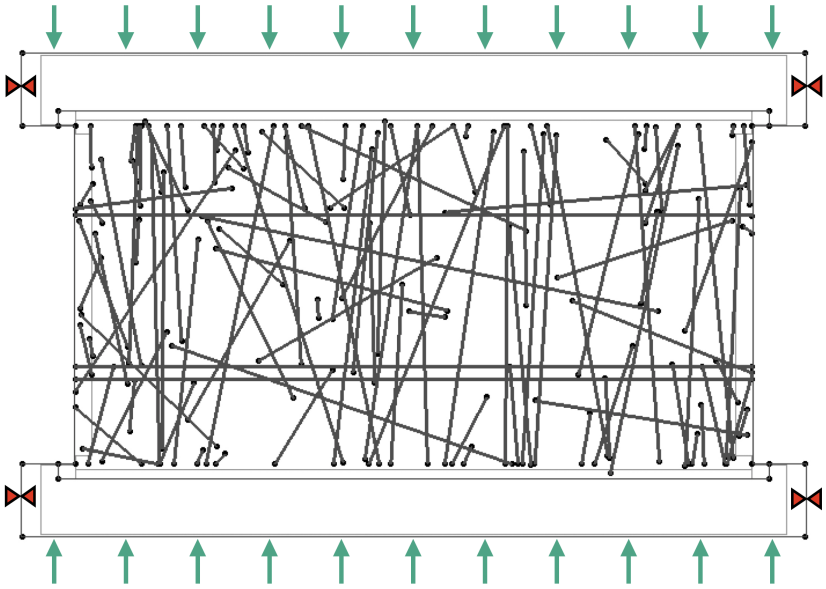

Figure 4.28. Boundary conditions of the pillar model.

The material properties are specified for both intact rock and integrated fracture networks as shown in Table 4.6.

Table 4.6. Material Properties

Rock Material Properties (Limestone)		**Unit**	**Value**
Intact Rock Material	Unified compressive strength, σ_{ci}	MPa	48
	Fracture energy, G_f	Jm^{-2}	19.47
	Tensile Strength, σ_t	MPa	3.84
	Young's Modulus, E	GPa	27.5
	Poisson's ratio, ν	-	0.23
	Density, ρ	kgm^{-3}	2600
	Internal Cohesion, c_i	MPa	9
	Internal Friction, ϕ_f	degrees	40
Platen material properties and discrete (contact) parameters		**Unit**	**Value**
Rock Fracture	Surface Cohesion, c_f	MPa	48
	Surface Friction, $\emptyset_f$	Jm^{-2}	19.47
	Normal Stiffness (Normal Penalty) P_n	MPa	3.84
	Shear Stiffness (Shear Penalty) P_t	GPa	27.5
Platen Properties	Young's Modulus of Platen	GPa	200
	Poisson's ratio of Platen	kgm^{-3}	0.3
	Density of Platen	MPa	7860
Rock-Platen Contacts	Rock/platen cohesion	MPa	0
	Rock/Platen friction	degrees	3
	Rock/platen normal stiffness (Normal Penalty P_n)	GPa/m	27
	Rock/platen shear stiffness (Shear Penalty P_t)	GPa/m	2.7

4.7.2 FEM/DEM-DFN Modelling Results

Selected results at peak stress are presented in Figure 4.29 with an indication of the associated cleaning method (Automated, Manual Intermediate Experience and Manual Senior Experience level). The results indicate that the dominant mode of failure (independent of the cleaning process for the embedded trace map) is progressive slabbing and spalling which eventually leads to an hour-glass shape.

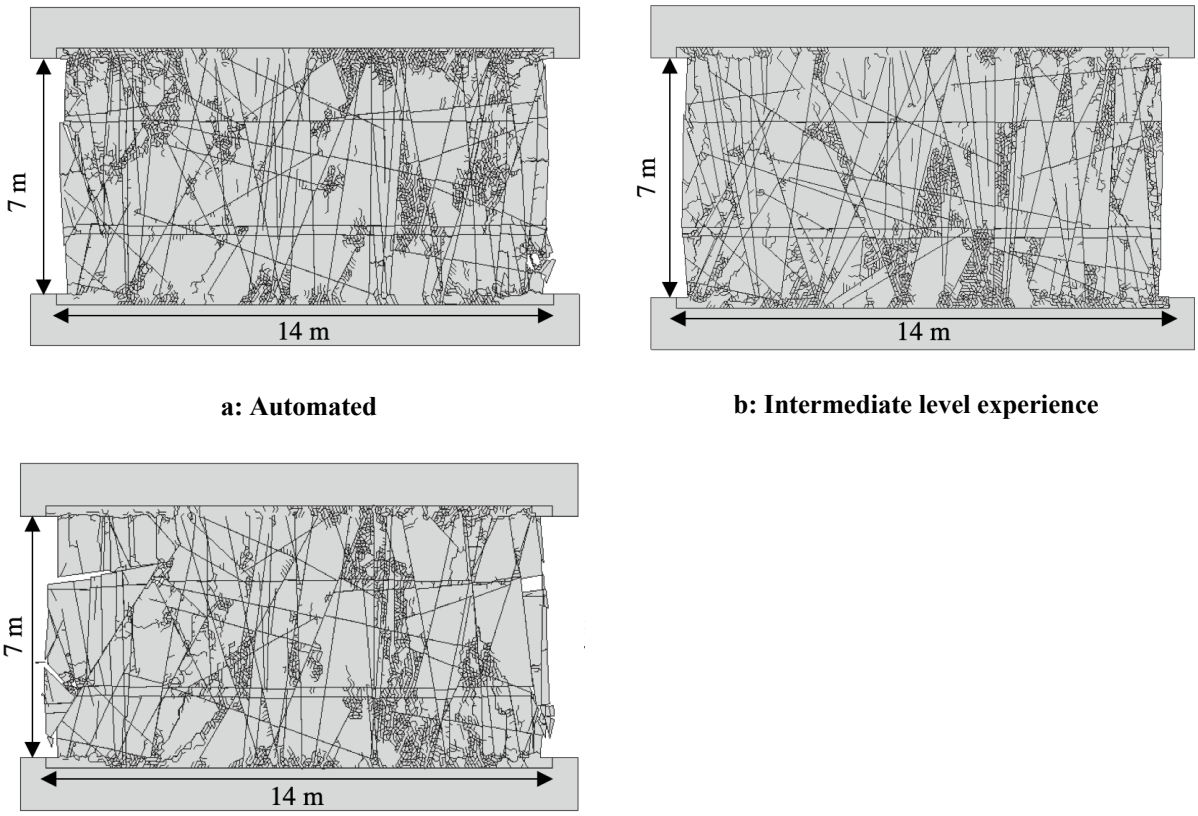

Figure 4.29. FEM-DEM-DFN analysis. Evolution of pillar fracturing at the peak stage, for (a) automated and (b) manual cleaning intermediate level experience and (c) manual cleaning senior level experience user.

The stress-strain plots for the different cleaning methods are shown in Figure 4.30.a. The stress values are then normalized by dividing the pillar axial stress by the uniaxial compressive strength of the limestone (48 MPa) and the results are shown in Figure 4.30.b. The proposed DFN cleaning process yielded the highest pillar strength and deformation modulus (16.7 MPa and 25 GPa secant modulus). The intermediate and senior experience user level models estimated a lower pillar strength (13.9 MPa and 12 MPa, respectively) and deformation modulus (16.6 GPa and 13.3 GPa, respectively). Table 4.7 shows a comparison between the strength and deformation modulus values using the different DFN cleaning methods. The percentage differences in the strength and

deformation moduli are shown for the two manual cleaning methods with respect to the proposed automated cleaning model. The results of Figure 4.30 show how important the cleaning process could be in terms of potentially altering the mechanical behaviour of the rock mass. Similarly, the results show that engineering judgment alone (experience user level versus intermediate user level) may not be a valid justification to either accept or discard modelling results. Whereas human bias and uncertainty may be transferred into the algorithm design, once formulated, the algorithm would analyze different DFN traces in a more objective manner.

Table 4.7. Pillar strength and deformation moduli for the Elfen simulation results.

Cleaning Methods	Pillar Strength ($\boldsymbol{MPa}$)	Deformation Modulus ($\boldsymbol{GPa}$)	% Strength difference of manual vs automated method	% Modulus difference of manual vs automated method
Automated	18.7	25	-	-
Intermediate	13.9	16.6	-16.7	-33.6
Senior	12.0	13.3	-28.14	-46.8

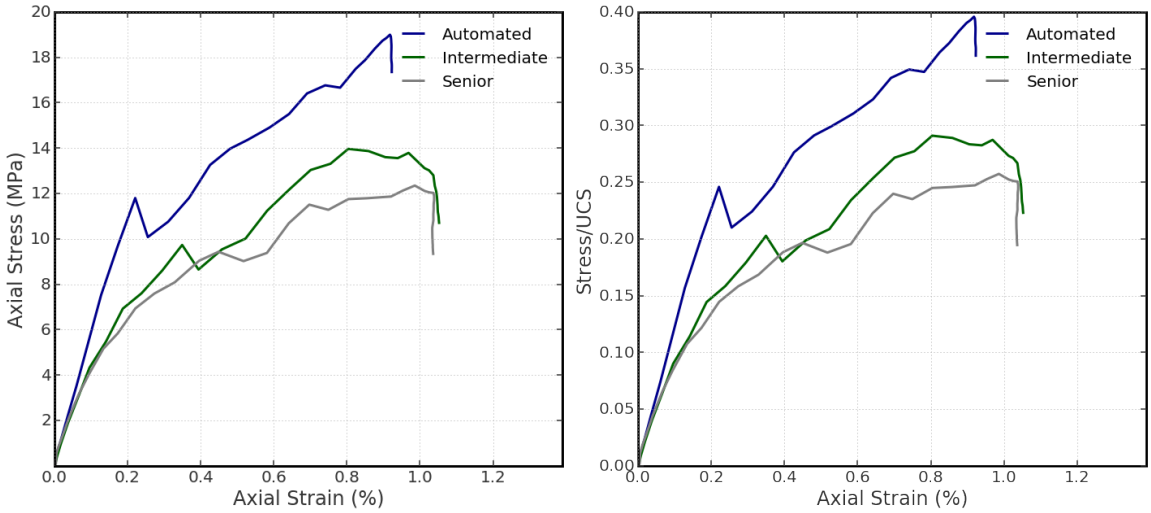

(a) Axial Stress-Strain (b) Normalized Axial Stress-Strain

Figure 4.30. (a) FEM-DEM -DFN analysis. Pillar axial stress vs. axial strain for automated and manual cleaning (intermediate and senior experience level users). (b) Pillar axial stress normalized with respect to the UCS vs. axial strain.

The empirical comparisons were made using a similar approach as given in Elmo, 2006 for the Middleton mine. As discussed in Elmo, 2006, the strength relationship for square pillars is shown in Equation 4.

$$\boldsymbol{\sigma_p = K_{mass} W^{0.5} H^{-0.7}} \qquad \textbf{[Eq. 4]}$$

σ_p is the ultimate pillar strength that is calculated for an effective width of 28 m, height of 7 m and a K_{mass} value of 9.03 MPa where K_{mass} is the strength of a unit cube of the pillar rock material. GSI of 70, σ_{ci} of 48 MPa and m_i of 10 is derived using the GSI-RocData approach (Rocscience Inc. 2017). This results in a pillar strength value of 18.3 MPa which agrees closely with FDEM

models incorporating the proposed cleaning algorithms which gave a simulated maximum pillar strength of 18.7 MPa.

The pillar vertical stress contour plots for the various DFN cleaning methods are shown in Figure 4.31. The pillar core appears to be stronger in the automated DFN cleaning model, while the presence of a larger destressed outer layer was observed in both intermediate and senior level experience models.

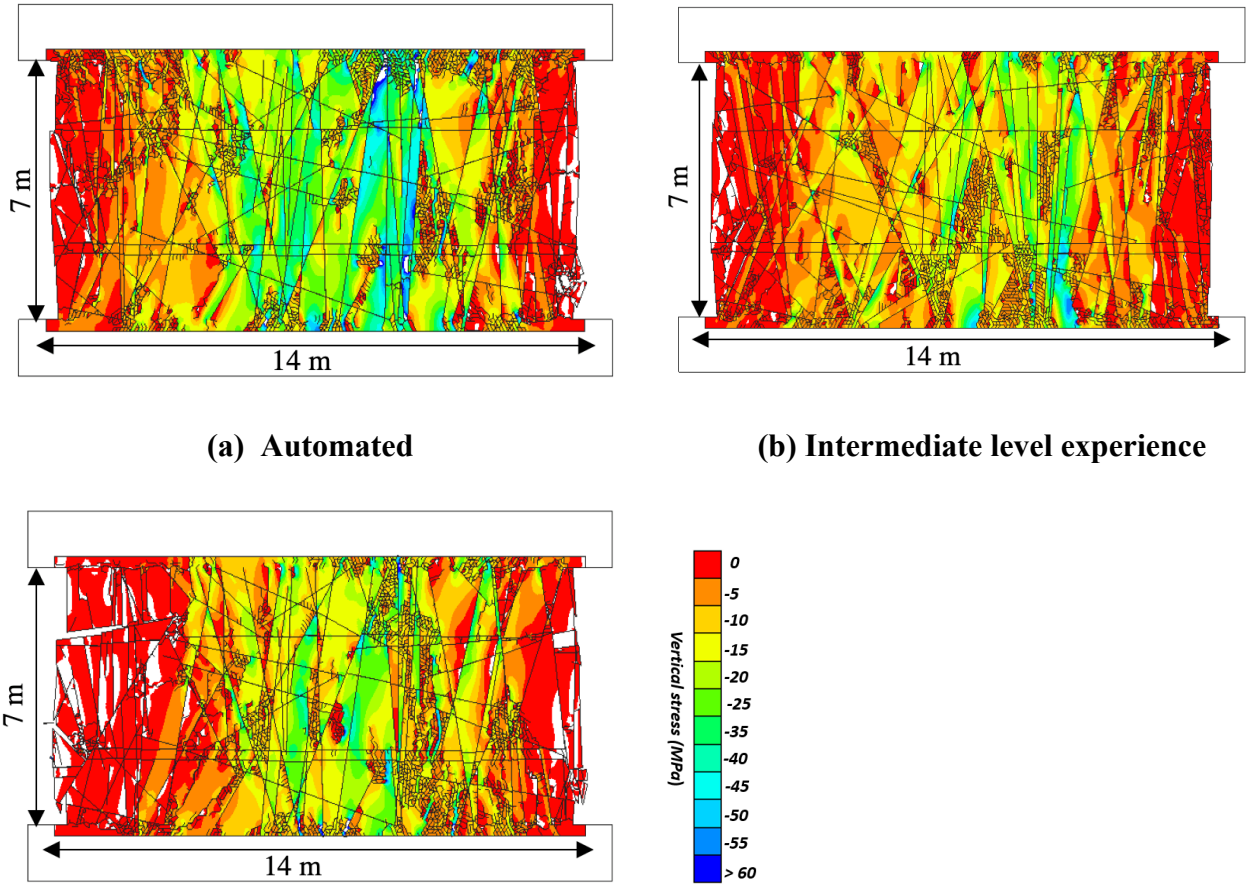

Figure 4.31. FEM-DEM-DFN analysis. Evolution of pillar stress at the peak stage, for (a) automated DFN cleaning (b) manual cleaning-intermediate level experience and (c) manual cleaning- senior level experience. Note negative convention for compressive fields (MPa).

The horizontal displacement contour plots for all models are shown in Figure 4.32. Larger horizontal deformations were observed in the senior level experience cleaned DFN model, which shows a relatively deeper depth of failure. Considering the orientation results from the DFN Analysis, in which the automated DFN cleaning model has the closest orientation similarity with the initial DFN (Figure 4.24 and Figure 4.25), it is suggested that the automated model maintains a more realistic block size and shape in comparison to the manual cleaning model results.

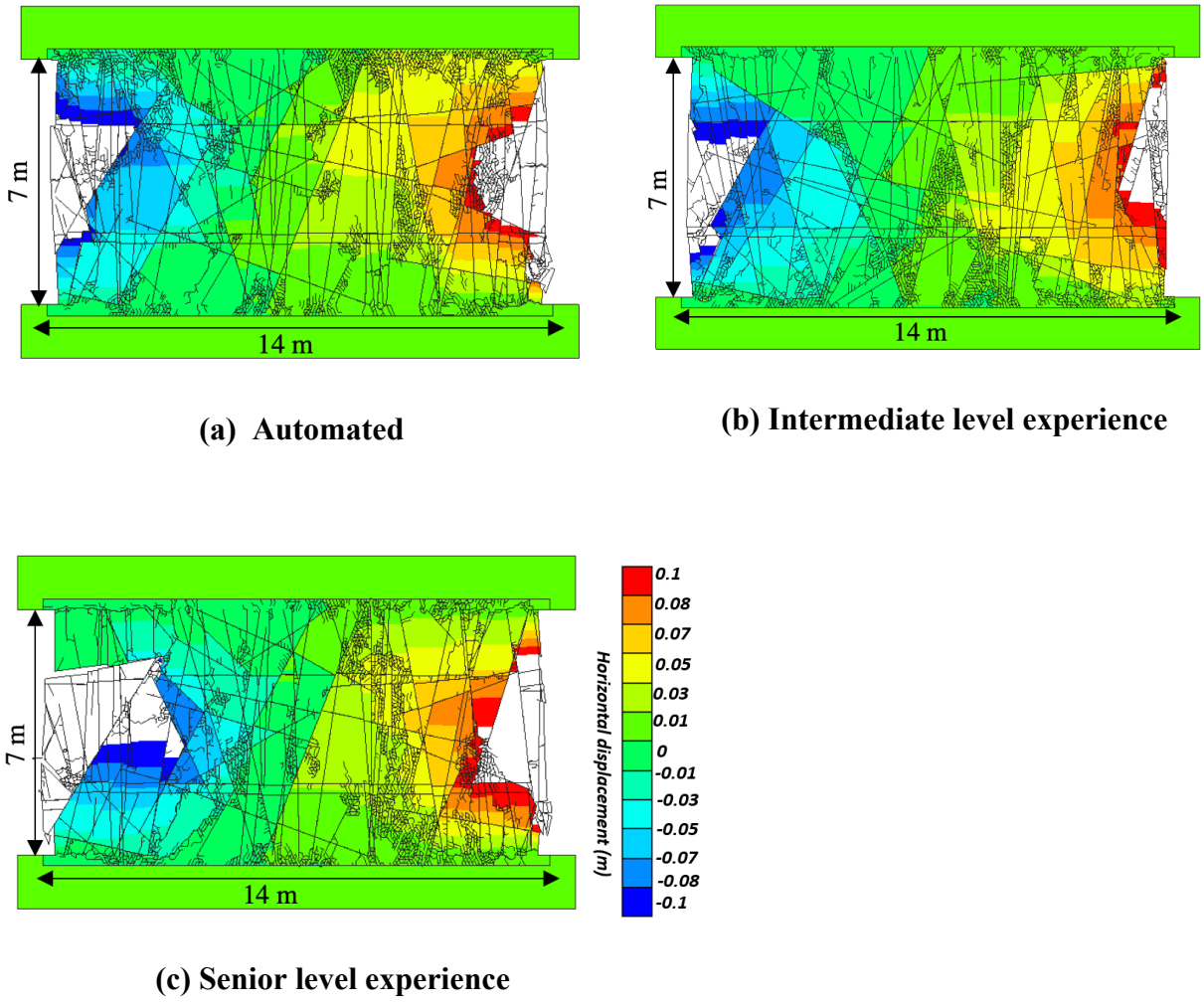

Figure 4.32. FEM-DEM-DFN analysis. Evolution of pillar horizontal displacement at the peak stage, for (a) automated and (b) manual cleaning, intermediate level experience user and (c) manual cleaning, senior level experience user.

The FDEM-DFN results indicate that the cleaning process applied to the embedded DFN trace map has a significant impact on the modelling results. Accordingly, a higher factor of safety may have to be applied to the results to be sufficiently conservative and account for human uncertainty (DFN cleaning bias). For instance, consider a simple elastic analysis of pillar stress based on a mine depth of 200 m (as at Middleton mine). For a pillar located at the centre of a 2D array of 5 pillars (pillar width of 14 m equal room width), the maximum pillar stress by tributary analysis would be 9.8 MPa. The corresponding Factors of Safety (FoS) would be 1.7, 1.4 and 1.2 for the automated, intermediate, and senior level experience user FEM-DEM models, respectively. A slight increase in depth to 250 m, would increase the average pillar stress to 12.5 MPa, and the FoS would be reduced to 1.3, 1.1 and 0.9, respectively. Therefore, under the same stress conditions and modelling assumptions, the risk of either overestimating or underestimating pillar strength (and stability) could be significant. However, it is suggested that the trace map yielding the lowest pillar strength could still be representative of the natural variability of the jointing conditions in the field (under the assumption that the cleaning process has not altered the overall network characteristics).

4.8 Summary and Concluding Remarks

New *DFN Analysis and Cleaning* methods are introduced that simplify fracture networks, while maintaining important properties such as fracture orientation, fracture intersection density, and fracture intensity. These methods are of fundamental importance for the integration of DFN models within geomechanical models, particularly when embedding rather complex 2D fracture networks within a finite element mesh.

The application of both *DFN Analysis and Cleaning* methods integrated with geomechanical software has far reaching implications, since the last decade has witnessed an increase in use of numerical modelling for simulating the mechanical behaviour of naturally fractured rock masses. Because of the underlying stochastic nature of DFN models, synthetic rock mass models with embedded DFN traces would need to consider running numerous models to account for the variability of the simulated fracture pattern. Whereas generating multiple realizations of the same DFN model is relatively straightforward and can be done relatively fast, FEM, FDEM, and DEM analysis in contrast are computationally very intensive; consequently, only a limited number of realizations can be accommodated in the analysis. The objective of this chapter is to present new methods that would allow to more objectively select which DFN model to consider for FEM, DEM or FDEM analysis. Only a set of DFN cleaning methods such as the ones presented can guarantee more objective and less biased modelling results, thus reducing the risks associated with the application of integrated DFN-geomechanical modelling to engineering design. Cleaning DFN traces requires a trade-off between optimum mesh quality and the need to maintain a degree of a fracture intensity value (e.g. P_{10} and P_{21}) and a network connectivity that closely match those of the original DFN trace map. The method presented in this chapter permits the tunability of the aggressiveness of the DFN cleaning. The methods take various parameters including the minimum and maximum trace length (line removal and line splitter), neighbor radius (point collapser), angle increment and maximum rotation (angle adjuster) and distance variation (fracture separator). Accordingly, these parameters control the cleaning procedure and the resulting fracture network characteristics.

Similarly, DFNs are increasingly used to analyze slope stability problems. Because the stability of rock slopes is intrinsically linked to the presence of rock bridges (Elmo et al., 2015), it is important that any cleaning of embedded trace maps is as objective as possible and maintains the original network connectivity to avoid introducing artificial rock bridges and potential design errors. Parameters such as P_{20} and P_{21} have inherent bias (e.g. P_{21} is orientation dependent) that may limit their ability to characterize DFN models. In the presented methodology, attempt has been made to combine as many parameters as possible to characterize DFN models and thereby reduce the inherent limitations in the characterization process if based on a single parameter. Furthermore, in the proposed methods selected parameters are used primarily to compare DFN traces before and after cleaning to ensure acceptable similarity between the original and cleaned DFN traces. The subject of DFN characterization goes hand-in-hand with the problem of rock mass characterization, since many of the parameters used in engineering practice to characterize the rock mass have important limitations (e.g. RQD). The existence of unbiased parameters that can be used to characterize rock masses and DFN models is a challenging area for future research, since most of the recorded bias and model limitations derive from the way data are collected in the field.

New techniques DFN Cleaning, DFN Quality and Mesh Quality have been introduced with the objective of being used at any scale, from laboratory tests to high rock slopes and underground block caving models. These DFN methods incorporate advanced optimization techniques, such as Monte Carlo simulation, to aid in the search for an optimal result while maintaining a reasonable runtime. In this chapter, pillars were used to demonstrate the potential influence of the adopted DFN cleaning approach on the modelled pillar strength. The presented results indicate that human uncertainty introduced as part of the DFN cleaning process can have a significant impact on model performance in terms of calculated pillar stress, displacements and block movement. By using an

automated DFN cleaning approach, it is possible to minimize the risks of underestimation or overestimation of the maximum strength and to provide an increased control over the final results. Considering that the modelled pillar factor of safety was shown to be highly sensitive to the location and connectivity of the DFN traces (and therefore to the presence of rock bridges); using the DFNAnlayzer methods offer a way to quickly compare the geomechanical results.

The proposed DFN Quality criteria for meshing and Mesh Quality assessments guarantee that a reasonable mesh quality is achieved thereby both improving computational times and eliminating spurious results that may be associated with the presence of poor geometry elements. A new Meshability Index is introduced to assess the DFN mesh quality prior to and after each cleaning method. A good correlation was achieved between the Meshability Index and Mesh Quality in the pillar case study. The use of the developed DFN techniques allows for a faster and more accurate assessment of a DFN model prior to incorporation within a geomechanical analysis.

Chapter 5: New Approaches to Quantify Progressive Damage and Rock Mass Blockiness

5.1 Introduction

The finite-discrete element method (FDEM) has proven itself valuable for simulating the initiation and propagation of brittle fractures in various surface and underground excavations (Elmo and Stead, 2010; Lisjak and Grasselli, 2010; Tatone, 2014; and Rougier, (2011)). However, there still exists the need to develop suitable techniques to better characterize fracturing processes, including the formation of fully formed blocks. This chapter describes how the results of FDEM models can be used in a detailed analysis of intact rock damage and associated block formation using several newly developed approaches: i) block-damage; ii) block size; iii) block detachment maps; iv) block tracking-tree; v) block fragmentation; and vi) block displacement. The proposed techniques are data driven, and rely solely on raw simulation data, thus eliminating the inherent inaccuracy and limited scalability of methods based on image processing.

Chapter 4 has introduced new methods to analyze discrete fracture network (DFN) models. However, those techniques are valid for "*static*" DFN models. When DFN traces are embedded into 2D FDEM models, the imposed loading conditions contribute to the extension of the pre-existing traces and the formation of new cracks. In other words, a new DFN configuration is progressively being generated as the loading conditions changes in the FDEM model. The objective of this chapter is to analyze "*dynamic*" DFN traces generated in FDEM simulations. A fracture calculator is developed that uses mesh data and timesteps of the FDEM numerical simulation. This new technique is independent of the simulation software and could also be applied to simpler DEM (Discrete Element Methods). An extension of the DFN Analyzer technique

described in chapter 4 is then proposed that allows to quantitatively analyze fractures, both spatially (within a timestep) and temporally (for varying timesteps). This new technique has the potential to offer significantly improved capabilities for the analysis of intact rock bridge failure (e.g. Elmo et al., 2018). The analysis is not limited to fracture traces, and a new Block Calculator and Block Analyzer are introduced that precisely calculate the number of fully formed blocks and analyze their characteristics based on geometrical methods and graph analysis (Hopcroft and Tarjan, 1973; Lewis and Papadimitriou, 1982; Diestel, 2017; Gross and Yellen, 2005).

As in chapter 4, pillar models developed based on data collected by Elmo (2006) have been used to test all the new analytical methods. The results show that the proposed techniques can provide a detailed portfolio of quantitative information and illustrations that can help in understanding brittle failure processes and highlight the relative control that pre-existing fractures and intact rock bridges play during the failure process.

5.2 Rock Mass Blockiness as the Key to Understanding Brittle Failure

The importance of identifying which fractures contribute to block formation has been demonstrated by various researchers; for instance, important examples include the application of the Geological Strength Index, GSI (Hoek et al. 1995; Marinos et al. 2007; Hoek and Brown, 2018). Even though blockiness is an important parameter which controls, for a given set of shear strength properties, the correct value of GSI to use, there are no procedures that can calculate both "static" and "dynamic" rock mass blockiness, i.e. changes in the in-situ block size distribution (IBSD) occurring as a result of external loading.

Quantification of GSI is proposed by Cai et al. (2004) emphasizing the drawbacks in attributing a single value of GSI to the structure under study. Bertuzzi (2018) found a high correlation between the GSI derived from the chart by Hoek (1994) and the approach proposed by Cai et al. (2004) in major rock types in Sydney. The GSI chart was quantified by Hoek et al. (2013) by introducing relationship between Joint Condition and Rock Quality Designation (RQD). In this paper, they encourage researchers to use the numerical modelling of rock fracture networks in order to gain a better knowledge of jointed rock mass behaviour.

Using GSI terminology, does not necessarily reflect a rock mass that is initially blocky will become very blocky when subjected to loading. To study the transition of a rock mass from massive to blocky and very blocky, it is necessary to analyze and quantify failure mechanisms, including failure of intact rock bridges. However, it is not just a matter of simply measuring block volumes (or area in 2D simulations). There is the need to track where blocks are initially nucleated, and how those blocks may further fragment into smaller blocks. In other words, the analysis of brittle damage requires more than just a measurement of areal intensity (D_{21} parameter; Gao, 2013) and crack orientation.

Static analysis of block systems has been conducted by many researchers in the past 50 years. The concept of block theory has been developed using graph theory, set theory and vector analysis for analyzing rock mass stability. For example, Warburton (1981) assessed block stability by using vector analysis and calculating blocks volume, mass and factors of safety with respect to a frictional failure criterion. Lin and Fairhurst (1988) performed static analysis of large-scale block systems using directed graph theory (ordered pair of nodes) in which the blocks are nodes and two

nodes are joined by an arc whenever the corresponding blocks are adjacent. The derived paths in the graph resembled the free face of the excavation. An example of such graphs by Lin and Fairhurst (1988) is shown Figure 5.1.

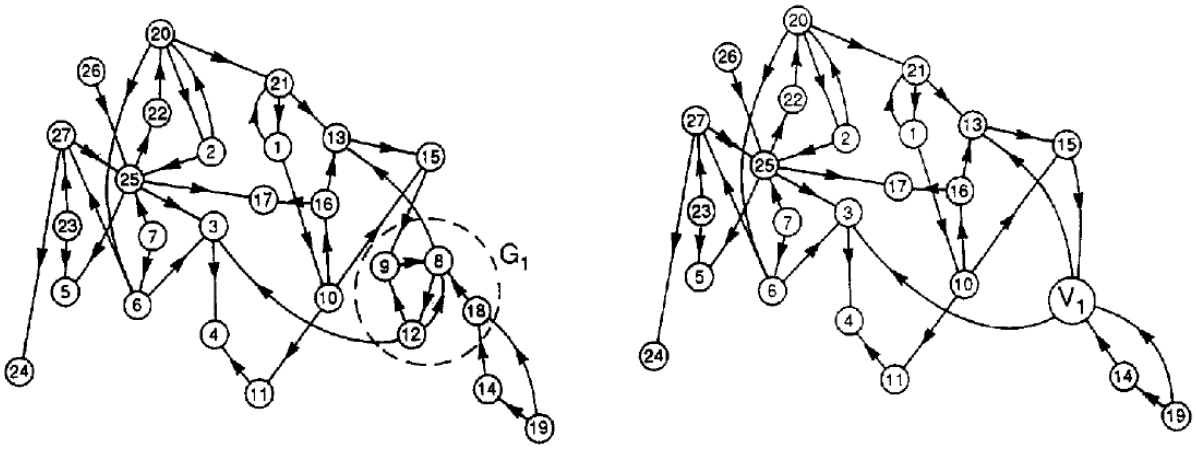

Figure 5.1. The directed graph and the reduced graph (after Lin and Fairhurst, 1988).

Various studies have been dedicated to the analysis of fracture configurations and potential block formation for static problems. GeneralBlock was written in Visual C++ 6.0 by Xia et al. (2015) using the OpenGL library. In this code, the modelling domain can be a complex shape, and the rock and fractures can be imported as heterogeneous materials. This program identifies all blocks formed by the excavations and the fractures and can show 3D graphics for each block. However, their methodology suffers from being restricted to rock blocks formed by complex excavations and finite-sized fractures, therefore filtering non-persistent fractures is one of the primary steps prior to using the code. Goodman and Shi (1985) proposed block theory as a 3D approach independent of pre-mapping of the joints and accounting for the shape of the excavation. Block theory does not offer analysis with large deformation (DDA) (Hatzor et al., 2017). However, the issue can be eliminated by using dynamic methods such as distinct element analysis, thus allowing for large block movements as well as considering complex geological sections (Cundall and

Strack, 2008). Cundall, (1988) proposed methods for detecting the contacts between blocks of various shapes (i.e., convex and concave) and characterizing the geometrical and physical properties defined by the contact between objects. This method utilized a linked-list data structure attached to a global pointer as an optimized search for rapid scanning through all contacts as the forces are updated in calculation cycles.

Numerical methods are well-suited to analyze problems that include inherent variability associated with natural fractures, including their spatial distribution, and physical properties. Examples include block theory and Displacement Discontinuity Analysis, DDA (Goodman and Shi, 1985), discrete element method, DEM (Cundall, 1988) and FDEM methods (e.g. Elmo and Stead, 2010; Vyazmensky et al., 2010; Mitelman and Elmo, 2014; Tatone and Grasselli, 2015). For dynamic problems, Lu (2002) implemented a dynamic linked-list to store topological information of a directed polyhedron. This was an automated approach for detecting 3D blocks formed by natural fractures, including cracks, joints, and faults. A computer language BGL (Block Generation Language) has been developed by Heliot (1988) to build the 3D block structure around excavations in rock. BGL has been developed using Lex and Yacc UNIX tools and consider both the geometrical description of the jointed rock mass and the available geological history process. More recently, Vazaios (2018) identified critical blocks using image processing algorithms applied to the output simulation results of Irazu (Geomechanica, 2017).

In general terms, numerical methods of discrete (blocks) problems have been gradually advanced by adopting various data structures such as arrays, linked lists and chained trees. Developing methods to continuously search for contact between blocks, requires an appropriate

implementation of data structure to identify rock blocks. Block calculations and analysis is predominantly static and independent of the progressive intact rock damage associated with brittle fracturing. Some numerical code is based on a discretization of the modelling domain to blocks, and subsequent calculation of the contact forces between these blocks. The method of updating the block information with simulation timestep is known as DEM (Cundall and Strack, 2008). The proposed methodologies introduced in this chapter use a similar data-driven approach integrated with FDEM models by using raw simulation output. One major difference between the method proposed in this chapter and previously developed methods for DEM modelling relates to the relationship between the blocks across timesteps. While DEM is based on calculating the blocks for one given step, the proposed method in this chapter can track finite element information across timesteps and build relationships between blocks using tree data structure.

Graph theory (Gibbons, 1985) is a rapidly developing concept in the mainstream of mathematics with potential applications in diverse fields such as electrical engineering (coding theory), computer science (algorithms and computations), biochemistry (genomics), and operations research (scheduling) and social networks. The same theory has been applied to solve problems such as block calculations within FDEM models by creating a tree of mesh elements and their connections. Solving the problem at a more abstract level using a hierarchical structure (across timesteps) was a fundamental and initial step to allow tracking of elements and the building of connected components (blocks). The proposed method in this chapter has enabled the application of various advanced analysis methods to the calculated blocks.

5.3 A Novel Approach to Analyze Fracture Traces in Finite-Discrete Element Models

The mechanical properties of a rock mass are directly related to its blocky (or massive) character. The geometry of the blocks is determined by the geometry of the fractures; therefore, fracture geometry needs to be carefully analyzed and studied. The fractures that form fully connected networks (with closed polygons) might be considered as unstable. DFN Analysis has been introduced in chapter 4 and relied on fracture line data being available and detailed the application of various analyses to these fracture traces. However, DFN Analysis was introduced for the initial DFN whereas the method in this chapter considers newly-generated fractures in FDEM models. When 2D fracture traces are imported into the FDEM models, they become the edges of meshed elements, whose nodes will sustain a much lower strength compared to nodes that represent intact rock. As discussed in chapter 2, FDEM techniques may use different approaches to simulate the generation and opening of new fractures. This section details how it is possible to compute fracture data by using information contained in the raw FDEM simulation output, with specific reference to the output of the FDEM code ELFEN. The same principles could easily be extended to other FDEM software.

The initial stage in constructing a FDEM model in ELFEN is the discretization of the domain into mesh elements of a given size. The size of the mesh element is an important parameter as it determines the direction along which the fractures initiate and propagate. In principle, ELFEN includes a remeshing option that would make the fracturing process independent of the mesh size, but this option is seldom used in the analysis of rock engineering problems due to the large computational time required (see also chapter 2). While using small meshed elements would provide a more detailed description of the fracturing process, the choice of the minimum element

size is a trade-off between accuracy of the modelled fracture path and the computational time required to complete the analysis. Accordingly, the number of elements in the FDEM model would differ based on the size of the problem under consideration and the assigned mesh size, as shown below in Figure 5.2 (after Stead and Elmo, 2015).

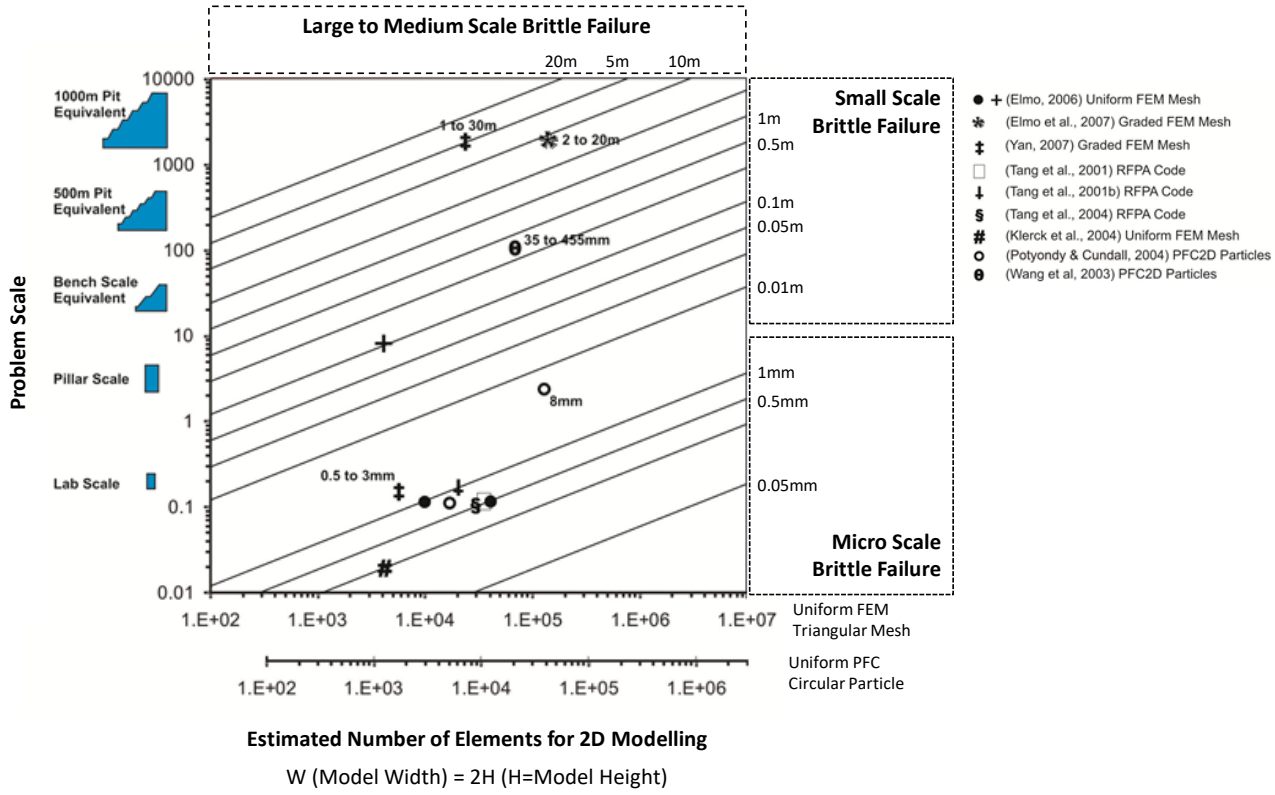

Figure 5.2. Relationship between model scale, mesh size and number of elements for 2D analysis of brittle failure processes (after Elmo and Stead, 2015).

The proposed methodology takes geometrical (mesh topology) information from simulation results and computes new fracture information. The process is independent of the mesh size used to discretize the rock mass problem.

As the simulation progresses, the mesh topology is updated as additional nodes and lines are added that represent the newly generated fractures. At every timestep it is possible to track the location of every node in the mesh and use this information to develop an "*opening*" criterion to define whether a new fracture has been introduced in the model. The process follows two steps (Figure 5.3):

1. Two nodes are still sharing one common edge (line), in which case no new open fracture is detected; or
2. Two nodes are no longer sharing one common edge (line), in which case a new open fracture is detected (process of opening).

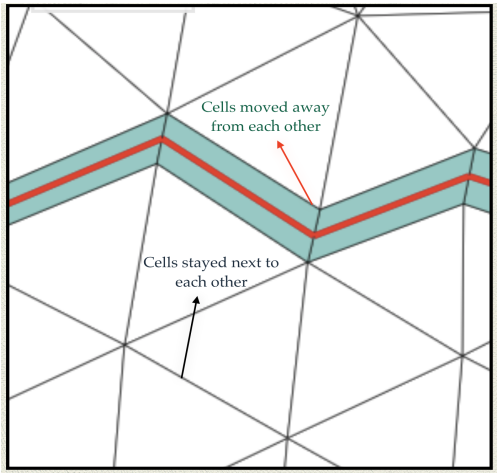

Figure 5.3. Mesh visualization for two cases, black arrow indicates the first case, in which cells remain in the initial location. Red arrow indicates the case in which the cell lines have moved away from each other.

Once new opening has been detected, the technique (herein called DEMFA) keeps track of the newly generated nodes and lines to detect whether a newly generated fracture is extending and/or branching out into new separate fractures as shown in Figure 5.4. This process is recursively completed for all meshed elements (nodes and lines) for all timesteps.

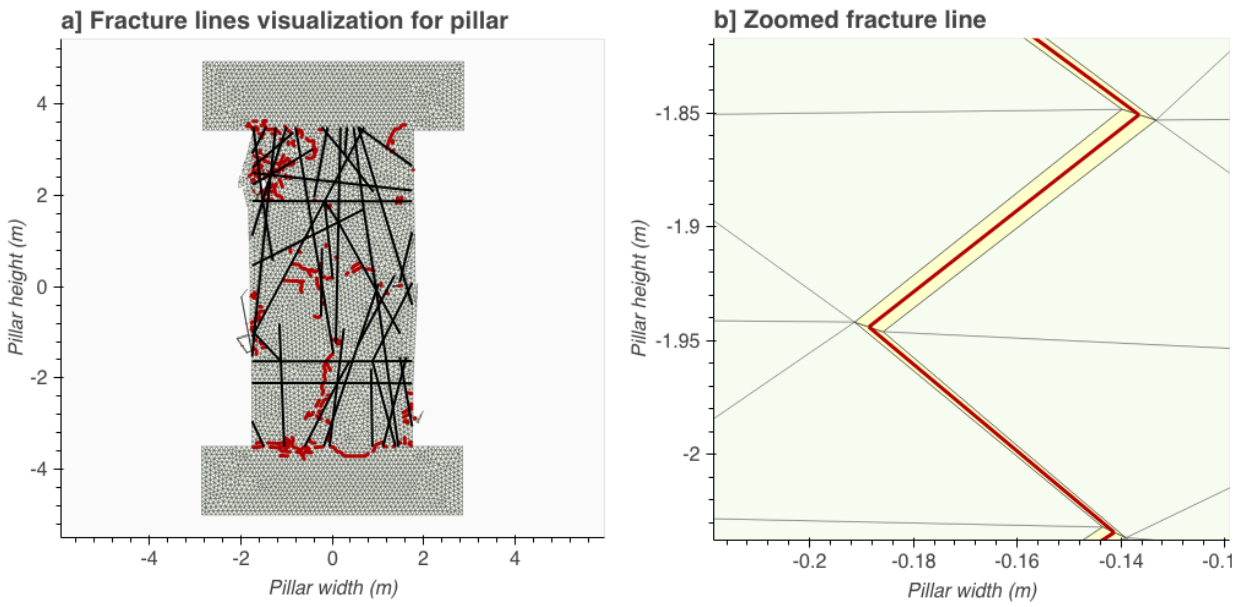

Figure 5.4.a) Pre-existing fracture lines in pillar model shown in black and newly-generated fractures shown in red b) Focused fracture line location indicates the yellow area as the opening of mesh cells and red line constructed using the mid-point of connected mesh elements.

5.3.1 Material Properties and Boundary Conditions

The suggested methodologies are applied on a pillar model with following boundary conditions (Figure 5.5) and material properties (Table 5.1) similar to the model used in Chapter 4.

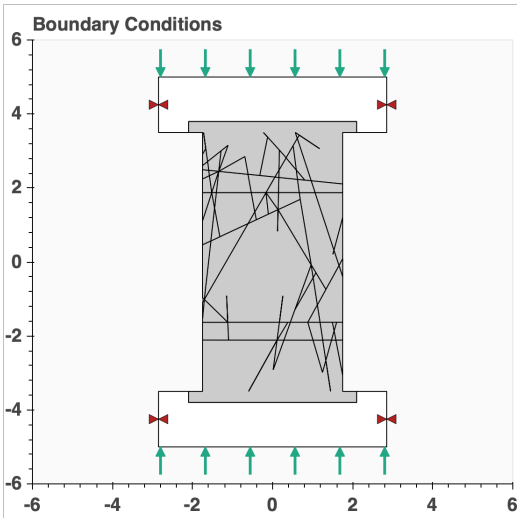

Figure 5.5. Boundary conditions of the pillar model.

Table 5.1. Material Properties

Rock Material Properties (Limestone)		**Unit**	**Value**
Intact Rock Material	Unified compressive strength, σ_{ci}	MPa	48
	Fracture energy, G_f	Jm^{-2}	19.47
	Tensile Strength, σ_t	MPa	3.84
	Young's Modulus, E	GPa	27.5
	Poisson's ratio, ν	-	0.23
	Density, ρ	kgm^{-3}	2600
	Internal Cohesion, c_i	MPa	9
	Internal Friction, ϕ_f	degrees	40
Platen material properties and discrete (contact) parameters		**Unit**	**Value**
Rock Fracture	Surface Cohesion, c_f	MPa	48
	Surface Friction, $\emptyset_f$	Jm^{-2}	19.47
	Normal Stiffness (Normal Penalty) P_n	MPa	3.84
	Shear Stiffness (Shear Penalty) P_t	GPa	27.5
Platen Properties	Young's Modulus of Platen	GPa	200
	Poisson's ratio of Platen	kgm^{-3}	0.3
	Density of Platen	MPa	7860
Rock-Platen Contacts	Rock/platen cohesion	MPa	0
	Rock/Platen friction	degrees	3
	Rock/platen normal stiffness (Normal Penalty P_n)	GPa/m	27
	Rock/platen shear stiffness (Shear Penalty P_t)	GPa/m	2.7

5.3.2 Analysis of Fracture Density and Fracture Intensity

Once all new fracture lines are computed using the technique introduced in section 5.3, the DFN Analysis approach introduced in chapter 4 can now be used to provide properties for the *dynamic* DFNs, i.e. as changes occur to the underlying fracture pattern as the simulation progresses (increasing timestep). The results can then be compared to the initial, *static*, DFN at timestep 0.

Dynamic DFNs would represent the onset and propagation of damage, while static DFNs represent the initial modelling conditions and initial rock mass blockiness.

Whereas calculating damage density (D_{20}) is straightforward in static DFN models, for dynamic DFNs one must consider how new fractures are defined in first place (see section 5.3). In the current approach, fractures are defined based on an opening criterion; however, the algorithm would count continuous fractures as two or more separate fractures if the fractures are not aligned perfectly in a straight line. To overcome this issue, it is proposed to use D_{21} as the key damage indicator for dynamic DFNs. The concept of D_{21} is not entirely new; for example, Gao (2013) employed the D_{21} to characterize brittle fracture above coal mine roadways. What is being introduced here is the use of D_{21} as a component part of a suite of damage indicators, Figure 5.7. The results in Figure 5.6 and Figure 5.7 refer to a sample pillar model with pre-defined fracture lines. The properties and loading conditions of the FDEM model are similar to those used in chapter 4 to test and validate the application of the developed analysis approaches.

The model is associated with some initial displacement prior to the load increment. Comparing the stress-strain plot (Figure 5.6) and DEM figures (Figure 5.7) indicates that the damage initiates and accumulates with a steep slope relationship between stress, and D_{20}, D_{21}. The peak stress occurs at 0.5% strain. When the stress drops, the damage accumulation continues until 0.56 % of strain.

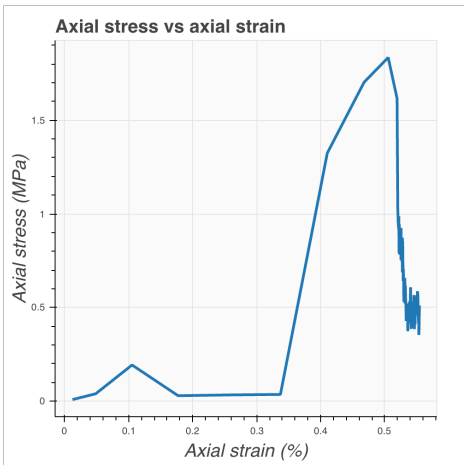

Figure 5.6. Axial Stress vs Axial Strain for Sample Model.

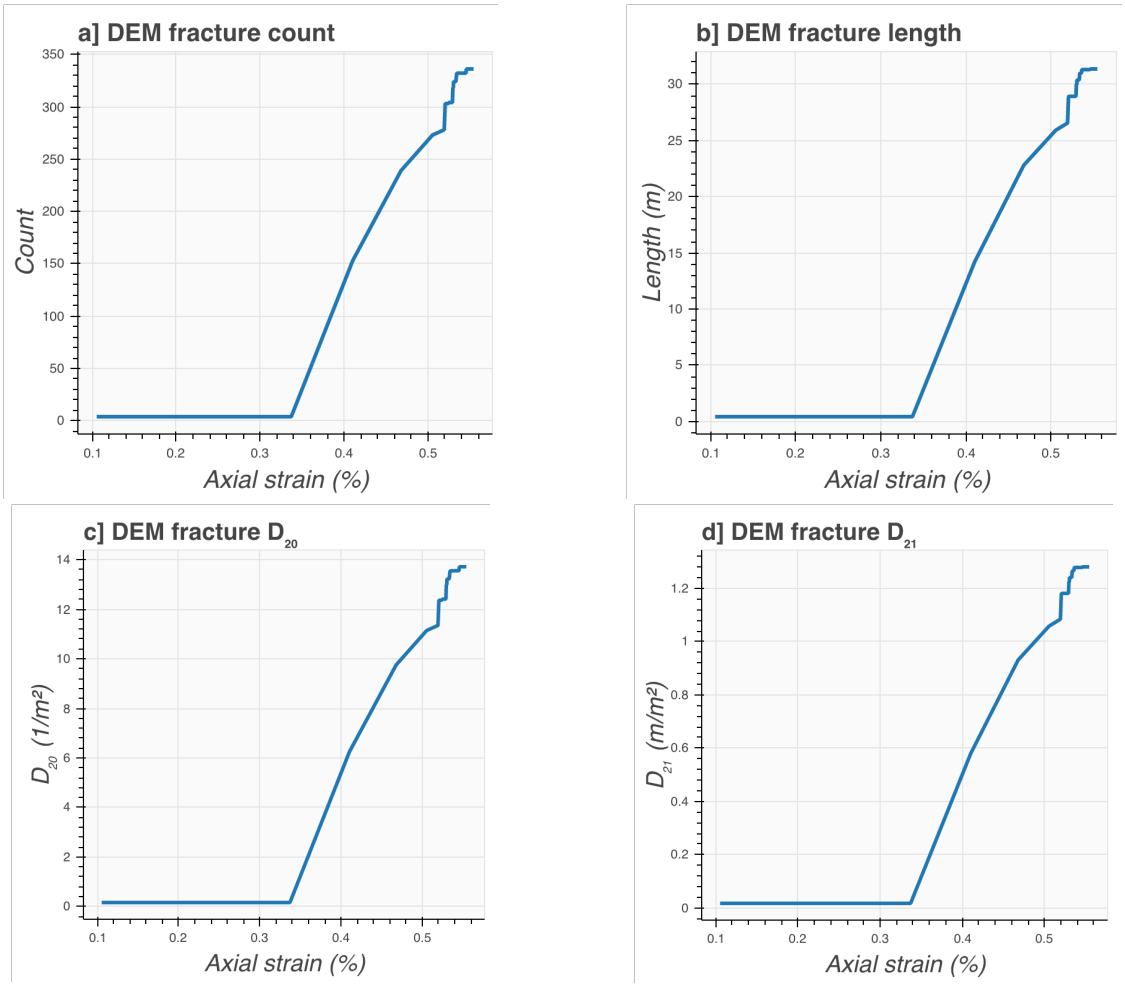

Figure 5.7. DEM Fracture Analyzer indicated, a) number of fractures, b) length of fractures, c) number of fractures per area D_{20} and d) total length of fractures per area D_{21} m/m^2.

5.4 A New Algorithm to Define Blocks Formation in FDEM models

This section introduces algorithms to compute static and dynamic block formation. The static blocks can be computed by calculating closed polygons, using fracture lines (DFN) as input. This is the same approach used in DFN Quality in chapter 4. In section 5.3, the calculation of the fracture lines is obtained per timestep, therefore, this data can be used as input to the polygon calculator to compute blocks per timestep. This method, however, treats the data of each timestep separately. It does not maintain information of how a single block gets broken into sub-blocks across timesteps. Mesh data contains the necessary information to be able to track those blocks across timestep. A second method of computing blocks is introduced here that utilizes mesh data to overcome this shortcoming. This algorithm has been developed to calculate the block formation per timestep. This is computed by analyzing mesh data and the connections between elements, subsequently identifying which group of elements form distinct blocks.

The Block Calculator algorithm, DEMBC, considers the data for every timestep separately, but it is also capable of logging information concerning one given block at timestep t_i being broken into sub-blocks as the simulation progresses (timestep t_{i+1}). To do so, the algorithm analyses mesh data and connections between elements, identifying which group of elements form distinct blocks. A graph data structure is generated based on elements and connections for every timestep, whereby nodes represent mesh elements, and edges (lines) represent connections between elements. Two mesh elements are considered connected if they are sharing element edges. When two elements are connected, a graph edge is added to link their nodes. Each group of connected components represent a distinct graph. Figure 5.7 provides illustration of a simple graph.

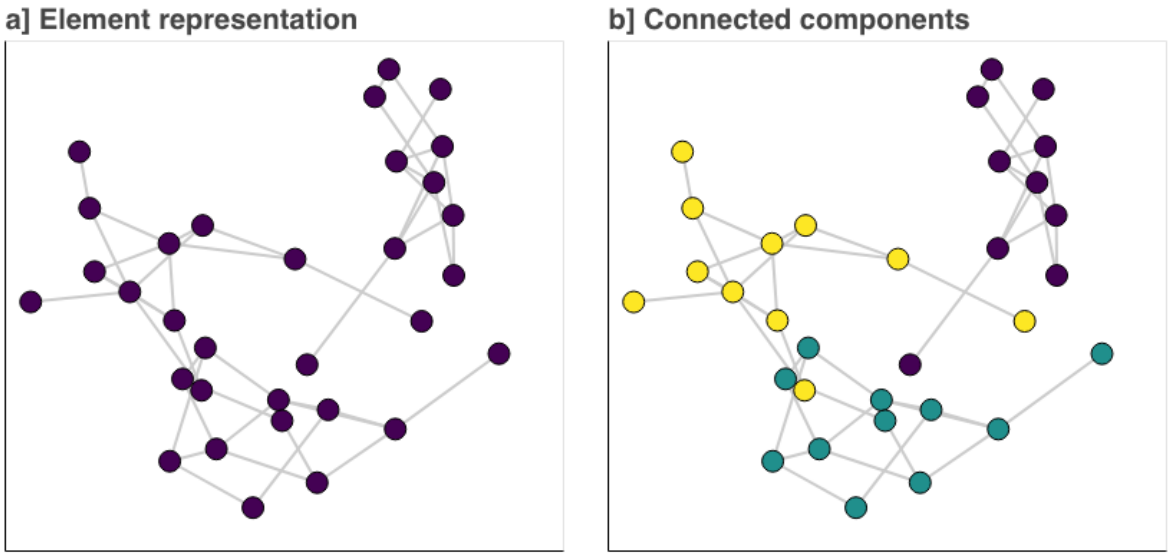

Figure 5.8. Graph visualization of block calculator. a) element representation and b) three clusters of connected components.

Computing connected components is a well-known technique in the field of graph theory (Hopcroft and Tarjan, 1973; Shiloach and Even, 1981; Lewis and Papadimitriou, 1982; Reingold 2008). A random node is initially selected, and then neighbouring nodes are progressively connected until there are no more neighbouring nodes to reach. The traversed components are called connected components. The process is then repeated by choosing a random node that has not been explored yet and repeating the traversal process. The result is a set of connected components, each one representing a distinct block.

Figure 5.7 a and b are simple examples (sparse graph) for illustration purposes; however, the graph is a lot denser for a real model. Figure 5.9 shows the connected mesh elements forming separate blocks in initial timestep.

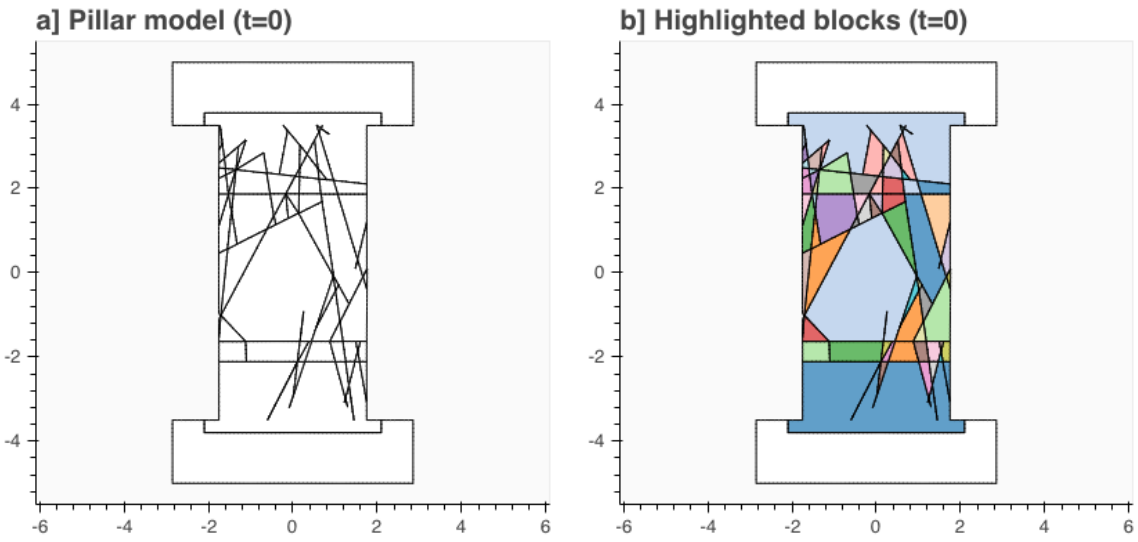

Figure 5.9. FDEM model of a fractured pillar. Static DFN traces and blocks at timestep 0. a) Showing blocks without highlighting connected components. b) With highlighting connected components.

Figure 5.10 and Figure 5.11 show FDEM simulated pillar model with a total of 12000 meshed elements. Figure 5.10.a shows the graph structure (where nodes represent mesh elements, and edges represent connections between those elements). Figure 5.10.b shows the same graph structure after applying the connected components algorithm. The colours are used to differentiate the components, each component representing the elements of a fully formed block. The graph information is converted into geometrical blocks by combining the mesh coordinates information with the knowledge of which block each element belongs to, as shown in Figure 5.11. Figure 5.10.a shows the mesh elements in the graph structure in the peak stress timestep. Figure 5.11 shows the connected mesh elements forming separate blocks at the peak stress timestep. The colours of Figure 5.10.b and Figure 5.11.b are correlated with each other.

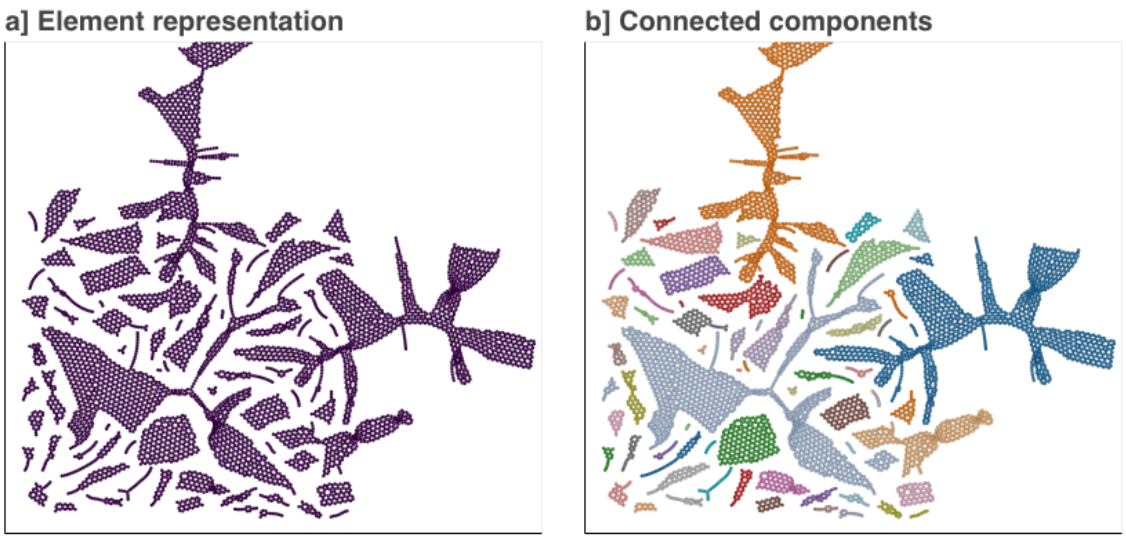

Figure 5.10. a) Element representation and b) connected components.

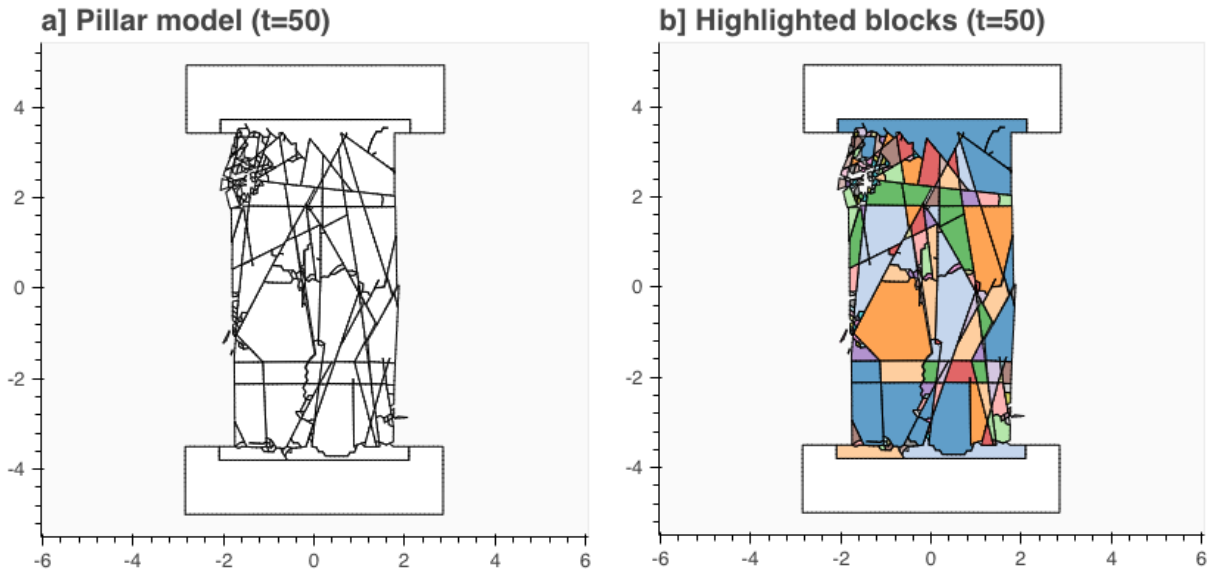

Figure 5.11. FDEM model of a fractured pillar. Dynamic DFN traces and blocks at timestep 50. a) Showing blocks without highlighting of connected components. b) With highlighting of connected components.

5.4.1 Simulated Block Analysis

Once blocks are identified, the objective is to group them into three categories, based on their kinematic character during and at the end of the simulation. The analysis could, in principle, be applied to any DFN model, and is not specific to FDEM software. The three categories are:

1) Blocks that remain stable (same volume or area) throughout the simulation;
2) Blocks that are removable, i.e. they detach from the rock mass due to external loading; and
3) Brittle blocks, i.e. blocks that exist at the beginning of the simulation and are fragmented in a series of smaller blocks by the end of the simulation.

These categories provide additional quantification of rock mass damage in addition and in relation to D_{21}. Under loading, a massive rock mass would likely yield a relatively large D_{21}, which may result in spalling blocks or failure of intact rock bridges separating existing blocks. Conversely, a blocky to very blocky rock mass would likely yield a relatively low D_{21}, as either existing blocks become kinematically unstable upon failure of critical rock bridges, or as damage is consumed to break existing tapered blocks into removable blocks. Dedicated analysis techniques have been introduced to test and validate this new approach to rock mass damage quantification, including:

- Combined block-damage analysis
- Block size distribution (BSD) and B_{10}, B_{25}, B_{50} (% passing size) parameters
- Block size and associated aggregations (Max, Min, average, median and quartiles)
- Block size density maps
- Block tracking trees
- Block fragmentation (single block being fragmented in sub-blocks)
- Block displacement

These are described in detail below with reference to the FDEM model shown in Figure 5.6.

The number of blocks that are generated during a given simulation time can be plotted in relation to timestep, damage and/or strain. An example is given in Figure 5.12, which includes the number of blocks per timestep, the number of blocks as a function of the damage parameter D_{21} and, finally, number of blocks as a function of axial strain (%). Despite being useful, this type of information alone does not provide direct insight as to how damage would eventually control the mechanical behaviour of the rock mass. The true value of this information will become apparent when combined with data such as block density maps, tracking trees and fragmentation.

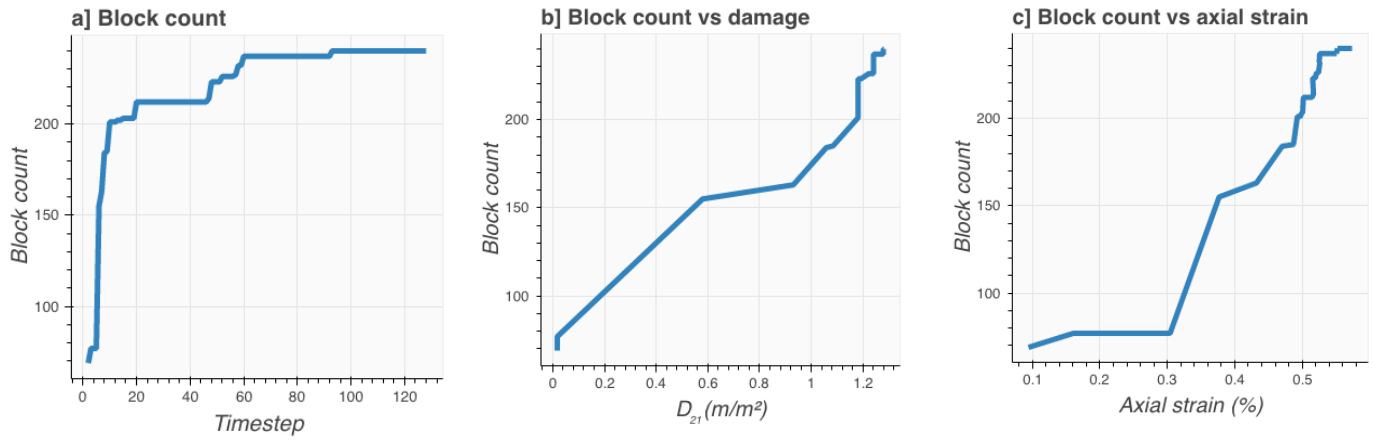

Figure 5.12. (a) Blocks count vs. timestep; b) blocks count vs. damage (m/m^2); and c) block count vs. axial strain (%).

One obvious approach to block size analysis is the generation of cumulative size distribution plots, Figure 5.12. Quantiles could then be used to study how specific block sizes change as the simulation progresses. It is argued that coarser sizes would be more likely to remain constant or show only a marginal decrease with increasing timestep if rock mass failure was predominately

structurally controlled. Likewise, spalling failure would be more likely to be indicated by a rapid increase in the number of small size blocks.

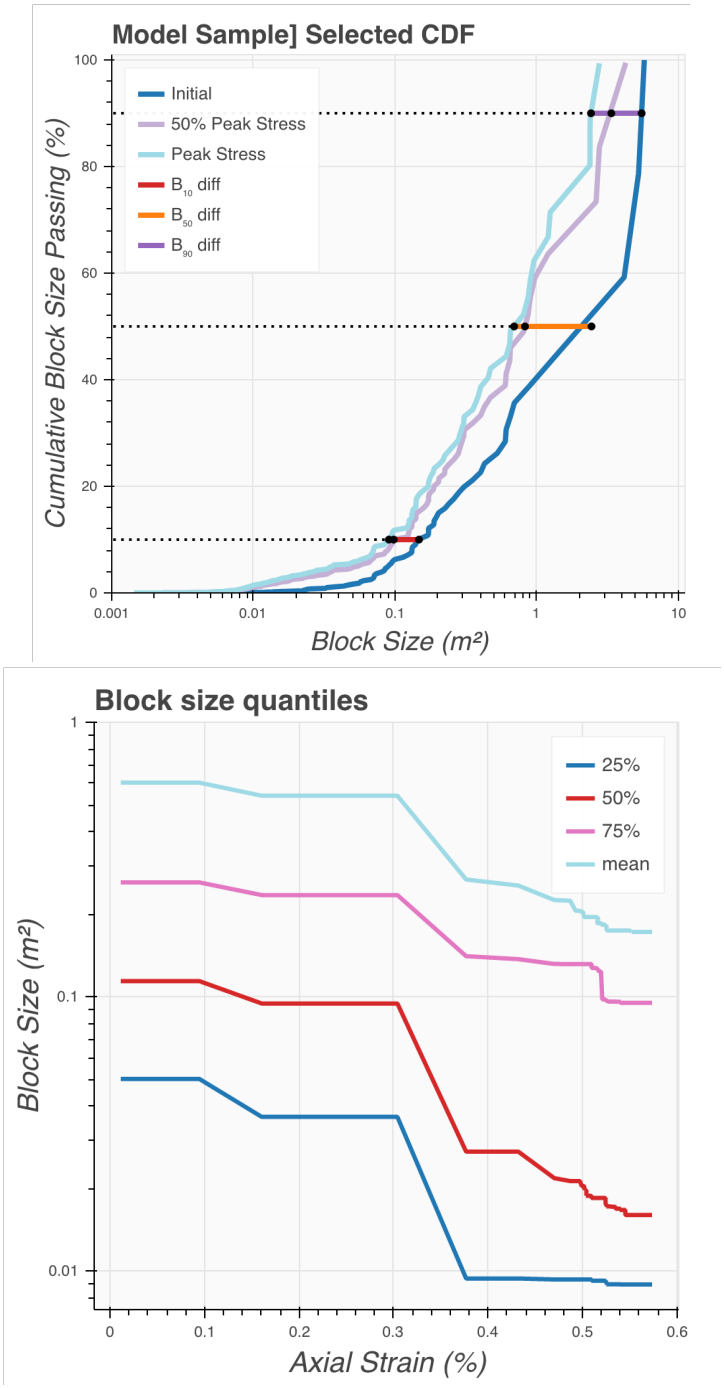

Figure 5.13. Block size versus timestep. Mean block size is shown in light blue, median in red, and the 25 % and 75 % of blocks sizes (m^2) are shown in dark blue and purple, respectively.

For better visualization of block size distribution, block size maps could be generated to show block formation at selected timesteps. An example is provided in Figure 5.14, which refers to the data included in Figure 5.12 above. Figure 5.15 shows the same block size density map with a common colour bar for block size.

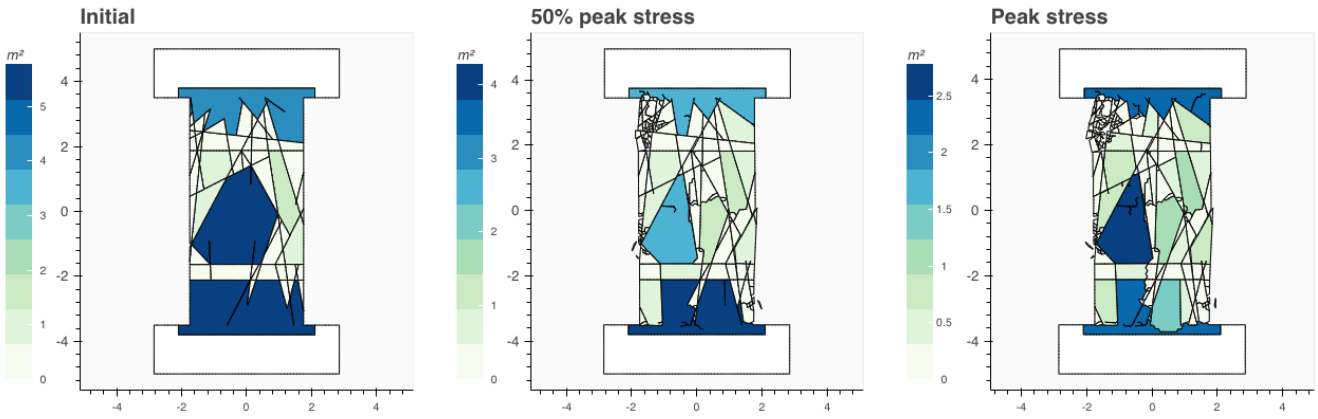

Figure 5.14. Example of block size maps visualization for three different timesteps using different colour density block size.

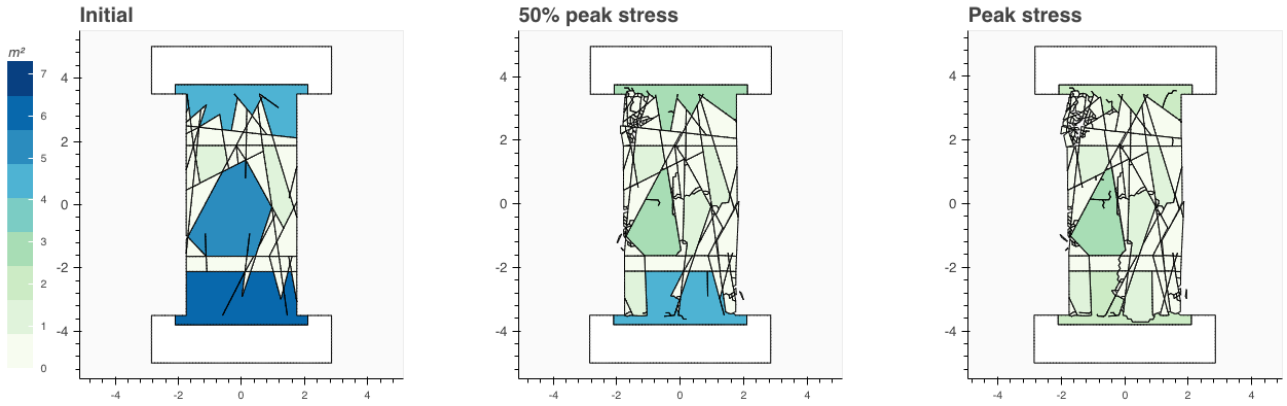

Figure 5.15. Block size density map visualization for three different timesteps using common scale for colour density block size.

More importantly, a novel block tracking tree approach is introduced as a method that could have important applications in terms of rockburst and rock fall analysis. The approach has at its core a

process that characterizes the relationship between blocks formed at different timesteps; a parent-child relationship is defined when an existing block (parent) at time step t_i is broken into several smaller blocks (children) at timestep t_{i+n}. At time step t_i, block properties (size and coordinates) are initially computed. The process is repeated at time step t_{i+n}, with the recording of an additional property that refer to the hierarchy between blocks. In Figure 5.16.a, this process is shown in the form of a graph, in which nodes represent distinct blocks (at a given timestep), and edges point to those blocks that have fragmented into new sub blocks in subsequent timesteps. Clearly, this type of dense graph visualization is not very effective for simulations that involve a large number of time steps. As an alternative, Figure 5.16.b, a circular tree layout could be used, in which each ring represents the blocks at one particular timestep. This conversion can be completed by organizing all nodes that belong to each time step and positioning them in a circle. The centre of this circle is an arbitrary node selected as a starting point and the timestep increases outwards.

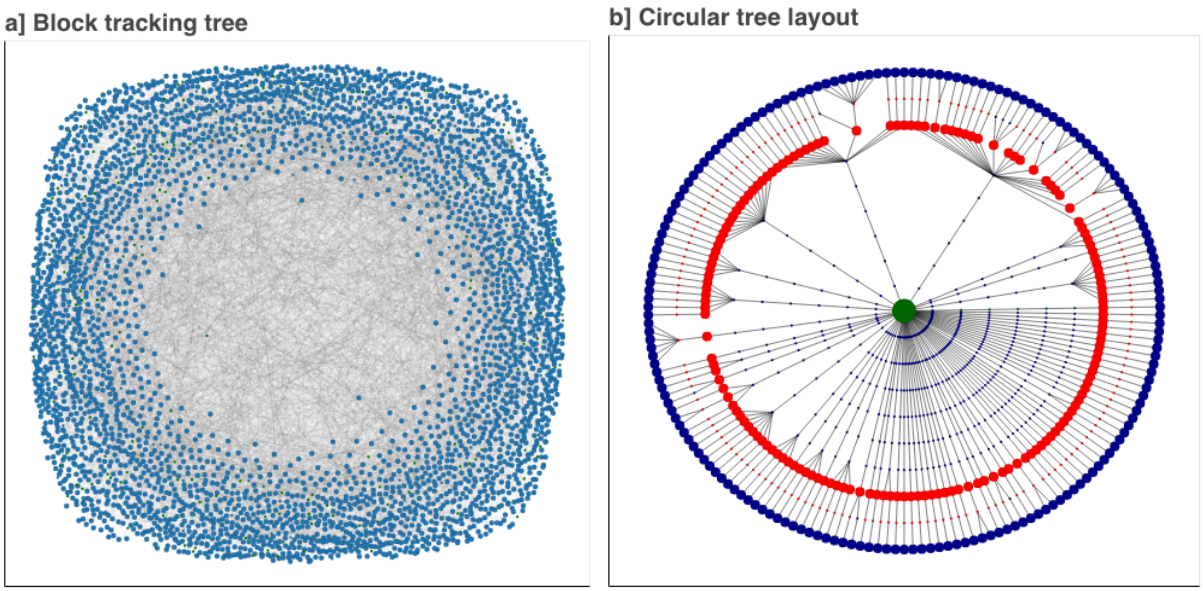

Figure 5.16. Examples of (a) Unorganized block tracking tree, and (b) circular tree layout in which green is the initial timestep, red is 50% peak stress and blue is peak stress. The circles correspond to the block size maps shown in Figure 5.14.

Due to the tracking tree layout, it would not be possible to explicitly illustrate the block size and damage using a circle size. Hence, it was necessary to further refine the visualization technique to illustrate the size and damage data along with block properties, in a quantitative manner. In Figure 5.17, the block tracking tree is updated to include a measurement of the "children" blocks generated from any given "parent" block. Areas within the pillar that do not undergo any significant fragmentation are shown in white. The warm colours refer to areas where a higher degree of damage (i.e. fragmentation) has been occurring. In Figure 5.17, damage in the simulated pillar is higher closer to the roof, floor and core, while sidewalls appear to fragment less, since failure is mostly structurally controlled.

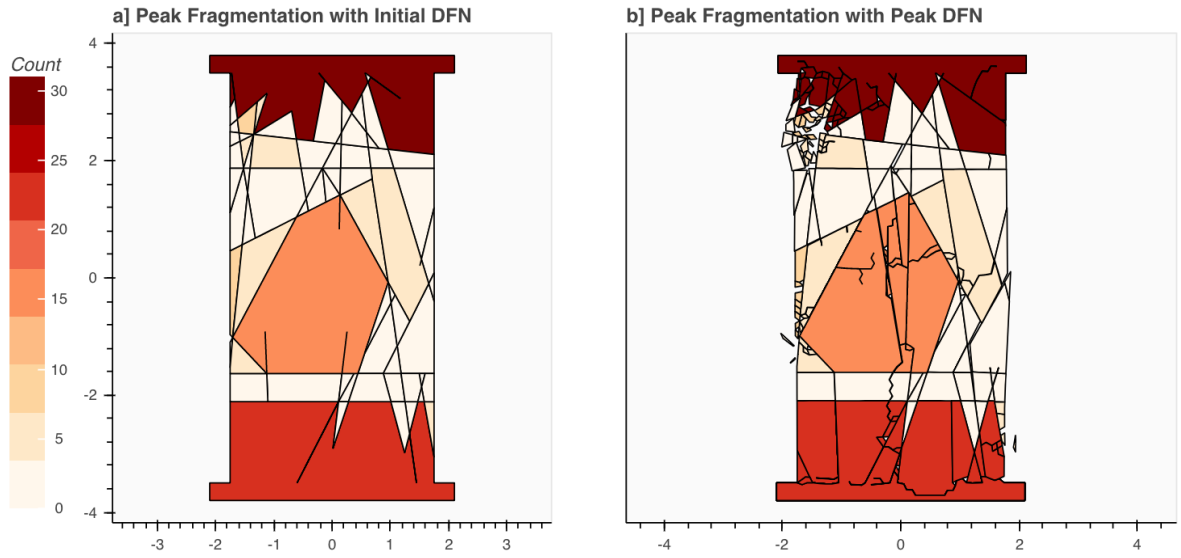

Figure 5.17. Fragmentation map calculated based on the number of fragmented blocks being generated at peak stress level and normalized to the initial timestep and shown for each block configuration in a) Initial DFN, b) Newly-generated fractures in peak stress overlaid with the blocks in the initial DFN.

Additionally, it is possible to plot (Figure 5.18 and Figure 5.19) the number of fragmented blocks (children) generated at every time step, and colour-code blocks in terms of the displacement and stress they are being subjected to.

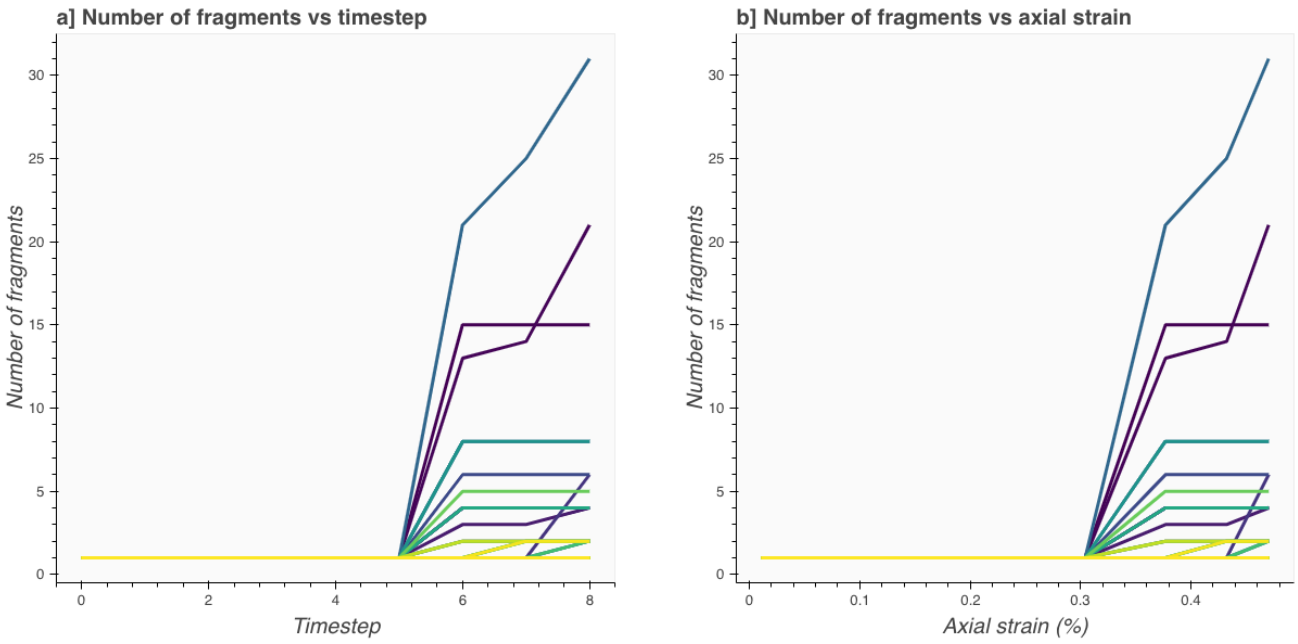

Figure 5.18. a) Number of fragments for each block vs timestep and b) Number of fragments for each block vs axial strain (%).

Note that using the FEM simulation data, the displacement and stress contour maps have been generated. However, a major drawback has been noted during this process. The FEM simulation data can be exported in the specific locations called as history points. The history points are usually defined across the model boundary. However, as the fractures initiates and propagated, some of the blocks detach from the model. Hence, using this method, the displacement, stress, speed and other features of the separated blocks will be lost. This drawback has been removed by developing a new displacement technique explained in chapter 6.

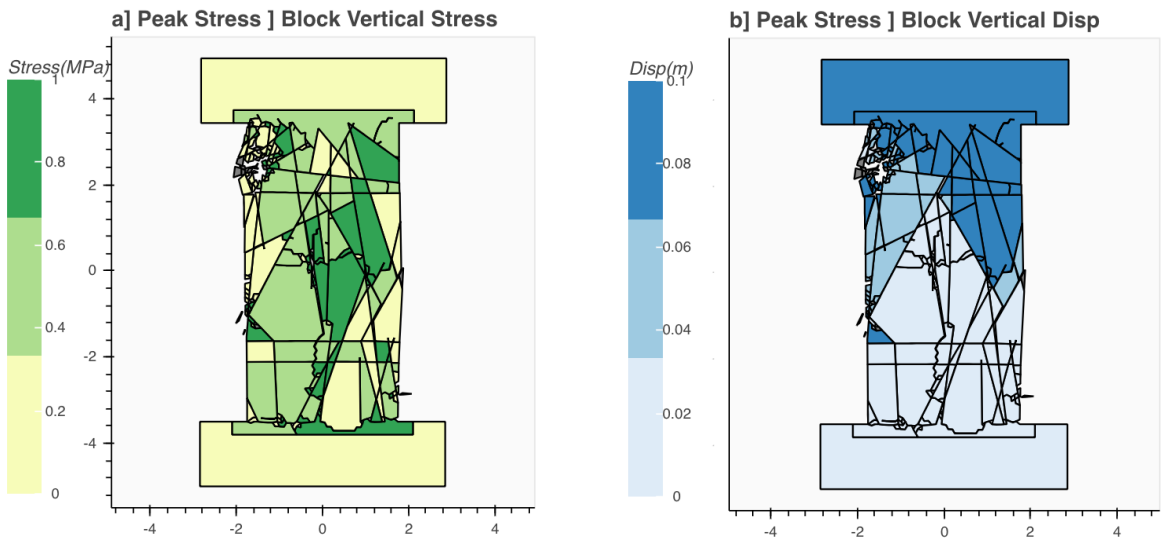

Figure 5.19. a) Vertical stress of individual blocks at peak stress. b) Vertical displacement of individual blocks at peak stress using Finite-Element simulation output. Gray indicates that the displacement is not output due to the location of history points that are specified inside the pillar.

5.5 Conclusions

The initiation and propagation of fractures can be captured using FDEM modelling technique. Understanding the path fractures join and create large and fragmented blocks depends on having the data of the newly-generated fractures and block information in each timestep, separately. Collecting the mesh elements data across timesteps is just the starting point in the fracture and block calculations workflow. Important aspects that should be considered during calculations: (1) the large amount of data can be collected for a given model per timestep and (2) the data might get much larger if the assigned mesh element size is small resulting in a large number of mesh elements (see Figure 5.2).

Techniques have been developed to extract newly-generated fracture lines from the simulation output using geometrical computations. The proposed technique (DEMFA) uses the mesh data generated during the modelling process. The Block Calculator technique (DEMBA) is then introduced by utilizing graph analysis. These methods provide information on the newly-generated blocks at each simulation timestep. The power of these methods would be as the initial step needed to relate the newly-generated fractures to the newly-generated blocks. The block tracking tree is introduced as a graphical representation of block growth across timesteps. The block fragmentation map was generated subsequently, indicating the number of block divisions throughout the simulation. This map provides a detailed analysis of the fragmented areas.

Results of 2D numerical analysis of a typical pillar model confirm that the definition of rock mass damage as a real-time analysis process can be achieved by using block formation. The developed approaches in extracting fracture lines and blocks provide us with the necessary information needed for further analysis of failure characterization. A sample pillar model was used to show the step-by-step application of the methods. The cumulative block distribution analysis of the simulation model is completed per timestep. The influence of brittle damage becomes more significant as the rock bridges connect and larger blocks form. Stress distribution and stress-strain fluctuations were investigated along with damage evolution and fracture propagation. The coalescence and further propagation of fractures were monitored in relation to each other. All the suggested approaches have been tested via a sample pillar model; however, they are well suited to analyze rock bridge problems in various engineering problems.

Chapter 6: Investigating the Factors Controlling Intact Rock Damage Mechanisms for Naturally Fractured Pillars

6.1 Introduction

Previous studies on the strength and deformability of pillars in hard-rock mines have demonstrated that the influence of natural fractures diminishes with increasing pillar width. Jointing conditions and fracture intensity/intersections play a critical role in the behaviour of slender pillars (width to height ratio less than 0.5). An important challenge is the characterization of the intact rock damage as a function of the in-situ fracture network and loading conditions. In this chapter, advanced pre- and post-processing algorithms introduced in chapter 4 and chapter 5 are used to address important limitations of empirical pillar formulae, and attempts are made to integrate brittle failure (i.e. rock bridge failure) and degree of natural rock mass blockiness using a combined discrete fracture network (DFN) and hybrid finite-discrete element method FDEM modelling approach. Pre-processing techniques can be used to determine parameters such as P_{20} (number of fractures per unit area), P_{21} (areal fracture intensity), intersection maps (e.g. Zhang et al., 1992; Xu et al., 2006), frequency orientation and persistence orientation plots. These are used to relate the failure process observed in the models to parameters directly associated with the natural fracture network (*static* DFN) prior to loading and with the progressive evolution of damage (intensity and density of the *dynamic* DFN) with increasing pillar load. The results show that pillars with different initial jointing conditions may yield similar strength but follow different stress paths. Detailed interpretation of the results has allowed the contribution of damage to block creation with increasing load to be highlighted.

6.2 Design of Hard-Rock Pillars

Rock pillars are designed to sustain the overburden load induced by the need to maximize the mine extraction ratio. The safety and economics of room and pillar mining is largely dependent on the room opening and pillars size, the mining depth and the characteristics of the pillar fracture network. Pillar stability analysis is consequently of major importance in underground mine design. The influence of scale on pillar strength has been investigated by Esterhuizen et al. (2011), showing that the strength of slender pillars (width-to-height ratio, W:H $\leq$ 0.5) may vary significantly compared to the strength of wider pillars (W:H >> 0.5), with important implications with respect to design and factor of safety calculations. The same authors described the process of brittle spalling and failure at low confinement in the behaviour and strength of slender pillars. One important conclusion of this earlier work is that the spalling limit for slender pillars may be relatively low, and close to the ultimate pillar strength, such that slender pillars may start undergoing overall failure when the induced stresses approach the spalling limit.

Pillar strength (i.e. ultimate load per cross section area of a pillar) is generally estimated using empirical formulae based on survey data from actual mining conditions (Martin and Maybee, 2000). However, empirical methods fail to directly consider brittle failure (spalling) and kinematic failure mechanisms. As a result, numerical models are well suited to study the mechanical behaviour of rock pillars, using either continuum or discontinuum methods. For example, (Fang and Harrison, 2002), and Martin and Maybee, (2000) have investigated brittle failure in pillars using a continuum approach. Nordlund et al. (1995) used a discrete element approach to study the mechanical behaviour of jointed pillars, while Elmo (2006), Tang and Kaiser (1998), Tang and Hudson (2010), Wang et al. (2011), Zhang (2014) and Grisi et al. (2016) have used numerical

codes that allow to explicitly model brittle fracture processes. Typical characteristics of stress-induced pillar failure include surface spalling, axial fracturing, “hour-glass” shape and necking. These failure types are typically observed in deep underground pillars (Zhang, 2014).

Elmo and Stead (2010), Esterhuizen (2006) and Esterhuizen et.al (2011) have shown that pillar strength may be greatly controlled by the existence of adversely inclined discontinuities. The impact of natural fractures would be greater for slender pillars, due to the possibility of a natural fracture transecting the full cross-sectional area of the pillar, or two or more fracture coalescing to form a failure plane transecting the pillar. This is shown graphically in Figure 6.1. An example of modelled combined brittle and kinematic failure mechanisms in pillars is shown in Figure 6.2.

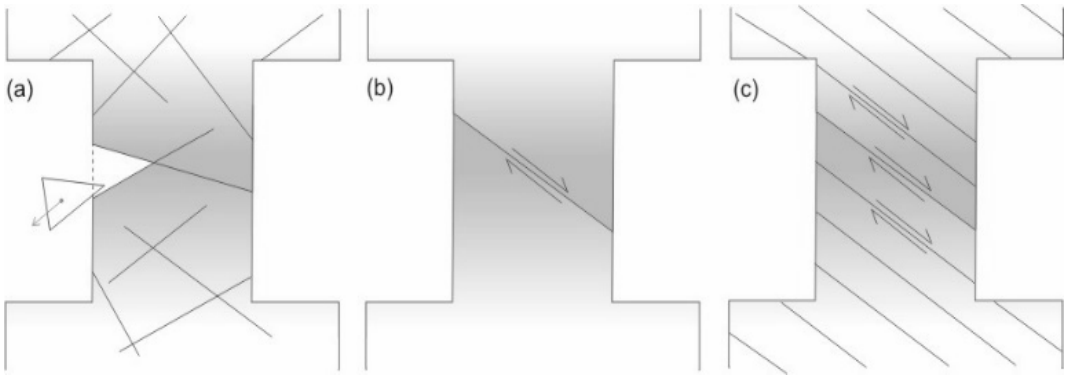

Figure 6.1. Typical failure mechanism of a naturally fractured pillar (after Nordlund et al., 1995 and Elmo and Stead, 2010). (a) occurrence of preformed blocks; (b) presence of inclined shear fractures and (c) transgressive fractures.

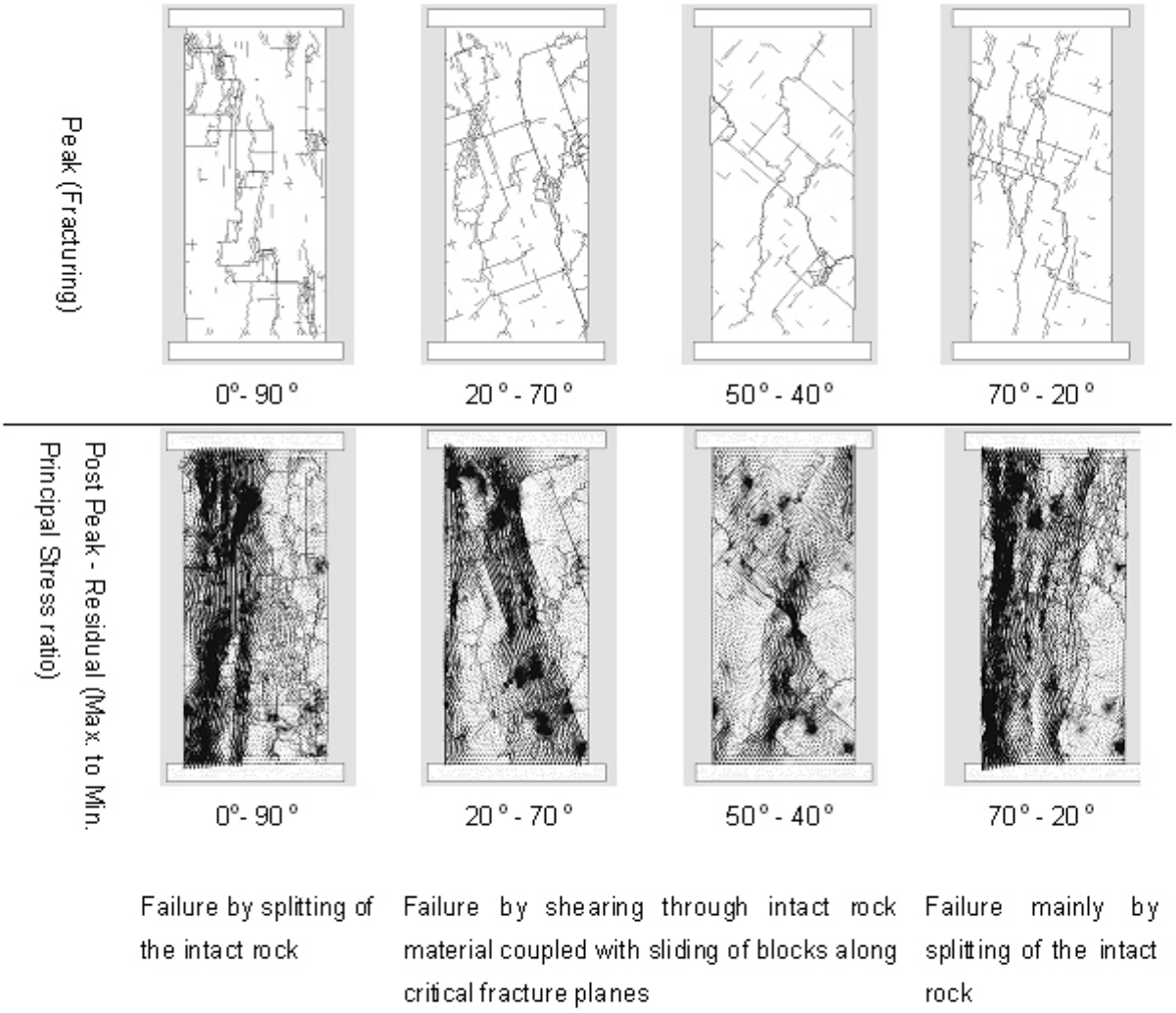

Figure 6.2. Examples of combined brittle-kinematic failure mechanisms in simulated slender pillars (modified from Elmo and Stead, 2010).

Using a FDEM approach, Elmo (2006) demonstrated that the strength of naturally fractured pillars could be related to areal fracture intensity (P_{21}, total length of fractures per sampling area) of the natural fracture network. In Elmo and Stead (2010), the authors introduced an *Anisotropy Index* for pillars, relating P_{21} and pillar dimensions, the Anisotropy Index being larger for slender pillars.

Ultimately, rock mass blockiness (degree of fully formed interlocking blocks) and intact rock bridges would be the two key parameters controlling the strength of hard pillars. Recently, Vazaios et al. (2018) have used a FDEM approach to study the relationship between rock mass blockiness, rock mass strength and deformability.

An alternative approach to quantify the rock mass structural character, as a combination of its degree of blockiness and the presence of rock bridges, has been proposed by Fadakar-A and Elmo (2018). The geometrical properties of the natural fracture network provide a basis to establish a rock mass structural quality index: for a given rock mass, the higher the rock mass degree of jointing and interlocking, the lower the number of rock bridges available, and the lower the degree of brittle failure that may associated with the rock mass failure process. However, when relating brittle failure processes to the failure of intact rock bridges, it is important to recognize that engineers and geoscientist still face several challenges related to the definition and measurement of the intact rock bridges (Elmo et al., 2018).

6.3 FDEM Analysis

6.3.1 Model Set Up and DFN Analysis

Using the same Middleton mine case study as Elmo (2006), large (14 m wide, 7 m high) 2D DFN sections were divided into smaller sections, resulting in sixteen different models with a W:H of 0.5, Figure 6.3. All the sections were used as part of the FDEM analysis, and in this section the results are provided with reference to the simulated pillar strength (Figure 6.5). In total sixteen models were considered in the analysis; the 2D DFN traces were generated using the DFN code FracMan (Golder, 2018; Dershowitz et al., 1998) and analyzed using the DFN Analysis methods

(shown in Table 6.1) introduced in Chapter 4. The traces were then imported, after being processed using the methods introduced in Chapter 4, DFN Cleaning, into the FDEM code ELFEN (Rockfield, 2014).

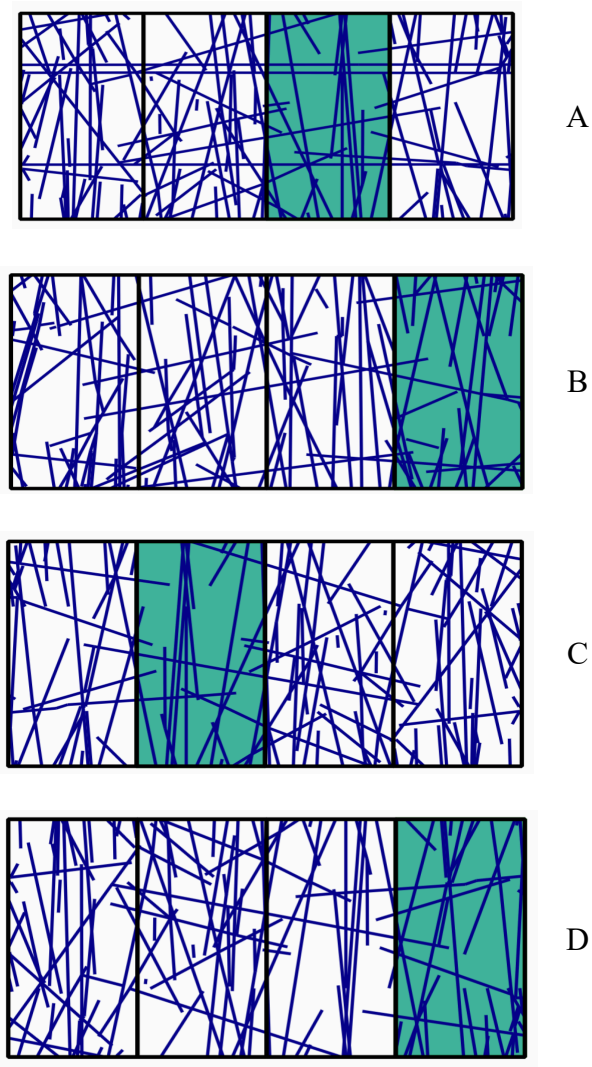

Figure 6.3. 14 m x 7 m DFN configurations used in the FDEM analysis. Green shows the selected Models A, B, C and D with four slender DFN sections each. DFN properties of sixteen DFN sections (Fracture count, fracture length, fracture intersection Count P_{20} and P_{21}) are presented in Table 6.1.

Table 6.1. DFN properties of all DFN Sections.

Model	Label	Fracture Length [72.46, 117.9]	Fracture Count [42, 98]	Intersection Count [60, 149]	P_{20} [1.7, 4]	P_{21} (m/m^2) [2.96, 4.91]
0	E	92.32	73	69	2.98	3.77
1	F	93.47	66	71	2.70	3.82
2	G	95.61	66	62	2.70	3.90
3	H	117.90	98	126	4.00	4.81
4	I	101.26	80	84	3.26	4.13
5	J	111.41	76	110	3.10	4.54
6*	A	82.90	49	111	2.00	3.38
7	K	89.47	68	76	3.65	3.65
8	L	101.26	80	85	3.26	3.9
9	M	94.68	55	89	2.24	3.86
10	N	93.53	47	60	2.40	3.30
11*	B	80.94	59	149	2.41	3.30
12	O	90.83	72	143	2.93	3.71
13	P	100.91	70	81	2.86	4.12
14*	C	72.46	42	77	1.70	2.96
15*	D	79.35	59	108	2.40	3.24

* Pillar sections shown in Figure. 6.3.

P_{21} is the ratio of total fracture length to sampling area [min, max] range in between brackets.

6.3.2 Material Properties and Boundary Conditions

The boundary conditions and material properties are shown in Figure 6.4 and Table 6.2, respectively similar to the model used in Chapter 4 and Chapter 5

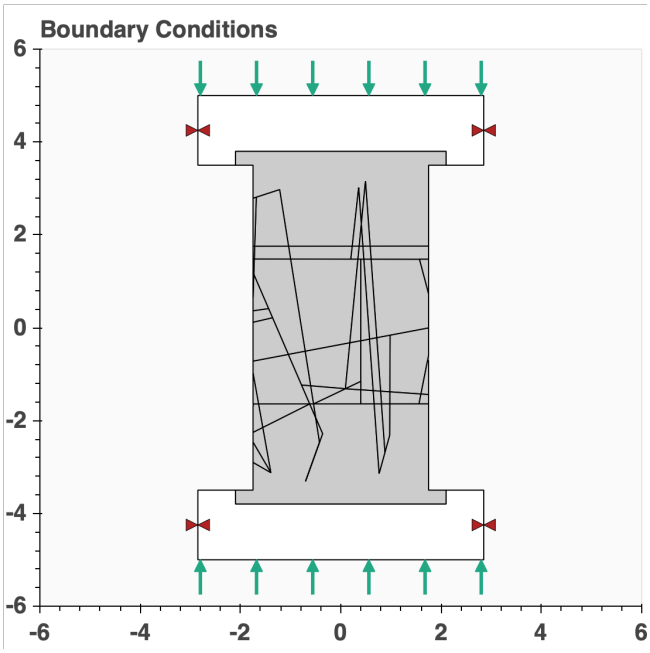

Figure 6.4. Boundary conditions of the pillar model.

Table 6.2. Material Properties

Rock Material Properties (Limestone)		**Unit**	**Value**
Intact Rock Material	Unified compressive strength, σ_{ci}	MPa	48
	Fracture energy, G_f	Jm^{-2}	19.47
	Tensile Strength, σ_t	MPa	3.84
	Young's Modulus, E	GPa	27.5
	Poisson's ratio, ν	-	0.23
	Density, ρ	kgm^{-3}	2600
	Internal Cohesion, c_i	MPa	9
	Internal Friction, ϕ_f	degrees	40
Platen material properties and discrete (contact) parameters		**Unit**	**Value**
Rock Fracture	Surface Cohesion, c_f	MPa	48
	Surface Friction, $\emptyset_f$	Jm^{-2}	19.47
	Normal Stiffness (Normal Penalty) P_n	MPa	3.84
	Shear Stiffness (Shear Penalty) P_t	GPa	27.5
Platen Properties	Young's Modulus of Platen	GPa	200
	Poisson's ratio of Platen	kgm^{-3}	0.3
	Density of Platen	MPa	7860
Rock-Platen Contacts	Rock/platen cohesion	MPa	0
	Rock/Platen friction	degrees	3
	Rock/platen normal stiffness (Normal Penalty P_n)	GPa/m	27
	Rock/platen shear stiffness (Shear Penalty P_t)	GPa/m	2.7

6.3.3 Simulation Results

Figure 6.4 shows the stress-strain plots associated with the sixteen models labeled as A-P in Figure 6.3. Four models are selected from sixteen simulated sections, based on 1) Similarity in P_{21} and 2) The highest difference in peak strength values.

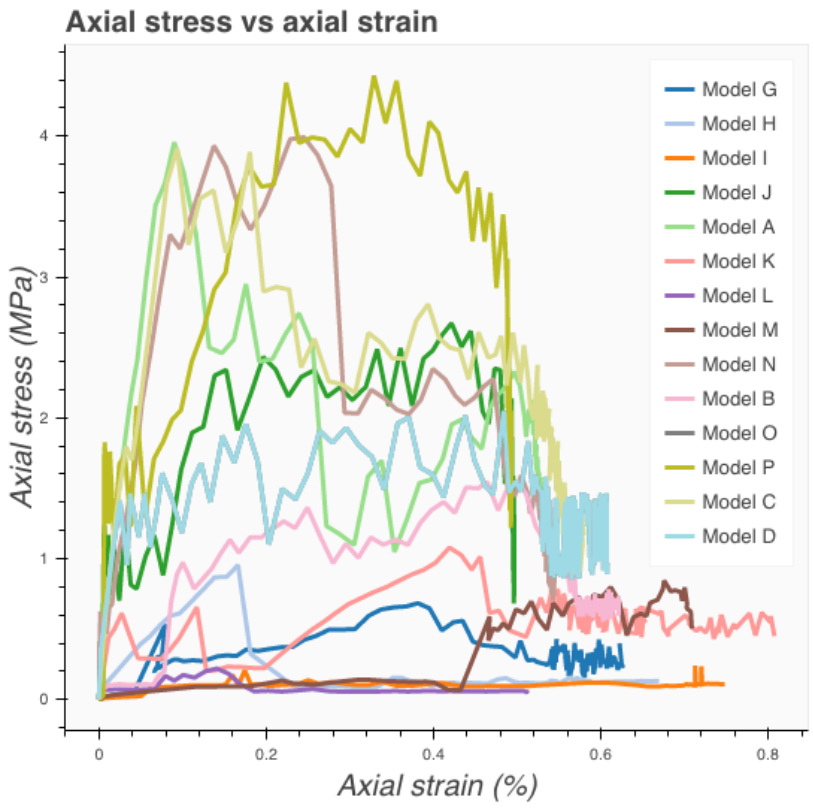

Figure 6.5. Stress-Strain plots for all models.

When the properties are analyzed with respect to the DFN listed in Table 6.1, the values of P_{20} range from 1.67 to 3.89, for modelled pillar strength in the range of 0.1 to 3.5 MPa (all models). Figure 6.6.a shows that there is no apparent relationship between P_{20} and the modelled pillar strength. This indicates that the number of fractures alone cannot be used to characterize pillar strength. P_{21}, ranges from 2.87 to 4.75 $^{m}/_{m^2}$, Figure 6.6.b. At first the results do not show a clear correlation between pillar strength and P_{21}; however, a correlation is shown to exist when the results are superimposed on earlier results included in Elmo (2006), Figure 6.6.c.

The numbers of intersection counts are plotted with respect to pillar strength, Figure 6.6.d. Once again, there is no apparent relationship between fracture intersection counts and pillar strength for

the simulated pillars, as a further demonstration that the characterization of pillar strength would require a combination of various DFN properties, as initially discussed in Elmo (2006). It is also important to consider how the fracture data relate spatially to the fracture intersection counts; this aspect is the focus of the following section, which draws from the discussion and numerical analysis methods introduced earlier in Chapter 4.

To focus our analysis, four models are selected based on the axial stress - P_{21} plot shown in Figure 6.6.b. P_{21} ranges from 3-3.5 $^{m}/_{m^2}$ while maximum strength ranges from 1-4 MPa. The objective of this Chapter is to analyze and interpret the results in the pre-and post-stages to understand the variations in maximum strengths associated with similar P_{21} values.

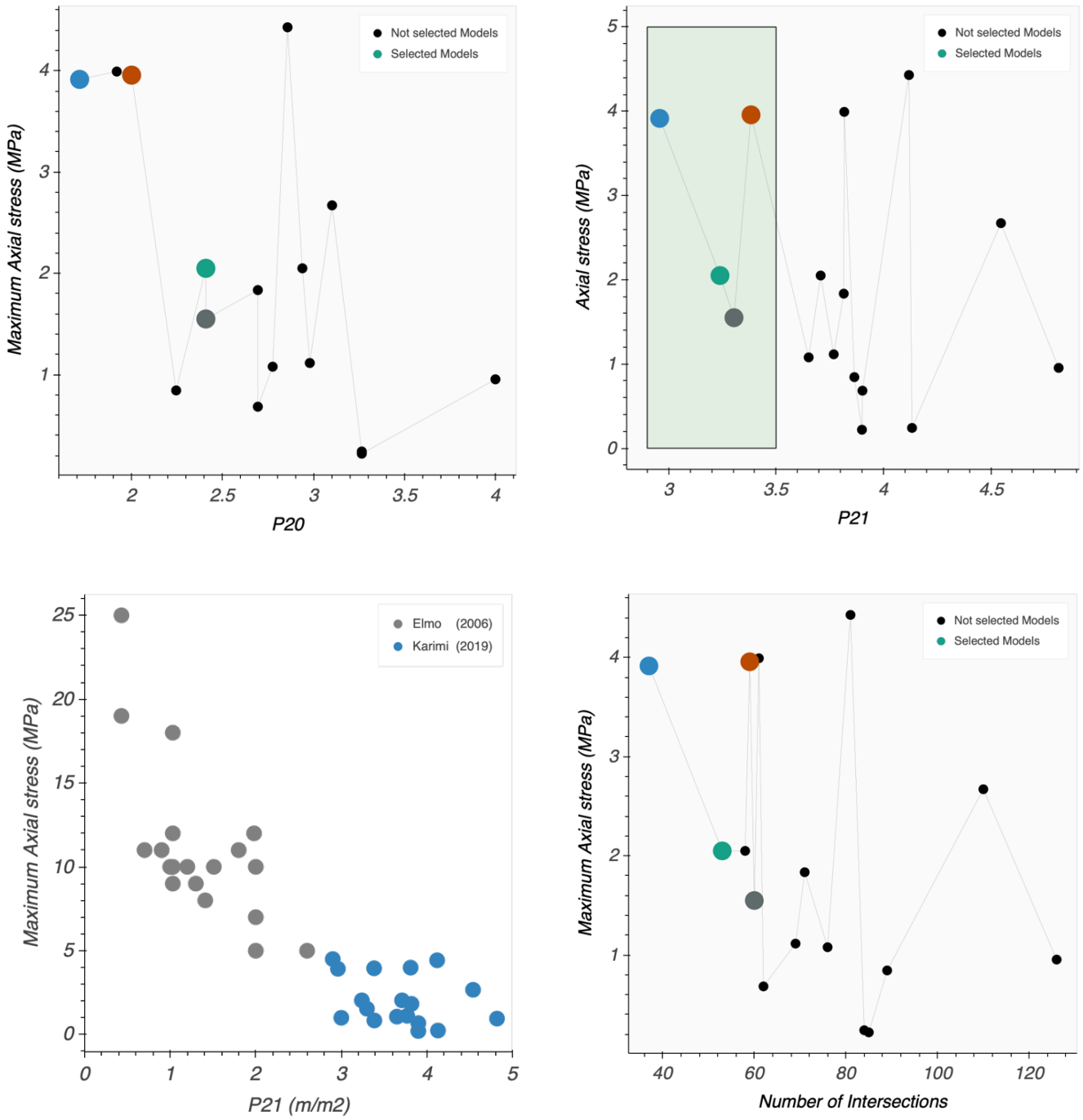

Figure 6.6. a) Plot of peak axial stress vs. P_{20} for all the models. b) Peak axial stress vs P_{21} (m/m^2). Green box indicates the selected A, B, C and D models based on Section 0. c) Correlation between pillar strength and P_{21} for slender pillars at Middleton mine (data added to Elmo, 2006). d) Plot of peak axial stress vs. I_{20}.

6.4 In-depth Analysis of Selected Models

This section considers four selected models (the selection procedure shown in 0), as an example of the level of in-depth analysis that would be possible to perform when integrating and processing the results of the DFN and FDEM models. The properties of the selected DFN sections are included in Table 6.3. Using the same approach as Zhanga et al. (1992), Figure 6.7 shows the fracture traces and the associated intersections for the four selected models. These are then contoured (using the KDE approach discussed in Chapter 4) in Figure 6.8 to show the corresponding fracture intersection density maps. Despite the very similar areal intensity P_{21}, the four sections show clear differences in the spatial location of the fracture intersections: Model A shows high fracture intersection density on the right side of the pillar and along the vertical axis; Model B shows a relatively high fracture intersection density in the very top portion of the pillar; Model C has almost half the number of fracture intersections compared to Model B, with a concentration at the base of the pillar. For Section D, fracture intersections appear to be located at the top and in the lower right corner.

Table 6.3. DFN properties of Selected DFN Sections.

Label	Fracture Length (m)	Fracture Count	Fracture Intersection Count	P_{20}	P_{21} ($1/m$)
A	82.90	49	111	2.0	3.38
B	80.94	59	149	2.4	3.30
C	72.46	42	77	1.7	2.96
D	79.35	59	108	2.4	3.24

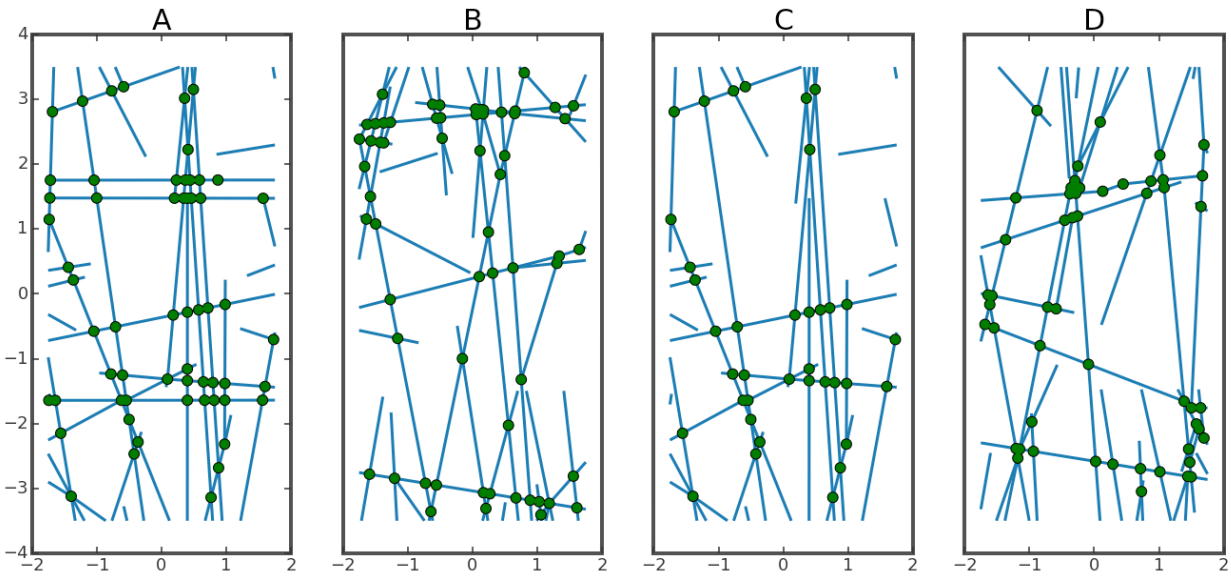

Figure 6.7. DFN sections for Models A, B, C and D. Fracture lines shown in blue and fracture intersection points in green.

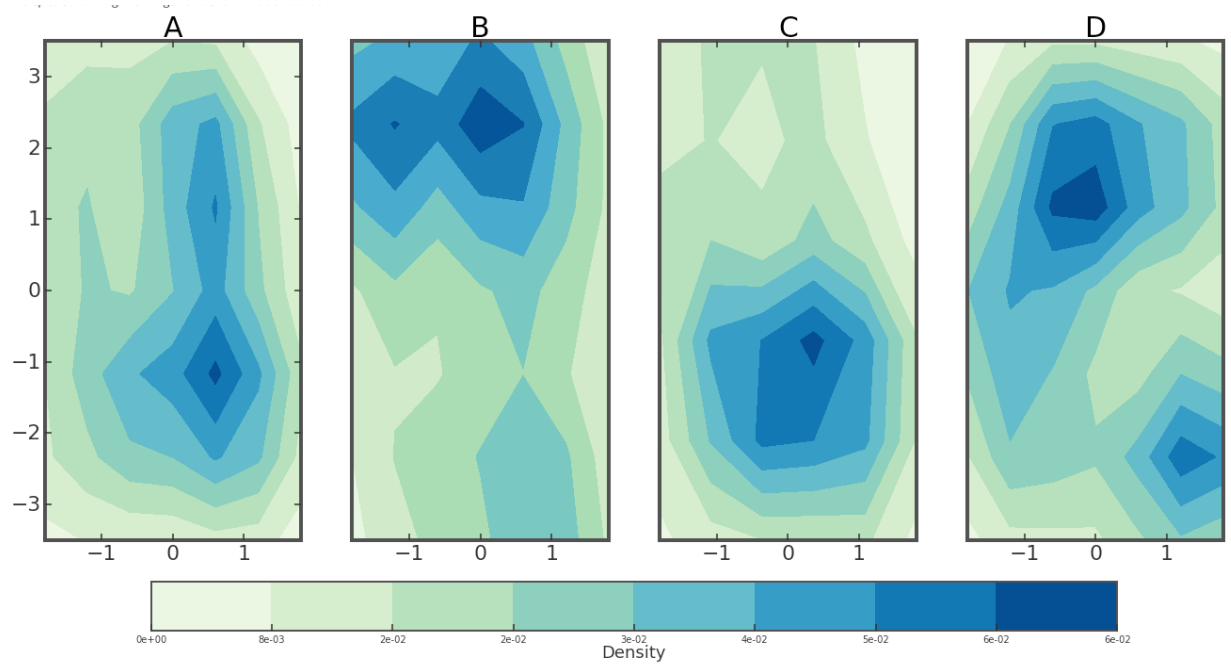

Figure 6.8. Fracture intersection density map for models A, B, C and D.

Figure 6.9 shows the distribution of fracture intersections with respect to their (x, y) coordinates. According to Figure 6.9 (A: red) the fracture intersection density follows a bimodal distribution in both the X and Y directions. Section B, Figure 6.9 (B: black), contains the highest concentration of fracture intersection density on very top portion of the section and the fracture intersection density follows a bimodal distribution with peak separation of 5 meters. Section C, Figure 6.9 (C: blue) indicates the vertical lines on the right side (like A), however it does not contain horizontal lines. The fracture intersection density map indicates a normal distribution in the X direction and follows a bimodal distribution in the Y direction with fracture concentration in the bottom of the section from -2 to 0 meters. The fracture density of section D, Figure 6.9 (D: green) follows a bimodal distribution in both the X and Y directions.

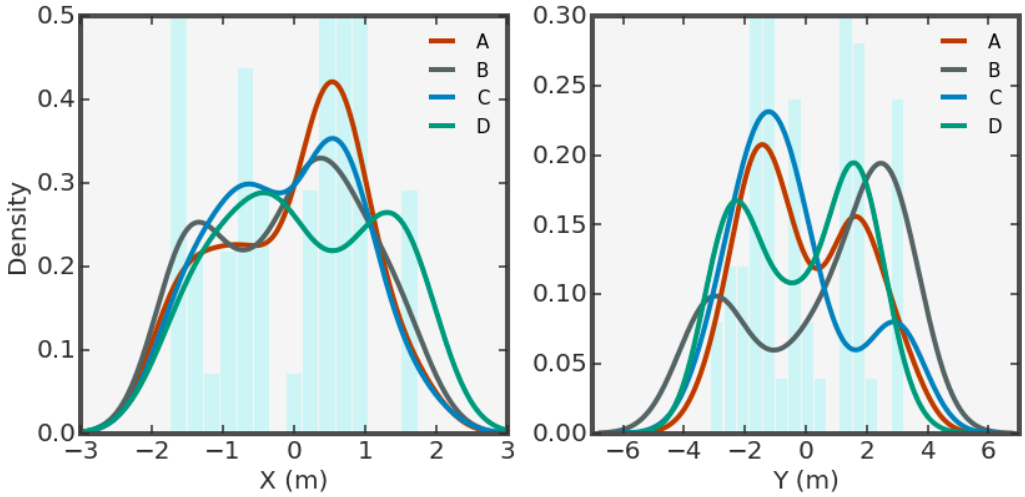

Figure 6.9. Fracture intersection density distribution along the a) X axis and b) Y axis.

With respect to the dip of the fractures, Figure 6.10, all sections show similar percentage of sub-vertical fractures (dip angle between 80 and 100 degrees). Note that the angle is measured counter clockwise from the horizontal, in which case a dip of 100 degrees would represent a fracture with true dip of 80 degrees dipping towards the right side of the pillar. Model A contains about 75% sub-horizontal (0 and 20 degrees), and 40% (160-180 degrees). Models B is almost the mirror image of Section A, while Models C and D have the lowest number of sub-horizontal features.

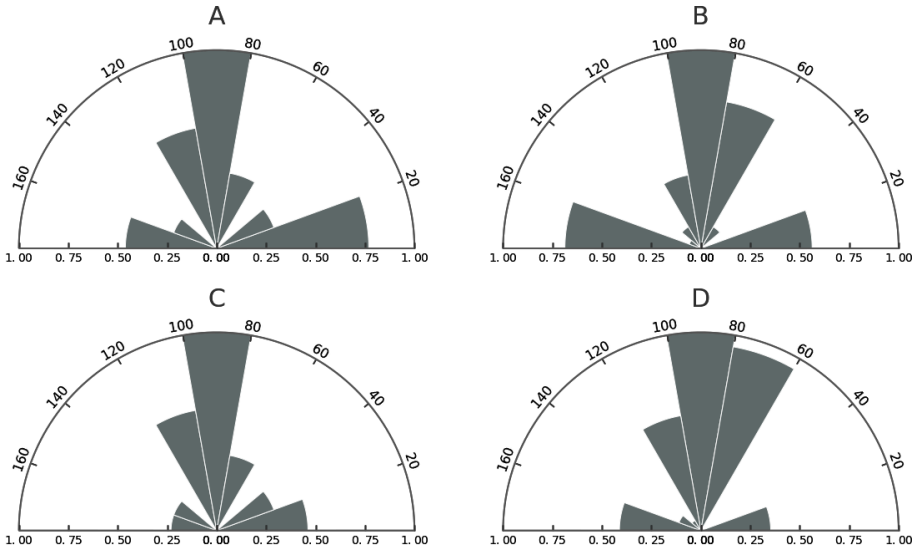

Figure 6.10. Fracture orientation Frequency for models A, B, C and D, respectively.

When considering the dip of the fractures in relation to their persistence, the longest fractures have a dip between 80 and 100 degrees, Figure 6.11. Models B and D have also some longer fractures with a dip of 60 to 80 degrees.

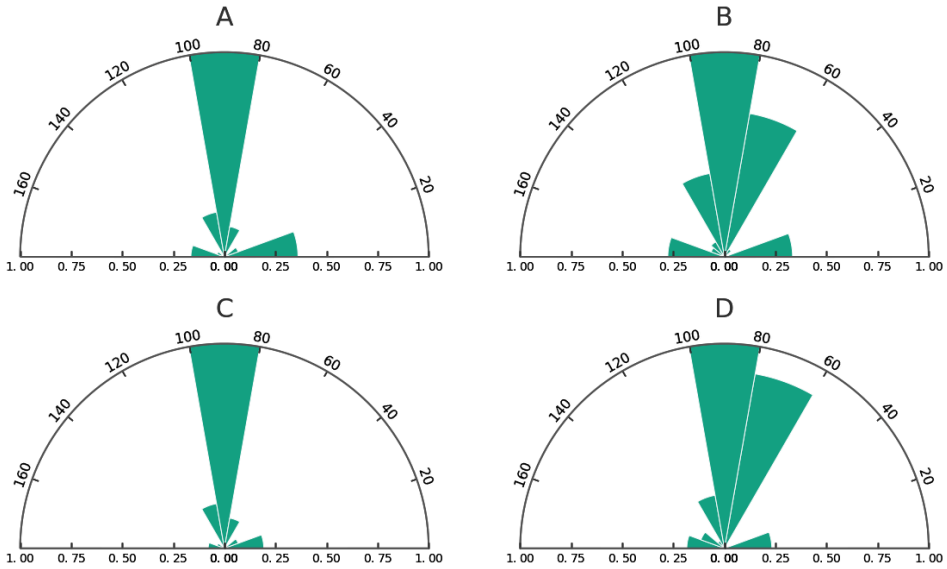

Figure 6.11. Fracture persistence according to orientation for models A, B, C and D, respectively.

6.5 Stress-Strain Results for the Selected Models

The stress-strain plots for Models A, B, C and D are shown in Figure 6.12. Models A and C have the highest peak strength, while Sections B and D have the lowest. These results could be preliminary interpreted considering that Sections A and C have similar fracture intersection density maps, while Model B has the largest number of fractures and the largest number of fracture intersections (see Figure 6.8).

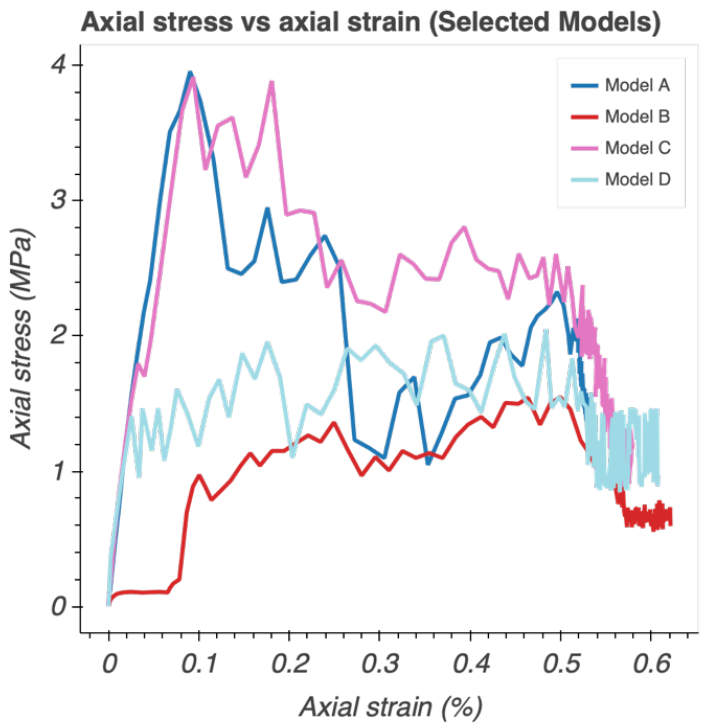

Figure 6.12. Stress-Strain plots for Models A, B, C and D.

6.6 Analysis of rock mass blockiness

To further characterize the behaviour of the selected four pillar models, new advanced methods were developed and applied to quantify the degree of damage (intact rock fracturing) and the progressive formation of new blocks, as well as the progressive breaking apart of existing blocks. For each pillar model, the average block size distribution (BSD) curves (m^2due to 2D nature of the models) have been determined for timesteps that correspond to: i) 0 MPa stress (initial conditions); ii) 50% of the modelled peak stress; and iii) peak stress. For these time steps, the 10^{th}, 50^{th} and 90^{th} percentile passing sizes are then measured. The results are presented in

 for Models A, B, C, and D, respectively.

Table 6.4. Summary of B_{10}, B_{50} and B_{90} for models A, B, C and D. The values are shown for t_0, $t_{50\%peak}$ and t_{peak}.

Model	B_{10} (%)			B_{50} (%)			B_{90} (%)		
	Initial	50% σ_{peak}	σ_{peak}	Initial	50% σ_{peak}	σ_{peak}	Initial	50% σ_{peak}	σ_{peak}
A	0.12	0.19	0.16	2.06	1.63	1.28	6.68	2.91	2.58
B	0.34	0.26	0.12	2.51	2.46	1.25	3.73	3.73	2.51
C	0.38	0.23	0.13	5.56	1.95	1.23	10.15	4.17	3.16
D	0.47	0.27	0.05	3.23	2.02	0.91	6.57	4.02	2.35

Figure 6.14 to Figure 6.17 show the differences in the 10th, 50th and 90th percentile passing size between initial and peak stress (B_{10}, B_{50} and B_{90} percent). For ease of comparison, B_{10}, B_{50} and B_{90} percent passing sizes are summarized in Table 6.4.

Changes in B_{10}, B_{50}, B_{90} are indicative of the type of failure the pillars are undergoing. In principle, the larger the amount of brittle failure and accumulated intact rock damage, the larger the shift between BSD curves (for a given model). A shift in B_{90}, and/or B_{50}, without a shift in B_{10} indicates a lack of brittle failure. It is argued that for a model with an embedded DFN that already has fully formed non-tapered finite blocks (Type I and II in Figure 6.13), changes in the BSD would be minimal, depending on whether these non-tapered blocks were to be potential key blocks or key blocks. The definition of non-tapered and tapered blocks herein is according to that given by block theory (Goodman and Shi, 1985), see also Figure 6.13. Note that the introduced block analysis is only capable of tracking block size and number of facets; the interpretation of which block would be tapered (Type IV in Figure 6.13) and which one would be non-tapered (Type

I and II in Figure 6.13) is based on qualitative observations. However, the following sections introduce quantitative algorithms, e.g., displacement, block detachment maps and fragmentation block maps, for better characterization of the failure mechanisms.

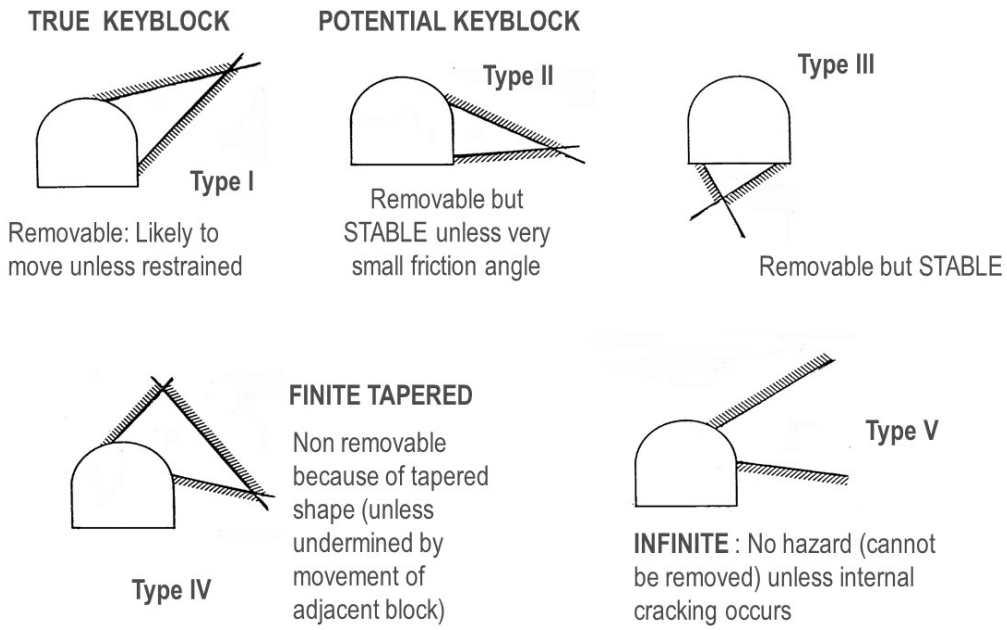

Figure 6.13. Definitions of blocks types in accordance with block theory, (Goodman and Shi, 1985).

One must account for the fact that failure in the pillar models would not necessarily be symmetrical. For instance, Models A and C show a relatively smaller increase in the B_{10} passing size, with most of the strain simulated in the models resulting in the formation of relatively large tapered blocks (nonremovable blocks). Conversely, relatively large non-tapered finite blocks are created for Models B and D as the strain (and stress) increases. Interestingly, Model D shows a mixed type of failure mechanism, more brittle on the left side (large number of small size blocks) and more structurally controlled on the right side with kinematic release of large blocks. In this

context, the results must be interpreted not just with reference to the BSD curves, but also with respect to accumulated damage (D_{21}) and axial strain, as shown in Figure 6.18 and Figure 6.19.

For example, in Model A, damage accumulates from the onset and grows rapidly. The accumulating damage is "*consumed*" to break existing large blocks into smaller tapered blocks rather than to nucleate isolated fractures (compare Figure 6.14 and Figure 6.19).

For model C, damage also accumulates quite rapidly, but in this instance, most of the damage is consumed in breaking-up the top and bottom portions of the pillar (infinite blocks) into smaller tapered blocks. Damage is also consumed to create spalling conditions in the right flank of the pillar (Figure 6.16 and Figure 6.19).

For model B (Figure 6.15 and Figure 6.19), damage starts accumulating when axial strain has reached 0.1% of the initial pillar height. Therefore, most of the failure up to this point would be structurally controlled (note the buckling mechanism on the right flank).

Similarly, Model D does not show significant damage being accumulated until 0.14% axial strain. Failure is mostly controlled by the rotation/displacement of large key blocks on the right flank of the pillar (Figure 6.17 and Figure 6.19). These findings are further validated by considering the relationship between damage D_{21} and the cumulative number of blocks being created, Figure 6.19.b. Models A and C are stronger than Models B and D because: i) more damage is required to fracture the pillar such that fully formed blocks are created; and ii) those fully formed blocks are tapered (non-removable) blocks, which in turn result in the concentration of stresses and the creation of additional damage until the pillar eventually fails.

Models A and C with similar slope changes indicate the requirement for additional newly-generated fractures to result in block formation. As seen in the stress-strain plots of these two models (Figure 6.12), they are both associated with higher peak strength and lower strain. This confirms that the DFN configuration is responsible for the higher peak strength of the rock mass structure relative to models B and D. Model D shows the highest block count-D_{21} changes in slope (Figure 103.b- green curve). It is observed that initially there is rapid increase in the number of blocks formed as the damage increases; there is a point where the damage increases, but no block is generated (constant portion of the green plot), then the slope of the plots starts to change again, and the new blocks are forming. Model B, with the smallest number of blocks of all shows the most structurally related behaviour of all the models.

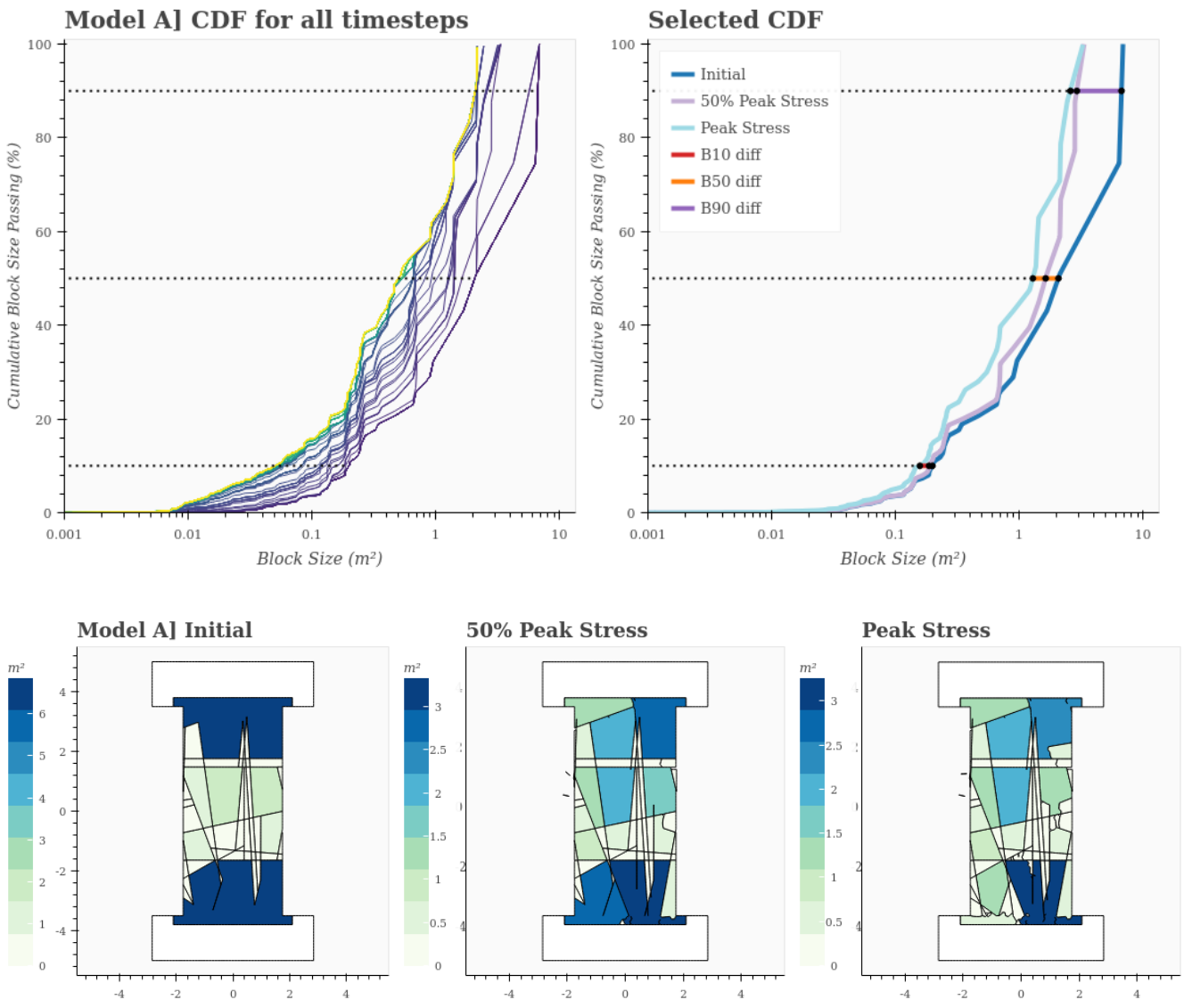

Figure 6.14. Blocks size analysis for Model A.

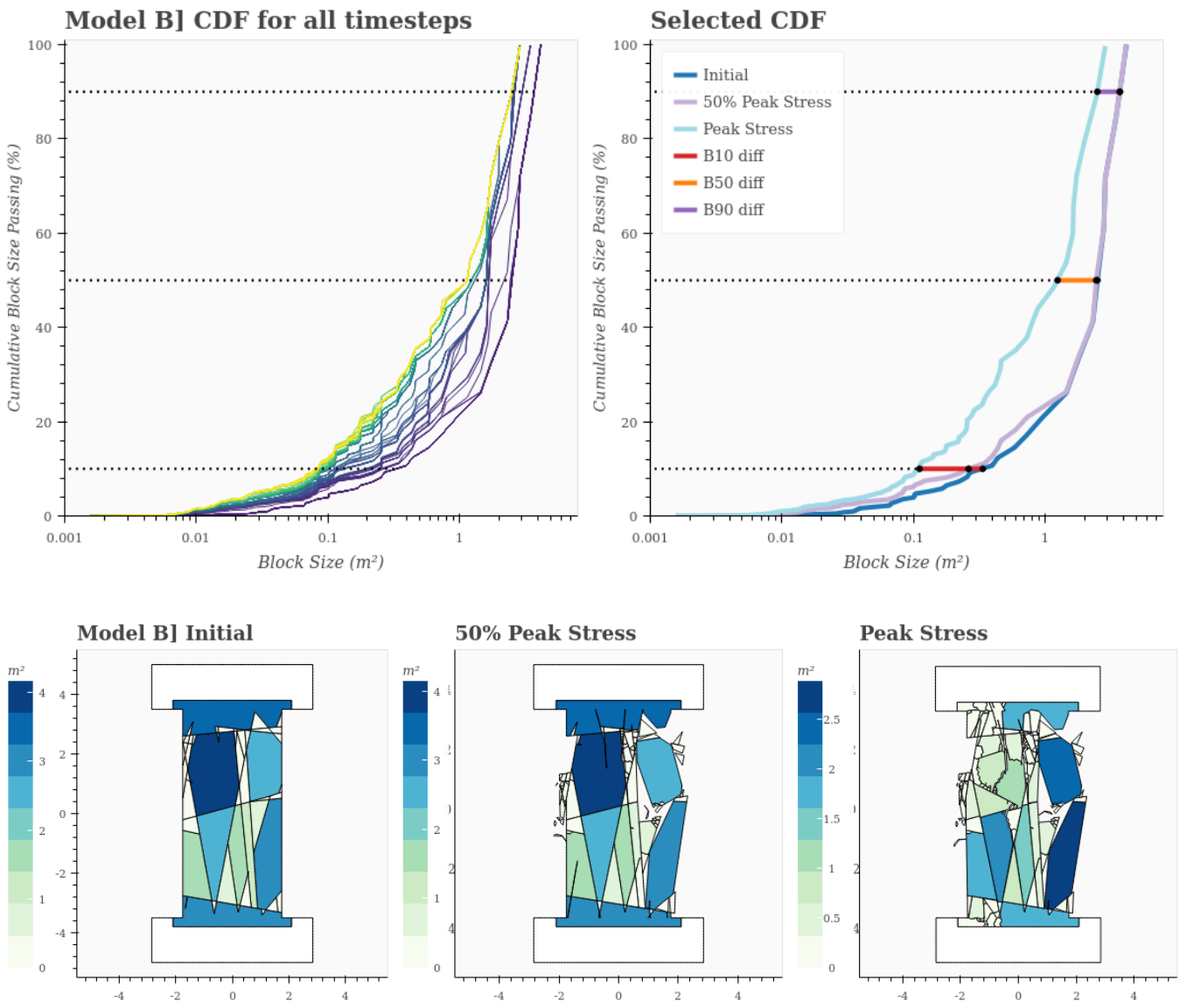

Figure 6.15. Blocks size analysis for Model B.

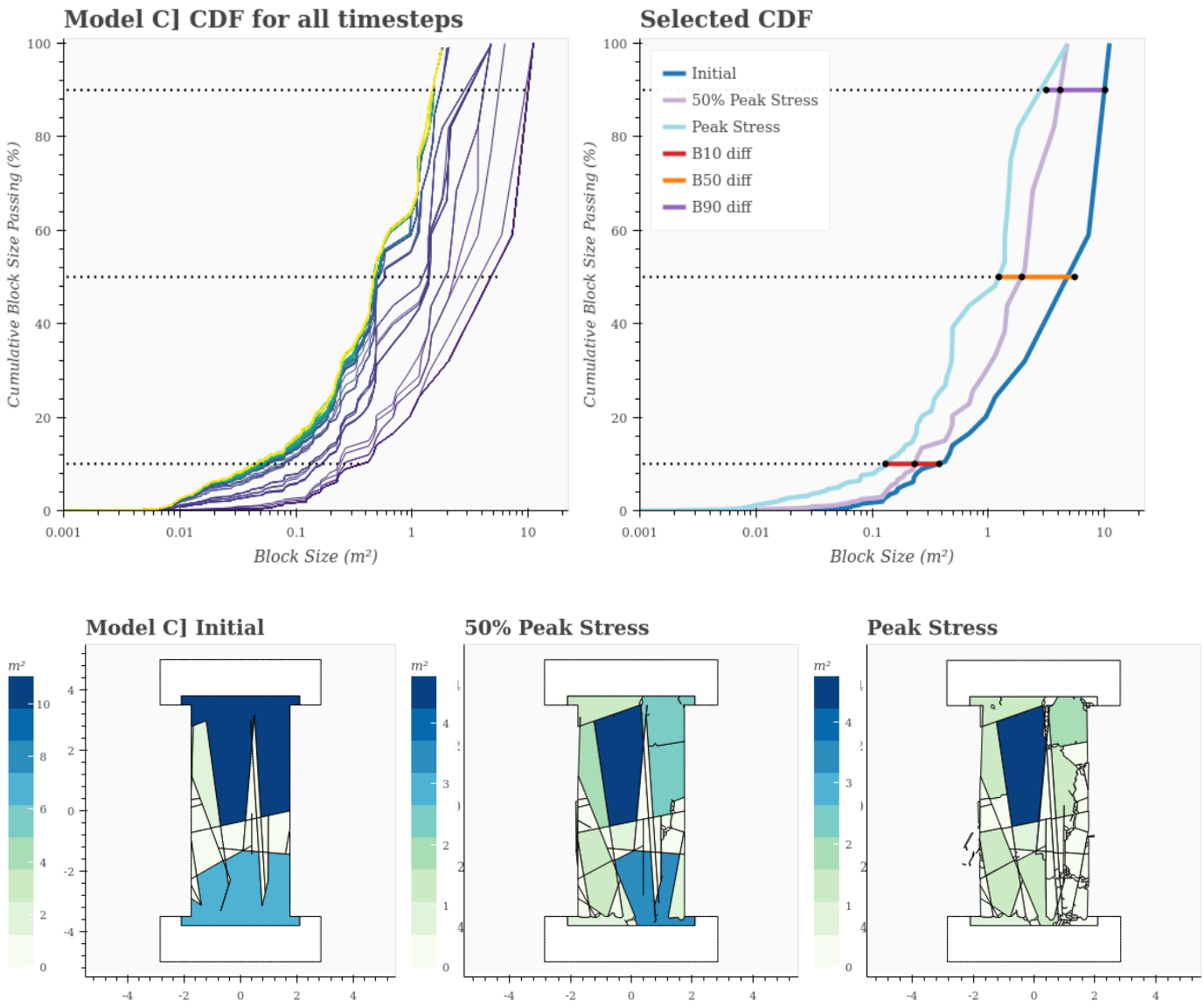

Figure 6.16. Blocks size analysis for Model C.

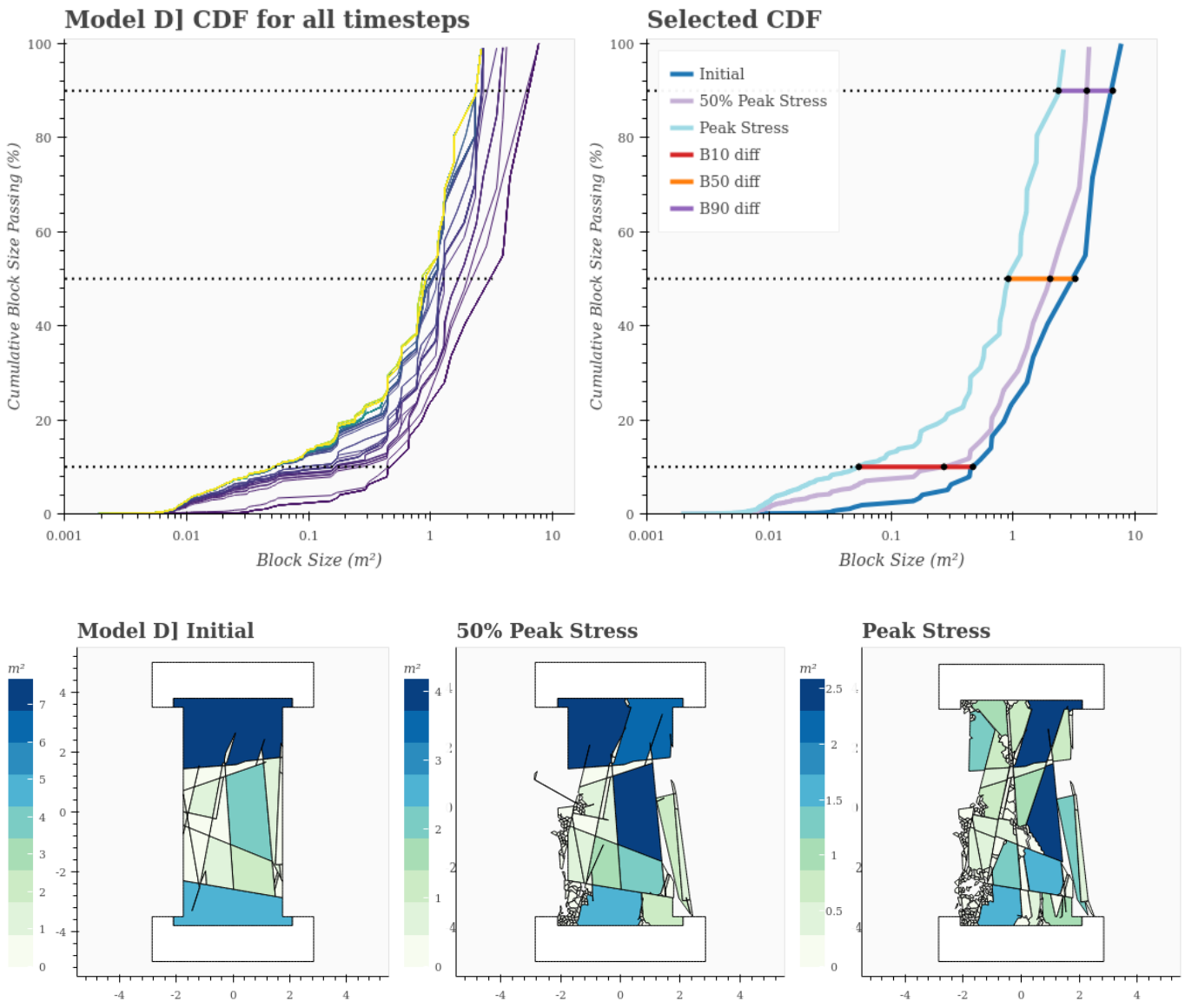

Figure 6.17. Blocks size analysis for Model D.

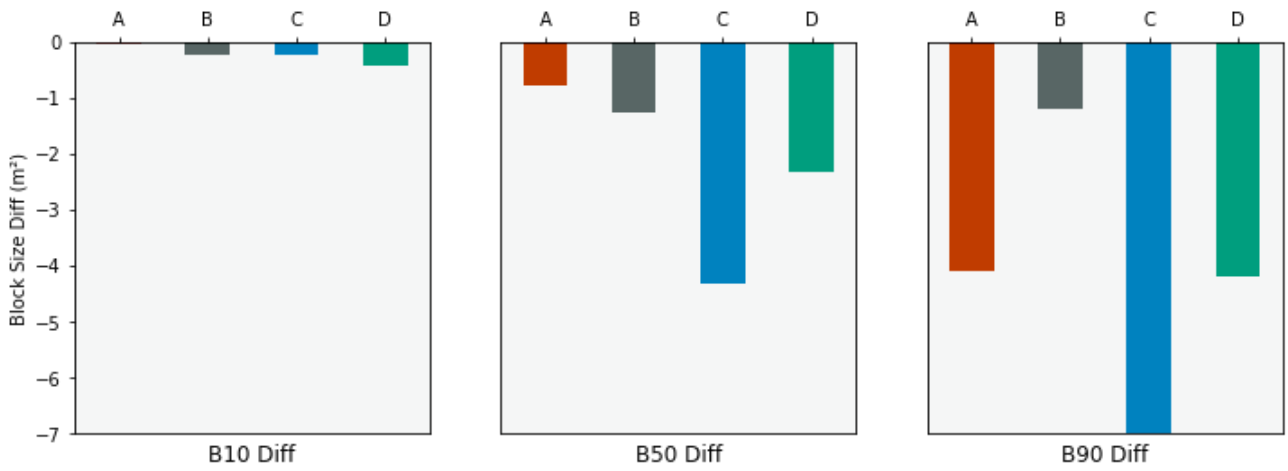

Figure 6.18. Difference in block size passing (10, 50 and 90%) between initial and peak stress for models A, B, C and D.

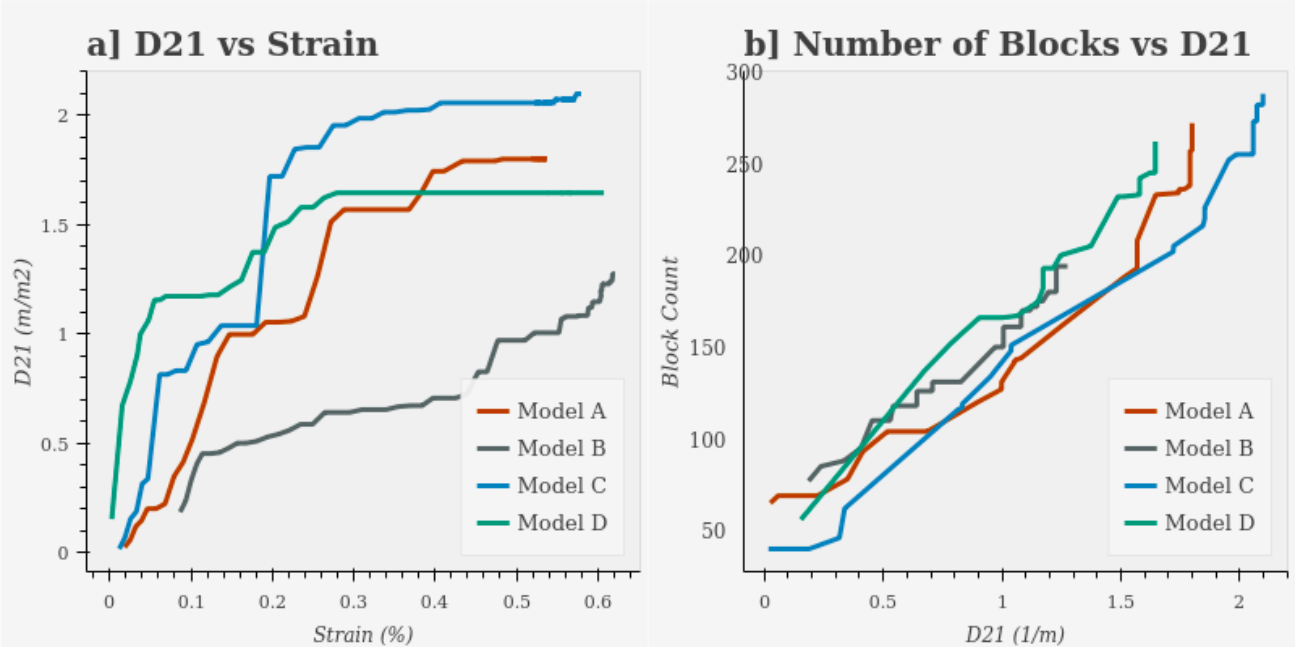

Figure 6.19. a) Pillar damage vs strain. b) Number of blocks vs damage for models A, B, C and D.

6.7 Block Detachment Maps and Study of Failure Mechanisms

In the previous section, studying damage and block formation proved to be an effective method to better understand how new cracks coalescence and potentially create new blocks. An attempt was made to answer the question as to whether the newly-generated cracks connect to create blocks, or whether the newly-generated blocks are solely dependent on the pre-existing fracture configuration and independent of rock bridge damage. The interpretation was based on block visualization, CDF (Cumulative Distribution Function), Passing %, Damage and Strain analyses along with the block count. However, this approach suffers from not categorizing the blocks with respect to their kinematic characteristics.

To better address this problem, block detachment maps are introduced. The block detachment map for a given timestep is computed by first computing all the blocks for that timestep, as described in Chapter 5. The geometry of these blocks is then subtracted from the rock. The remaining space in the rock is the detachment. Note the detachment is computed through geometrical analysis, and not using image analysis of the visual model simulation output. This geometrical detachment area is then quantified per timestep. For illustration, detachment area is viewed as an orange colour, which serves to highlight movement and fracture opening. The combined presence of damage, in the form of new fractures (D_{21} parameter), and newly-generated blocks in areas where detachment has occurred is taken to indicate the presence of Type I and Type II blocks. However, the absence of detachment may indicate the presence of Type II and Type IV blocks. Figure 6.20 shows the detachment maps for the four selected models that are part of the current study.

According to the simulation results in Figure 6.20, Model A shows almost no blocks detachment, despite new fractures being generated. Failure of intact rock bridges results in the formation of blocks elongated in a sub-vertical direction; this geometry would be equivalent to that of a rock

sample with vertical fractures being loaded parallel to the direction of the fractures, which would explain the relatively stronger response of Model A compared to the rest of the models (B, C and D). Model B, on the contrary, shows significant kinematic failure along the right side of the pillar. The absence of newly created blocks indicates that failure in this case is largely structurally controlled, along pre-existing (Type I) blocks. The behaviour of Model C is very similar to Model A; the higher fracture intersection density and the spatial location of the pre-existing cracks may explain why Model C is slightly weaker than Model A. Model D shows a combination of failure through intact rock (high degree of damage) and block kinematics, whereby blocks were mostly already fully formed at the beginning of the simulation.

The results support the conclusions of Elmo et al. (2018), who suggested that both block forming potential and kinematics are instrumental in the definition of rock bridges in terms of block stability. Whereas the proposed detachment computation provides a reasonable estimate to quantify structural damage, there are two technical limitations that must be addressed when considering developing a quantitative indicator that combines both intact rock damage and blocks kinematics: 1) accuracy; and 2) computing the block contribution to structural damage, and relating them to initial blocks. With respect to (1), a block might have fallen, at a given time step, outside of the rock boundary used to define detachment, or a block might have fallen inside the space created by other dilating blocks. Falling inside the space created by other detaching blocks would not contribute to the calculated detachment area as it should be. In terms of block identification and relationship to initial blocks (2), the proposed method needs to be modified to consider which specific blocks contributed to the structural damage, effectively obtaining their size, shape, and relevant block information. In addition, we need to be able to find the relationship

between the structure damage blocks and their parent blocks at the initial timestep, to enable further analysis. The following sections propose a solution that solves these limitations.

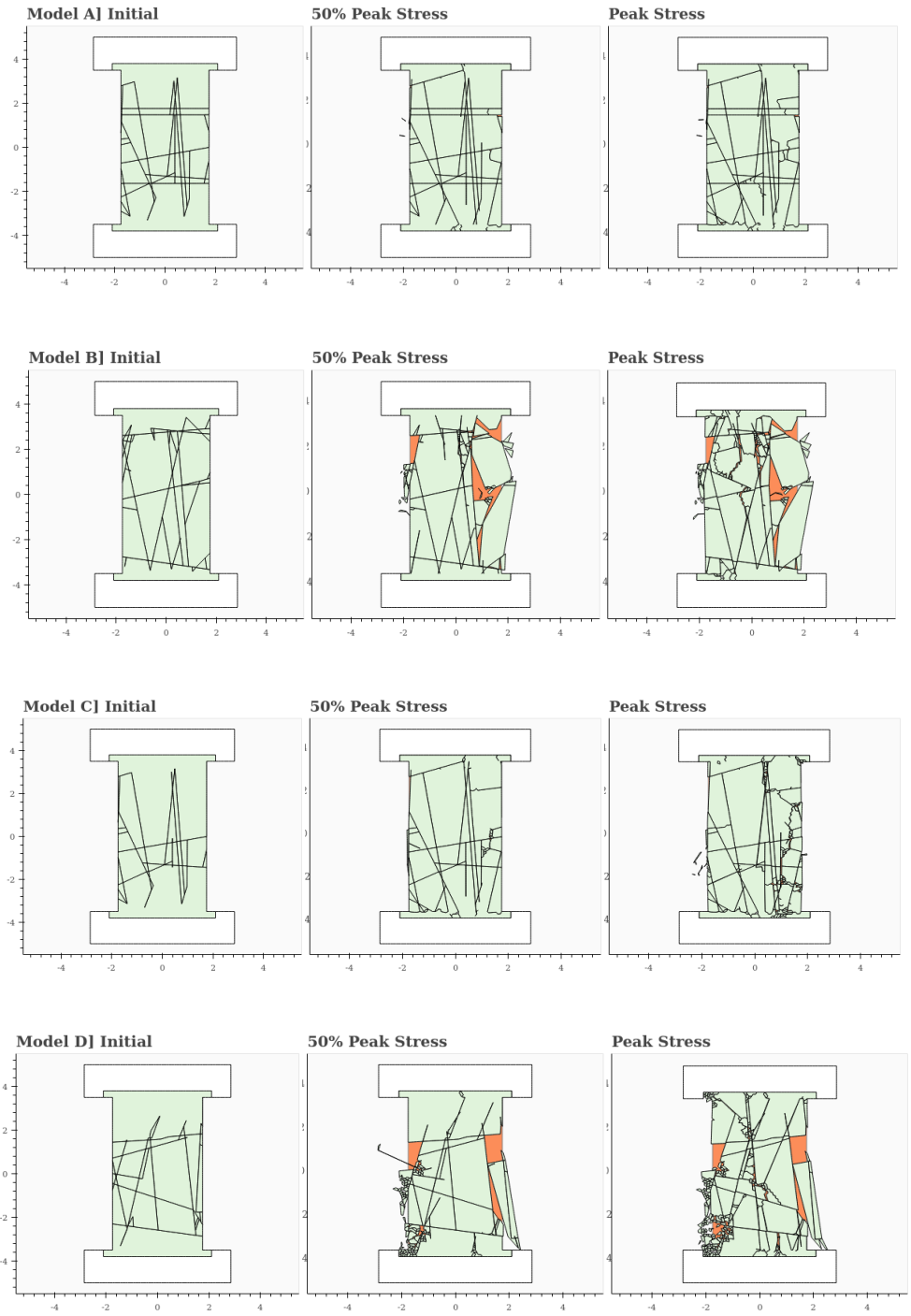

Figure 6.20. Detachment maps at initial stage, 50% peak stress and peak stress for: Model A, Model B, Model C and Model D.

6.8 Mapping Block Displacement at Peak Stress in relation to Initial Block Geometry

The previous section described the limitations of the detachment computation method. This section provides an initial step in solving these problems, by using block displacement. First, the block displacement from the initial timestep to the peak stress timestep needs to be computed. Block displacement is computed by aggregating the displacement of the elements making up each block. The simulation output provides the location of each element. This information is used to compare the original location of each element at the peak stress, against the location at the initial timestep, therefore capturing the displacement of each element. The Block Calculator, described in Chapter 5, computed what groups of elements formed blocks; therefore, it also contained the information of which block each element belonged to. Displacement of all elements in each block is averaged, effectively computing the block displacement.

Figure 6.21 shows the displacement values associated with each block at the peak stress.

Second, we need to be able to relate the displacement of blocks at the peak stress timestep, to their parent blocks at the initial timestep. Chapter 5 introduced the Block Tracking Tree, which tracks block formation across timesteps. This tracking tree provides the necessary information to relate blocks at peak stress timestep to their parent blocks at the initial timestep. The remaining step is to map the displacement of these blocks at the peak stress timestep to their parent blocks at the initial timestep. The computed displacement contribution of each block at the initial timestep is the average of the displacement of its children blocks at the peak stress timestep, weighted by block size.

Figure 6.21 demonstrates how the displacement for each model at peak stress that are normalized to the overall surface area (left plots) and mapped to their initial timesteps (right plots).

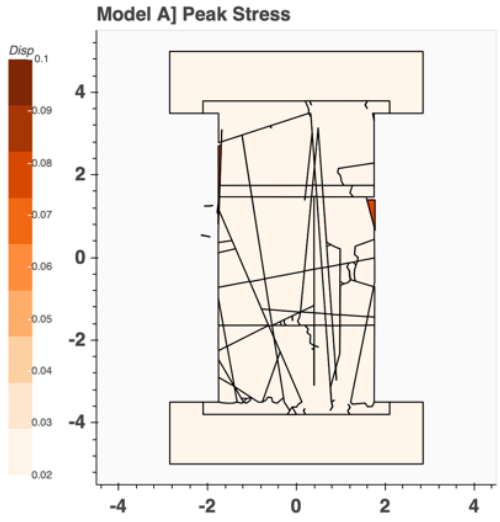

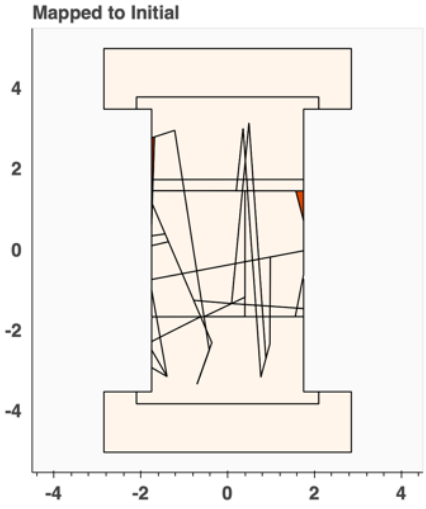

Model A

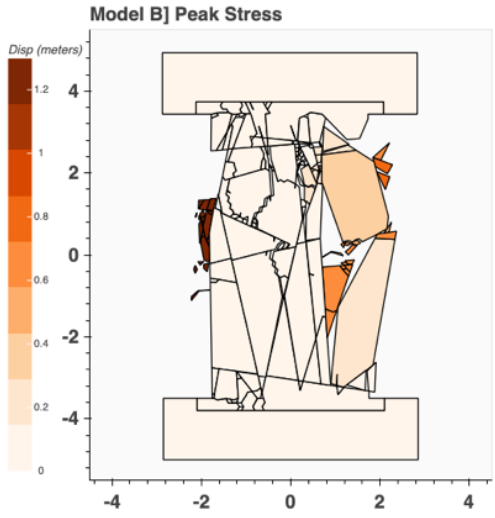

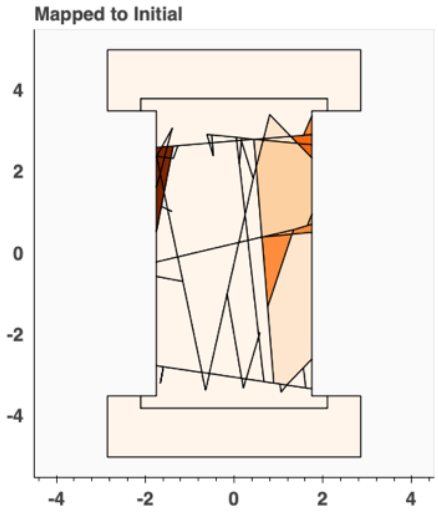

Model B

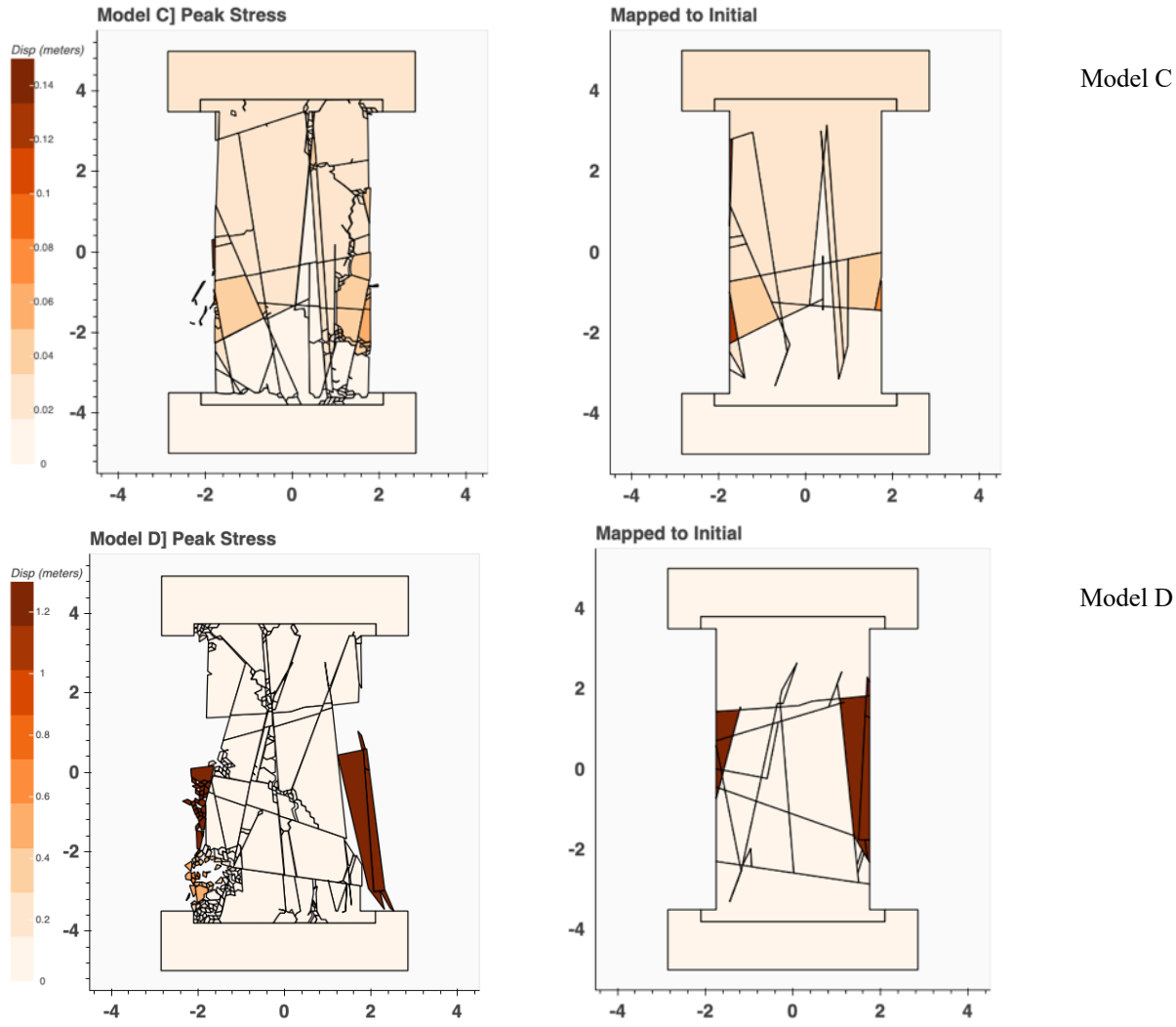

Figure 6.21. Displacement per block for models A, B, C and D at the peak stress (left) overlain by the blocks at the initial timestep associated with displacement in the peak strength (right).

6.9 Structural Failure Characterization

In the previous section a method was described for computing block displacement at peak stress and relating it to the initial blocks. This section leverages that method, and introduces an approach to compute structural damage, identifying which blocks contributed to the structural damage and by how much, in addition to relating them to their parent blocks in the initial DFN configuration.

For each model, a threshold is set for what amount of displacement would be considered as structural damage. This value is dependent on the model. An algorithm for computing a reasonable value for this threshold could be developed. In this section, the values are assumed based on observations at the Middleton mine. This provides a characterization criterion for each block, effectively marking each block as a structural damage block, or non-structural damage block. Examples are given in Figure 6.22-Figure 6.25 for Models A, B, C, and D, respectively, in which the blocks characterized as structural damage are shown in brown. The figures show the characterized blocks at the peak stress timestep, and then the plot shows where this information is mapped relative to the initial DFN configuration.

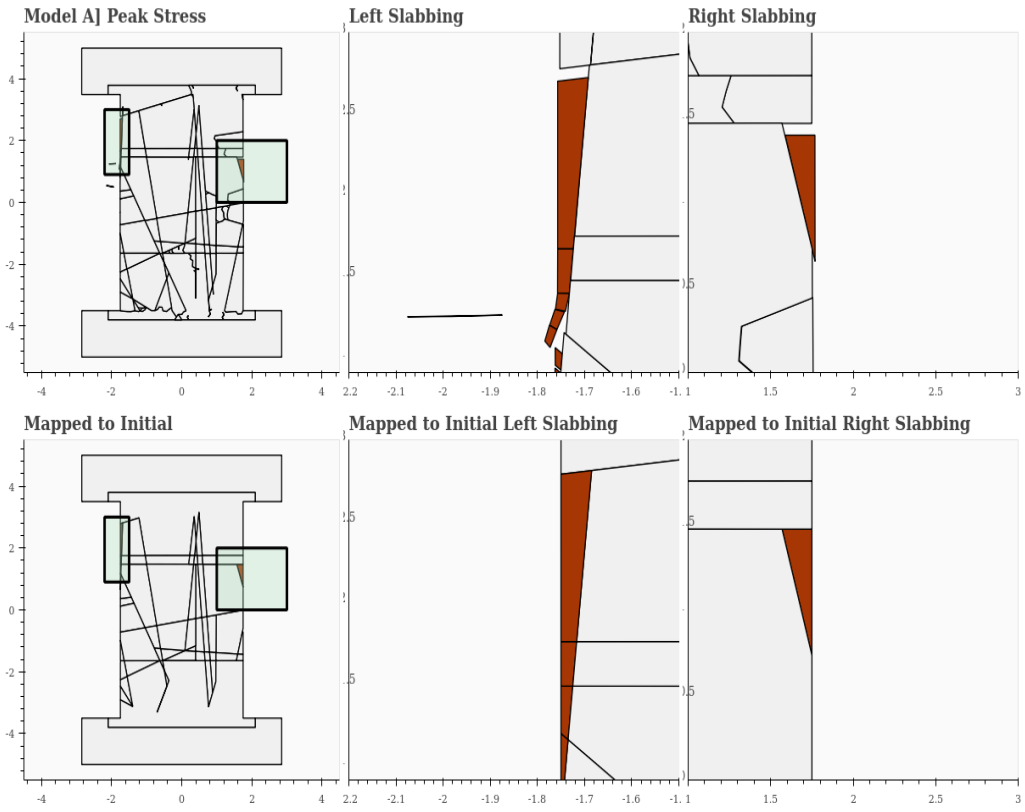

Figure 6.22. Model A. Displacement at peak stress (left) overlain with blocks at the initial timestep associated with displacement at peak stress (right).

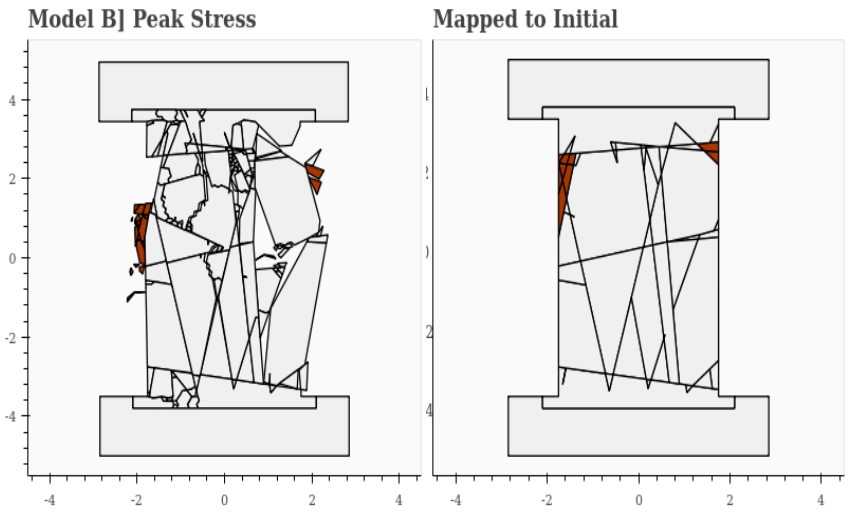

Figure 6.23. Model B. Displacement at peak stress (left) overlain with blocks at the initial timestep associated with displacement at peak stress (right).

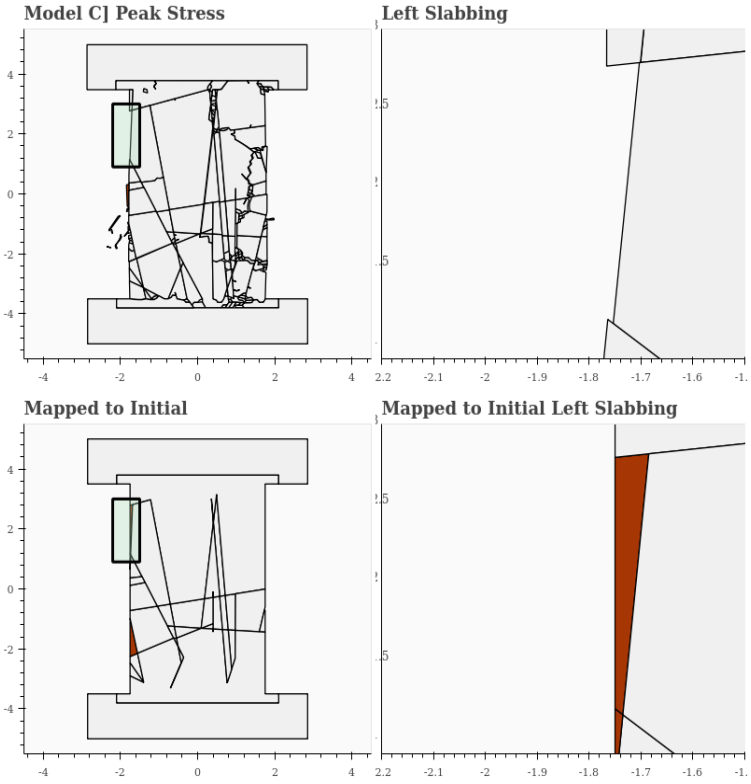

Figure 6.24. Model C. Displacement at peak stress (left) overlain with blocks at the initial timestep associated with displacement at peak stress (right).

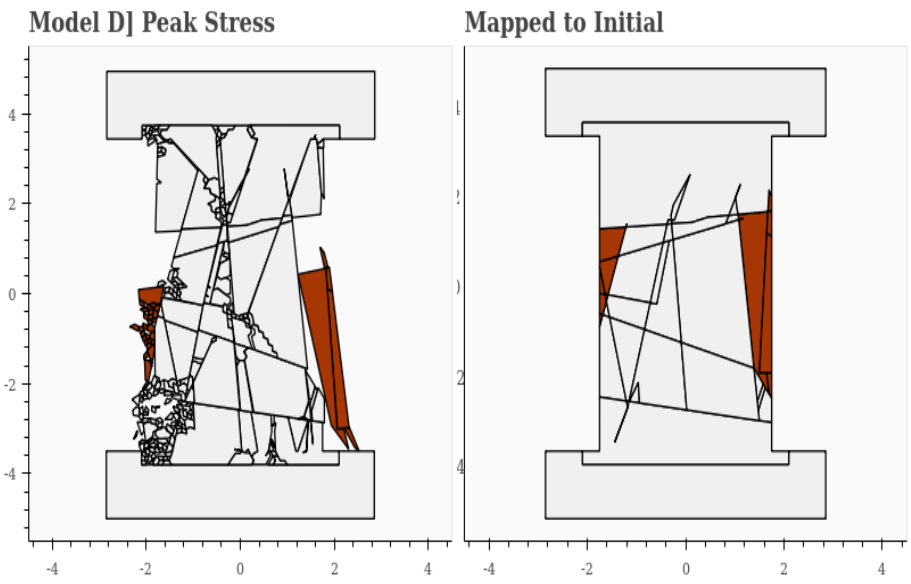

Figure 6.25. Model D. Displacement at peak stress (left) overlain with blocks at the initial timestep associated with displacement at peak stress (right).

This method provides a valuable new approach for characterizing structural damage blocks. Relating them to the initial DFN configuration provides the ground work needed for future research of predictive analysis that would identify at the DFN level which area or blocks might result in structural damage.

6.10 Block Characterization using a Block Tracking Tree Approach

Figure 6.26 illustrates the results of the block tracking tree for selected models A, B, C and D, respectively. The computation of the block tracking tree was previously detailed in Chapter 5. The circles initiate from the root (yellow circle) and continue to spread outwards for increasing timesteps. Each blue circle represents a block fragment from which it can be seen that some of the lines start from the root and continue without breaking to smaller fragments (example Model A, right blue radius lines). For others (for example Model C), significant breaking occurred in the

model and therefore a higher level of fragments can be seen in these circles. Each circle contains black and red lines, representing the 50% peak stress and peak stress, respectively. Comparing block tracking trees across models provides a general sense of how much fragmentation is occurring per model, across timesteps. As an example, model A shows the lowest and more concentrated degree of fragmentation. This indicates the lower dependency of the pillar to fail due to rock bridges and newly-generated fractures relative to failure through the kinematic instability of some the structure bounded blocks. Confirmation of this observation can be seen in Figure 6.22 and Figure 6.20.a and

Figure 6.21.a. Figure 6.25.b indicates a combination of brittle and structural failure. The closeness of black line (50% peak stress) to the root also indicates the proximity of pillar failure in a more rapid manner in comparison to other models. Model C, (Figure 6.25.c) is experiencing significant fracturing prior to 50% peak stress. However, the DFN configuration resulted in a relatively unique situation for Model C where the brittle components are not contributing to the final failure of the pillar and kinematic block instability is the main reason for the failure. Model C with the greatest distance between root and 50% peak (the longer time it takes to fail) is the strongest model of all the models. Model D (Figure 6.25.d) shows the highest fragments density of the simulated models. The model failure is at combination of brittle fracturing and structural failure.

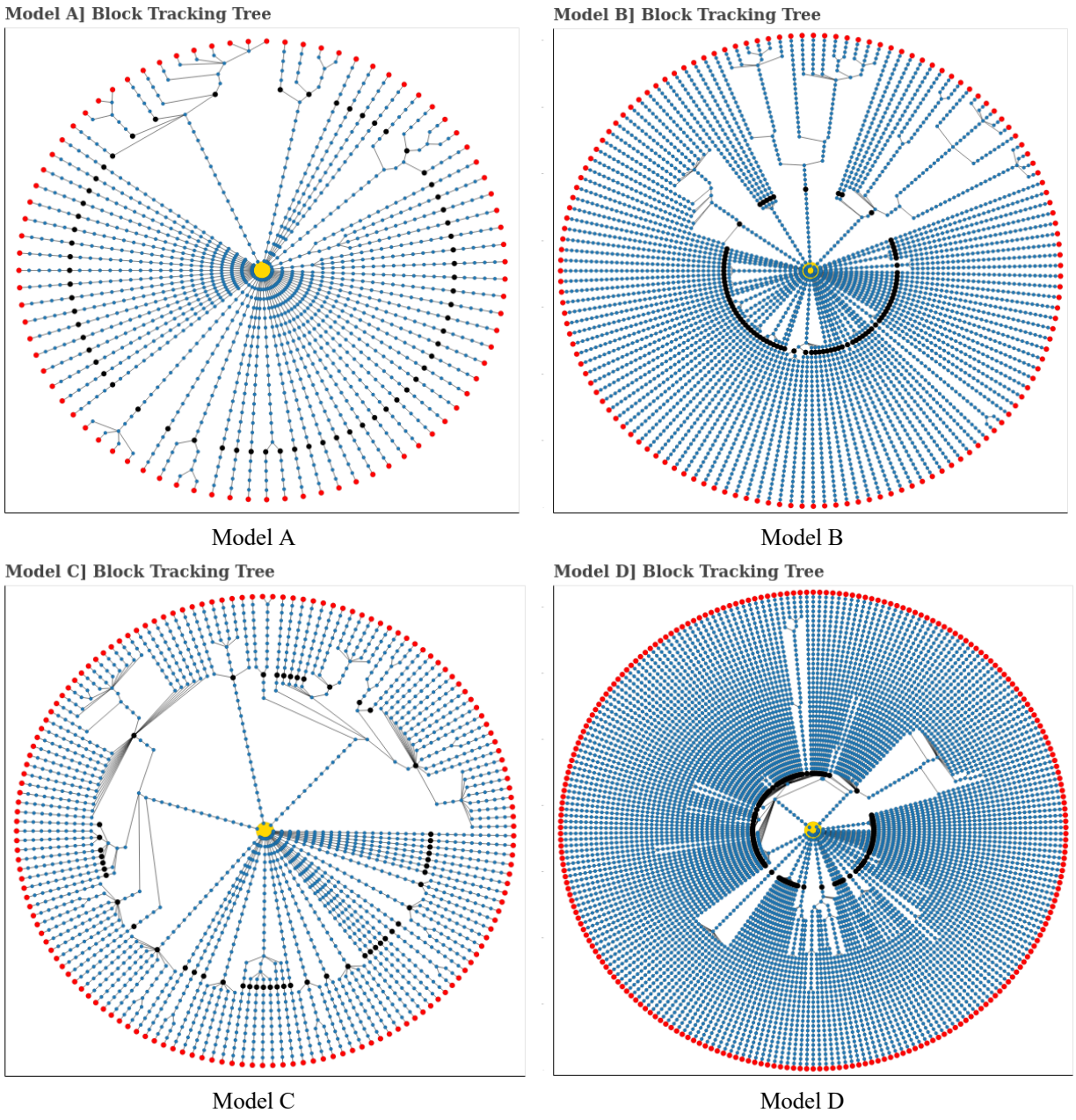

Figure 6.26. Block tracking tree for model A, B, C and D. Each circle represents a separate timestep. Black denotes block fragments at 50% peak stress and red denotes peak stress.

This analysis of brittleness can be explored further. Similar to the previous section where we were able to identify blocks contributing to structural damage, this section aims to identify blocks

contributing to brittleness damage. The block tracking tree proves itself useful again in providing the necessary information for this identification. This is achieved here by computing, for each initial block, how many children blocks are present at the peak stress timestep. This value is used in the density plots for Figure 6.27, left. This information is then mapped into the blocks at the initial timesteps, Figure 6.27, right. This mapping provides a quantitative measurement of how brittle each block is, based on the result of the simulation. Similar to the previous section, this kind of powerful analysis enables predictive analysis that identify at the DFN level which area or blocks might result in brittle damage.

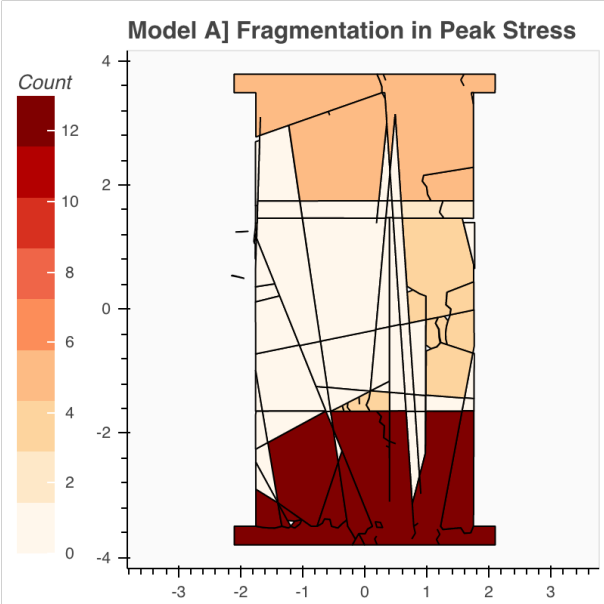
Model A] Fragmentation in Peak Stress
Count
12
10
8
6
4
2
0
4
2
0
-2
-4
-3
-2
-1
0
1
2
3

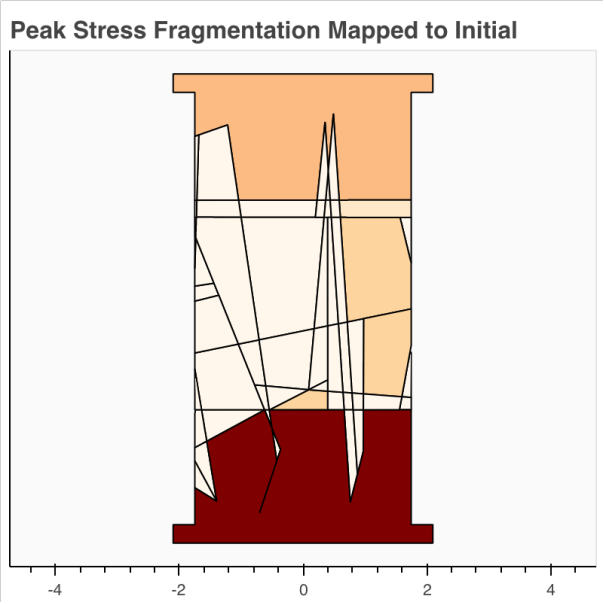
Peak Stress Fragmentation Mapped to Initial
-4
-2
0
2
4

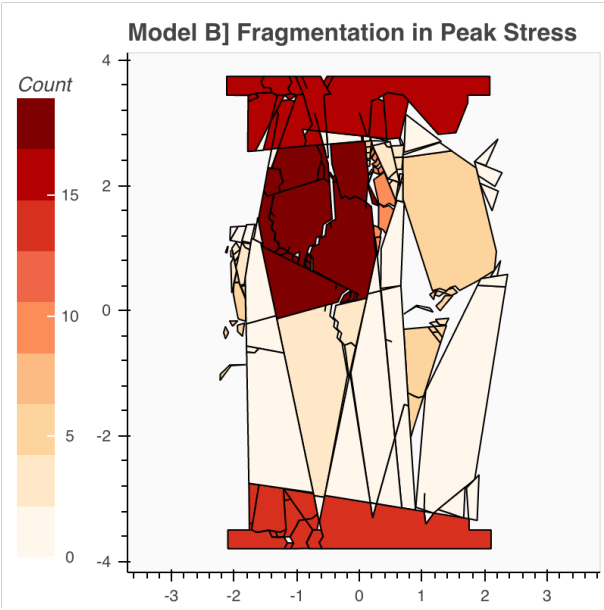
Model B] Fragmentation in Peak Stress
Count
15
10
5
0
4
2
0
-2
-4
-3
-2
-1
0
1
2
3

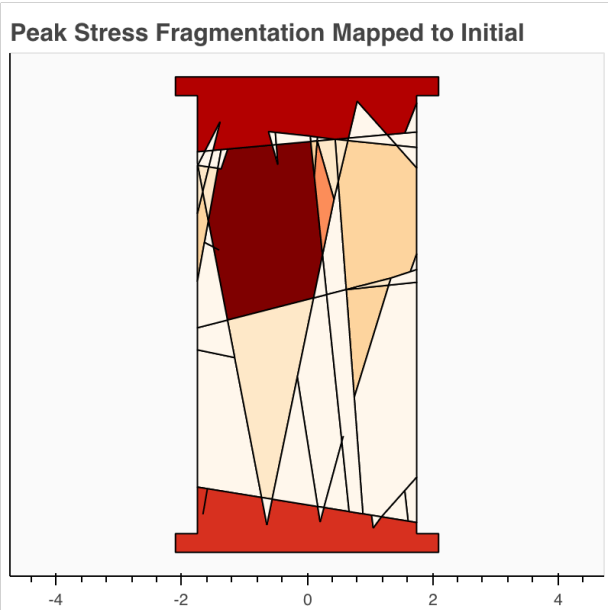
Peak Stress Fragmentation Mapped to Initial
-4
-2
0
2
4

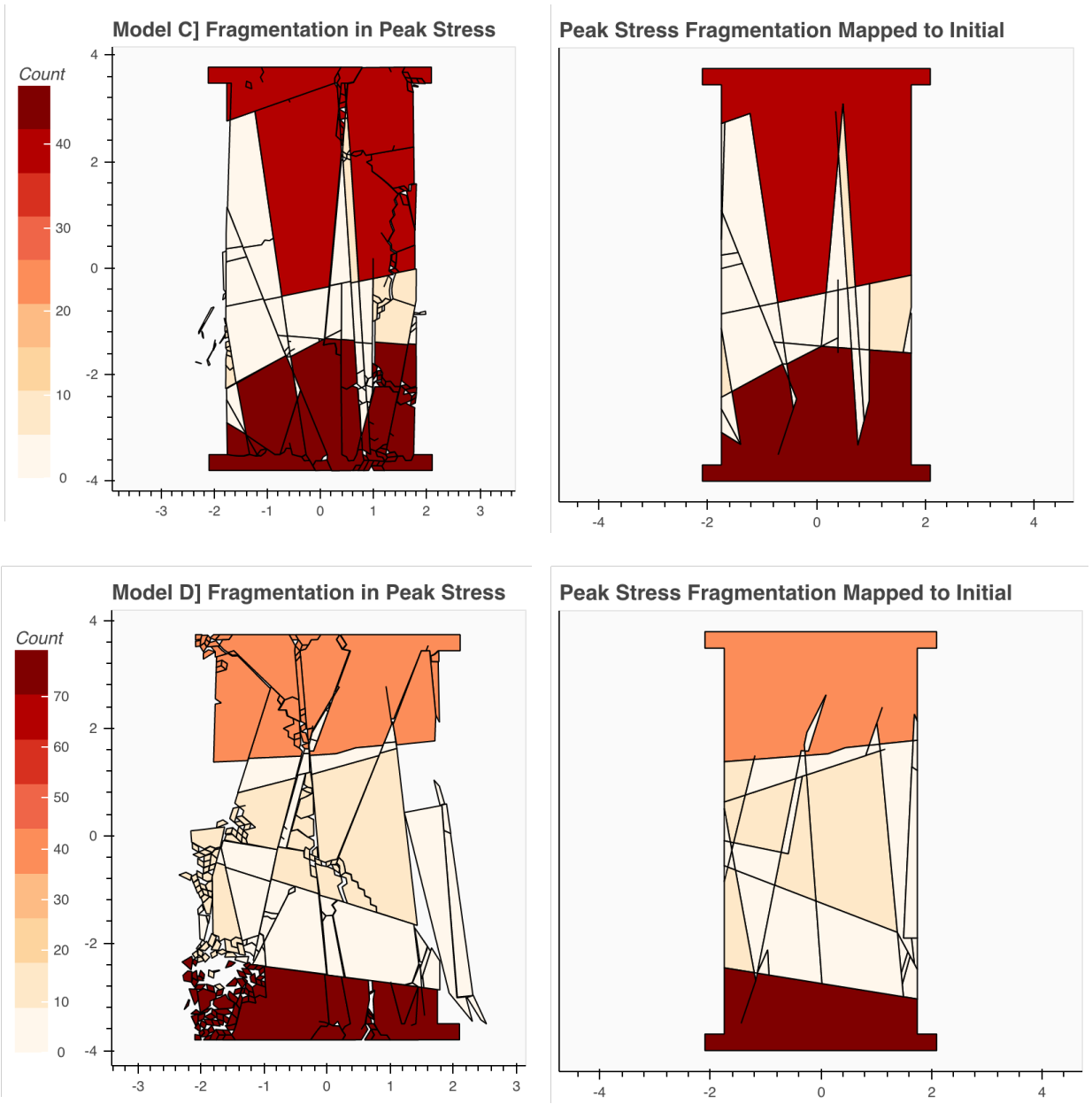

Figure 6.27. Block fragmentation per block for models A and B, C and D in the peak stress (left) mapped with blocks in the initial timestep (right).

6.11 Summary

Damage caused by brittle fracturing can be realistically investigated using DFN-FDEM approach. The ability of FDEM to capture initiation, coalescence and propagation of fracture lines makes the method favorable to study complex failure mechanisms associated with the study of hard rock masses.

Slender pillars (W:H ratio of 0.5) represent the ideal case to study the failure mechanisms associated with considering different DFN configurations. These models were used to develop quantitative methods to characterize newly-generated fractures and their relationship with newly generated blocks. The results can be grouped into four categories: i) failure due to blocks kinematics (Type I blocks), without contribution of intact rock damage; ii) failure due intact rock damage, whereby newly generated blocks are Type IV blocks (finite tapered blocks); iii) failure due to a combination of intact rock damage and block kinematics (Type I and Type II blocks); and iv) failure due to intact rock damage without new blocks being generated (Type V blocks).

Block size analysis at three different stress conditions during loading (initial, 50% of peak stress and peak stress), was used to calculate the 10, 50 and 90% block-passing values. The difference between these values as the loading is increased are indicative as to whether failure may be primarily structurally controlled or is due a combination of intact rock damage and kinematics.

Newly introduced detachment area computations, block displacement, structural damage block characterization, brittle damage block characterization, in combination with the tracking tree methods presented in Chapter 5 provide alternative innovative methods to better capture the role

of brittle and structural failure mechanisms in combination with blocks kinematics. The results confirm that failure in naturally fractured rock masses is the result of complex mechanisms associated with the frequency, persistence and interactions of the natural fracture network. The results of this Chapter are not confined to rock pillars, but could be applied to slope stability, tunneling and block caving analysis.

Models B and D showed a larger amount of displacement prior to the generation of new cracks. This by itself was indicative of free blocks moving downwards. This observation was confirmed in the detachment maps in which the orange areas were clearly indicative of large block movements. Block count vs damage plots showed the lower dependency in model B on damage to generate blocks. This can indicate structurally-controlled behaviour in model B. The observations in model D indicate a higher dependency on the structure in the development of the newly-generated cracks and formation of new blocks. Therefore, the behaviour of this model is due to a combination of brittle damage and structurally-controlled behaviour. It was observed that models B and D are both associated with a more distributed fracture intersection density map across the pillar section.

Chapter 7: Conclusions and Future Research

7.1 Conclusions and Key Contributions

The primary objective of this thesis was to develop a consistent approach in the consideration of Discrete Fracture Networks in numerical models in rock engineering practice. The proposed approach is built upon the ability to extract as much information as possible about the numerical models. This includes the geometrical configuration of the initial DFN model and extends to encompass both temporal and spatial analysis of geomechanical simulations. The geomechanical modelling used in the thesis is based on the FDEM technique, but the newly developed methods could in principle be adapted to work with different FEM and DEM techniques. The focus of the numerical analysis is the characterization of strength and possible failure mechanisms of fractured rock pillars; these represent numerical models that can be calibrated against empirical methods and for which there exist several examples in the literature that were used to constrain and validate the modelling results. This thesis includes several important and original contributions. These are briefly summarized below.

- *Development of new methods to better integrate DFN and FDEM models.* Fracture traces can be easily imported into numerical models such as FEM, DEM and FDEM model; however, the stochastic nature of DFN models requires the selection of representative DFN realizations since it would be impractical and computationally expensive to simulate a large number (>10) of DFN realizations. A new numerical approach, DFN Analysis, was introduced to help practitioners address this problem. DFN Analysis details methods that make full use of DFN

statistics, including fracture count, fracture length, fracture intersection count and density, fracture orientation frequency and length, to provide objective and robust results.

Previous research has shown the difficulty that may arise when integrating DFN with FDEM models. The critical component of the DFN-FDEM integration is the ability to embed and mesh complex fracture patterns. This has required to considered several geometrical aspects, including: i) the existence of very acute angles between intersecting fracture traces, which would result in distorted meshed elements; ii) the presence of traces shorter than the minimum mesh size; iii) duplication of points that would result in the duplication of meshed nodes; and iv) the occurrence of fracture traces spaced at distance that is less than the minimum mesh size. A new numerical approach, DFN Cleaning, was introduced to analyze each of the geometrical problems above independently. This is combined with DFN Quality and Mesh Quality that use advanced optimization techniques, such as Monte Carlo simulations, to produce an optimal meshed fractured network in the FDEM model. The proposed methods significantly reduce the human effort otherwise required to mesh DFN-FDEM models and reduce the human uncertainty associated with the process.

- *Development of new methods to make better sense of simulations results.* Providing a comprehensive procedure for calculating fracture lines and blocks in FDEM modelling using geometry and graph analysis FDEM models have been commonly used in simulating various rock mechanics engineering problems. However, there is a lack of a unified approach for the computation and analysis of the resulting fractures and blocks. This limits the analysis to the consideration of typical outputs, such strength and deformability, without proper consideration of the role that brittle fracture and kinematics plays in the modelled results. In various cases,

researchers have attempted to quantify induced fractures and resulting blocks by applying image processing techniques; however, that may not feasible for large models and furthermore the analysis is limited by the resolution of the images. This thesis introduces a new approach for a quantitative analysis of induced fractures and blocks from FDEM simulation results. The proposed DEMFA technique use an opening criterion for finding fractures lines for every modelling timestep and makes full use of the modelling results. Subsequently, a newly developed Block Calculator technique (DEMBA) is introduced that represents meshed elements using graph data structures and graph theory concepts. Combined, the two methods offer the opportunity of tracking the generation of new blocks temporally (by timestep), thus relating the generation of new fractures to the formation of new blocks. A child-parent block relationship map is generated by introducing a block tracking tree approach.

- *Development and applications of new methods to characterize rock mass behaviour*. This part has included the study of failure mechanisms for sixteen pillar models with different DFN configurations. Notably, it was possible to define and characterize pillar failure with respect to blocks formation (increasing rock mass blockiness) using an approach similar to the key block theory. Innovative mapping methodologies were introduced to characterize blocks, including the development of detachment maps, block displacement maps, and block tracking tree and brittleness maps.
- *Providing a path to Machine Learning applied to rock engineering problems*. The initial DFN can be further related to the damage, blocks, and failure at the peak stress. This has the potential to be integrated within machine learning schemes and could be used to highlight the critical features behind failure mechanisms.

7.2 Recommendations for Future Work

It is anticipated that the results and key contributions presented in this thesis could be further extended and applied to address a variety of rock engineering problems. For instance, the use of DFN analysis and DFN cleaning could provide a path to analyze a large number of DFN sections to allow the definition of "*critical*" DFN patterns with respect to fracture networks. The proposed methods could therefore be integrated within a risk analysis assessment of rock engineering problems, by looking at the probability of occurrence of critical pathways within a given fracture network. Whereas the techniques are herein shown for 2D applications, future work could expand the techniques for 3D applications. Engineers need solutions to address future challenges such as the development of underground spaces, which are not limited to mining. To do so, there is a need to create unified methods to analyze rock mass failure mechanism that goes beyond the sole consideration of rock mass strength and deformability, and better integrate the mutual role of fracturing processes, blocks formation and kinematics. This thesis has introduced a new set of numerical procedures that could help address this important aspect of the future of rock engineering.

Machine learning could be used to relate stress at failure, rock mass deformations, fracture network interaction and induced failure mechanisms. The methods presented in this thesis could be adapted to include machine learning to improve rock engineering design by facilitating decision making processes.

In order to gain better modelling results, it is suggested to consider the heterogeneity of material grains and fracture properties in the modelling process. The proposed methodologies in the thesis consider the geometry of fractures and blocks as the main components for being critical. It is suggested to also consider the friction of discontinuities in critical fracture and block investigations.

Bibliography

Ahn, S.H, C. Lee. (2004). Removability analysis of rock blocks by block theory and a probabilistic approach. International Journal of Rock Mechanics and Mining Sciences, Proceedings of the ISRM SINOROCK 2004 symposium, 41 (3): 429. https://doi.org/10.1016/j.ijrmms.2003.12.069.

Alehossein, H. M. Hood. (1996). State of the art review of rock models for disc roller cutters, In: Rock Mechanics. Ed. Aubertin, F. Hassani, H. Mitri. Balkema /CRC Press. Taylor and Francis Group. 2&4 Park Square, Milton ParkAbingdon OX14 4RN UK. 693-700.

Alzo' ubi, A.M. (2009). The effect of tensile strength on the stability of rock slopes. PhD. Thesis, University of Alberta, Canada.

American Geological Institute. (1962). Dictionary of geological terms. Dolphin Books, Garden City, N.Y (1962). https://trove.nla.gov.au/work/10849194.

Bagheri M. (2009). Model uncertainty of design tools to analyze block stability. Stockholm, Sweden: Engineering Geology and Geophysics Research Group Royal Institute of Technology (KTH).

Berkowitz, B. (1995). Analysis of fracture network connectivity using percolation theory. Mathematical Geology, 27(4), 467-483.

Bertuzzi, R. (2018). Revisiting rock classification to estimate rock mass properties. Journal of Rock Mechanics and Geotechnical Engineering. 1674-7755. https://doi.org/10.1016/j.jrmge.2018.08.011.

Bieniawski, Z. T. (1967). Mechanism of brittle fracture of rock: Part I—Theory of the Fracture Process. International Journal of Rock Mechanics and Mining Sciences & Geomechanics. Volume 4, Issue 4. 395–406. https://doi.org/10.1016/0148-9062(67)90030-7.

Brace, W.F. (1964). Brittle fracture of rocks. In State of Stress in the Earth's Crust (Ed Judd)." American Elsevier Publishing Co., 111–80.

Cai, M, and P. K. Kaiser. (2004). Numerical simulation of the Brazilian test and the tensile strength of anisotropic rocks and rocks with pre-existing cracks. International Journal of Rock Mechanics and Mining Sciences, Proceedings of the ISRM SINOROCK 2004 Symposium, 41 (May): 478–83. https://doi.org/10.1016/j.ijrmms.2004.03.086.

Cai, M, P. K Kaiser, Y. Tasaka, T. Maejima, H. Morioka, and M. Minami. (2004). Generalized crack initiation and crack damage stress thresholds of brittle rock masses near underground excavations. International Journal of Rock Mechanics and Mining Sciences. 41 (5): 833–47. https://doi.org/10.1016/j.ijrmms.2004.02.001.

Christianson, M, M. Board, D. Rigby. (2006). UDEC simulation of triaxial testing of lithophysal tuff. Proceedings of the 41st US Symposium on Rock Mechanics (USRMS), American Rock Mechanics Association, Golden, USA. ARMA-06-968

Cundall, P. A. (1988a). Formulation of a three-dimensional distinct element model—Part I. A scheme to detect and represent contacts in a system composed of many polyhedral blocks. International Journal of Rock Mechanics and Mining Sciences & Geomechanics. Abstracts 25 (3): 107–16. https://doi.org/10.1016/0148-9062(88)92293-0.

Cundall, P. A., and O. D. L. Strack. (2008). A discrete numerical model for granular assemblies. in the essence of geotechnical engineering: 60 Years of Géotechnique. Thomas Telford Publishing: 305–329.

Cundall, Peter A., and Otto DL Strack. (1979). A discrete numerical model for granular assemblies. Geotechnique. 29 (1): 47–65.

Darcel, C., O. Bour., P. Davy. (2003). Stereological analysis of fractal fracture networks. Journal of Geophysical Research: Solid Earth. 108(B9). doi:10.1029/2002JB002091.

Dershowitz, W., and J. Carvalho. (1996). Key-block tunnel stability analysis using realistic fracture patterns. American Rock Mechanics Association. https://www.onepetro.org/conference-paper/ARMA-96-1747.

Dershowitz, W., G. Lee, J. Geier, T. Foxford, P. LaPointe, and A. Thomas. (1998). User documentation, FracMan Interactive Discrete Feature Data Analysis, Geometric Modelling, and Exploration Simulation. Version.

Dershowitz, W. S., and H.H. Herda. (1992a). Interpretation of fracture spacing and intensity. American Rock Mechanics Association. https://www.onepetro.org/conference-paper/ARMA-92-0757.

Diederichs, M. S, P. K Kaiser, and E. Eberhardt. (2004). Damage initiation and propagation in hard rock during tunnelling and the influence of near-face stress rotation. International Journal of Rock Mechanics and Mining Sciences 41 (5): 785–812. https://doi.org/10.1016/j.ijrmms.2004.02.003.

Diestel, R. (2017). Graph Theory. Vol. 173. Graduate Texts in Mathematics. Berlin, Heidelberg: Springer Berlin Heidelberg. https://doi.org/10.1007/978-3-662-53622-3.

Mas Ivars, D. D.O. Potyondy, M. Pierce, P. A. Cundall. (2008). The smooth-joint contact model. Venice: Proceedings of the 8th World Congress on Computational Mechanics - 5th European Congress on Computation Mechanics and Applied Science and Engineering. Proceedings of WCCM8-ECCOMAS, p. 8th

Duong, T. (2007). Ks: Kernel density estimation and kernel discriminant analysis for multivariate data in R. Journal of Statistical Software 21 (1): 1–16. https://doi.org/10.18637/jss.v021.i07.

Elmo, D. (2006). Evaluation of a hybrid FEM/DEM approach for determination of rock mass dtrength using a combination of discontinuity mapping and fracture mechanics modelling, with particular emphasis on modelling of jointed pillars. Ph.D., University of Exeter. https://ethos.bl.uk/OrderDetails.do?uin=uk.bl.ethos.439831.

Elmo D., D. Stead and S. Rogers. (2008). Quantitative analysis of a fractured rock mass using a discrete fracture network approach: Characterisation of natural fragmentation and implications for current rock mass classification systems. Proceedings of the 5th Conference and Exhibition on Mass Mining, June. Lulea, Sweden.

Elmo D., S. Rogers, D. Stead and E. Eberhardt. (2014). A Discrete fracture network approach to characterise rock mass fragmentation and implications for geomechanical upscaling. Mining Technology Journal. Vol. 123(3), pp. 149-161.

Elmo, D., D. Stead, and S. Rogers. (2015). Guidelines for the quantitative description of discontinuities for use in discrete fracture network modelling. International Society for Rock Mechanics and Rock Engineering. https://www.onepetro.org/conference-paper/ISRM-13CONGRESS-2015-246.

Elmo, D., K. Moffitt, and J. Carvalho. (2016). Synthetic rock mass modelling: Experience gained and lessons learned. American Rock Mechanics Association. https://www.onepetro.org/conference-paper/ARMA-2016-777.

Elmo, D, D. Donati, and D. Stead. (2018). Challenges in the characterisation of intact rock bridges in rock slopes. Engineering Geology. 245 (November): 81–96. https://doi.org/10.1016/j.enggeo.2018.06.014.

Elmo D. and D. Stead. (2016). Applications of fracture mechanics to rock slopes, Invited Chapter, Rock Mechanics and Engineering. Volume 3: Analysis, Modeling & Design, Chapter 23, 34 pages, Invited.

Elmo, D, and D. Stead. (2010a). An integrated numerical modelling–discrete fracture network approach applied to the characterisation of rock mass strength of naturally fractured pillars. Rock Mechanics and Rock Engineering. 43 (1): 3–19.

Elmouttie, M. K., and G. V. Poropat. (2012). A method to estimate in situ block size distribution. Rock Mechanics and Rock Engineering. 45 (3): 401–7. https://doi.org/10.1007/s00603-011-0175-0.

Elmouttie, M, and G. Poropat. (2012). Uncertainty propagation in structural modeling. Proceedings, Slope Stability, Vancouver. https://publications.csiro.au/rpr/download?pid=csiro:EP113214&dsid=DS4.

Esterhuizen, G.S. (2006). Evaluation of the Strength of Slender Pillars. SME Annual Meeting and Exhibit, March 27-29, St. Louis, Missouri, preprint 06-003. Littleton, CO: Society for Mining, Metallurgy, and Exploration, Inc., March, pp.1-7.

Esterhuizen, G. S., D. R. Dolinar, and J. L. Ellenberger. (2011). Pillar strength in underground stone mines in the United States. International Journal of Rock Mechanics and Mining Sciences. 48 (1): 42–50. https://doi.org/10.1016/j.ijrmms.2010.06.003.

Fadakar-A, Y. (2014). Stochastic modelling of fractures in rock masses. PhD thesis. University of Adelaide, Adelaide.

Fadakar-A, Y, and D. Elmo. (2018). Application of graph theory for robust and efficient rock bridge analysis. American Rock Mechanics Association. https://www.onepetro.org/conference-paper/ARMA-DFNE-18-0733.

Fakhimi, A, F. Carvalho, T Ishida, and J. F Labuz. (2002). Simulation of failure around a circular opening in rock. International Journal of Rock Mechanics and Mining Sciences, Numerical Methods in Rock Mechanics, 39 (4): 507–15. https://doi.org/10.1016/S1365-1609(02)00041-2.

Fang, Z., and J. P. Harrison. (2002). Development of a local degradation approach to the modelling of brittle fracture in heterogeneous rocks. International Journal of Rock Mechanics and Mining Sciences, Numerical Methods in Rock Mechanics, 39 (4): 443–57. https://doi.org/10.1016/S1365-1609(02)00035-7.

Gao, F. Q., and D. Stead. (2014). The application of a modified voronoi logic to brittle fracture modelling at the laboratory and field scale. International Journal of Rock Mechanics and Mining Sciences. 68 (June): 1–14. https://doi.org/10.1016/j.ijrmms.2014.02.003.

Gao, F. (2013). Simulation of failure mechanisms around underground coal mine openings using discrete element modelling. PhD. Thesis, Science: Department of Earth Sciences. http://summit.sfu.ca/item/13680.

Geomechanica. (2015). Toronto, Canada: *Geomechanica*. https://www.geomechanica.com/.

Ghazvinian, E., M. S. Diederichs, and R. Quey. (2014). 3D random voronoi grain-based models for dimulation of brittle rock damage and fabric-guided micro-fracturing. Journal of Rock Mechanics and Geotechnical Engineering. 6 (6): 506–21. https://doi.org/10.1016/j.jrmge.2014.09.001.

Gibbons, Alan. (1985). Algorithmic graph theory. Cambridge University Press.

Glynn, E. F., and H. H. Einstein. (1979). Probability of kinematic instability in rock slopes - A numerical approach. American Rock Mechanics Association. https://www.onepetro.org/conference-paper/ARMA-79-0317.

Goodman, R E, and Gen-hua Shi. (1985). Block theory and its application to rock engineering. Englewood Cliffs, N.J.: Prentice-Hall.

Golder Associates. (2018). FracMan Version 7.70. FracMan Technology Group. http://www.fracman.com/.

Grisi, S., R. Castellanza, F. Agliardi, G. Crosta, and D. Elmo. (2016). Failure mechanism of a gypsum pillar by 2D and 3D FEM/DEM numerical analyses. International Society for Rock Mechanics and Rock Engineering. https://www.onepetro.org/conference-paper/ISRM-EUROCK-2016-085.

Gross, J. L., and J. Yellen. (2005). Graph theory and its applications. 2nd Edition. Boca Raton: Chapman and Hall/CRC.

Hajiabdolmajid, V., P. K. Kaiser, and C. D. Martin. (2002). Modelling brittle failure of rock. International Journal of Rock Mechanics and Mining Sciences. 39 (6): 731–41. https://doi.org/10.1016/S1365-1609(02)00051-5.

Hamdi, P. (2015). Characterization of brittle damage in rock from the micro to macro scale. PhD. Thesis, Science: Department of Earth Sciences. http://summit.sfu.ca/item/15770.

Hatzor, Y. H., G. Ma, G. Shi. (2017). Discontinuous deformation analysis in rock mechanics practice. CRC Press. https://doi.org/10.4324/9781315687032.

Heliot, D. (1988). Generating a blocky rock mass. International Journal of Rock Mechanics and Mining Sciences & Geomechanics. Abstracts 25 (3): 127–38. https://doi.org/10.1016/0148-9062(88)92295-4.

Havaej, M. (2015). Characterisation of high rock slopes using an integrated numerical modelling - remote sensing approach. PhD. Thesis, Science: Department of Earth Sciences. http://summit.sfu.ca/item/15681.

Hoek, E., and E. T. Brown. (2018). The Hoek–Brown failure criterion and GSI – 2018 Edition. Journal of Rock Mechanics and Geotechnical Engineering, August. https://doi.org/10.1016/j.jrmge.2018.08.001.

Hoek, E. (1994). Strength of rock and rock masses. ISRM News Journal 2: 4–16.

Hoek, Et, T.G Carter, and M.S. Diederichs. (2013). Quantification of the geological strength index chart. San Francisco, CA, USA.

Hoek, Evert, P. K. Kaiser, and W. F. Bawden. (1995). Support of underground excavations in hard rock. Rotterdam: Balkema.

Hopcroft, J., and R. Tarjan. (1973). Algorithm 447: Efficient algorithms for graph manipulation." Commun. ACM 16 (6): 372–378. https://doi.org/10.1145/362248.362272.

International Society for Rock Mechanics Commission on Standardization of Laboratory and Field Tests: Suggested Methods for the Quantitative Description of Discontinuities in Rock Masses. (1978). International Journal of Rock Mechanics and Mining Sciences & Geomechanics Abstracts 15 (6): 319–68. https://doi.org/10.1016/0148-9062(78)91472-9.

Insana. A., M. Barla, D. Elmo. (2016). Multi scale numerical modelling related to hydrofracking for deep geothermal energy exploitation. Procedia Engineering. 158: 314-319. https://doi.org/10.1016/j.proeng.2016.08.448.

Irwin, G. (1957). Analysis of stresses and strains near the end of a crack traversing a plate. Journal of Applied Mechanics. 24: 361–64.

Itasca. (1995). PFC-Particle Flow Code. Modelling Software. (Version 1.0). Itasca Ltd. Minneapolis, USA.

Itasca. (2013). Consulting Group Inc. UDEC (Universal Distinct Element Code). Itasca Ltd. Minneapolis, USA.

Itasca. (2018). 3DEC (v. 5.2), UDEC (v. 6.2). Itasca Consulting Group, Minneapolis, MN, USA.

Jennings, J E. (1970). A mathematical theory for the calculation of the stability of open cast mines. Proceedings of the Symposium on the Theoretical Background to the Planning of Open Pit Mines, Johannesburg..pp. 87-102.

Jing, L. (2003). A review of techniques, advances and outstanding issues in numerical modelling for rock mechanics and rock engineering. International Journal of Rock Mechanics and Mining Sciences. 40 (3): 283–353. https://doi.org/10.1016/S1365-1609(03)00013-3.

Karimi Sharif, L, D. Elmo, and D. Stead. (2016). Simulation of rock bridge failure at the laboratory scale using a combined FDEM modeling and discrete crack network approach. American Rock Mechanics Association. https://www.onepetro.org/conference-paper/ARMA-2016-588.

Karimi Sharif, L, D. Elmo, and D. Stead. (2018). DFNAnalyzer: A web-based application for discrete fracture network analysis. American Rock Mechanics Association. https://www.onepetro.org/conference-paper/ARMA-DFNE-18-0663.

Karimi Sharif, L, D. Elmo and D. Stead. (2018). DFNCleaner: A novel automated approach to improve DFN integration for geomechanical analysis. American Rock Mechanics Association. https://www.onepetro.org/conference-paper/ARMA-DFNE-18-0664.

Karimi Sharif, L, D. Elmo, D. Stead. (2019). Improving DFN-geomechanical model integration using a novel automated approach. Computers and Geotechnics. Volume 105. Pages 228-248, ISSN 0266-352X/ https://doi.org/10.1016/j.compgeo.2018.10.005.

Kemeny, J. (2003). The time-dependent reduction of sliding cohesion due to rock bridges along discontinuities: A fracture mechanics approach. Rock Mechanics and Rock Engineering. 36 (1): 27–38. https://doi.org/10.1007/s00603-002-0032-2.

Kim, B. H., M. Cai, P. K. Kaiser, and H. S. Yang. (2006). Estimation of block sizes for rock masses with non-persistent joints. Rock Mechanics and Rock Engineering 40 (2): 169. https://doi.org/10.1007/s00603-006-0093-8.

Kim, B.-H., R. L. Peterson, T. Katsaga, and M. E. Pierce. (2015). Estimation of rock block size distribution for determination of geological strength index (GSI) using discrete fracture networks (DFNs). Mining Technology. 124 (3): 203–11. https://doi.org/10.1179/1743286315Y.0000000015.

Klerck, P.A. (2000a). The finite element modelling of discrete fracture in quasi-brittle materials. PhD thesis, University of Wales Swansea.

Klerck, P.A., E.J. Sellers, and D.R.J. Owen. (2004). Discrete fracture in quasi-brittle Materials under compressive and tensile stress states. Computational Failure Mechanics for Geomaterials 193 (27–29): 3035–56. https://doi.org/10.1016/j.cma.2003.10.015.

Klerck, Paul Alexander. (2000). The finite element modelling of discrete fracture in quasi-brittle materials. Ph.D., *University of Wales.* Swansea. https://ethos.bl.uk/OrderDetails.do?uin=uk.bl.ethos.539299.

Kozicki J, F.V. Donze. (2008). A new open-source software developer for numerical simulations using discrete modeling methods. Computer Methods in Applied Mechanics and Engineering; 197: 4429-4443.

Lewis, H. R., and C.H. Papadimitriou. (1982). Symmetric space-bounded computation. Theoretical Computer Science 19 (2): 161–87. https://doi.org/10.1016/0304-3975(82)90058-5.

Lin, D., and C. Fairhurst. (1988). Static analysis of the stability of three-dimensional blocky systems around excavations in rock. International Journal of Rock Mechanics and Mining Sciences & Geomechanics. Abstracts 25 (3): 139–47. https://doi.org/10.1016/0148-9062(88)92296-6.

Lisjak, A., and G. Grasselli. (2014a). A review of discrete modeling techniques for fracturing processes in discontinuous rock masses. Journal of Rock Mechanics and Geotechnical Engineering. 6 (4): 301–14. https://doi.org/10.1016/j.jrmge.2013.12.007.

Lisjak, A., Q. Liu, Q. Zhao, O. K. Mahabadi, and G. Grasselli. (2013). Numerical simulation of acoustic emission in brittle rocks by two-dimensional finite-discrete element analysis. Geophysical Journal International. 195 (1): 423–43.

Lisjak, A, and G. Grasselli. (2010). Rock impact modelling using FEM/DEM. In Conference: 5th International Conference on Discrete Element Methods. London.

Lorig, L. J., C. Darcel, B. Damjanac, M. Pierce, and D. Billaux. (2015). Application of discrete fracture networks in mining and civil geomechanics. Mining Technology. 124 (4): 239–254.

Lu, Jun. (2002). Systematic identification of polyhedral rock blocks with arbitrary joints and faults. Computers and Geotechnics. 29 (1): 49–72. https://doi.org/10.1016/S0266-352X(01)00018-0.

Mahabadi, O. K., G. Grasselli, and A. Munjiza. (2010). Y-GUI: A graphical user interface and pre-processor for the combined finite-discrete element code, Y2D, Incorporating Material Heterogeneity. Computers & Geosciences. 36 (2): 241–52. https://doi.org/10.1016/j.cageo.2009.05.010.

Mahabadi, O. K., A. Lisjak, L. He, B. S. A. Tatone, P. Kaifosh, and G. Grasselli. (2016). Development of a new fully-parallel finite-discrete element code: Irazu. American Rock Mechanics Association. https://www.onepetro.org/conference-paper/ARMA-2016-516.

Mahabadi, O. K., A. Lisjak, A. Munjiza, and G. Grasselli. (2012). Y-Geo: New combined finite-discrete element numerical code for geomechanical applications. International Journal of Geomechanics.12 (6): 676–88.

Manzocchi, T. (2002). The connectivity of two-dimensional networks of spatially correlated fractures. Connectivity of two-dimensional networks. Journal of Water Resources Research. 38(9).

Marinos, P, V Marinos, and Evert Hoek. (2007). The geological strength index (GSI): A characterization tool for assessing engineering properties of rock masses. In Proceedings International Workshop on Rock Mass Classification for Underground Mining, 13–21. https://doi.org/10.1201/NOE0415450287.ch2.

Martin, C.D, and W.G Maybee. (2000). The strength of hard-rock pillars. International Journal of Rock Mechanics and Mining Sciences. 37 (8): 1239–46. https://doi.org/10.1016/S1365-1609(00)00032-0.

Mauldon, M. (1998). Estimating mean fracture trace length and density from observations in convex windows. Rock Mechanics and Rock Engineering. 31 (4): 201–16. https://doi.org/10.1007/s006030050021.

Mayer, J. (2015). Applications of uncertainty theory to rock mechanics and geotechnical mine design. M.Sc. Thesis, Dept Earth Sciences, Simon Fraser University. https://doi.org/10.13140/RG.2.1.2983.2085.

Mayer, J. D. Stead. (2017). Exploration into the causes of uncertainty in UDEC Grain Boundary Models. Computers and Geotechnics. 82. 110-123. 10.1016/j.compgeo.2016.10.003.

McQueen, L. B., A. Purwodihardjo, and S. V. L. Barrett. (2019). Rock mechanics for design of Brisbane tunnels and implications of recent thinking in relation to rock mass strength. Journal of Rock Mechanics and Geotechnical Engineering. https://doi.org/10.1016/j.jrmge.2019.02.001.

Mehranpour, M. H, and P.H. S. W. Kulatilake. (2017). Improvements for the smooth joint contact model of the particle flow code and its applications. Computers and Geotechnics. 87 (July): 163–77. https://doi.org/10.1016/j.compgeo.2017.02.012.

Meyer, T., and Einstein, H.H. (2002). Geologic stochastic modeling and connectivity assessment of fracture systems in the Boston area. Rock Mechanics and Rock Engineering, 35 (1), 23-44. doi:10.1007/s006030200007.

Miller, J. T. (2008). Crack coalescence in granite. PhD. Thesis, Massachusetts Institute of Technology. https://dspace.mit.edu/handle/1721.1/47771.

Min, K-B, and A. Thoraval. (2012). Comparison of two- and three-dimensional approaches for the numerical determination of equivalent mechanical properties of fractured rock masses. https://hal-ineris.archives-ouvertes.fr/ineris-00963408.

Mitelman, A, and D. Elmo. (2014). Modelling of blast-induced damage in tunnels using a hybrid finite-discrete numerical approach. Journal of Rock Mechanics and Geotechnical Engineering. 6 (6): 565–73. https://doi.org/10.1016/j.jrmge.2014.09.002.

Miyoshi, T, D. Elmo, and S. Rogers. (2018). Influence of data analysis when exploiting DFN model representation in the application of rock mass classification systems. Journal of Rock Mechanics and Geotechnical Engineering. 10 (6): 1046–62. https://doi.org/10.1016/j.jrmge.2018.08.003.

Moradian, Z, H. Einstein, and G. Ballivy. (2015). Detection of cracking levels in brittle rocks by parametric analysis of the acoustic emission signals. Rock Mechanics and Rock Engineering, June, 1–16. https://doi.org/10.1007/s00603-015-0775-1.

Munjiza, A. (2004). The combined finite-discrete element method. Wiley, Chichester. West Sussex, England; Hoboken, NJ.

Munjiza, A., and K. R. F. Andrews. (2000). Penalty function method for combined finite–discrete element systems comprising large number of separate bodies. International Journal for Numerical Methods in Engineering. 49 (11): 1377–96. https://doi.org/10.1002/1097-0207(20001220)49:11<1377::AID-NME6>3.0.CO;2-B.

Munjiza, A., D. R. J. Owen, and N. Bicanic. (1995a). A combined finite-discrete element method in transient dynamics of fracturing solids. Engineering Computations. 12 (2): 145–174.

Nasseri, M. H. B., B. Mohanty, and R. P. Young. (2006). Fracture toughness measurements and acoustic emission activity in brittle rocks. Pure and Applied Geophysics. 163 (5): 917–45. https://doi.org/10.1007/s00024-006-0064-8.

Nordlund, E., G. Radberg, and L. Jing. (1995). Determination of failure modes in jointed pillars by numerical modelling. Fractured and Jointed Rock Masses. Balkema, Rotterdam, 345–350.

Olofsson, and Fredriksson. (2005). Strategy for a numerical rock mechanics site descriptive model: Further Development of the Theoretical/Numerical Approach. SKB Rapport R-05-43.

Owen, D. R. J., Y. T. Feng, E. A. de Souza Neto, M. G. Cottrell, F. Wang, F. M. Andrade Pires, and J. Yu. (2004). The modelling of multi-fracturing solids and particulate media." International Journal for Numerical Methods in Engineering 60 (1): 317–339.

Owen, D.r.j., and Y.t. Feng. (2001). Parallelised finite/discrete element simulation of multi-fracturing solids and discrete systems. Engineering Computations. 18 (3/4): 557–76. https://doi.org/10.1108/02644400110387154.

Palmstrom, A. (1974). Characterization of jointing density and the quality of rock masses (in Norwegian). Norway: A.B. Berdal.

Pierce, M., P. Cundall, D. Potyondy, and D. Mas Ivars. (2007). A synthetic rock mass model for jointed rock. American Rock Mechanics Association. https://www.onepetro.org/conference-paper/ARMA-07-042.

Pine, R. J., J. S. Coggan, Z. N. Flynn, and D. Elmo. (2006). The development of a new numerical modelling approach for naturally fractured rock masses. Rock Mechanics and Rock Engineering. 39 (5): 395–419. https://doi.org/10.1007/s00603-006-0083-x.

Pine, R. J., and J. P. Harrison. (2003). Rock mass properties for engineering design. Quarterly. Journal of Engineering Geology and Hydrogeology. 36 (1): 5–16. https://doi.org/10.1144/1470-923601-031.

Priest, S. D. (1993). Discontinuity analysis for rock engineering. Springer Netherlands. https://www.springer.com/gp/book/9789401046565.

Reingold, Omer. (2008). Undirected connectivity in log-space. J. ACM 55 (4): 17:1–17:24. https://doi.org/10.1145/1391289.1391291.

Robinson, P. C. (1984). Connectivity, flow and transport in network models of fractured media. Ph.D. Thesis, St. Catherine's College, Oxford University, UK.

Rockfield Software Ltd. (2014). ELFEN 2D/3D Numerical Modelling Package. Swansea, UK: Rockfield Software Ltd.

Rogers, S. F., D. K. Kennard, W. S. Dershowitz, and A. Van As. (2007). Characterising the in situ fragmentation of a fractured rock mass using a discrete fracture network approach. American Rock Mechanics Association. https://www.onepetro.org/conference-paper/ARMA-07-018.

Rougier, E. (2011). The combined finite-discrete element method applied to the study of rock fracturing behaviour in 3D. American Rock Mechanics Association. https://www.onepetro.org/conference-paper/ARMA-11-517.

Schlotfeldt, P, D. Elmo, and B. Panton. (2018). Overhanging rock slope by design: An integrated approach using rock mass strength characterisation, large-scale numerical modelling and limit equilibrium methods. Journal of Rock Mechanics and Geotechnical Engineering. 10 (1): 72–90. https://doi.org/10.1016/j.jrmge.2017.09.008.

Shiloach, Y, and S. Even. (1981). An on-line edge-deletion problem. J. ACM 28 (1): 1–4. https://doi.org/10.1145/322234.322235.

Silverman, B. W. (1986). Density estimation for statistics and data analysis. London: Chapman and Hall. http://dx.doi.org/10.1007/978-1-4899-3324-9.

Stead, D., E. Eberhardt, and J. S. Coggan. (2006). Developments in the characterization of complex rock slope deformation and failure using numerical modelling techniques. Engineering Geology. 83 (1): 217–235.

Stead, D, and E. Eberhardt. (2013). Understanding the mechanics of large landslides. Invited Keynote and Paper. Italian J. Eng. Geol. Environ. Book Ser 6: 85–112.

Tang, C.A, and P.K Kaiser. (1998). Numerical simulation of cumulative damage and seismic energy release during brittle rock failure—Part I: Fundamentals. International Journal of Rock Mechanics and Mining Sciences. 35 (2): 113–21. https://doi.org/10.1016/S0148-9062(97)00009-0.

Tang, C.A., P. Lin, R.H.C. Wong., K.T. Chau. (2001). Analysis of crack coalescence in rock-like materials containing three flaws – Part II: numerical approach. Int. J. Rock Mechanics and Mining. Science. 38, 925-939.

Tang, Chun'an, and J. A. Hudson. (2010). Rock Failure Mechanisms : Explained and Illustrated. Boca Raton, FL : CRC Press.

Tannant, Dwayne D. (2015). Review of photogrammetry-based techniques for characterization and hazard assessment of rock faces. International Journal of Georesources and Environment - IJGE (Formerly Int'l J of Geohazards and Environment) 1 (2): 76–87. https://doi.org/10.15273/ijge.2015.02.009.

Tatone, B. S. A., and G. Grasselli. (2015). A calibration procedure for two-dimensional laboratory-scale hybrid finite–discrete element simulations. International Journal of Rock Mechanics and Mining Sciences. 75 (April): 56–72. https://doi.org/10.1016/j.ijrmms.2015.01.011.

Tatone, B.S.A. (2014). Investigating the evolution of rock discontinuity asperity degradation and void space morphology under direct shear. PhD. Thesis. Toronto, Canada: University of Toronto.

Tuckey, Z. (2012). An integrated field mapping-numerical modelling approach to characterising discontinuity persistence and intact rock bridges in large open pit slopes. M.Sc. Thesis, Science: Department of Earth Sciences. http://summit.sfu.ca/item/12708.

Vazaios, I., K. Farahmand, N. Vlachopoulos, and M.S. Diederichs. (2018). Effects of confinement on rock mass modulus: A synthetic rock mass modelling (SRM) study. Journal of Rock Mechanics and Geotechnical Engineering, March. https://doi.org/10.1016/j.jrmge.2018.01.002.

Vazaios, I. (2018). Modelling of hard rock masses with non-persistent joints to stress induced damage of deep induced damage of deep excavations. PhD Thesis. https://qspace.library.queensu.ca/handle/1974/24877.

Vivas, J., Z. Tuckey, D. Stead, A. Wolter, D. Elmo, and S. D'Ambra. (2013). Seepage characterization in high rock slopes using remote sensing. American Rock Mechanics Association. https://www.onepetro.org/conference-paper/ARMA-2013-462.

Vyazmensky, A, D. Stead, D. Elmo, and A. Moss. (2010). Numerical analysis of block caving-induced instability in large open pit slopes: A Finite Element/Discrete Element Approach. Rock Mechanics and Rock Engineering 43 (1): 21–39. https://doi.org/10.1007/s00603-009-0035-3.

Wand, M. P, and M. C Jones. (1995). Kernel Smoothing. London; New York: Chapman & Hall.

Wang, C., D.D. Tannant, P.A. Lilly. (2003). Numerical analysis of the stability of heavily jointed rock slopes using PFC2D. Int. J. Rock Mech. Min. Sci. 40 (2003), pp. 415-424.

Warburton, P. M. (1981). Vector stability analysis of an arbitrary polyhedral rock block with any number of free faces. International Journal of Rock Mechanics and Mining Sciences & Geomechanics. Abstracts 18 (5): 415–27. https://doi.org/10.1016/0148-9062(81)90005-X.

Warburton, P.M. (1987). Implications of keystone action for rock bolt support and block theory. International Journal of Rock Mechanics and Mining Sciences & Geomechanics. Abstracts 24 (5): 283–90. https://doi.org/10.1016/0148-9062(87)90864-3.

Wawrzynek, P., A.R. Ingraffea. (1989). An interactive approach to local remeshing around a propagation crack. Finite Element in Analysis & Design, 5. 87-96.

Xia, L, Q. Yu, Y. Chen, M. Li, G. Xue, and D. Chen. (2015). GeneralBlock: A C++ program for identifying and analyzing rock blocks formed by finite-sized fractures. In Environmental Software

Systems. Infrastructures, Services and Applications, edited by R. Denzer, R. M. Argent, G. Schimak, and J. Hřebíček, 512–19. IFIP Advances in Information and Communication Technology. Springer International Publishing.

Xu, C., P. A. Dowd, K. V. Mardia, and R. J. Fowell. (2006). A connectivity index for discrete fracture networks. Mathematical Geology. 38 (5): 611–34. https://doi.org/10.1007/s11004-006-9029-9.

Yang, X. X., P. Kulatilake, X. Chen, H. W. Jing, and S. Q. Yang. (2016). Particle flow modeling of rock blocks with nonpersistent open joints under uniaxial compression. International Journal of Geomechanics. 16 (6): 04016020. https://doi.org/10.1061/(ASCE)GM.1943-5622.0000649.

Zhang, L., and E. Herbert H. (1998). End bearing capacity of drilled shafts in rock. Journal of Geotechnical and Geoenvironmental Engineering. 124 (7): 574–84. https://doi.org/10.1061/(ASCE)1090-0241(1998)124:7(574).

Zhang, Y., D. Stead, and D. Elmo. (2015). Characterization of strength and damage of hard rock pillars using a synthetic rock mass method. Computers and Geotechnics. 65 (April): 56–72. https://doi.org/10.1016/j.compgeo.2014.12.002.

Zhang, Y. (2014). Modelling hard rock pillars using a synthetic rock mass approach. PhD. Thesis, Science: Department of Earth Sciences. http://summit.sfu.ca/item/13996.

Zhang, X, R. M. Harkness, and N.C. Last. (1992). Evaluation of connectivity characteristics of naturally jointed rock masses. Engineering Geology. 33 (1): 11–30. https://doi.org/10.1016/0013-7952(92)90032-T.

Zuo, L., X.Tan, W. Yu, and X. Hu. (2019). Fracture detection and numerical modeling for fractured Reservoirs. Energies 12 (3): 386. https://doi.org/10.3390/en12030386.

Appendices

Appendix A Procedure for How to Export 2D Sections from 3D Model

Step 1: Generating Random Fractures

In a very simple format, fractures can be created using a random triangle in a (100, 100, 100) 3D geometry field. This data is simple, and the same information can be extracted from different fracture data formats.

Step 2: Creating cross sections

Various number of cross sections can be presented as planes in the 3D field

Step 3: Calculating Cross-Section Fracture Algorithm

Detecting the intersection of the triangles and each cross-section plane. The intersections represent lines (fractures)

Step 4: Visualization

It can be seen that the triangle (3D fracture) results in lines in the cross sections.

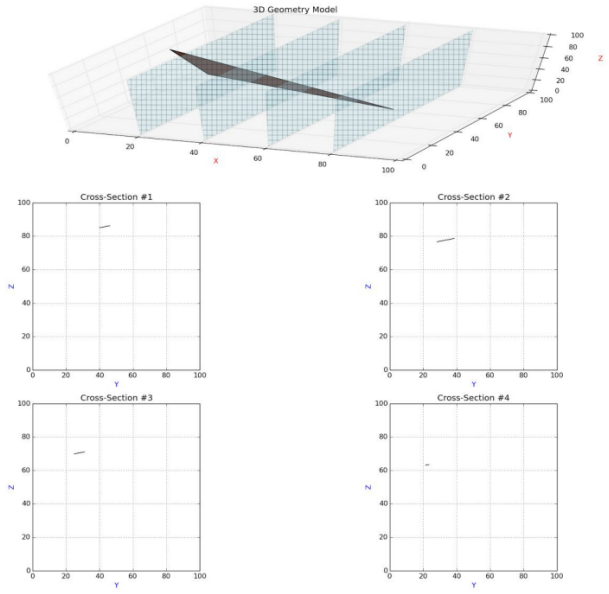

Figure A.1. Sample with one fracture.

The number of fractures then increased to 20 fractures.

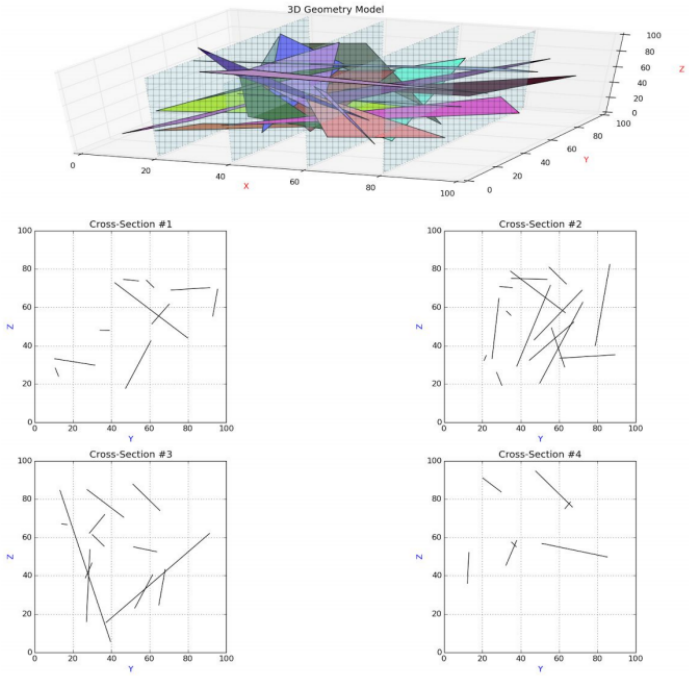

Figure A.2. Sample with 20 fractures.

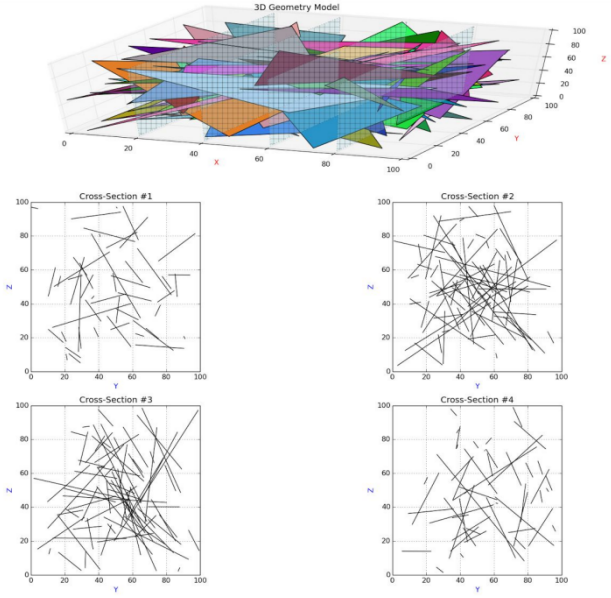

Figure A.3. Sample with 100 fractures.

Appendix B DFN Analysis and Cleaning Algorithms

Algorithm 1: Fracture Density - P_{20} $(1/m^2)$

```
   Input  : fracture lines, area
1  count ← 0
2  for line in fractureLines do
3  |  count ← count + 1
4  return count/area
```

Algorithm 2: Fracture Intensity - P_{21} (m/m^2)

```
   Input  : fracture lines, area
1  totalLength ← 0
2  for line in fractureLines do
3  |  totalLength ← totalLength + lineLength
4  return totalLength/area
```

Algorithm 3: Fracture Intersection Density $(1/m^2)$

```
   Input  : fracture lines, area
1  intersectionCount ← 0
2  for line1, line1Index in fractureLines do
3  |  for line2 in fractureLines[line1Index+1:end] do
4  |  |  if line1 intersects line2? then
5  |  |  |  intersectionCount ← intersectionCount + 1
6  return intersectionCount/area
```

Algorithm 4: Fracture Orientation Frequency

```
   Input  : fracture lines, number of bins
1  orientationFrequency ← [ ]
2  for line in fractureLines do
3      orientationFrequency(lineHorizontalOrientation)
   /* bin by angle, counting fractures per bin */
4  frequencyBins ← bin(orientationFrequency, numberOfBins)
5  return normalize(frequencyBins)
```

Algorithm 5: Fracture Orientation Persistence

```
   Input  : fracture lines, number of bins
1  orientationPersistence ← [ ]
2  for line in fractureLines do
       /* store both angle and length */
3      orientationPersistence.add((lineHorizontalOrientation, lineLength))
   /* bin by angle, summing up length of fractures per bin */
4  persistenceBins ← bin(orientationPersistence, numberOfBins)
5  return normalize(persistenceBins)
```

Algorithm 6: Bedding Excluder

```
   Input  : fracture lines, bedding length, bedding orientation
 1 beddingLines ← [ ]
 2 for line in fractureLines do
 3     if lineLength = beddingLength then
 4         if lineOrientation = beddingOrientation then
 5             beddingLines.add(line)
 6 fractureLinesWithoutBedding ← [ ]
 7 for line in fractureLines do
 8     if line not in beddingLines then
 9         fractureLinesWithoutBedding.add(line)
10 return fractureLinesWithoutBedding
```

Algorithm 7: Short Fracture Remover

```
   Input  : fracture lines, minimum length
 1 result ← [ ]
 2 for line in fractureLines do
 3     if lineLength > minimumLength then
 4         result.add(line)
 5 return result
```

Algorithm 8: Points Collapser

```
   Input  : fracture lines, buffer zone radius
 1 for line1 in fractureLines do
 2     for referencePoint in [line1 p1, line1 p2] do
 3         bufferZone ← createBufferZone(referencePoint, radius)
 4         for line2 in fractureLines[line1Index+1:end] do
 5             if line2 p1 within bufferZone then
 6                 line2 p1 ← referencePoint
 7             if line2 p2 within bufferZone then
 8                 line2 p2 ← referencePoint
 9 return fractureLines
```

Algorithm 9: Angle Adjuster

```
1  Function singleIteration
       Input  : fracture lines, minimum angle
2      for line1 in fractureLines do
3          for line2 in fractureLines [line1Index+1:end] do
4              if line1 intersects line2 then
5                  if intersectionAngle < minimumAngle then
6                      rotate(line1, minimumAngle - intersectionAngle)
7                      break
8      return fractureLines
1  Function angleAdjusterMonteCarlo
       Input  : fracture lines, minimum angle, number of iterations
2      bestLines ← [ ]
3      bestQuality ← 0
4      for iteration in numberOfIterations do
5          shuffledLines ← shuffle(fractureLines)
6          potentialLines ← singleIteration(shuffledLines, minimumAngle)
7          quality ← measureDFNQuality(potentialLines)
8          if quality > bestQuality then
9              bestLines ← potentialLines
10             bestQuality ← quality
11     return bestLines
```

Algorithm 10: Fracture Separator

```
Function singleIteration
    Input  : fracture lines, minimum distance
    for line1 in fractureLines do
        for line2 in fractureLines [line1Index+1:end] do
            if line1 intersects line2 then
                if distance(line1, line2) < minimumDistance then
                    separate line1 from line2 to minimumDistance
    return fractureLines
Function fractureSeparatorMonteCarlo
    Input  : fracture lines, minimum distance, number of iterations
    bestLines ← [ ]
    bestQuality ← 0
    for iteration in numberOfIterations do
        shuffledLines ← shuffle(fractureLines)
        potentialLines ← singleIteration(shuffledLines, minimumDistance)
        quality ← measureDFNQuality(potentialLines)
        if quality > bestQuality then
            bestLines ← potentialLines
            bestQuality ← quality
    return bestLines
```

Algorithm 11: KDE Comparison

```
Input  : initial KDE, other KDE
difference ← [ ]
for index in initialKDE.length do
    difference ← abs(initialKDE[index] - otherKDE[index])
return sum(difference)
```